

CO Oxidation Catalysis with Substituted Ceria Nanoparticles

by

Joseph Spanjaard Elias

B.A. Chemistry
Reed College, 2009

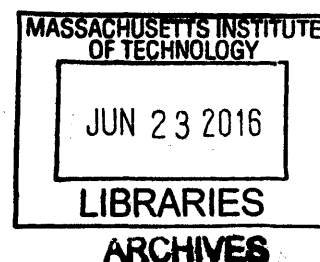
Submitted to the Department of Chemistry
in Partial Fulfillment of the Requirements for the Degree of

DOCTOR OF PHILOSOPHY
IN INORGANIC CHEMISTRY

at the

Massachusetts Institute of Technology

June 2016



© 2016 Massachusetts Institute of Technology.
All rights reserved

Signature redacted

Signature of Author: _____

Department of Chemistry
April 8, 2016

Signature redacted

Certified by: _____

Yang Shao-Horn
W.M. Keck Professor of Energy
Thesis Supervisor

Signature redacted

Accepted by: _____

Robert W. Field
Haslam and Dewey Professor of Chemistry
Chairman, Department Committee on Graduate Theses

This doctoral thesis has been examined by a committee of the Department of Chemistry as follows:

Signature redacted

Mircea Dincă
Associate Professor of Chemistry
Committee Chairman

Signature redacted

Yang Shao-Horn
W.M. Keck Professor of Energy
Thesis Supervisor

Signature redacted

Timothy M. Swager
John D. MacArthur Professor of Chemistry

CO Oxidation Catalysis with Substituted Ceria Nanoparticles

by

Joseph Spanjaard Elias

Submitted to the Department of Chemistry on April 8, 2016 in Partial Fulfillment of the Requirements for the Degree of Doctor of Philosophy in Inorganic Chemistry

Abstract

The low-temperature and cost-effective oxidation of carbon monoxide to carbon dioxide remains a fundamental challenge in heterogeneous catalysis that would enable a diverse range of technologies for electrochemical storage and respiratory health. The development of new catalysts is often driven by high-throughput screening and many of the resulting compounds are mixed-phase, which obscures a rigorous identification of active sites and mechanisms at play for catalysis. In this thesis, the preparation of substituted ceria nanoparticles is described to bring about a fundamental understanding of the structure of the active sites, mechanism and design descriptors for CO oxidation on ceria-based catalysts.

Monodisperse, single-phase nanoparticles of late first-row transition-metal-substituted ceria ($M_yCe_{1-y}O_{2-x}$, $M = Mn, Fe, Co, Ni$ and Cu) are prepared from the controlled pyrolysis of heterobimetallic precursors in amine surfactant solutions. By means of kinetic analyses, X-ray absorption spectroscopy (XAS) and transmission electron microscopy (TEM), the active site for CO oxidation catalysis is identified as atomically-dispersed, square-planar M^{3+} and M^{2+} moieties substituted into the surface of the ceria lattice. The introduction of CuO does not contribute to the catalytic activity of $Cu_yCe_{1-y}O_{2-x}$, lending support to the hypothesis that the substituted ceria itself is responsible for the catalytic rate enhancement in mixed-phased catalysts like CuO/CeO₂.

Under oxygen-rich conditions, the kinetic parameters for CO oxidation are consistent with lattice oxygen from the dispersed copper sites contributing directly to the oxidation of CO in the rate-determining step. *In-situ* X-ray photoelectron spectroscopy (XPS) and FTIR studies indicate that adsorbed CO can be directly oxidized to CO₂ in the absence of gaseous O₂, while *in-situ* XAS confirms that electron transfer is localized to the copper sites. XAS studies demonstrate that the reversible reducibility of dispersed copper ions is a contributing factor for the special catalytic activity of CuO/CeO₂ catalysts.

The oxygen-ion vacancy formation energy is introduced as an activity descriptor to rationalize trends in the catalytic activities measured for $M_yCe_{1-y}O_{2-x}$ nanoparticles that span over three orders of magnitude. As such, the DFT-calculated vacancy formation energy serves to guide in the rational design of catalysts through computational, rather than experimental, screening of candidate compounds for CO oxidation catalysis.

Thesis Supervisor: Yang Shao-Horn

Title: W.M. Keck Professor of Energy

For Maggie

Table of Contents

Title Page	1
Thesis Committee	3
Abstract	5
Dedication	7
Table of Contents	9
List of Figures	11
List of Tables	17
List of Abbreviations	19
Chapter 1 – Introduction and Motivation	23
1.1 The Global Relevance of Heterogeneous Catalysis	24
1.2 Rate Laws and Free Energy Diagrams	26
1.3 Linear Free-Energy Scaling Relationships	29
1.4 Mechanisms for CO Oxidation Catalysis	33
1.4.1 The Langmuir-Hinshelwood Mechanism for CO Oxidation Catalysis	34
1.4.2 The Mars-van Krevelen Mechanism for CO Oxidation Catalysis	36
1.5 Low-Temperature CO Oxidation Catalysts	38
1.5.1 Au/TiO ₂ and Other Gold-Based Catalysts	38
1.5.2 Nanoparticulate Co ₃ O ₄	41
1.5.3 Unsupported and Supported CuO Catalysts	42
1.5.4 Three Open Questions	49
1.6 Scope of the Thesis	51
1.7 References	52
Chapter 2 – The Incorporation of Metal Ions into the Lattice of CeO₂	59
2.1 Introduction	60
2.2 Synthesis of M _{0.1} Ce _{0.9} O _{2-x} (M = Mn, Fe, Co, Ni, Cu)	60
2.3 Identification of the local structure of transition-metal ions in M _{0.1} Ce _{0.9} O _{2-x}	65
2.4 CO oxidation catalysis on CeO ₂ and Cu _{0.1} Ce _{0.9} O _{2-x}	74
2.5 Conclusions	76
2.6 Experimental Methods	77
2.7 References	95
Chapter 3 – Identification of the Active Phase in Cu_yCe_{1-y}O_{2-x}	101
3.1 Introduction	102
3.2 CO Oxidation Catalysis on CuO/Cu _y Ce _{1-y} O _{2-x} catalysts	102
3.3 Determination of the Surface Segregation and Speciation of Copper in Cu _y Ce _{1-y} O _{2-x}	106
3.4 Conclusions	111
3.5 Experimental Methods	112
3.6 References	126
Chapter 4 – The Mechanism for CO Oxidation on Cu_yCe_{1-y}O_{2-x}	129
4.1 Introduction:	130
4.2 Partial Pressure Dependence of CO Oxidation Catalysis	130
4.3 Evolution of Surface Adsorbates	133
4.4 Structural Evolution of Cu in Cu _y Ce _{1-y} O _{2-x}	140
4.5 Revisiting the Mechanism for CO Oxidation on Cu _y Ce _{1-y} O _{2-x}	143
4.6 Conclusions	147
4.7 Experimental Methods	147
4.8 References	152

Table of Contents

Chapter 5 – A Design Descriptor for CO Oxidation on Substituted Ceria	155
5.1 Introduction	156
5.2 General Trends in CO Oxidation Activity for $M_{0.1}Ce_{0.9}O_{2-x}$	156
5.3 E_{vac} as a Descriptor for CO Oxidation on $M_{0.1}Ce_{0.9}O_{2-x}$	160
5.4 Going Beyond $Cu_{0.1}Ce_{0.9}O_{2-x}$ and E_{vac}	162
5.5 Conclusions	165
5.6 Experimental Methods	166
5.7 References	168
Appendix A – Derivation of Rate Expressions	171
A.1 Mars-van Krevelen	172
A.2 Langmuir-Hinshelwood	174
Biographical Note	179
Curriculum Vitae	181
Acknowledgements	183

List of Figures

- Figure 1.1** Reaction coordinate diagram for an arbitrary reaction with (gray trace) and without (black trace) the aid of a heterogeneous catalyst surface. 27
- Figure 1.2** Linear free-energy scaling relationships and their implications for catalysis. (A) Reaction coordinate diagram demonstrating the case when there is a linear relationship between ΔG^\ddagger and ΔG and (B) a schematic Sabatier plot using linear free-energy relationships. 30
- Figure 1.3** The specific catalytic activity for (A) oxygen reduction and (B) CO oxidation as a function of the DFT-calculated d-band center for platinum alloys. Measurements for ORR were recorded in 0.1 M HClO₄ and those for CO oxidation were acquired in a reactor with 0.02 atm CO and 0.01 atm O₂ at a flow rate of 0.67 mL min⁻¹ mg⁻¹ at 200 °C. Adapted with permission from references 22 and 28. 32
- Figure 1.4** Mechanisms for CO oxidation; (A) the Langmuir-Hinshelwood and (B) the Mars-van Krevelen mechanisms. 35
- Figure 1.5** Mass-normalized rates of CO oxidation on CuO/CeO₂, Au/TiO₂ and nanoparticulate Co₃O₄. Rates were measured under carbon monoxide lean conditions in differential flow conditions. Data taken from references 99 (CuO/CeO₂), 68 (Au/TiO₂) and 54 (Co₃O₄). 38
- Figure 1.6** Proposed mechanisms for CO oxidation over CuO/CeO₂ catalysts; (A) the Flytzani-Stephanopoulos, (B) Harrison and (C) Martínez-Arias models. 45
- Figure 2.1** The synthesis of M_{0.1}Ce_{0.9}O_{2-x} from heterobimetallic 3-MeO-salpn complexes. Representative crystal structures for Ni^{II}-Ce^{III}-3-MeO-salpn and Cu^{II}-Ce^{III}-3-MeO-salpn are included, with thermal ellipsoids plotted at 50% probability and hydrogen atoms omitted for clarity. 61
- Figure 2.2** The crystal structures of Co^{III}-Ce^{III}-3-MeO-salpn, Ni^{II}-Ce^{III}-3-MeO-salpn and Cu^{II}-Ce^{III}-3-MeO-salpn. Thermal ellipsoids are plotted at 50% probability and hydrogen atoms are omitted for clarity. 62
- Figure 2.3** PXRD patterns for as-synthesized nanocrystalline M_{0.1}Ce_{0.9}O_{2-x} and CeO₂ compounds taken at room temperature (copper K α source). 63
- Figure 2.4** TEM, histogram of particle sizes, HRTEM and FFT images of as-synthesized M_{0.1}Ce_{0.9}O_{2-x}. 64
- Figure 2.5** The crystal habit of M_{0.1}Ce_{0.9}O_{2-x} catalysts; (A) a model truncated octahedron, (B) crystallographic assignments at the [01 $\bar{1}$] zone axis and (C) a representative HRTEM of Fe_{0.1}Ce_{0.9}O_{2-x} at the [01 $\bar{1}$] zone axis. Crystallographic assignments of the FFT of the image in (C) are given in the inset. 64
- Figure 2.6** Cerium L_{III}-edge and transition-metal K-edge and XAS spectra for annealed CeO₂, Cu_{0.1}Ce_{0.9}O_{2-x} and Fe_{0.1}Ce_{0.9}O_{2-x} samples; (A) Cerium L_{III}-edge XANES spectra and (B) the magnitude of the k^2 -weighted Fourier transform of the EXAFS of Cu_{0.1}Ce_{0.9}O_{2-x} (purple), Fe_{0.1}Ce_{0.9}O_{2-x} (green) and ceria references; (C) Iron K-edge XANES spectra and (D) the magnitude of the k^2 -weighted Fourier transform of the EXAFS of Fe_{0.1}Ce_{0.9}O_{2-x} (green) and relevant iron oxides; (E) Copper K-edge XANES spectra and (F) the magnitude of the k^2 -weighted Fourier transform of the EXAFS of Cu_{0.1}Ce_{0.9}O_{2-x} (purple) and relevant copper oxides. Ce L_{III}-edge spectra were collected in transmission mode, while Cu and Fe K-edge spectra were collected in total fluorescence yield mode. Lighter traces in (B), (D) and (F) are results of EXAFS fitting (see Tables 2.6 – 2.7). 67

- Figure 2.7** XAS spectra for $\text{Mn}_{0.1}\text{Ce}_{0.9}\text{O}_{2-x}$. (A) Ce L_{III}-edge XANES and (B) the k^2 -weighted Fourier transform of the EXAFS spectra for $\text{Mn}_{0.1}\text{Ce}_{0.9}\text{O}_{2-x}$ and nanometer-sized CeO_2 ; (C) Mn K-edge XANES and (D) the k^2 -weighted Fourier transform of the EXAFS spectra for $\text{Mn}_{0.1}\text{Ce}_{0.9}\text{O}_{2-x}$ and relevant binary oxides and oxy-hydroxides of Mn. Lighter trace in (B) is the result of EXAFS fitting. 68
- Figure 2.8** XAS spectra for $\text{Co}_{0.1}\text{Ce}_{0.9}\text{O}_{2-x}$. (A) Ce L_{III}-edge XANES and (B) the k^2 -weighted Fourier transform of the EXAFS spectra for $\text{Co}_{0.1}\text{Ce}_{0.9}\text{O}_{2-x}$ and nanometer-sized CeO_2 ; (C) Co K-edge XANES and (D) the k^2 -weighted Fourier transform of the EXAFS spectra for $\text{Co}_{0.1}\text{Ce}_{0.9}\text{O}_{2-x}$ and relevant binary oxides and hydroxides of Co. The lighter traces in (B) and (D) are results from EXAFS fitting. 69
- Figure 2.9** XAS spectra for $\text{Ni}_{0.1}\text{Ce}_{0.9}\text{O}_{2-x}$. (A) Ce L_{III}-edge XANES and (B) the k^2 -weighted Fourier transform of the EXAFS spectra for $\text{Ni}_{0.1}\text{Ce}_{0.9}\text{O}_{2-x}$ and nanometer-sized CeO_2 ; (C) Ni K-edge XANES and (D) the k^2 -weighted Fourier transform of the EXAFS spectra for $\text{Ni}_{0.1}\text{Ce}_{0.9}\text{O}_{2-x}$ and relevant binary oxides of Ni. The lighter traces in (B) and (D) are results from EXAFS fitting. 70
- Figure 2.10** Oxygen K-edge and Copper L_{II,III}-edge XAS spectra, collected in partial fluorescence yield mode, for annealed $\text{Cu}_{0.1}\text{Ce}_{0.9}\text{O}_{2-x}$; (A) Oxygen K-edge XAS spectra and (B) Copper L_{II,III}-edge XAS spectra of $\text{Cu}_{0.1}\text{Ce}_{0.9}\text{O}_{2-x}$ (purple) and reference oxides. Dashed grey lines represent charge-transfer multiplet satellites for Cu^{3+} . 71
- Figure 2.11** Phase diagram and local molecular structure computed for $\text{Cu}^{(4-x)+}_2\text{Ce}_{34}\text{O}_{72-x}$ models; (A) computed ΔG_{F} as a function of oxygen chemical potential for three oxidation states of copper in $\text{Cu}^{(4-x)+}_2\text{Ce}_{34}\text{O}_{72-x}$; the local coordination of (B) Ce^{4+} in CeO_2 and of (C) Cu^{3+} in $\text{Cu}^{3+}_2\text{Ce}_{34}\text{O}_{71}$ as viewed down the [111] zone axis. The pressure dependence was calculated at 700 K, with 0.21 atm O_2 indicated by the dashed grey lines and the model $\text{Cu}^{4+}_2\text{Ce}_{34}\text{O}_{72}$ was taken as the reference for computing ΔG_{F} . 73
- Figure 2.12** CO oxidation catalysis on annealed 3 nm $\text{Cu}_{0.1}\text{Ce}_{0.9}\text{O}_{2-x}$, 3 nm CeO_2 and commercial 5 μm CeO_2 (Sigma-Aldrich); (A) “Light off” curves and (B) Area-normalized Arrhenius plots, measured in 1% CO, 2.5% O_2 balanced in He at a flow rate of 1300 mL min^{-1} $\text{g}^{-1}_{\text{cat}}$ for 20 mg catalyst loadings. 75
- Figure 3.1** Phase identification of $\text{CuO/Cu}_y\text{Ce}_{1-y}\text{O}_{2-x}$ compounds by (A) PXRD acquired with Cu $\text{K}\alpha$ radiation and (B) HRTEM. Asterisks indicate CuO phases in A. Shown in B are representative FFT images of the two phases in $\text{CuO/Cu}_{0.05}\text{Ce}_{0.95}\text{O}_{2-x}$ outlined in the bright-field image; outlined in blue are nanoparticles of $\text{Cu}_{0.05}\text{Ce}_{0.95}\text{O}_{2-x}$ (the middle nanoparticle was chosen for the FFT) on the surface of a large crystal of CuO, outlined by the red box. 103
- Figure 3.2** Raman spectra of $\text{Cu}_y\text{Ce}_{1-y}\text{O}_{2-x}$ and $\text{CuO/Cu}_y\text{Ce}_{1-y}\text{O}_{2-x}$ acquired at room temperature. (A) Raw spectra and (B) measured frequency of the $\text{F}_{2\text{g}}$ mode as a function of copper substitution in $\text{Cu}_y\text{Ce}_{1-y}\text{O}_{2-x}$ (y). 104
- Figure 3.3** Arrhenius plots for CO oxidation over $\text{CuO/Cu}_y\text{Ce}_{1-y}\text{O}_{2-x}$ (A) normalized by mass and (B) normalized by surface copper site in $\text{Cu}_y\text{Ce}_{1-y}\text{O}_{2-x}$. Rates were measured in 1% CO, 2.5% O_2 balanced in He at a flow rate of 1300 mL min^{-1} g^{-1} and TOFs were estimated assuming homogeneous copper substitution in $\text{Cu}_y\text{Ce}_{1-y}\text{O}_{2-x}$. 105
- Figure 3.4** Arrhenius plots for CO oxidation over $\text{CuO/Cu}_y\text{Ce}_{1-y}\text{O}_{2-x}$ normalized by surface copper site in $\text{Cu}_y\text{Ce}_{1-y}\text{O}_{2-x}$ assuming surface segregation of copper. Rates were measured in 1% CO, 2.5% O_2 balanced in He at a flow rate of 1300 mL min^{-1} g^{-1} . 105
- Figure 3.5** STEM-EELS analysis of a cluster of three $\text{Cu}_{0.08}\text{Ce}_{0.92}\text{O}_{2-x}$ nanoparticles. (A) Ce $\text{M}_{4,5}$ EELS spectra corresponding to surface and core areas highlighted in (B), (B) Dark field

image acquired simultaneously with the spectrum image, (C) map corresponding to the signal in the ranges 880.4–882.4 eV and 898.4–900.4 eV (red windows in (A)), (D) map corresponding to the signal in the ranges 882.4–884.4 eV and 900.4–902.4 eV (green windows in (A)) and (E) sum of (C) and (D); scale bars: 5 nm. 106

Figure 3.6 Computational modeling of $\text{Cu}_y\text{Ce}_{1-y}\text{O}_{2-x}$ catalysts by DFT + U and artificial neural network potential Monte-Carlo simulations. (A) Relative Gibbs free energy of formation for three {111}-terminated $\text{Cu}_2\text{Ce}_{34}\text{O}_{72-x}$ models at various oxidation states, (B) radial probability of Cu substitution and (C) pair distribution function for Cu-Cu distances in 3.6 nm $\text{Cu}_{54}\text{Ce}_{405}\text{O}_{834}$ nanoparticles. Relative values for ΔG_f were calculated at 700 K using the oxygen chemical potential associated with 0.21 atm O_2 ; Monte Carlo calculations were carried out simulating annealing from 5000 to 300 K. 107

Figure 3.7 DFT + U -calculated phase diagrams for (A) ss-, (B) nnn- and (C) nn- $\text{Cu}_2\text{Ce}_{34}\text{O}_{72-x}$ slab models computed at 700 K. The dashed grey lines correspond to 0.21 atm O_2 (i.e. air). The lowest-energy slabs for each of the three models (D), corresponding to the stoichiometry $\text{Cu}^{3+}_2\text{Ce}_{34}\text{O}_{71}$, are also shown for comparison. 108

Figure 3.8 Cu K-edge XAS measurements of $\text{Cu}_{0.08}\text{Ce}_{0.92}\text{O}_{2-x}$ performed under reaction conditions; (A) near-edge spectra and (B) the Fourier transform of the EXAFS in air at 25 °C (blue traces), in 1% CO + 2.5% O_2 at 25 °C (green traces) and in 1% CO + 2.5% O_2 at 300 °C (orange traces). Measurements were performed in fluorescent yield mode. When calibrated to the copper oxide references in (A), the mean oxidation states were determined to be 2.86+ (air at 25 °C), 2.85+ (1% CO + 2.5% O_2 at 25 °C) and 2.81+ (1% CO + 2.5% O_2 at 300 °C). 109

Figure 3.9 STEM-EELS analysis of an individual $\text{Mn}_{0.1}\text{Ce}_{0.9}\text{O}_{2-x}$ nanoparticle. (A) Dark field image acquired simultaneously with the spectrum images (scale bar: 2 nm), (B) Ce $\text{M}_{4,5}$ -edge spectra corresponding to the boxed regions in A. The dotted line in B refers to the peak at 882 eV ascribed to Ce^{3+} . 110

Figure 3.10 Graphical solution of the surface area ratio as function of the surface distance from the particle center. The solid black and red lines indicate the {111} and {100} surface areas, respectively. The dotted black line corresponds to 1/3 of the {111} surface area and the blue circle points out the {111}:{100} ratio of 3:1. 123

Figure 3.11 Comparison of the cohesive energies predicted by the ANN potential and their DFT reference values. The diagonal (blue line) corresponds to perfect correlation. The energies of structures from the training and test sets are shown as black and red points, respectively. 125

Figure 4.1 The partial pressure dependence of CO oxidation on $\text{Cu}_{0.1}\text{Ce}_{0.9}\text{O}_{2-x}$; (A) recorded at 75 °C and (B) 300 °C under differential flow conditions. Reaction rates were measured with flow rates of $1300 \text{ mL min}^{-1} \text{ g}^{-1}_{\text{cat}}$ for 20 mg catalyst loadings, holding either the partial pressure of CO (0.01 atm) or O_2 (0.025 atm) constant while varying the partial pressure of the other gas. 131

Figure 4.2 Schematic reaction mechanism for CO oxidation on $\text{Cu}_y\text{Ce}_{1-y}\text{O}_{2-x}$ catalysts. Light grey wedges correspond to Ce – O bonds in the subsurface layer. 132

Figure 4.3 DRIFTS spectra (top) and difference spectra (Δ , bottom) for $\text{Cu}_{0.1}\text{Ce}_{0.9}\text{O}_{2-x}$ upon thermal desorption of CO_2 . CO_2 was first adsorbed at rt and then desorbed in He. Spectra were recorded every 20 °C. 133

Figure 4.4 DRIFTS spectra (top) and difference spectra (Δ , bottom) for $\text{Cu}_{0.1}\text{Ce}_{0.9}\text{O}_{2-x}$ upon heating under CO_2 desorption conditions. (A) $\text{Cu}_{0.1}\text{Ce}_{0.9}\text{O}_{2-x}$ heated under a flow of 1% CO_2 and (B) CO_2 was adsorbed and then the catalyst was heated in 2.5% O_2 . Spectra were recorded every 20 °C. 135

List of Figures

- Figure 4.5** DRIFTS spectra (top) and difference spectra (Δ , bottom) for $\text{Cu}_{0.1}\text{Ce}_{0.9}\text{O}_{2-x}$ upon CO desorption experiments in He. CO was adsorbed and then the catalyst was heated in He; shown in (A) is the carbonate region and in (B) the CO region. Spectra were recorded every 20 °C. 136
- Figure 4.6** DRIFTS spectra (top) and difference spectra (Δ , bottom) for $\text{Cu}_{0.1}\text{Ce}_{0.9}\text{O}_{2-x}$ upon heating in an oxygen-rich CO oxidation stream. The catalyst was heated under a flow of 1% CO + 2.5% O_2 , recording spectra every 20 °C. 137
- Figure 4.7** Raw NAP-XPS spectra for $\text{Cu}_{0.1}\text{Ce}_{0.9}\text{O}_{2-x}$ during and after annealing at 400 °C in 75 mTorr O_2 and under different CO oxidation conditions. Shown are the O and C 1s spectra acquired at 650 and 490 eV, respectively. Circles indicate data from cycle 1 while solid lines indicate data from cycle 2. 138
- Figure 4.8** Fitted NAP-XPS spectra at four partial-pressure conditions at the (A) O 1s and (B) C 1s regions and (C) the surface-normalized intensities at the O 1s region as a function of oxygen partial pressure at 300 °C. The incident energies used for NAP-XPS were 490 eV (C 1s) and 650 eV (O 1s), and only data from the first cycle are displayed in A and B. 139
- Figure 4.9** Cu K-edge XANES spectra of $\text{Cu}_{0.1}\text{Ce}_{0.9}\text{O}_{2-x}$ in 1% CO and 300 °C as a function of O_2 partial pressure cycling. The raw Cu K-edge spectra are given in (A), while (B) tracks the nominal oxidation state of the Cu absorber as a function of oxygen partial pressure. 141
- Figure 4.10** Structural changes in $\text{Cu}_{0.1}\text{Ce}_{0.9}\text{O}_{2-x}$ under CO oxidation conditions at 300 °C as measured by Cu K-edge EXAFS. (A) The k^2 -weighted magnitude of the Fourier transform of the EXAFS and (B) the extracted changes in the first coordination sphere of Cu in $\text{Cu}_{0.1}\text{Ce}_{0.9}\text{O}_{2-x}$ in 1% CO as a function of oxygen partial pressure. 142
- Figure 4.11** The DFT-computed reaction mechanism of CO oxidation on {111}-terminated $\text{Cu}_y\text{Ce}_{1-y}\text{O}_{2-x}$. For each step, the total energy is the sum of the slab (including bound adsorbates) and any non-participating adsorbates. The calculated total reaction energy for the overall reaction $2\text{CO} + \text{O}_2 \rightarrow 2\text{CO}_2$ is given by the dashed grey line. CO adsorbs to Cu^{3+} in step 1 followed by the oxygen-atom transfer in step 2 to form a bent CO_2 adduct. CO_2 desorbs in step 3 to leave an oxygen vacancy on the surface. O_2 adsorbs to this vacancy forming an O_2^{2-} intermediate (step 4), which then adsorbs the second equivalent of CO (step 5). A second oxygen-atom transfer to CO (step 6) gives another bent CO_2 intermediate, which desorbs in step 7 and closes the catalytic loop. 144
- Figure 4.12** The density of states for oxidized ($\text{Cu}^{3+}_2\text{Ce}_{34}\text{O}_{71}$) and reduced ($\text{Cu}^{2+}_2\text{Ce}_{34}\text{O}_{71}$) as calculated for {111}-terminated slab models for $\text{Cu}_{0.1}\text{Ce}_{0.9}\text{O}_{2-x}$. Highlighted in purple are the occupied and unoccupied partial density of states of copper parentage. 145
- Figure 4.13** The hydroxide insertion reaction of carbon monoxide by a Ni(II) PNP pincer complex (A) and the crystal structure of the resulting η^1 hydroxycarbonyl adduct (B). Hydrogen atoms (besides the hydroxycarbonyl) are omitted for clarity. Crystallographic data are from reference 28. 145
- Figure 4.14** Reaction coordinate diagram for CO adsorption to nn- $\text{Cu}_2\text{Ce}_{34}\text{O}_{71}$. Intermediate 1 simulates non-interacting gaseous CO. Intermediates 2 – 4 were calculated by constraining the CO adsorbate 2.4, 2.1 and 1.9 Å from the copper center, while intermediate 5 represents fully adsorbed CO. Total energies ($\text{Cu}_2\text{Ce}_{34}\text{O}_{71} + \text{CO}$) along the adsorption pathway were calculated by constraining the z-height of the carbon of CO. 146
- Figure 5.1** CO oxidation catalysis on $\text{M}_{0.1}\text{Ce}_{0.9}\text{O}_{2-x}$ nanoparticles; (A) light-off curves and (B) site-normalized Arrhenius plots for CO oxidation under CO lean conditions. Rates were measured at a flow rate of 1300 mL min^{-1} g^{-1} and with 0.01 atm CO and 0.025 atm O_2

balanced in He. TOFs were estimated assuming homogeneous transition-metal substitution in $M_{0.1}Ce_{0.9}O_{2-x}$. 157

Figure 5.2 The partial pressure dependence of CO oxidation on $M_{0.1}Ce_{0.9}O_{2-x}$ catalysts; (B) $Mn_{0.1}Ce_{0.9}O_{2-x}$ at 195 °C, (B) $Fe_{0.1}Ce_{0.9}O_{2-x}$ at 195 °C, (C) $Co_{0.1}Ce_{0.9}O_{2-x}$ at 120 °C and (D) $Ni_{0.1}Ce_{0.9}O_{2-x}$ at 120 °C. Reaction rates were measured with flow rates of $1300 \text{ mL min}^{-1} \text{ g}^{-1}_{cat}$ for 20 mg catalyst loadings, holding either the partial pressure of CO (0.01 atm) or O_2 (0.025 atm) constant while varying the partial pressure of the other gas. 158

Figure 5.3 Calculated phase diagrams for {111}-terminated $nn-M_2Ce_{34}O_{72-x}$ model slabs for M = (A) Mn, (B) Fe, (C) Co and (D) Ni. Gibbs free energies of formation, relative to $nn-M_2Ce_{34}O_{72}$ for each metal, were computed at 700 K with energies calculated at the DFT + U level of theory. The dashed grey lines correspond to 0.21 atm O_2 . 160

Figure 5.4 The lowest energy structures calculated for {111}-terminated $nn-M_2Ce_{34}O_{72-x}$ slabs at 700 K and 0.21 atm O_2 , as determined by Figure 5.3. 161

Figure 5.5 Oxygen vacancy formation in {111}-terminated slabs of $M_2Ce_{34}O_{71}$. 161

Figure 5.6 Turnover frequencies for $M_{0.1}Ce_{0.9}O_{2-x}$ measured at 100 °C as a function of the calculated oxygen ion vacancy formation energies of $M_2Ce_{34}O_{71}$. 162

Figure 5.7 Reversible CO oxidation at the C cluster of CODH II; (A) the proposed mechanism and (B) the structure of the key reactive intermediate (C_{redCO_2}) from crystallography. Hydrogen atoms are omitted for clarity. Crystallographic data are from reference 13. 165

List of Tables

Table 2.1 Crystallographic and refinement parameters for $\text{Co}^{\text{III}}\text{-Ce}^{\text{III}}\text{-3-MeO-salpn}$, $\text{Ni}^{\text{II}}\text{-Ce}^{\text{III}}\text{-3-MeO-salpn}$ and $\text{Cu}^{\text{II}}\text{-Ce}^{\text{III}}\text{-3-MeO-salpn}$.	82
Table 2.2 Crystallographic and refinement parameters for $\text{M}_y\text{Ce}_{1-y}\text{O}_{2-x}$ powders, their BET surface areas (S_{BET}) and elemental compositions (y). Standard uncertainties in the last digits are included in parentheses.	83
Table 2.3 Crystallographic and refinement parameters for post-mortem analysis of $\text{Cu}_{0.1}\text{Ce}_{0.9}\text{O}_{2-x}$. Standard uncertainties in the last digits are included in parentheses.	83
Table 2.4 Fourier transform and fitting parameters for EXAFS.	87
Table 2.5 Edge energies (E_0) and nominal oxidation states from transition-metal K-edge XANES spectra of $\text{M}_{0.1}\text{Ce}_{0.9}\text{O}_{2-x}$ and binary oxides. Values for E_0 were taken at half the edge jump and estimated oxidation states for $\text{M}_{0.1}\text{Ce}_{0.9}\text{O}_{2-x}$ were calculated from calibration curves with the binary oxides.	87
Table 2.6 Parameters from the refinement of cerium L_{III} -edge EXAFS of $\text{M}_{0.1}\text{Ce}_{0.9}\text{O}_{2-x}$ powders. Standard uncertainties in the last digits are included in parentheses.	88
Table 2.7 Parameters from the refinement of cerium L_{III} -edge EXAFS of $\text{M}_{0.1}\text{Ce}_{0.9}\text{O}_{2-x}$ powders fixing the path degeneracies. Standard uncertainties in the last digits are included in parentheses.	88
Table 2.8 Parameters from the refinement of transition-metal K-edge EXAFS of $\text{M}_{0.1}\text{Ce}_{0.9}\text{O}_{2-x}$ powders from binary oxides. Standard uncertainties in the last digits are included in parentheses.	89
Table 2.9 Oxygen non-stoichiometry and vacancy content as determined by TGA and XPS analysis of Ce 3d spectra.	92
Table 2.10 DFT energies of formation of bulk $\text{Cu}^{(4-2x)+}\text{Ce}_{31}\text{O}_{64-x}$ from CuO and CeO_2 .	94
Table 3.1 Apparent activation energies (E_A) for CO oxidation on $\text{CuO}/\text{Cu}_y\text{Ce}_{1-y}\text{O}_{2-x}$ powders, their BET surface areas, (A_S) and crystallographic parameters for the $\text{Cu}_y\text{Ce}_{1-y}\text{O}_{2-x}$ phase. Standard uncertainties in the last digits are included in parentheses.	114
Table 3.2 Crystallographic parameters for the CuO phase in $\text{CuO}/\text{Cu}_y\text{Ce}_{1-y}\text{O}_{2-x}$ powders. Standard uncertainties in the last digits are included in parentheses.	114
Table 3.3 Parameters from the refinement of Cu K-edge EXAFS of $\text{Cu}_{0.1}\text{Ce}_{0.9}\text{O}_{2-x}$ powders under catalytically-relevant conditions at room temperature and 300 °C. Standard uncertainties in the last digits are included in parentheses.	117
Table 3.4 Parameters of the radial basis function (Behler <i>symmetry function</i>) G^2 of reference ⁴² used for the description of the local atomic structure within a cutoff radius of $R_c = 6.5 \text{ \AA}$.	124
Table 3.5 Parameters of the angular basis function (Behler <i>symmetry function</i>) G^4 of reference ⁴² used for the description of the local atomic structure within a cutoff radius of $R_c = 6.5 \text{ \AA}$. Each set of parameters listed in the table corresponds to 6 equivalent functions for the 6 possible combinations of atomic species (Ce-Ce, Ce-O, Ce-Cu, O-O, O-Cu, Cu-Cu) among neighboring atom pairs in the local structural environment of an atom (Ce, O, Cu).	125
Table 4.1 NAP-XPS fitting parameters for studies on $\text{Cu}_{0.08}\text{Ce}_{0.092}\text{O}_{2-x}$ and CeO_{2-x} in the C 1s region.	149

List of Tables

- Table 4.2** NAP-XPS fitting parameters for studies on $\text{Cu}_{0.08}\text{Ce}_{0.092}\text{O}_{2-x}$ and CeO_{2-x} in the O 1s region. **149**
- Table 4.3** Parameters from the refinement of Cu K-edge EXAFS of $\text{Cu}_{0.1}\text{Ce}_{0.9}\text{O}_{2-x}$ powders under catalytically-relevant conditions at 300 °C. Standard uncertainties in the last digits are included in parentheses. **151**
- Table 5.1** Calculated oxygen vacancy formation energies for substituted slabs of {111}-terminated CeO_2 . **163**
- Table 5.2** BET surface areas (A_S), apparent activation energies (E_A) and kinetic orders for CO oxidation catalysis on $\text{M}_{0.1}\text{Ce}_{0.9}\text{O}_{2-x}$. **167**

List of Abbreviations

A	pre-exponential factor or attempt frequency
ANN	artificial neural network
A_s	surface area per mass
BEP	Brønsted (or Bell)-Evans-Polanyi scaling
BET	Brunauer–Emmett–Teller theory of the adsorption of gases
CODH II	carbon monoxide dehydrogenase II
d	crystallite diameter
DFT	density functional theory
DOS	density of states
DRIFTS	diffuse reflectance infrared Fourier transform spectroscopy
ΔG	Gibbs energy of reaction
ΔG^\ddagger	activation barrier for a transition state
E_0	XAS edge energy
E_A	activation energy of a reaction
E_{vac}	oxygen ion vacancy formation energy
EDS	energy-dispersive X-ray spectroscopy
EELS	electron energy loss spectroscopy
EXAFS	extended X-ray absorption fine structure
F	effective scattering amplitude in EXAFS
FFT	fast Fourier transform
GGA	generalized gradient approximation
HAADF	high-angle annular dark-field imaging

List of Abbreviations

HRTEM	high resolution transmission electron microscopy
\hbar	reduced Plank's constant
ICP-AES	inductively-coupled plasma atomic emission spectroscopy
K	equilibrium constant
k	photoelectron wavevector
k_B	Boltzmann constant
k_n	rate constant of reaction n
λ	photoelectron mean free path length
m_e	electron mass
μ	chemical potential
n	reaction order
N	path degeneracy in EXAFS
PAW	projector augmented wave pseudopotential
PBE	Perdew–Burke–Ernzerhof exchange model
PD	planar density of atoms along a given crystal plan
PROX	preferential CO oxidation catalysis
PXRD	powder X-ray diffraction
φ	effective scattering phase shift in EXAFS
r	rate of reaction
R	path length in EXAFS
salpn	N,N'-bis(salicylidene)-propylene-1,3-diamine
STEM	scanning transmission electron microscopy
S_0^2	passive electron reduction factor

σ^2	mean squared displacement in EXAFS
TEM	transmission electron microscopy
TGA	thermogravimetric analysis
TOF	turnover frequency
θ	surface coverage
U	Hubbard on-site Coulombic interaction
XAFS	X-ray absorption fine structure
XANES	X-ray absorption near edge spectroscopy
XAS	X-ray absorption spectroscopy
XPS	X-ray photoelectron spectroscopy
XRD	X-ray diffraction
YBCO	yttrium barium cuprate ($\text{YBa}_2\text{Cu}_3\text{O}_{7-x}$)

Chapter 1 – Introduction and Motivation

1.1 The Global Relevance of Heterogeneous Catalysis

The transformation of chemical species through catalysis is at the heart of various aspects of modern life, from agriculture to the synthesis of pharmaceuticals and will certainly pave the way for future technologies such as alternative energy storage and conversion and carbon sequestration. The direct societal implications of catalysis are nowhere more obvious than the development of the Haber-Bosch process for the synthesis of ammonia in the early 20th century. Stressed by a rapidly expanding population without access to adequate foodstuffs to meet dietary demands in Europe and North America, the western world of the 19th and early 20th centuries saw some of the worse famines in recorded history. In order to meet the demands of an increasingly urbanizing population, modern agriculture relied on the use of nitrogen-rich fertilizers acquired from non-sustainable sources such as guano and sodium nitrate mining to improve crop yield.¹ By the turn of the century, however, many in the scientific community, most notably the English chemist William Crookes, emphasized the importance of scientific discovery towards the artificial fixation of dinitrogen. Crookes concluded in 1898 that without nitrogen-fixation, the world would stand to have a global wheat deficiency by 1930. Thus the discovery and subsequent commercialization of an efficient means to fix nitrogen into ammonia at high temperatures and pressures using an iron catalyst by German chemists Fritz Haber and Carl Bosch has been credited as the most important scientific accomplishment of the 20th century. The Haber-Bosch process, as it has subsequently been come to be known, is largely responsible for the acceleration of the global population from 1.6 billion people in 1900 to the 7.4 billion people we have today and over half of the nitrogen atoms in our bodies have been processed through the Haber-Bosch process.² In this case, chemical catalysis has transformed the world we live in by intervening in the natural nitrogen cycle. Looking to the future, we find ourselves in an analogous situation with regards to our energy economy and it will likely be advances in catalytic sciences that will bring about the implementation of sustainable energy conversion and storage in modern society.

The catalytic oxidation of carbon monoxide (CO) to carbon dioxide (CO₂) has also made a lasting impact on the modern world. For instance, the invention and mass commercialization of the internal combustion engine at the turn of the century led to renewed scientific interest in CO oxidation catalysis. Car manufacturers needed a way to

efficiently convert the poisonous gas, among others, into more benign gaseous products. These scientific endeavors ultimately lead to the development of the modern three-way catalytic converter in use today.³ Renewed interest in developing low-cost, earth-abundant catalysts for CO oxidation has stemmed from a need to remove CO from hydrogen sources (most notably synthesis gas, an industrial mixture of H₂ and CO from the steam reforming of methane) since CO adsorbs and poisons the surface of platinum anodes in proton exchange membrane fuel cells.^{4,5} Under such hydrogen-rich conditions where other products can be formed, the oxidation of CO to CO₂ is referred to as preferential CO oxidation, PROX for short and constitutes a major field of scientific inquiry.^{6,7} Other real-world applications for CO oxidation catalysis abound. There is continued interest in removing CO from gas streams in the petrochemical industry, for example. The development of respirator filter technologies for use in mining applications is another notable example.

Scientific research into CO oxidation catalysis is also inspired by the need to understand the fundamental reactivity of carbon monoxide, a key intermediate in C₁ chemistry, with surfaces of metals and metal oxides.⁸ CO oxidation serves as an important model system, from which new experimental and theoretical tools and techniques have been developed to better understand fundamental aspects of modern catalysis. Some of the most notable examples of this include the work of Gerhard Ertl, who's work applying techniques such as ultraviolet photoelectron spectroscopy (UPS), scanning tunneling microscopy (STM) and photoemission electron microscopy (PEEM) to topics in surface science was recognized with the 2007 Nobel Prize in Chemistry.

As opposed to homogeneous catalysis, the catalyst and the substrate are in separate phases in heterogeneous catalysis. In most cases, the substrate occupies a gaseous or liquid phase and is transformed at the surface of a solid catalyst. Heterogeneous catalysts have distinct advantages over homogeneous catalysts in terms of their applicability to relevant industrial practices. In contrast to the molecular species that make up all homogeneous catalysts, solid heterogeneous catalysts typically are quite robust under strenuous conditions and can maintain their activity over many catalytic turnovers. When solid catalysts are deactivated, thermal treatments can recondition the catalyst surface, which is not the case for molecular species. Additionally, the separation of the solid catalyst from the substrate and products is straightforward in heterogeneous catalysis. Heterogeneous catalysis does have

distinct disadvantages when compared to homogeneous catalysis when it comes to active site specificity. Unlike in molecular species where the reactive site is isolated and well characterized, the identity of the active sites on traditional heterogeneous catalysts can be difficult to rigorously characterize since they occupy only the very top atomic layer of the surface of an extended solid. Even the very notion of a static ensemble of active sites has come into question recently, with much work demonstrating that active sites in heterogeneous catalysis are very fluxional in their behavior and are highly dependent on the catalytic conditions. Recently, techniques such as coherent Bragg rod analysis (COBRA)⁹ and sum frequency generation spectroscopy,^{10,11} which probe the first atomic layer of solids, have been successfully applied to study the atomic structure of surface active sites. However, these advanced techniques generally require specialized instrumentation and ideal conditions not feasible for most studies. Another related disadvantage to heterogeneous catalysis is the paucity of methods available to the synthetic chemist to tune the atomic structure of these catalytically active sites. Inspired by the field of enzymatic catalysis, much work has been done in the field of homogeneous catalysis to tune not only the first coordination sphere, but also the secondary coordination sphere of molecular catalysts. As we will see later, the introduction of a second coordination sphere to the surfaces of heterogeneous catalysts is one way to potentially break restricting scaling relationships in catalysis.

1.2 Rate Laws and Free Energy Diagrams

Catalysts, whether homogeneous or heterogeneous, alter the rate of chemical transformations by changing the overall activation energy (E_A) of the reaction without being consumed. For most applications, a faster catalytic rate and hence a lower E_A , is desired. In the case of heterogeneous catalysis, the substrate interacts with the catalyst surface to form surface-bound intermediates with a lower overall E_A (Figure 1.1). For each elementary reaction step, the reaction coordinate diagram goes through a local maximum, known as the transition state (\ddagger), which governs the speed of the step. The higher this activation barrier (ΔG^\ddagger), the slower the reaction step is.

The rate of any elementary reaction step, such as step B in Figure 1.1, is given by

$$r = k \prod_i^{\rightarrow} P_i^{n_i} \theta_i^{n_i} - k' \prod_j^{\leftarrow} P_j^{n_j} \theta_j^{n_j} \quad (1.1)$$

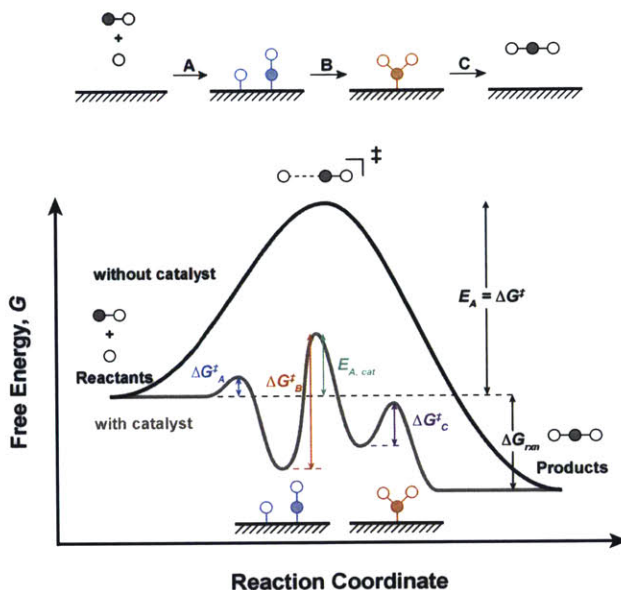
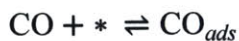


Figure 1.1 Reaction coordinate diagram for an arbitrary reaction with (gray trace) and without (black trace) the aid of a heterogeneous catalyst surface.

where the products are taken over species, either gaseous or surface sites, in the forward (\rightarrow) and in the backwards (\leftarrow) directions, which each has a kinetic rate constant (k). The partial pressure of species i is given by P_i and the coverage of a particular site i is represented by θ_i . The kinetic orders n_i are taken directly from the stoichiometry of the elementary step and are rarely more than 2 since most elementary steps are monomolecular or bimolecular. To take an example from CO oxidation, the first elementary step for the Langmuir-Hinshellwood mechanism for metallic catalysts (Appendix A.2) is the adsorption of CO onto a vacant metal surface site (*),



Since the forward reaction is bimolecular and the backwards reaction is monomolecular, $n_{\text{CO}} = 1$, $n_* = 1$ and $n_{\text{CO}_{ads}} = 1$. The rate expression for this elementary reaction step will therefore depend on the partial pressure of CO, the coverage of vacant metallic sites and the coverage of CO-adsorbed metallic sites according to

$$r = kP_{\text{CO}}\theta_* - k'\theta_{\text{CO}}$$

The kinetic rate constant (k) for each elementary step is in turn governed by the Arrhenius equation, which relates k to the logarithm of the Gibbs free energy of activation (ΔG^\ddagger) through a pre-exponential factor A

$$k = Ae^{\frac{-\Delta G^\ddagger}{k_B T}} \quad (1.2)$$

where T is temperature and k_B is the Boltzmann constant. For the overall reaction, Equation 1.2 follows when ΔG^\ddagger is replaced with E_A . The pre-exponential factor A , also referred to as the *attempt frequency*, is another important quantity in chemical catalysis and it relates to the frequency at which adsorbed molecules collide with each other at the catalyst surface. According to transition-state theory, in the absence of changes in entropy when forming the transition state, A is on the order of $k_B T/h = 10^{13} \text{ s}^{-1}$, where h is the Planck constant.

The overall, macroscopically observable rate expression for any given reaction mechanism can be considered as the solution to the individual reaction rate expressions (Equation 1.1) for each elementary step, taking into consideration site balance and boundary conditions. Such *microkinetic modeling* is indispensable as a tool to help support a reaction mechanism, as the overall rate expression has the general form of Equation 1.1. A careful measurement of the kinetic orders (n_i) can give experimental evidence for any given reaction mechanism through this microkinetic treatment. Additionally, detailed microkinetic modeling can also aid in the optimization of real catalysts. Often, it is convenient to introduce a *rate-determining step* (rds) when considering a reaction mechanism. As the name implies, the rate-determining step is the elementary reaction step in a mechanism that governs the overall rate of the reaction. The rds need not be the elementary step with the highest ΔG^\ddagger , which is a common misconception. By definition, the rate-determining step includes the least energetically favorable transition-state along the reaction coordinate diagram. The rates of all steps prior to and following the rate-determining step depend on the reaction coordinate diagram going through this high-energy state. In Figure 1.1, step 3 would be considered to be the rate-determining step as its transition-state is the global maximum. When there is an obvious rate-determining step, it is often convenient to make the assumption that the overall rate of reaction is given by the rate expression for the rds and that all other elementary steps are under steady-state conditions ($r = 0 \text{ s}^{-1}$). With this simplifying assumption the

mathematics of microkinetic modeling is made considerably easier and most rate expressions can be solved algebraically. As we shall see, the introduction of a rate-determining step also serves as a powerful pedagogical tool to understand catalysis.

1.3 Linear Free-Energy Scaling Relationships

A rigorous, *a priori* prediction of the overall catalytic activity for a given solid surface depends on calculating accurate transition-state energies and applying microkinetic modeling to a mechanism. While the attempt frequency A can be easily predicted from theory, values for ΔG^\ddagger are notoriously difficult to calculate since transition-states lie at saddle points in the potential energy surfaces of reactions. As such, the search for new heterogeneous catalysts has traditionally been empirical, depending on large-scale screening and combinatorial approaches. Recent years have seen an increase in the application of linear free-energy scaling relationships to the rational search for better heterogeneous catalysts. At the heart of this approach is the notion that for a set of related catalysts, the transition-state energy ΔG^\ddagger is linearly dependent on the change in free energy (ΔG) for a given elementary reaction step through a proportionality constant α :

$$\Delta G^\ddagger = \alpha \Delta G + \beta \quad (1.3)$$

The physical basis for Equation 1.3 is summarized in Figure 1.2A. The stabilization of the reaction intermediate in Figure 1.2A in turn stabilizes the transition-state, thus lowering ΔG^\ddagger and speeding up the rate of the elementary reaction step. A notable advantage to this phenomenological model is that given a training set of data for a number of previously characterized catalysts, a value for ΔG^\ddagger can be predicted from ΔG . Values for ΔG are calculated from intermediate species, which are the local minima of potential energy surfaces and are therefore computationally less expensive than calculating transition-states. Once the values for α and β are determined for this training set, Equation 1.3 can be substituted into Equation 1.2, making the microkinetic solution a function of thermodynamic binding energies (ΔG) as opposed to transition-state energies. Equation 1.3, known as the Brønsted (or Bell)-Evans-Polanyi (BEP) relation after the chemists who developed it,¹²⁻¹⁴ should come to no surprise to most chemists. The Hammett equation from organic chemistry is a well-known manifestation that interrelates kinetic and equilibrium constants in substituted benzoic acid derivatives.^{15,16} It is important to note that the BEP relation is entirely phenomenological

and the linear dependence of ΔG^\ddagger on ΔG is by no means universal for all heterogeneously catalyzed reactions.

A direct consequence of applying the BEP relation to heterogeneous catalysis is the Sabatier principle (Figure 1.2B). Named after the French chemist Paul Sabatier, the principle states that the optimal heterogeneous catalyst should bind the substrate neither too weakly nor too strongly.^{17,18} A catalyst that binds the substrate too weakly (ΔG more positive) will not be able to supply sufficient reactants to the surface of the solid for catalysis to turn over. On the other end of the spectrum, a catalyst that binds the substrate too strongly (ΔG more negative) will have difficulty turning over surface reactions since the strength of adsorption with the intermediates is too great to overcome.

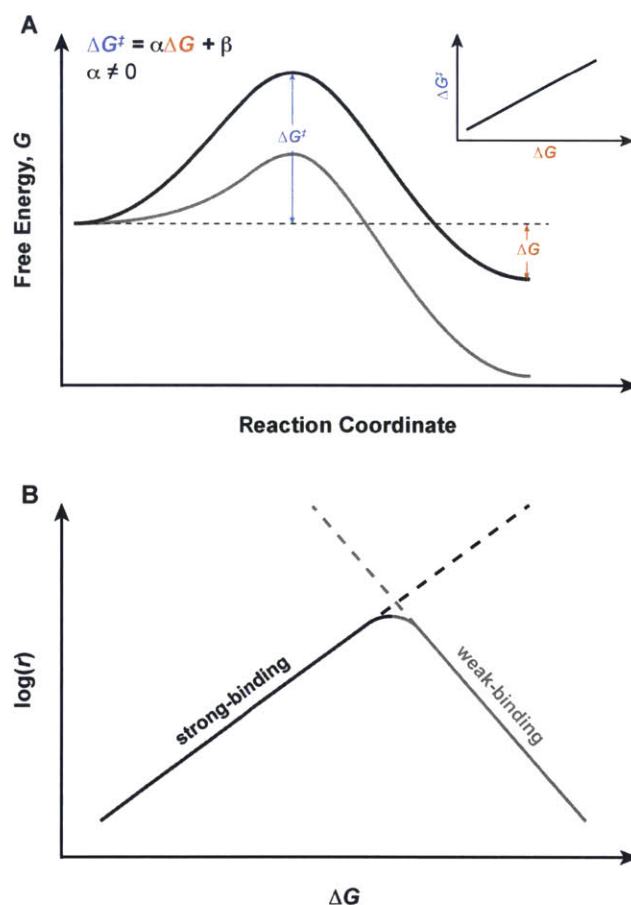


Figure 1.2 Linear free-energy scaling relationships and their implications for catalysis. (A) Reaction coordinate diagram demonstrating the case when there is a linear relationship between ΔG^\ddagger and ΔG and (B) a schematic Sabatier plot using linear free-energy relationships.

An important consequence of applying the BEP relation (Equation 1.3) to microkinetic analysis, as demonstrated schematically in Figure 1.2B, is that the overall catalytic activity of

a solid can be optimized by tuning an easily calculated thermodynamic term (ΔG), which is known as an *activity descriptor*. Remember that ΔG is just the reaction free energy for one elementary process in a multi-step mechanism. Thus, the choice of an adequate descriptor relies heavily on the proposed reaction mechanism. In some cases, values for ΔG for intermediates are linear dependent with themselves, which has important consequences for catalysis. In other cases, the elementary step will not follow the BEP relation (*i.e.* $\alpha = 0$), suggesting that the ΔG for that step is not a suitable descriptor for catalysis. For the case where it is safe to apply the rate-determining step assumption, ΔG for the rds may serve as a suitable descriptor for the catalytic process.

While predicting kinetic parameters based on thermodynamic free energies is a particularly attractive approach to rational catalyst design, an intuitive understanding of ΔG for a particular elementary step may not come easily to an experimental chemist. Fortunately, thermodynamic free energies often correlate with observable, physical properties of catalysts. A notable example is the correlation of oxygen and carbon monoxide binding strengths (ΔG_{O} and ΔG_{CO}) to the relative position of the d-band of 3d – 5d metal surfaces, which was pioneered by Danish physicists Jens Nørskov, Bjørk Hammer and collaborators.¹⁹ Electronic states of d-orbital parentage for metal surfaces are of appropriate energy and symmetry to participate in σ and π bonding and anti-bonding interactions with oxygen and carbon monoxide adsorbates. For surfaces with a center of mass of the electronic density of states (DOS) of d-parentage sufficiently lower than the Fermi level of the system, both bonding and anti-bonding orbitals are occupied leading to a relative weak surface-adsorbate interaction. As the d-band increases towards the Fermi level, however, the anti-bonding orbitals of the surface-adsorbate interaction fall above the Fermi level and become partially unoccupied. Therefore, metals with higher d-band centers participate in stronger surface-adsorbate interactions (ΔG becomes more negative), which has been verified spectroscopically in several cases for 3d – 5d metal and metal-alloy surfaces.^{20,21} The success of the Hammer-Nørskov d-band model, as it has been come to be called, has guided much of the research into next-generation platinum alloy catalysts for the oxygen reduction reaction (ORR) as well as for CO oxidation as demonstrated in Figure 1.3.²²⁻²⁸ Platinum alloys with lower d-band centers correspond to the weak-binding branch of the Sabatier plot while higher d-band centers correspond to the strong-binding branch. Catalysts such as Pt₃Co and Pt₃Ta alloys

have intermediate d-band centers and hence intermediate O and CO binding strengths and optimized catalytic activities.

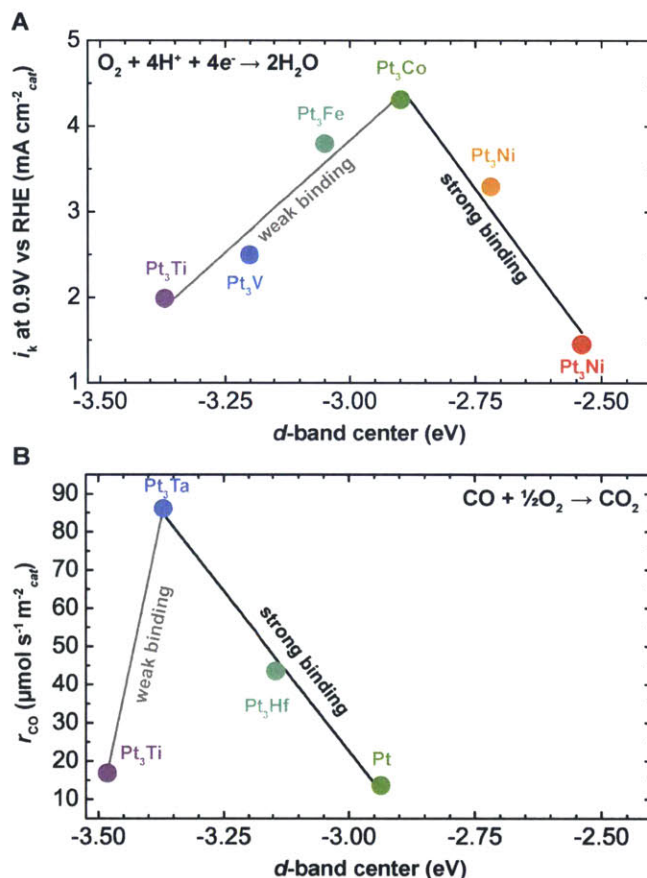


Figure 1.3 The specific catalytic activity for (A) oxygen reduction and (B) CO oxidation as a function of the DFT-calculated d-band center for platinum alloys. Measurements for ORR were recorded in 0.1 M HClO₄ and those for CO oxidation were acquired in a reactor with 0.02 atm CO and 0.01 atm O₂ at a flow rate of 0.67 mL min⁻¹ mg⁻¹ at 200 °C. Adapted with permission from references 22 and 28.

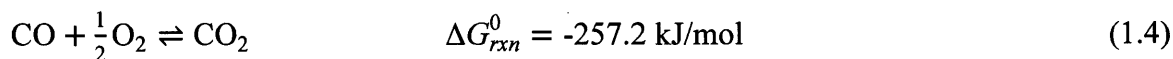
The Hammer-Nørskov d-band model is a notable example of a descriptor-based approach to catalyst discovery and design. Instead of relying on exhaustive catalyst screening, this approach correlates tunable physical properties of a solid (the descriptor) with the free energy of an elementary step (ΔG). Through the BEP relation and microkinetic analyses of the reaction mechanism, the Sabatier principle (Figure 1.2B and Figure 1.3) follows naturally. It's important to note that ΔG can correlate with many different physical properties of the catalyst and any given descriptor should not be thought of as unique. Indeed, in our example of the oxygen reduction reaction and the related oxygen evolution reaction (OER), the last decade of research has put forth a diverse family of descriptors for catalytic activity on both

transition-metals and their oxides. While some correlate activity with the position of bands in the DOS,^{29,30} others correlate with the electronic configuration of the transition-metal (the number of valence electrons, the number of electrons in the e_g antibonding set, *etc.*),³¹⁻³³ and still others correlate with structural features of the coordination center.³⁴ Common to these is the underlying approach outlined here that the descriptor follows directly from a careful treatment of the reaction mechanism, which is in contrast to the activity descriptors found empirically in earlier studies.³⁵⁻³⁷ These earlier studies, which linked activity with enthalpies of reduction and metal hydroxide formation, do not presume a direct link between the mechanism and the descriptor.

Another shortcoming to descriptor-based catalyst design is the possibility of multiple mechanisms for a given set of catalyst candidates. The construction of quantitative Sabatier plots (Figure 1.2B and Figure 1.3) assumes that all evaluated catalysts share a common reaction mechanism. As such, care should be taken when proposing activity descriptors to give evidence that each catalyst follows the same general mechanism. Similarly, descriptors ought to reflect the physical and chemical properties of the catalyst surface under the relevant reaction conditions. As we shall see, the structure of catalytically active sites can change dramatically under different reaction conditions, which can alter the properties of the catalyst. Thus, a rigorous correlation between the descriptor and catalytic activity should take any of these transformations into account.

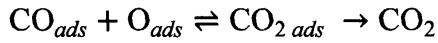
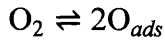
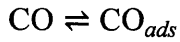
1.4 Mechanisms for CO Oxidation Catalysis

In the case of CO oxidation, one atom of oxygen is transferred to carbon monoxide to produce gaseous carbon dioxide,



While the gas-phase reaction itself is exergonic, kinetically it is impossible. In fact, we cannot even draw a free-energy diagram or measure E_A for CO oxidation in the gas phase as we've done for the arbitrary reaction in Figure 1.1. The reaction is forbidden by spin selection rules. The total spin of the reactants ($S = 0$ for CO and $S = 1$ for O_2) and the product ($S = 0$ for CO_2) are not identical, hence the role of a catalyst in this special case is also to introduce a reaction pathway that is spin-allowed. Indeed, the two prevailing reaction

mechanisms for CO oxidation both rely on the formation of reactive oxygen species for oxidative catalysis and follow the general pathway



In this simplified reaction mechanism, both CO and O₂ have to adsorb to the catalyst surface as intermediates before they can react to form a molecule of CO₂. In the case of oxygen, we see that some substrates can adsorb dissociatively. The origin and nature of the activated oxygen species involved in the catalytic reaction, represented here rather generally as “O_{ads},” is an important distinguishing feature between two accepted mechanisms for CO oxidation.

1.4.1 The Langmuir-Hinshelwood Mechanism for CO Oxidation Catalysis

The Langmuir-Hinshelwood mechanism, along with the Eley-Rideal mechanism, can be used to describe most catalytic processes occurring on base- and noble-metal surfaces.³⁸ Originally conceived to explain the kinetics of platinum catalysts for CO oxidation, the Langmuir-Hinshelwood mechanism involves the adsorption of CO and O₂ onto metal (M) surfaces, where they react to form CO₂ (Figure 1.4A).³⁹ In the first two steps (the order of which is arbitrary in Figure 1.4A), the gases adsorb to the surface of the metal with O₂ adsorbing dissociatively to form two O_{ads} species. Since CO and O₂ adsorb to the same metal site M, gas adsorption is considered competitive, with the relative binding strengths (ΔG_{ads}) depending on the electronic structure of the center M. After the diffusion of CO_{ads} and O_{ads} to adjacent metal sites, these species react in step 3 to form a surface-bound CO₂ intermediate, which desorbs rapidly in step 4 completing the reaction cycle.

Since it involves the breaking of strong surface-adsorbate bonds, the third step is typically considered rate-determining. Thus the overall rate law expression can be written as

$$r_{L-H} = k_3\theta_{\text{CO}}\theta_{\text{O}} - k_3'\theta_{\text{CO}_2}\theta_* \quad (1.5)$$

where θ_{CO} , θ_{O} and θ_{CO_2} are the surface coverages of CO_{ads}, O_{ads} and CO_{2 ads}, respectively and θ_* corresponds to the coverage of free metal sites (denoted historically as *). Immediately we

see that the rate will depend on the thermodynamic driving forces for CO and O₂ dissociative adsorption onto M. In terms of linear free energy scaling relations, we note that ΔG_{CO} and ΔG_{O} may be suitable activity descriptors. Indeed, rigorous computational studies on noble-metal catalyst surfaces have shown that ΔG_{CO} and ΔG_{O} serve as independent descriptors for CO oxidation; the Sabatier plots for these catalysts are three-dimensional, with ΔG_{CO} and ΔG_{O} as the *x*- and *y*-axes and catalytic activity as the *z*-axis.^{40,41}

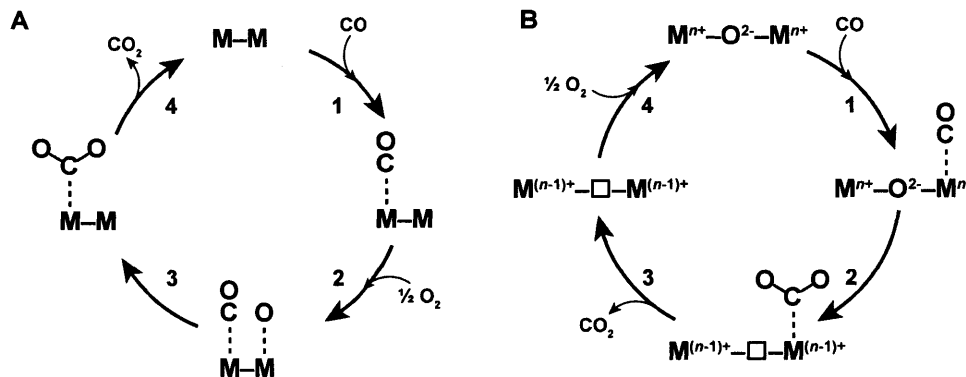


Figure 1.4 Mechanisms for CO oxidation; (A) the Langmuir-Hinshelwood and (B) the Mars-van Krevelen mechanisms.

Assuming the other steps are under steady-state conditions and defining equilibrium constants K for CO and O₂ adsorption and CO₂ desorption, we can expand Equation 1.5 (See Appendix A.2) to relate the overall reaction rate in terms of partial pressures;

$$r_{L-H} = \frac{k_3 K_{\text{CO ads}} K_{\text{O}_2 \text{ ads}}^{1/2} P_{\text{CO}} P_{\text{O}_2}^{1/2} - \frac{k_3'}{K_{\text{CO}_2 \text{ des}}} P_{\text{CO}_2}}{\left(1 + K_{\text{CO ads}} P_{\text{CO}} + K_{\text{O}_2 \text{ ads}}^{1/2} P_{\text{O}_2}^{1/2} + \frac{1}{K_{\text{CO}_2 \text{ des}}} P_{\text{CO}_2}\right)^2} \quad (1.6)$$

A few more generally accepted assumptions can be made to simplify Equation 1.6. First, the desorption of CO₂ from the surface is generally considered very favorable ($1/K_{\text{CO}_2 \text{ des}} \approx 0$). Additionally, CO adsorption is typically much stronger than O₂ dissociative adsorption ($K_{\text{CO ads}} P_{\text{CO}} \gg (1 + K_{\text{O}_2 \text{ ads}}^{1/2} P_{\text{O}_2}^{1/2})$). Thus Equation 1.6 simplifies to

$$r_{L-H} = \frac{k_3 K_{\text{O}_2 \text{ ads}}^{1/2} P_{\text{O}_2}^{1/2}}{K_{\text{CO ads}} P_{\text{CO}}} \quad (1.7)$$

A few salient features of Equation 1.7 are important to note. As we have discussed, CO and O₂ adsorption processes are competitive within Langmuir-Hinshelwood kinetics. This is

reflected by the position of the equilibrium constants in Equation 1.7 on either side of the fraction bar. Additionally, we see that the reaction is $\frac{1}{2}$ order with respect to O_2 and inverse first order with respect to CO. This partial pressure dependence is an important clue when proposing reaction mechanisms, since the second common mechanism for CO oxidation catalysis, the Mars-van Krevelen mechanism, has a significantly different partial pressure dependence.

1.4.2 The Mars-van Krevelen Mechanism for CO Oxidation Catalysis

In contrast to the classical Langmuir-Hinshelwood mechanism, many studies on transition-metal oxide catalysts have proposed an alternative mechanism for CO oxidation. The Mars-van Krevelen mechanism (Figure 1.4B) was originally used to describe the catalytic oxidation of aromatic compounds with vanadium oxides, and the defining feature of the mechanism is the direct involvement of framework O^{2-} ions in the oxidative step.⁴² The Mars-van Krevelen mechanism has been implicated for CO oxidation catalysis on a wide array of oxide catalysts such as RuO_2 ,⁴³ single-phase CuO_x ,⁴⁴ mixed-phase Cu/CeO_2 ,^{45,46} and even Pt under high-pressure conditions.⁴⁷

After the adsorption of CO onto a metal site M, an oxygen atom from the oxide lattice is transferred to CO to form the CO_2 adduct in step 2 (Figure 1.4B). Taken together, elementary steps 1 and 2 in Figure 1.4B are analogous to the insertion of carbon monoxide into the metal-oxygen bond of molecular platinum, iridium and nickel hydroxides to form metal-hydroxycarbonyl adducts in organometallic chemistry (see Figure 4.13 and the discussion in Section 4.5).⁴⁸⁻⁵¹ The desorption of gaseous CO_2 in step 3 results in the formation of an oxygen vacancy (denoted \square), effectively reducing the surface by two electrons. The dissociative adsorption and reduction of O_2 refills this vacancy in step 4, thus closing the catalytic cycle. Similar to the Langmuir-Hinshelwood mechanism, the transfer of the lattice oxygen atom to CO (step 2) can be considered the rate-determining step; not only are strong M-O bonds broken, but the surface is reduced by two electrons. Upon first glimpse, the Langmuir-Hinshelwood and Mars-van Krevelen mechanisms may appear nearly identical. Both mechanisms adsorb CO and O_2 onto metal sites and both have rate-determining steps involved with C-O bond formation. There are subtle but important features of the Mars-van Krevelen mechanism that distinguish it from Langmuir-Hinshelwood kinetics. While CO and O_2 must compete for adsorption at metal sites in the Langmuir-Hinshelwood mechanism, the

same is not strictly true for the Mars-van Krevelen mechanism. In our oversimplified mechanistic picture in Figure 1.4B, CO adsorbs to coordinatively unsaturated transition metal centers at the surface of the bulk oxide, while oxygen only adsorbs into oxygen vacancies created upon C-O bond making in step 2. While it is certainly true that CO can adsorb into oxygen vacancy sites and O₂ can compete with CO at unsaturated surface sites, these interactions are thermodynamically unfavorable. In the case of CO adsorption to oxygen vacancy sites, geometric constraints imposed by the extended metal oxide preclude the binding of adsorbates other than oxygen. Of course the oxygen filling the vacancy could come from CO, but that would require breaking one of the strongest bonds in chemistry. The C-O bond in carbon monoxide has a bond dissociation energy (1077 kJ/mol) over twice that of the O-O bond in O₂ (498 kJ/mol).⁵² In the case of O₂ binding to unsaturated surface sites, we have already noted that CO preferentially binds to these sites over O₂ during our discussion of the Langmuir-Hinshelwood mechanism.

These important features are highlighted by the rate expression we derive from Figure 1.4B. Since we propose the C-O bond formation step (step 2) to be the rate-determining step, our overall rate law has the form

$$r_{M-vK} = k_2\theta_{CO} - k_2'\theta_{CO_2} \quad (1.8)$$

Since CO and O₂ adsorption processes are noncompetitive, the forward reaction rate is a function only of the coverage of CO bound to the unsaturated transition metal sites, in contrast to the rate expression for Langmuir-Hinshelwood kinetics (Equation 1.5). As we have done previously for the Langmuir-Hinshelwood mechanism, we assume that the other elementary steps in Figure 1.4B are under steady state conditions governed by their equilibrium constants. Expressing Equation 1.8 in terms of partial pressures (see Appendix A.1 for full derivation) gives us the extended rate expression for Mars-van Krevelen kinetics:

$$r_{M-vK} = \frac{k_2 K_{CO\ ads} P_{CO} - \frac{k_2' K_{vac} P_{CO_2}}{K_{CO_2\ des} P_{O_2}^{1/2}}}{1 + K_{CO\ ads} P_{CO} + \frac{K_{vac}}{P_{O_2}^{1/2}} \left(1 + \frac{P_{CO_2}}{K_{CO_2\ des}} \right)} \quad (1.9)$$

As we have discussed previously in 1.4.1, CO₂ desorption from transition metal sites can be considered nearly irreversible ($1/K_{CO_2\ des} \approx 0$). We can further simplify Equation 1.9 by

noting that oxygen vacancy formation is thermodynamically unfavorable ($K_{vac} \approx 0$), which gives us

$$r_{M-vK} = \frac{k_2 K_{CO\ ads} P_{CO}}{1 + K_{CO\ ads} P_{CO}} \quad (1.10)$$

Thus, we see that at sufficiently low partial pressures of CO, Mars-van Krevelen predicts that CO oxidation is first order with respect to CO and zeroth order with respect to oxygen, in contrast to the orders expected from Langmuir-Hinshelwood kinetics (Equation 1.7).

1.5 Low-Temperature CO Oxidation Catalysts

As noted in 1.1, the demand for efficient and cost-effective catalysts for CO oxidation extends beyond the three-way catalytic converter. A notable challenge is the development of catalysts that oxidize CO to CO₂ at or near room temperature. In contrast, traditional platinum-group metal catalysts used in automotive exhaust have been optimized for performance under high temperature conditions (up to 650 – 1100 °C).³ Over the past three decades, Au/TiO₂,⁵³ nanoparticulate forms of Co₃O₄⁵⁴ and heterogeneous CuO/CeO₂ mixtures⁵⁵ have emerged as champion CO oxidation catalysts at low temperatures and atmospheric pressures (Figure 1.5).

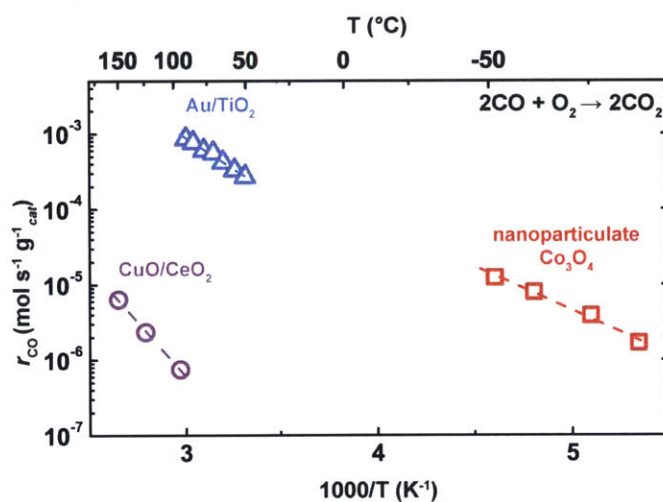


Figure 1.5 Mass-normalized rates of CO oxidation on CuO/CeO₂, Au/TiO₂ and nanoparticulate Co₃O₄. Rates were measured under carbon monoxide lean conditions in differential flow conditions. Data taken from references 99 (CuO/CeO₂), 68 (Au/TiO₂) and 54 (Co₃O₄).

1.5.1 Au/TiO₂ and Other Gold-Based Catalysts

Initially considered chemically and catalytically inert, materials based on gold represent some of the best catalysts for CO oxidation at or below room temperature. Since the initial

discovery by Japanese chemist Masatake Haruta that small ($d < 5$ nm) nanoparticle deposits of gold on TiO_2 are catalytically active for CO oxidation,^{53,56} researchers have proposed a myriad of explanations to explain the surprising catalytic activity.⁵⁷ While the field of CO oxidation by gold-based catalysts is contentious and to this day there is no consensus as to the origin of the special catalytic activity of gold, there are a number of important general phenomena that most researchers in the field agree upon. These include the observations that bulk forms of gold are not active, that the highest rates are found for gold nanoparticles 2-3 nm in diameter supported on transition-metal oxide supports and that the method of depositing and annealing the gold is critical for achieving reproducibly high rates for catalysis.⁵⁸ Points of contention in the literature include the identification of the active site or interface, the oxidation state of the active form of gold (Au^0 , Au^{3+} or Au^+), whether the support has a direct role in catalysis and the mechanism for the catalytic turnover. Furthermore, the recorded activation energies and kinetic orders vary from study to study. Generally speaking, the activation energies lie in one of three regimes, around 50 – 60, 24 – 41 or 10 – 18 kJ mol^{-1} , with the highest activities averaging 30 kJ mol^{-1} . The kinetic orders with respect to CO are generally close to zero, although there are some reports of orders as high as 0.25 – 0.60. The partial-pressure dependence on O_2 is generally characterized by kinetic orders between 0.20 and 0.40. The heterogeneity reported in the literature therefore reflect the complexity and the inherent difficulty in fully understanding catalytic reactions in two-phase systems.

A popular explanation of the special catalytic activity of supported gold nanoparticles, originally posited by Geoffrey Bond and David Thompson, relies on direct participation of the interface between the metallic nanoparticle and the oxide support. Trying to reconcile the differences in measured activities and kinetic constants in the literature, Bond and Thompson proposed that CO adsorbs non-competitively onto the metallic Au sites. The adsorbed CO subsequently migrates to the Au/ TiO_2 interface, where OH groups from perimeter Au^{3+} or TiO_2 are transferred to form a hydroxycarbonyl intermediate. Oxygen will then adsorb at the oxide perimeter as superoxide, which will deprotonate the hydroxycarbonyl intermediate to form bound CO_2 , which then desorbs.⁵⁸ In this mechanism, CO and O_2 adsorption are non-competitive since they occur at distinct sites. Also noteworthy is the assertion, from spectroscopic evidence, that gold is present in metallic and cationic forms in Au/ TiO_2 . The

Au⁰ sites that make up the majority of the nanoparticle, participate in CO adsorption, while the Au³⁺ sites are responsible for anchoring the nanoparticle to the oxide surface.

While some researchers disagree with the details of the Bond-Thompson model, most would argue that the Au/TiO₂ perimeter is necessary for catalysis of CO. Kung *et al.* argue that Au⁺ cations are present at the perimeter and that O₂ dissociatively adsorbs on Au before migrating to the gold-oxide interface.^{59,60} The direct participation of Au⁺ in supported gold nanoparticle CO oxidation is further supported through ¹⁹⁷Au Mössbauer spectroscopic studies, which showed a correlation between the concentration of Au⁺ measured with the catalytic activity.⁶¹ As a counterpoint to this, Haruta himself argues that cationic gold is not present at the interface and that O₂ is activated directly by metallic gold sites at the perimeter.⁶² This hypothesis is supported in part by X-ray absorption spectroscopic studies that indicated that cationic gold need not be present for Au/TiO₂ to exhibit high catalytic activities.^{63,64} Still others argue, on the basis of ¹⁹⁷Au Mössbauer spectra, that no metallic gold is required for the unusually high activity of supported gold catalysts and that AuO(OH) and its interface with the oxide support is key to catalysis.⁶⁵ In a set of elegant experiments, Chen and Goodman offered another take on Au/TiO₂.⁶⁶ After depositing varying coverages of gold onto the surface of epitaxial thin films of TiO_x, these researchers found that (1x1) monolayer films, where electron-rich Au^{δ-} atoms are directly bonded to Ti³⁺ sites, do not bind CO and are not active for its oxidation. Only after depositing 1.2 monolayers, which gives (1x3) bilayers of gold, does the surface exhibit high rates for CO oxidation. The authors proposed that the surface-bound Au^{δ-} atoms activate O₂ directly, and that the second layer of metallic Au sites is responsible for CO adsorption. Despite differences in the details of these models, these researchers argue that the key to the special activity of Au/TiO₂ lies at the perimeter sites, which serves to decouple CO binding from O₂ activation. In terms of linear free-energy scaling relationships, Au/TiO₂ provides a glimpse into a strategy to tune ΔG_{CO} and ΔG_O independently. While it has been proposed that these parameters are optimized in Au/TiO₂ by controlling the crystal size of Au alone,^{40,41} the idea that tuning ΔG_{CO} and ΔG_O independently is much more appealing since the adsorbates bind to the separate phases of Au and TiO₂ which can in turn be tuned independently. On the other hand, it has been argued that such support effects are considered secondary to particle size effects when determining catalytic activity.^{67,68}

1.5.2 Nanoparticulate Co_3O_4

The catalytic behavior of Co_3O_4 powders for CO oxidation was noted as early as 1974, when researchers found catalytic activities higher than any other common first-row transition-metal binary oxide.⁶⁹ These studies also demonstrated that the catalytic activity for CO oxidation was highly dependent on the method with which the powders were conditioned and annealed. The sensitivity of the catalyst to water vapor, however, has prevented the consideration of Co_3O_4 for technological applications.^{70,71} The origin of the deactivation of Co_3O_4 by water includes the poisoning of catalytic sites by chemisorbed H_2O . Early studies on substituted Co_3O_4 suggested that catalysts with a higher proportion of octahedrally-coordinated Co^{3+} sites at the surface were significantly more active,⁷² and a Mars-van Krevelen mechanism has been proposed following isotopic labeling studies.⁷³ Rigorous XPS, EELS and LEED studies on $\{110\}$ - and $\{111\}$ -terminated single crystals of Co_3O_4 exposed to O_2 and H_2O treatments showed the facile interconversion of Co^{3+} with Co^{2+} at the surface without perturbation to the bulk crystal structure, which offers an explanation for the high catalytic activities found for these compounds.⁷⁴

Recent reports of CO oxidation catalysis on nanoparticulate Co_3O_4 give evidence that the reaction is structure sensitive; the intrinsic turnover frequency (TOF) is a function of the crystallographic termination, with $\{110\}$ facets giving higher activities than $\{111\}$ -terminated facets.^{54,75} The origin of the structure sensitivity appears to be a preference for the catalytically-active octahedrally-coordinated Co^{3+} centers to be present in $\{110\}$ facets over the $\{111\}$ facets. Thus, the synthesis of high aspect ratio nanorods and nanoribbons, with preferential $\{110\}$ termination, has led to the improved catalytic performance of Co_3O_4 .^{54,75} Interestingly, these nanoparticulate Co_3O_4 catalyst exhibit significantly improved stability under H_2O -containing gas streams.⁵⁴ Recent density functional theory (DFT) calculations have supported a Mars-van Krevelen mechanism driven by the $\text{Co}^{3+}/\text{Co}^{2+}$ redox. These calculations suggest that after adsorption to octahedrally-coordinated Co^{3+} centers, CO abstracts reactive two-coordinate lattice oxygen atoms to form a CO_2 adduct.⁷⁶ The researchers also suggested that the dissociative adsorption of O_2 occurs spontaneously, returning the catalyst surface to its resting state. DFT calculations also gave evidence of the structure sensitivity of CO oxidation on these surfaces; although the reaction goes through a similar Mars-van Krevelen mechanism for both surfaces, the calculated activation energies

were significantly smaller for {110} terminated surfaces compared to {111}.⁷⁷ The exemplary activity of nanoparticulate Co_3O_4 is illustrative of CO oxidation catalysis on transition-metal oxide materials. The identification of active sites, the participation of structural O^{2-} in catalysis, facile surface redox chemistry and the low-cost of this family of materials are hallmarks that differentiate it from noble-metal catalysts such as Au/TiO_2 . Since Mars-van Krevelen kinetics tend to dominate in transition-metal oxide systems,⁷⁸ a strategy to optimize catalytic rates would be to stabilize the formation of oxygen-vacancies, which constitutes part of the rate determining step in Figure 1.4B. Exploiting structure sensitivity is certainly one strategy to optimize Co_3O_4 catalysts, but to tune the intrinsic reversibility of oxygen vacancy formation on a metal oxide surface requires altering its electronic structure. Analogous to the case of perturbing Pt-adsorbate bond formation energetics through alloying discussed in 1.3, the further optimization of transition-metal oxides for CO oxidation catalysis requires tuning the electronic structure of the catalyst through transition-metal substitution. While this may seem obvious, the implementation of this strategy is complicated by inhomogeneous incorporation of guest transition-metals into host matrices. Unlike fcc metals such as Pt where alloying with other fcc metals is common practice, the transition-metal oxides constitute a wide range of structural types. Therefore, the incorporation of different transition-metal ions into the host lattice may result in inhomogeneous incorporation or even the formation of distinct phases. One notable example of this, which serves as the basis for this thesis, is the study of the so-called CuO/CeO_2 family of catalysts.

1.5.3 Unsupported and Supported CuO Catalysts

Copper and the copper oxides were identified as potential catalysts for the oxidation of CO as early as 1923.⁷⁹ In these early studies, it was found that the catalytic activity of CuO increased when physically mixed with MnO_2 , an example of the “promoter effect” in heterogeneous catalysis (often rebranded as the synergetic effect in contemporary reports),^{80,81} a phenomena in which a mixture gives catalytic activity greater than the sum of its components. Initial studies of CO and O_2 adsorption and CO oxidation focused on thin films of Cu_2O prepared from Cu substrates. Garner *et al.* used calorimetry to determine that O_2 could dissociatively adsorb to Cu^+ sites on the surface of Cu_2O . Cu^+ centers from subsurface layers freely diffuse to the surface to accommodate the formation of the negative

charge,⁸² a hypothesis which was supported by microbalance measurements of similar films.⁸³ Upon exposure to CO, surface carbonates form spontaneously at surface Cu^+ sites where they react with the activated surface O^{2-} species. The authors argued that the dissociative adsorption of O_2 is likely rate-determining at lower temperatures and proposed that CO reacts directly with lattice O^{2-} at higher temperatures.⁸³ Subsequent catalytic studies by Gabor Somorjai on epitaxial thin films of Cu, Cu_2O and CuO under CO oxidation conditions supplemented with characterization using Auger electron and X-ray photoelectron spectroscopies suggested that surface copper easily interconverts between Cu^0 , Cu^+ and Cu^{2+} at elevated temperatures (200 – 350 °C) depending on the reaction atmosphere.⁸⁴ These studies concluded that of the three structures, Cu_2O was the most active for CO oxidation catalysis. Despite the facile redox properties of the films, a Langmuir-Hinshelwood mechanism was proposed for Cu_2O , in which Cu^+ would adsorb both CO and O_2 without electron transfer at the copper centers.

In response to these measurements on well-defined thin films, Sadykov and collaborators pointed out that defects such as twin-boundaries and dislocations can dictate catalytic activity in powders of Cu, Cu_2O and CuO.⁸⁵ In contrast to Somorjai's study on thin films, Sadykov found that CO oxidation on non-stoichiometric CuO_{1-x} is superior to Cu_2O . In particular, these researchers argued that Cu^+-Cu^+ dimers, found in the vicinity of extended defects, contribute the most to the catalytic activities of CuO_{1-x} powders.⁸⁶ Consistent with the previous studies, they stressed a Langmuir-Hinshelwood mechanism in which CO and O_2 adsorb non-competitively at these Cu^+ centers. On the other hand, others have argued that the facile Cu^+/Cu^0 interconversion at these defect sites in CuO_{1-x} are responsible for contributing lattice O^{2-} to the oxidation of CO in a Mars-van Krevelen mechanism.⁴⁴

A notable example of the “promoter effect” mentioned previously includes the study of CuO and Al_2O_3 mixtures for CO oxidation, which have been under scrutiny since the 1960s.⁸⁷ Yu Yao and coworkers concluded that the promoter effect in thermally treated mixtures of CuO and Al_2O_3 could be explained by the ability of Al_2O_3 to disperse small clusters of CuO, effectively increasing the catalytically-active surface area of CuO.⁸⁸ Pierron *et al.*, however, suggested that the interface between metallic Cu and Cu_2O phases formed by the thermal activation of these mixtures was responsible for the promotion of CO oxidation kinetics.⁸⁷ Kinetic measurements coupled with FTIR spectroscopy indicated that CO adsorbs

at the Cu/Cu₂O interface of Cu-impregnated Al₂O₃ catalysts, lending support to the hypothesis of Pierron.⁸⁹ Much like the mechanisms proposed by Chen and Goodman for gold-based catalysts, a Langmuir-Hinshelwood mechanism was proposed in which CO and O₂ adsorption are non-competitive. CO preferentially adsorbs at Cu⁺ sites while O₂ adsorbs at metallic Cu sites; catalytic turnover commences when CO_{ads} and O_{ads} meet at the Cu/Cu₂O interface. This mechanism is supported by the observation that while oxidizing pretreatments of CuO/Al₂O₃ lead to a better dispersion of CuO onto Al₂O₃, their catalytic activities are inferior to the same catalysts after reductive pretreatments in which crystallites of metallic Cu form due to sintering.⁹⁰

The use of ceria (CeO₂) as a support for heterogeneous catalyst has dated back almost 100 years, where it was found to promote the preferential oxidation of CO with transition-metal oxides.⁹¹ The ability of the ceria lattice to act as a buffer to reversibly exchange O²⁻ with gaseous O₂, known as the oxygen storage capacity or OSC,⁹²⁻⁹⁴ is often cited as a major contributing factor for its success in oxidative catalysis and other applications.⁹⁵ Although not a good catalyst under ambient temperature conditions in its own right, CO oxidation does occur for unmodified, stoichiometric CeO₂ at temperatures above 250 °C, where it follows a Mars-van Krevelen mechanism in which O₂ dissociatively adsorbs into oxygen vacancy sites after the transfer of a lattice oxygen atom to CO.⁹⁶ In order to increase the catalytic activity of CeO₂, Maria Flytzani-Stephanopoulos discovered that the incorporation of small amounts of copper into CeO₂ through coprecipitation dramatically enhanced the CO oxidation kinetics of ceria.^{55,97} Copper, as a known oxidative catalyst, modulates the catalytic activity of ceria somehow,

Thus, we postulated that a general oxidation catalyst may be achieved by promoting fluorite oxides with active transition metals, such as copper. In such a catalyst configuration, the transition metals are used in minor amounts and stabilized in the fluorite oxide matrix, while the fluorite oxide is the essential and major catalyst component and not an inert support.⁹⁷

According to Flytzani-Stephanopoulos, CO oxidation on such CuO/CeO₂ catalysts follows the mechanism for CeO₂, with surface Cu species serving as sites for CO adsorption. Remarkably, Flytzani-Stephanopoulos and coworkers found that CuO/CeO₂ mixtures gave rates of CO oxidation several orders of magnitude higher than previous state-of-the-art catalysts such as CuO/Al₂O₃.⁹⁷ At the heart of the catalytic rate enhancement, they argued,

was the insolubility of transition-metal oxides into the fluorite crystal structure of CeO_2 . Due to this mismatch, small crystallites of CuO were finely dispersed along the CeO_2 surface, akin to the previous discussions on $\text{CuO}/\text{Al}_2\text{O}_3$. These initial reports introduced a mechanism, based on *ex-situ* XPS observations, which proposed that Cu^+ ions play a major role in catalysis.⁹⁸ Much like the case of $\text{CuO}/\text{Al}_2\text{O}_3$, Cu^+ ions, detectable by XPS, serve to anchor the CuO particles to CeO_2 and to preferentially adsorb CO . The CO that adsorbs to the Cu^+ sites within the CuO/CeO_2 interface would abstract an oxygen atom from the associated CeO_2 , either as lattice O^{2-} or as activated superoxide ($\text{O}_2^{\cdot-}$) radical anions.

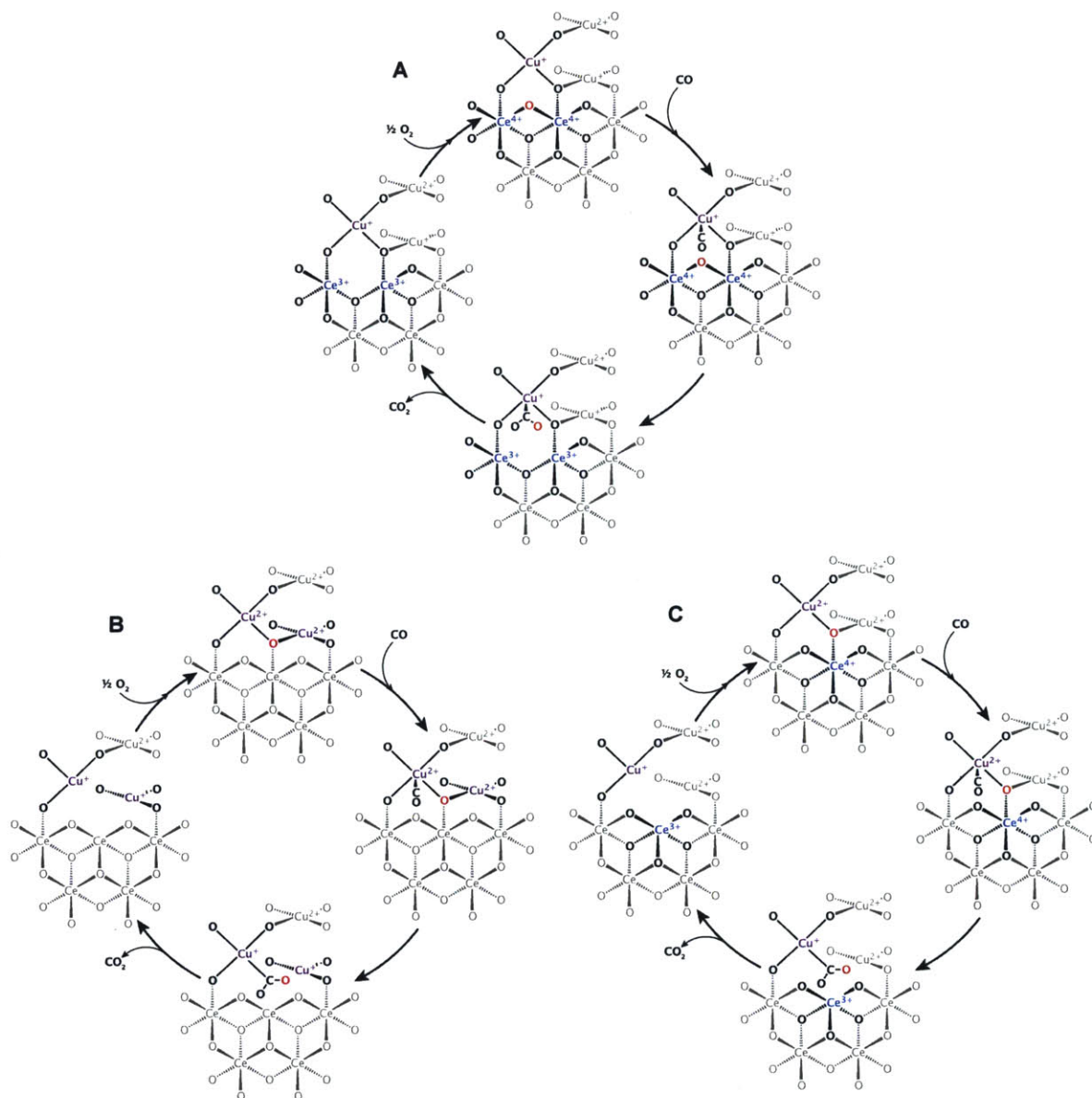


Figure 1.6 Proposed mechanisms for CO oxidation over CuO/CeO_2 catalysts; (A) the Flytzani-Stephanopoulos, (B) Harrison and (C) Martínez-Arias models.

The proposed mechanism (Figure 1.6A), akin to a non-competitive Langmuir-Hinshelwood model, draws upon the previous discussions on Cu, Cu₂O, CuO and CeO₂ to exclude any electron transfer at the copper centers. Rather, Cu⁺ serves only to adsorb CO and deliver it to the interfacial reaction zone with CeO₂. The observation that only minute amounts of copper are required for the improved catalytic rate enhancement of CeO₂ and that the activity of these catalysts decreases with copper contents greater than 5% seems to support this conclusion; catalysis is not limited by CO adsorption, but rather, by the redox chemistry occurring at the interfacial zone localized at Ce⁴⁺ centers.⁹⁹ The “strong interaction between the transition metal and the fluorite oxide” lies in the ability of CeO₂ to stabilize the formation of interfacial Cu⁺ ions.

However, electron paramagnetic resonance (EPR) measurements of CuO/CeO₂ before and after thermal treatments suggested otherwise. One year before Flytzani-Stephanopoulos used CuO/CeO₂ for CO oxidation, a group of Spanish chemists including José Carlos Conesa Cegarra and Arturo Martínez-Arias studied the interaction of copper ions with ceria in CuO/CeO₂ samples by EPR.¹⁰⁰ Apart from CuO, which is proposed to make up 75% of the copper composition but is difficult to detect by EPR, copper exists as isolated Cu²⁺ sites, O²⁻-bridged Cu²⁺-Cu²⁺ dimers and aggregated Cu²⁺ clusters in CuO/CeO₂.¹⁰¹ The dispersed Cu²⁺ sites are incorporated into the surface through the aid of surface oxygen vacancies in CeO₂. Additionally, the dispersed Cu²⁺ doesn't irreversibly reduce to Cu⁺ or Cu⁰ until heated to 400 °C under hydrogen streams, suggesting that copper most likely exists as Cu²⁺ in CuO/CeO₂ samples and not Cu⁺ as proposed by Flytzani-Stephanopoulos.¹⁰² In contrast to the mechanism proposed by Flytzani-Stephanopoulos, Harrison *et al.* used *in-situ* EPR spectroscopy, among other techniques such as X-ray absorption spectroscopy (XAS), to monitor changes in the oxidation state and chemical structure of Cu²⁺ ions in CuO/CeO₂ under catalytically-relevant conditions for CO oxidation.¹⁰³ These studies found that Cu²⁺ sites can be reversibly reduced under relatively mild atmospheres of CO. The authors found that the aggregated Cu²⁺ clusters are the first to be reduced, followed by O²⁻-bridged Cu²⁺-Cu²⁺ dimers, isolated Cu²⁺ centers and finally Ce⁴⁺. In light of these studies, a new mechanism was proposed in which Cu²⁺ centers are solely responsible for electron transfer during oxygen atom transfer to Cu-bound CO (Figure 1.6B).¹⁰³ In contrast to the Flytzani-Stephanopoulos model, which envisioned Cu⁺ sites as promoting CO oxidation activity at

CeO₂, the reversible reducibility of dispersed Cu²⁺ species is at the heart of the special catalytic activity of CuO/CeO₂. Indeed, measuring the redox potentials of Cu^{2+/+} and Cu⁺⁰ by means of cyclic voltammetry in aqueous solutions, Bera *et al.* showed that both of these redox couples were more accessible in CuO/CeO₂ composite materials compared to bulk CuO powders.¹⁰⁴

Martínez-Arias and coworkers used EPR, XPS, FTIR and other techniques to further investigate interactions between dispersed Cu²⁺ ions and CeO₂ under CO and O₂ atmospheres. These researchers found that the reducibility of the dispersed Cu²⁺ species decreases with increased aggregation,¹⁰¹ which is in contrast to the trends found by Harrison *et al.*¹⁰³ Noteworthy, the interaction between copper and cerium sites was found to modulate the reducibility of Ce⁴⁺ in addition to Cu²⁺. In light of these measurements, the authors proposed that the special catalytic activity for CO oxidation in CuO/CeO₂ arises from a synergism between the redox couples of both Cu²⁺ and Ce⁴⁺ that lowers the energy penalty associated with vacancy formation and the reduction of the catalyst surface.¹⁰⁵ In the Martínez-Arias mechanism, CO adsorbs to Cu²⁺ centers on dispersed CuO clusters (Figure 1.6C). The transfer of the surface lattice oxygen occurs at the interface between the CuO phase and the CeO₂ phase and is facilitated by the redox synergy between Cu²⁺ and Ce⁴⁺. Under more reducing conditions, this leads to a reversible reduction of both the CuO and CeO₂ phases that propagates from the interfacial region.¹⁰⁶ While it is difficult to differentiate the two redox mechanisms proposed by Harrison and Martínez-Arias (the main difference being whether the reduction of the catalyst surface is localized around Cu²⁺ only or is shared with Ce⁴⁺ sites), transient kinetic measurements seem to favor the Mars-van Krevelen mechanism over the Langmuir-Hinshelwood mechanism initially proposed by Flytzani-Stephanopoulos.¹⁰⁷ Recently, kinetic data pertaining to the CuO/CeO₂ catalyst system compiled from a wealth of literature obtained over fifteen years were evaluated according to different mechanistic models. This study found that the compiled kinetic data fit a mechanism analogous to Harrison and Martínez-Arias (Figure 1.6B and C) better than the mechanism proposed by Flytzani-Stephanopoulos (Figure 1.6A).¹⁰⁸

While bulk kinetic measurements can reveal a wealth of information about the reaction mechanisms of catalyst mixtures, the inherent heterogeneity of systems such as CuO/CeO₂ and Au/TiO₂ makes the identification of the active site a troublesome prospect. As we've

already seen for CuO/CeO₂, at least four different forms of copper can be detected by XPS and EPR; bulk CuO, isolated Cu²⁺ ions, O²⁻-bridged Cu²⁺-Cu²⁺ dimers and aggregated Cu²⁺ clusters that are distinct from CuO. The immiscibility of copper and cerium oxides mentioned by the initial reports by Flytzani-Stephanopoulos suggest that the dispersed Cu²⁺ ions form surface coordination complexes on CeO₂ facets, which is consistent with electron diffraction, HRTEM, XPS and XAFS studies on nanocrystalline CuO/CeO₂.¹⁰⁹ Thermal treatments tend to favor the formation of a copper-rich “crust” at the surfaces of ceria nanoparticles. A careful analysis of these Cu_xCe_{1-x}O_{2-y} compounds with XRD, XAFS, Raman spectroscopy and DFT suggest that the dispersed copper ions may have oxidation states higher than 2+.¹¹⁰ In order to investigate the role that the Cu_xCe_{1-x}O_{2-y} phase has with respect to its interface with CuO, comparative CO oxidation studies were carried out with well-defined Janus CuO/CeO₂ nanoparticles. The researchers found that the catalytic TOFs correlated with the relative abundance of CuO/CeO₂ perimeters.¹¹¹ While this interfacial phenomenon has been observed for other systems, notably in CeO₂-supported metal catalysts for CO oxidation by the group of Chris Murray,¹¹² the role of the superficial Cu_xCe_{1-x}O_{2-y} phase is still not known. Previous studies demonstrated that this phase forms under thermal treatments of mixtures of crystalline CuO and CeO₂,¹⁰⁹ hence the attribution of the interface of CuO and CeO₂ crystallites to the special catalytic activity of CuO/CeO₂ mixtures may be complicated by the participation of the surface Cu_xCe_{1-x}O_{2-y} compound. In a recent publication, Jia *et al.* addressed this point by showing with XPS that the underlying support for CuO/CeO₂ catalysts is in fact the Cu_xCe_{1-x}O_{2-y} phase.⁴⁶ These researchers also found that the underlying Cu_xCe_{1-x}O_{2-y} support was at least an order of magnitude less active for CO oxidation catalysis than the CuO/CeO₂ ensemble. In line with the mechanisms proposed by Harrison and Martínez-Arias (Figure 1.6B and C), the authors proposed that the CuO/Cu_xCe_{1-x}O_{2-y} interface is the site of CO oxidation, with the Cu_xCe_{1-x}O_{2-y} acting as a promoter for the delivery of activated O²⁻ equivalents to CO-bound Cu²⁺ sites at the perimeter of bulk CuO particles.⁴⁶ Unfortunately, the means by which the underlying Cu_xCe_{1-x}O_{2-y} phase was revealed included the etching of bulk CuO from CuO/CeO₂ catalysts with solutions of nitric acid. While this treatment removes any bulk CuO, it would also remove any ionic copper sites at the surface of the Cu_xCe_{1-x}O_{2-y} phase, leaving only subsurface copper ions. As a result, the uncovered Cu_xCe_{1-x}O_{2-y} sample would have no surface copper sites for CO

adsorption and catalysis, which would help to explain the low catalytic activities of such samples. The complexity of the CuO/CeO₂ system provides a poignant example of the problems currently experienced when attempting to describe heterogeneous catalysis in any scientifically meaningful way.

1.5.4 Three Open Questions

As highlighted in the previous section, research into CO oxidation catalysis over CuO/CeO₂ mixed-phase catalysts is fraught with disagreement and conflicting hypotheses. While it is generally agreed upon that the interface between CuO and CeO₂ phases is critical for the promotion of CO oxidation catalysis, researchers cannot reach a consensus regarding the nature of the interaction between the copper and ceria phases. While some suggest that the transfer of the oxygen atom occurs at the ceria lattice, with the copper phase as an adsorbant of CO (Figure 1.6A), others hypothesize that the redox properties of the copper are modulated by its association with ceria and that oxygen and electron transfer occurs at the copper ion (Figure 1.6B and C). The differences between the three mechanisms proposed in Figure 1.6 seem trivial and open to interpretation. Assigning formal oxidation states to copper and cerium during the mechanism should be thought of as nothing more than a pedagogical tool to understand the role of these ions during catalysis. In that way, one interpretation of the data collected so far could call for a linear combination of the mechanisms proposed in Figure 1.6B and C, where the two-electron reduction of the catalyst surface isn't localized to any one or two atoms, but rather shared between three (or more) surface sites. Ultimately, the distribution and transfer of electrons in a complicated solid such as CuO/CeO₂ should be treated in a delocalized manner over the entire surface, but the localized picture exemplified in Figure 1.6 serves as a useful tool to understand the fundamental processes occurring at the surface and how to tune it to enhance catalysis.

As we've mentioned in 1.1, a formidable barrier to understanding catalytic processes on surfaces is the very fact that surfaces are heterogeneous in nature. No matter how well we control the surface termination in a single crystal, or the crystallite habit of a nanoparticle, the catalytic surface will inevitably have defects and heterogeneities in addition to the idealized surface sites we envision. The information we extract from analysis of these surfaces by microscopy and spectroscopy, even "surface-sensitive" techniques such as XPS, give us a sketch of the surface that is the average of idealized and defect surface sites as well

as sites found in the bulk, although techniques such as COBRA and sum frequency generation spectroscopy have made progress to eliminate the latter. Heterogeneous catalysis is the study of rare events occurring at surfaces. As such, any family of surface sites could be responsible for the reaction kinetics that are measured macroscopically, even those that cannot be detected within the limits of the characterization techniques. Thus, a rigorous investigation of heterogeneous catalysis requires the use of multiple, complementary characterization techniques. The picture is considerably more complex once we extend this reasoning to multi-phase catalyst systems such as CuO/CeO₂. As previous research has made evident, copper is distributed in a myriad of configurations ranging from extended crystallites of CuO to site-isolated Cu²⁺ centers. There is also evidence for Cu⁺ as well as copper in oxidation states above 2+ in CuO/CeO₂. The existence of two phases also necessitates the introduction of interfaces between them. Any or all of these sites and defects could contribute to the special catalytic activity found in CuO/CeO₂. The thesis that follows addresses three open questions concerning CO oxidation catalysis on ceria-based materials, the first of which concerns identifying the active site: **(i) What is the active site for CO oxidation on CuO/CeO₂?**

As we have seen in our review of the literature, the chemical and oxidation states of both copper and cerium in CuO/CeO₂ are fluxional and dependent on the catalytic conditions, even at room temperature. The characterization of the catalytic sites under catalytically relevant conditions is therefore of prime importance when formulating a hypothesis regarding the mechanism of any heterogeneously catalyzed process. As we have seen in 1.3, the electronic structure of the active site can describe its catalytic activity and therefore guide the design of better catalysts. Given the complexity of the CuO/CeO₂ system, this thesis also hope to address a second line of enquiry: **(ii) How does CuO/CeO₂ catalyze CO oxidation and what is the structure of the catalytically active site under reaction conditions?**

A close study of the second question leads naturally to a hypothesis regarding the mechanism of CO oxidation on CuO/CeO₂. As we have seen in 1.5.3, previous experiments have lead to at least three mechanistic models for CO oxidation on CuO/CeO₂ mixtures. What each of these studies lacks, however, is any conceptual framework of CO oxidation catalysis that extends beyond the CuO/CeO₂ system. The inherent complexity of CuO/CeO₂ presumably prevents the extension of what we've learned about CO oxidation to other CeO₂-

based catalysts. The third question this thesis endeavors to answer can be restated as: **(iii) Why is CuO/CeO₂ active for CO oxidation catalysis?** Why was copper and not nickel, for example, selected for CO oxidation on CeO₂? The CO oxidation activity on carbon monoxide dehydrogenase II (CODH-II) throws this question in sharp relief. X-ray crystallographic studies of CODH II have identified reaction intermediates analogous to those proposed in the mechanisms for CO oxidation on CuO/CeO₂ (Figure 1.6B and C).¹¹³ However, in contrast to CuO/CeO₂, millions of years of evolution have optimized CODH II to contain nickel and not copper in the active site, which is nearly 7 orders of magnitude more active than CuO/CeO₂ and four orders of magnitude more active than state-of-the-art Au/TiO₂.¹¹⁴ Why does CODH-II contain a nickel active site while CuO/CeO₂ contains a copper active site if they share a similar reaction mechanism? While this question is inherently naïve (CO oxidation occurs in drastically different media for these two catalysts and may not strictly follow the same mechanism), there is value in exploring it as a thought experiment. As we have seen throughout this chapter, heterogeneous catalysts are often discovered through serendipity. Copper and ceria were originally chosen as candidate materials for CO oxidation based on their previously measured properties.⁹⁷ The essence of question (iii) boils down to whether the special activity of CuO/CeO₂ could have been predicted in the absence of previously measured properties. The advantage of applying linear free-energy scaling relationships to topics in catalysis is that it provides a conceptual framework to answer questions such as (iii), while providing a strategy for the rational design of better catalysts.

1.6 Scope of the Thesis

Studies in the following chapters serve to shed light on CO oxidation catalysis over transition-metal substituted CeO₂ catalysts, with a particular emphasis on Cu_xCe_{1-x}O_{2-y}, by addressing questions (i) – (iii). Any conclusion about CO oxidation catalysis on M_xCe_{1-x}O_{2-y} requires the preparation of a well-characterized catalyst library where differences in crystallite size, habit and the local molecular structure of the transition-metal center are minimized. Chapter 2 demonstrates that a suitable library of monodisperse M_xCe_{1-x}O_{2-y} nanoparticles can be prepared from the pyrolysis of surfactant solutions of heterobimetallic Schiff base compounds. A close look at the molecular structure of the transition-metal ions in M_xCe_{1-x}O_{2-y} using a suite of characterization techniques suggests that they are dispersed into the CeO₂ matrix as isolated, square-planar M³⁺ and M²⁺ species. Chapter 3 addresses (i) by

comparing the CO oxidation kinetics of phase-pure $\text{Cu}_x\text{Ce}_{1-x}\text{O}_{2-y}$ with mixed-phase $\text{CuO}/\text{Cu}_x\text{Ce}_{1-x}\text{O}_{2-y}$. We find that the dispersed Cu^{3+} ions of $\text{Cu}_x\text{Ce}_{1-x}\text{O}_{2-y}$, and not the interface between CuO and $\text{Cu}_x\text{Ce}_{1-x}\text{O}_{2-y}$, are solely responsible for the high catalytic activity of CuO/CeO_2 catalysts. Experimental and computational investigations suggest that the copper ions segregate to the surface of the $\text{Cu}_x\text{Ce}_{1-x}\text{O}_{2-y}$ nanoparticle. With the knowledge garnered from Chapters 2 and 3, a suite of *in-situ* characterization techniques was employed in Chapter 4 to determine the mechanistic underpinnings of CO oxidation catalysis on $\text{Cu}_x\text{Ce}_{1-x}\text{O}_{2-y}$, thereby addressing (ii). We propose that the rate-determining step for CO oxidation on $\text{Cu}_x\text{Ce}_{1-x}\text{O}_{2-y}$ involves the formation of an oxygen vacancy adjacent to the copper centers. In Chapter 5, we tackle (iii) by demonstrating that the oxygen-ion vacancy formation energy is a suitable descriptor for CO oxidation catalysis with $\text{M}_x\text{Ce}_{1-x}\text{O}_{2-y}$ nanoparticles. The stabilization of reversibly reducible Cu^{3+} by the CeO_2 host lattice serves as the major contributing factor for its special activity for CO oxidation catalysis.

1.7 References

- (1) Smil, V. *Enriching the Earth: Fritz Haber, Carl Bosch, and the Transformation of World Food Production*; The MIT Press, 2001.
- (2) Ritter, S. K. *Chem. Eng. News* **2008**, 86, Web Edition.
- (3) Kaspar, J.; Fornasiero, P.; Hickey, N. *Catal. Today* **2003**, 77, 419.
- (4) Oetjen, H. F.; Schmidt, V. M.; Stimming, U.; Trila, F. *J. Electrochem. Soc.* **1996**, 143, 3838.
- (5) Li, Q.; He, R.; Jensen, J. O.; Bjerrum, N. J. *Chem. Mater.* **2003**, 15, 4896.
- (6) Faur Ghenciu, A. *Curr. Opin. Solid State Mater. Sci.* **2002**, 6, 389.
- (7) Park, E. D.; Lee, D.; Lee, H. C. *Catal. Today* **2009**, 139, 280.
- (8) Freund, H.-J.; Meijer, G.; Scheffler, M.; Schlögl, R.; Wolf, M. *Angew. Chem. Int. Ed.* **2011**, 50, 10064.
- (9) Feng, Z.; Yacoby, Y.; Gadre, M. J.; Lee, Y.-L.; Hong, W. T.; Zhou, H.; Biegalski, M. D.; Christen, H. M.; Adler, S. B.; Morgan, D.; Shao-Horn, Y. *J. Phys. Chem. Lett.* **2014**, 5, 1027.
- (10) Su, X.; Cremer, P. S.; Shen, Y. R.; Somorjai, G. A. *J. Am. Chem. Soc.* **1997**, 119, 3994.

- (11) Dellwig, T.; Rupprechter, G.; Unterhalt, H.; Freund, H. J. *Phys. Rev. Lett.* **2000**, *85*, 776.
- (12) Brønsted, J. N. *Chem. Rev.* **1928**, *5*, 231.
- (13) Bell, R. P. *Proc. R. Soc. London, Ser. A* **1936**, *154*, 414.
- (14) Evans, M. G.; Polanyi, M. *Trans. Faraday Soc.* **1936**, *32*, 1333.
- (15) Hammett, L. P. *J. Am. Chem. Soc.* **1937**, *59*, 96.
- (16) Carey, F. A.; Sundberg, R. J. *Advanced Organic Chemistry*; Springer, 2007.
- (17) Sabatier, P. *Ber. Dtsch. Chem. Ges.* **1911**, *44*, 1984.
- (18) Sabatier, P. *La Catalyse en Chimie Organique*; Béranger: Paris, 1920.
- (19) Hammer, B. *Top. Catal.* **2006**, *37*, 3.
- (20) Nilsson, A.; Pettersson, L. G. M.; Hammer, B.; Bligaard, T.; Christensen, C. H.; Nørskov, J. K. *Catal. Lett.* **2005**, *100*, 111.
- (21) Mun, B. S.; Watanabe, M.; Rossi, M.; Stamenkovic, V.; Markovic, N. M.; Ross, P. N. *J. Chem. Phys.* **2005**, *123*, 204717.
- (22) Stamenkovic, V. R.; Mun, B. S.; Arenz, M.; Mayrhofer, K. J. J.; Lucas, C. A.; Wang, G.; Ross, P. N.; Markovic, N. M. *Nat. Mater.* **2007**, *6*, 241.
- (23) Stamenkovic, V. R.; Fowler, B.; Mun, B. S.; Wang, G.; Ross, P. N.; Lucas, C. A.; Markovic, N. M. *Science* **2007**, *315*, 493.
- (24) Stamenkovic, V.; Mun, B. S.; Mayrhofer, K. J. J.; Ross, P. N.; Markovic, N. M.; Rossmeisl, J.; Greeley, J.; Nørskov, J. K. *Angew. Chem. Int. Ed.* **2006**, *45*, 2897.
- (25) Nilekar, A. U.; Xu, Y.; Zhang, J.; Vukmirovic, M. B.; Sasaki, K.; Adzic, R. R.; Mavrikakis, M. *Top. Catal.* **2007**, *46*, 276.
- (26) Lima, F. H. B.; Zhang, J.; Shao, M. H.; Sasaki, K.; Vukmirovic, M. B.; Ticianelli, E. A.; Adzic, R. R. *J. Phys. Chem. C* **2007**, *111*, 404.
- (27) Adzic, R. R.; Zhang, J.; Sasaki, K.; Vukmirovic, M. B.; Shao, M.; Wang, J. X.; Nilekar, A. U.; Mavrikakis, M.; Valerio, J. A.; Uribe, F. *Top. Catal.* **2007**, *46*, 249.
- (28) Abe, H.; Yoshikawa, H.; Umezawa, N.; Xu, Y.; Saravanan, G.; Ramesh, G. V.; Tanabe, T.; Kodiyath, R.; Ueda, S.; Sekido, N.; Yamabe-Mitarai, Y.; Shimoda, M.; Ohno, T.; Matsumoto, F.; Komatsu, T. *Phys. Chem. Chem. Phys.* **2015**, *17*, 4879.
- (29) Lee, Y.-L.; Kleis, J.; Rossmeisl, J.; Shao-Horn, Y.; Morgan, D. *Energy Environ. Sci.* **2011**, *4*, 3966.

- (30) Grimaud, A.; May, K. J.; Carlton, C. E.; Lee, Y.-L.; Risch, M.; Hong, W. T.; Zhou, J.; Shao-Horn, Y. *Nat. Commun.* **2013**, *4*.
- (31) Suntivich, J.; Gasteiger, H. A.; Yabuuchi, N.; Nakanishi, H.; Goodenough, J. B.; Shao-Horn, Y. *Nat. Chem.* **2011**, *3*, 546.
- (32) Suntivich, J.; May, K. J.; Gasteiger, H. A.; Goodenough, J. B.; Shao-Horn, Y. *Science* **2011**, *334*, 1383.
- (33) Calle-Vallejo, F.; Inoglu, N. G.; Su, H.-Y.; Martinez, J. I.; Man, I. C.; Koper, M. T. M.; Kitchin, J. R.; Rossmeisl, J. *Chem. Sci.* **2013**, *4*, 1245.
- (34) Hong, W. T.; Welsch, R. E.; Shao-Horn, Y. *J. Phys. Chem. C* **2016**, *120*, 78.
- (35) Trasatti, S. *J. Electroanal. Chem. Interfacial Electrochem.* **1980**, *111*, 125.
- (36) Bockris, J. O.; Otagawa, T. *J. Phys. Chem.* **1983**, *87*, 2960.
- (37) Bockris, J. O. M.; Otagawa, T. *J. Electrochem. Soc.* **1984**, *131*, 290.
- (38) Somorjai, G. A. *Introduction to Surface Chemistry and Catalysis, Second Edition*; John Wiley & Sons, 2010.
- (39) Langmuir, I. *Trans. Faraday Soc.* **1922**, *17*, 621.
- (40) Falsig, H.; Hvolbæk, B.; Kristensen, I.; Jiang, T.; Bligaard, T.; Christensen, C.; Nørskov, J. *Angew. Chem. Int. Ed.* **2008**, *47*, 4835.
- (41) Jiang, T.; Mowbray, D. J.; Dobrin, S.; Falsig, H.; Hvolbæk, B.; Bligaard, T.; Nørskov, J. K. *J. Phys. Chem. C* **2009**, *113*, 10548.
- (42) Mars, P.; van Krevelen, D. W. *Chem. Eng. Sci.* **1954**, *3*, *Supplement 1*, 41.
- (43) Over, H.; Kim, Y. D.; Seitsonen, A. P.; Wendt, S.; Lundgren, E.; Schmid, M.; Varga, P.; Morgante, A.; Ertl, G. *Science* **2000**, *287*, 1474.
- (44) Huang, T.-J.; Tsai, D.-H. *Catal. Lett.* **2003**, *87*, 173.
- (45) Sedmak, G.; Hocevar, S.; Levec, J. *J. Catal.* **2003**, *213*, 135.
- (46) Jia, A.-P.; Hu, G.-S.; Meng, L.; Xie, Y.-L.; Lu, J.-Q.; Luo, M.-F. *J. Catal.* **2012**, *289*, 199.
- (47) Hendriksen, B. L. M.; Frenken, J. W. M. *Phys. Rev. Lett.* **2002**, *89*, 046101.
- (48) Bennett, M. A.; Robertson, G. B.; Rokicki, A.; Wickramasinghe, W. A. *J. Am. Chem. Soc.* **1988**, *110*, 7098.
- (49) Bennett, M. A.; Jin, H.; Willis, A. C. *J. Organomet. Chem.* **1993**, *451*, 249.

- (50) Lee, D. W.; Jensen, C. M.; Morales-Morales, D. *Organometallics* **2003**, *22*, 4744.
- (51) Yoo, C.; Kim, J.; Lee, Y. *Organometallics* **2013**, *32*, 7195.
- (52) Ruscic, B.; Feller, D.; Peterson, K. A. *Theor. Chem. Acc.* **2013**, *133*, 1.
- (53) Haruta, M.; Yamada, N.; Kobayashi, T.; Iijima, S. *J. Catal.* **1989**, *115*, 301.
- (54) Xie, X.; Li, Y.; Liu, Z.-Q.; Haruta, M.; Shen, W. *Nature* **2009**, *458*, 746.
- (55) Liu, W.; Sarofim, A. F.; Flytzani-Stephanopoulos, M. *Chem. Eng. Sci.* **1994**, *49*, 4871.
- (56) Haruta, M.; Kobayashi, T.; Sano, H.; Yamada, N. *Chem. Lett.* **1987**, 405.
- (57) Hashmi, A. S. K.; Hutchings, G. J. *Angew. Chem. Int. Ed.* **2006**, *45*, 7896.
- (58) Bond, G. C.; Thompson, D. T. *Gold Bull. (Berlin, Ger.)* **2000**, *33*, 41.
- (59) Kung, H. H.; Kung, M. C.; Costello, C. K. *J. Catal.* **2003**, *216*, 425.
- (60) Kung, M. C.; Davis, R. J.; Kung, H. H. *J. Phys. Chem. C* **2007**, *111*, 11767.
- (61) Boyd, D.; Golunski, S.; Hearne, G. R.; Magadzu, T.; Mallick, K.; Raphulu, M. C.; Venugopal, A.; Scurrrell, M. S. *Appl. Catal., A* **2005**, *292*, 76.
- (62) Haruta, M. *Gold Bull. (Berlin, Ger.)* **2004**, *37*, 27.
- (63) Schwartz, V.; Mullins, D. R.; Yan, W.; Chen, B.; Dai, S.; Overbury, S. H. *J. Phys. Chem. B* **2004**, *108*, 15782.
- (64) Yang, J. H.; Henao, J. D.; Raphulu, M. C.; Wang, Y.; Caputo, T.; Groszek, A. J.; Kung, M. C.; Scurrrell, M. S.; Miller, J. T.; Kung, H. H. *J. Phys. Chem. B* **2005**, *109*, 10319.
- (65) Finch, R. M.; Hodge, N. A.; Hutchings, G. J.; Meagher, A.; Pankhurst, Q. A.; Siddiqui, M. R. H.; Wagner, F. E.; Whyman, R. *Phys. Chem. Chem. Phys.* **1999**, *1*, 485.
- (66) Chen, M. S.; Goodman, D. W. *Science* **2004**, *306*, 252.
- (67) Lopez, N.; Janssens, T. V. W.; Clausen, B. S.; Xu, Y.; Mavrikakis, M.; Bligaard, T.; Nørskov, J. K. *J. Catal.* **2004**, *223*, 232.
- (68) Walther, G.; Mowbray, D. J.; Jiang, T.; Jones, G.; Jensen, S.; Quaade, U. J.; Horch, S. *J. Catal.* **2008**, *260*, 86.
- (69) Yao, Y.-F. Y. *J. Catal.* **1974**, *33*, 108.

Chapter 1

- (70) Cunningham, D. A. H.; Kobayashi, T.; Kamijo, N.; Haruta, M.; Springer Netherlands: 1994; Vol. 25, p 257.
- (71) Grillo, F.; Natile, M. M.; Glisenti, A. *Appl. Catal., B* **2004**, *48*, 267.
- (72) Omata, K.; Takada, T.; Kasahara, S.; Yamada, M. *Appl. Catal. A* **1996**, *146*, 255.
- (73) Jansson, J. *J. Catal.* **2000**, *194*, 55.
- (74) Petitto, S. C.; Marsh, E. M.; Carson, G. A.; Langell, M. A. *J. Mol. Catal. A: Chem.* **2008**, *281*, 49.
- (75) Hu, L.; Sun, K.; Peng, Q.; Xu, B.; Li, Y. *Nano Res.* **2010**, *3*, 363.
- (76) Jiang, D.-e.; Dai, S. *Phys. Chem. Chem. Phys.* **2011**, *13*, 978.
- (77) Pang, X.-Y.; Liu, C.; Li, D.-C.; Lv, C.-Q.; Gui-Chang, W. *ChemPhysChem* **2013**, *14*, 204.
- (78) Royer, S.; Duprez, D. *ChemCatChem* **2011**, *3*, 24.
- (79) Almquist, J. A.; Bray, W. C. *J. Am. Chem. Soc.* **1923**, *45*, 2305.
- (80) Pease, R. N.; Taylor, H. S. *J. Phys. Chem.* **1920**, *24*, 241.
- (81) Shi, J. *Chem. Rev.* **2013**, *113*, 2139.
- (82) Garner, W. E.; Stone, F. S.; Tiley, P. F. *Proc. R. Soc. London, Ser. A* **1952**, *211*, 472.
- (83) Jennings, T. J.; Stone, F. S. In *Proceedings of the International Congress on Catalysis*; Farkas, A., Ed.; Academic Press: 1957; Vol. Volume 9, p 441.
- (84) Jernigan, G. G.; Somorjai, G. A. *J. Catal.* **1994**, *147*, 567.
- (85) Sadykov, V. A.; Tikhov, S. F. *J. Catal.* **1997**, *165*, 279.
- (86) Sadykov, V. A.; Tikhov, S. F.; Bulgakov, N. N.; Gerasev, A. P. *Catal. Today* **2009**, *144*, 324.
- (87) Pierron, E. D.; Rashkin, J. A.; Roth, J. F. *J. Catal.* **1967**, *9*, 38.
- (88) Yu Yao, Y. F.; Kummer, J. T. *J. Catal.* **1977**, *46*, 388.
- (89) Choi, K. I.; Vannice, M. A. *J. Catal.* **1991**, *131*, 22.
- (90) Huang, T.-J.; Yu, T.-C.; Chang, S.-H. *Appl. Catal.* **1989**, *52*, 157.
- (91) Rideal, E. K.; Taylor, H. S. *Analyst (Cambridge, U. K.)* **1919**, *44*, 89.

- (92) Yao, H. C.; Yao, Y. F. Y. *J. Catal.* **1984**, *86*, 254.
- (93) Martin, D.; Duprez, D. *J. Phys. Chem.* **1996**, *100*, 9429.
- (94) Madier, Y.; Descorme, C.; Le Govic, A. M.; Duprez, D. *J. Phys. Chem. B* **1999**, *103*, 10999.
- (95) Sun, C.; Li, H.; Chen, L. *Energy Environ. Sci.* **2012**, *5*, 8475.
- (96) Breysse, M.; Guenin, M.; Claudel, B.; Veron, J. *J. Catal.* **1973**, *28*, 54.
- (97) Liu, W.; Flytzani-Stephanopoulos, M. *J. Catal.* **1995**, *153*, 304.
- (98) Liu, W.; Flytzani-Stephanopoulos, M. *J. Catal.* **1995**, *153*, 317.
- (99) Liu, W.; Flytzani-Stephanopoulos, M. *Chem. Eng. J. (Amsterdam, Neth.)* **1996**, *64*, 283.
- (100) Soria, J.; Conesa, J. C.; Martinez-Arias, A.; Coronado, J. M. *Solid State Ionics* **1993**, *63 - 65*, 755.
- (101) Martinez-Arias, A.; Fernandez-Garcia, M.; Soria, J.; Conesa, J. C. *J. Catal.* **1999**, *182*, 367.
- (102) Aboukhis, A.; Bennani, A.; Lamonier-Dulongpont, C.; Abi-Aad, E.; Wrobel, G. *Colloids Surf., A* **1996**, *115*, 171.
- (103) Harrison, P. G.; Ball, I. K.; Azelee, W.; Daniell, W.; Goldfarb, D. *Chem. Mater.* **2000**, *12*, 3715.
- (104) Bera, P.; Mitra, S.; Sampath, S.; Hegde, M. S. *Chem. Commun.* **2001**, 927.
- (105) Martinez-Arias, A.; Fernandez-Garcia, M.; Galvez, O.; Coronado, J. M.; Anderson, J. A.; Conesa, J. C.; Soria, J.; Munuera, G. *J. Catal.* **2000**, *195*, 207.
- (106) Martinez-Arias, A.; Hungria, A. B.; Fernandez-Garcia, M.; Conesa, J. C.; Munuera, G. *J. Phys. Chem. B* **2004**, *108*, 17983.
- (107) Sedmak, G.; Hocevar, S.; Levec, J. *J. Catal.* **2004**, *222*, 87.
- (108) Moreno, M.; Bergamini, L.; Baronetti, G. T.; Laborde, M. A.; Mariño, F. J. *Int. J. Hydrogen Energy* **2010**, *35*, 5918.
- (109) Skarman, B.; Grandjean, D.; Benfield, R. E.; Hinz, A.; Andersson, A.; Wallenberg, L. *R. J. Catal.* **2002**, *211*, 119.
- (110) Wang, X.; Rodriguez, J. A.; Hanson, J. C.; Gamarra, D.; Martinez-Arias, A.; Fernandez-Garcia, M. *J. Phys. Chem. B* **2005**, *109*, 19595.

Chapter 1

- (111) Jia, A.-P.; Jiang, S.-Y.; Lu, J.-Q.; Luo, M.-F. *J. Phys. Chem. C* **2010**, *114*, 21605.
- (112) Cargnello, M.; Doan-Nguyen, V. V. T.; Gordon, T. R.; Diaz, R. E.; Stach, E. A.; Gorte, R. J.; Fornasiero, P.; Murray, C. B. *Science* **2013**, *341*, 771.
- (113) Fessler, J.; Jeoung, J.-H.; Dobbek, H. *Angew. Chem. Int. Ed.* **2015**, *54*, 8560.
- (114) Svetlitchnyi, V.; Peschel, C.; Acker, G.; Meyer, O. *J. Bacteriol.* **2001**, *183*, 5134.

Chapter 2 – The Incorporation of Metal Ions into the Lattice of CeO₂

Portions of this chapter have appeared in print:

Elias, J. S.; Risch, M.; Giordano, L.; Mansour, A. N. & Shao-Horn, Y., “Structure, Bonding and Catalytic Activity of Monodisperse, Transition-Metal-Substituted CeO₂ Nanoparticles,” *J. Am. Chem. Soc.*, **2014**, *136*, 17193-17200. – Reproduced with permission. Copyright 2014 American Chemical Society.

2.1 Introduction

As we have discussed in the previous chapter, the presence of multiple phases in CuO/CeO₂ catalysts along with differences in crystallite size and surface termination may all influence the kinetics of CO oxidation on ceria-based catalysts. A rigorous examination of the active site and mechanism for CO oxidation catalysis on CuO/CeO₂ and the influence of aliovalent substitution on the catalytic activity of ceria-based catalysts necessitates the preparation of a library of these compounds with superior homogeneity in phase, crystallite size and crystallographic termination. The presence of inseparable impurities complicates even the identification of the oxidation state and local structure of M in M_yCe_{1-y}O_{2-x}. In the case of CuO/CeO₂, traditional preparation methods include coprecipitation¹⁻⁵ and excess-solution impregnation⁶⁻⁸ techniques, which lead to the formation of the solid solution Cu_yCe_{1-y}O_{2-x} in addition to dispersed CuO phases, which prevents the rigorous identification of the catalytic site for CO oxidation.^{9,10}

In this chapter, we summarize a generalizable synthetic strategy for the preparation of monodisperse, phase-pure nanocrystals of M_{0.1}Ce_{0.9}O_{2-x} with aliovalent transition-metal substitution (M = Mn, Fe, Co, Ni and Cu). Surprisingly, X-ray absorption spectroscopy at the transition-metal L-, K-, cerium L- and oxygen K-edges confirms that the transition-metal species are stabilized in the 3+ oxidation state upon incorporation into the CeO₂ lattice, in contrast to previous studies on CuO/CeO₂.^{1,5} CO oxidation on Cu_{0.1}Ce_{0.9}O_{2-x} reveals that Cu species in the lattice are responsible for an increase in catalytic activity by an order of magnitude in comparison to undoped, nanocrystalline CeO₂. This finding provides insights into developing novel strategies to design highly active and uniform catalysts for the oxidation of CO and hydrocarbon fuels and for other applications.

2.2 Synthesis of M_{0.1}Ce_{0.9}O_{2-x} (M = Mn, Fe, Co, Ni, Cu)

Monodisperse, hexanes-soluble single crystallites of oleylamine-stabilized M_{0.1}Ce_{0.9}O_{2-x} (M = Mn, Fe, Co, Ni, Cu) were prepared according to Figure 2.1. The synthetic scheme involves the preparation and subsequent decomposition of a library of heterobimetallic Schiff base complexes¹¹⁻¹⁴ derived from the ligand N,N'-bis(3-methoxysalicylidene)-propylene-1,3-diamine (**H₂-3-MeO-salpn**). After the initial coordination of the transition-metal into the inner N₂O₂ site of **H₂-3-MeO-salpn**, the outer O₄ lacunary site is poised for coordination of hard Lewis-acidic rare earth ions, such as Ce³⁺ (Figure 2.1). The choice of heterobimetallic

Schiff base complexes as inorganic precursors was made in order to ensure close association between cerium and transition-metal ions during the nucleation and growth of the M_{0.1}Ce_{0.9}O_{2-x} crystallites in solution, thereby preventing the formation of separate bulk transition-metal oxide phases.

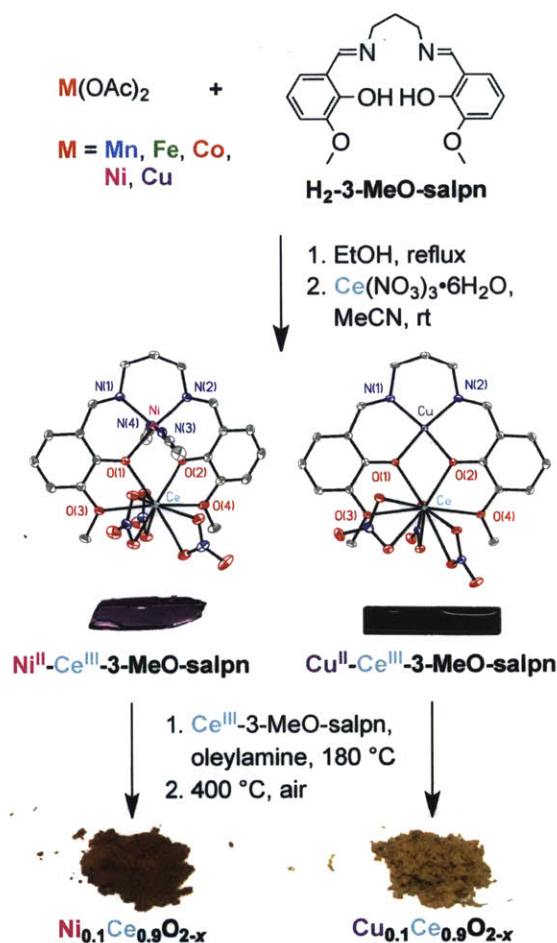


Figure 2.1 The synthesis of M_{0.1}Ce_{0.9}O_{2-x} from heterobimetallic 3-MeO-salpn complexes. Representative crystal structures for Ni^{II}-Ce^{III}-3-MeO-salpn and Cu^{II}-Ce^{III}-3-MeO-salpn are included, with thermal ellipsoids plotted at 50% probability and hydrogen atoms omitted for clarity.

Single crystals of M-Ce^{III}-3-MeO-salpn (M = Co^{III}, Ni^{II}, Cu^{II}) suitable for X-ray crystal structure analysis were obtained from the slow evaporation of the complexes in acetonitrile solutions. The crystal structures of the novel M-Ce^{III}-3-MeO-salpn complexes were found to share similar structural motifs (Figure 2.2). Coordination around the transition-metal site is square planar with respect to the N₂O₂ pocket of the 3-MeO-salpn ligand. 6-fold coordination to the nickel center of Ni^{II}-Ce^{III}-3-MeO-salpn is completed by two axially-coordinated

acetonitrile molecules, while the 6-fold coordination of the cobalt center of $\text{Co}^{\text{III}}\text{-Ce}^{\text{III}}\text{-3-MeO-salpn}$ is achieved by two acetate groups that bridge with the cerium center (Figure 2.2). The copper center is 5-coordinate with a long (2.4236 Å) axial Cu-O bond to a nitrate group that bridges the two asymmetric units that make up the unit cell of $\text{Cu}^{\text{II}}\text{-Ce}^{\text{III}}\text{-3-MeO-salpn}$. Trivalent cerium ions were shown to occupy the lacunary O_4 site, bridging the transition-metal via a pair of μ^2 -phenoxy groups, resulting in short M-Ce interatomic distances (3.3613, 3.5617 and 3.5848 Å for the cobalt, nickel and copper crystal structures, respectively). FTIR, ^1H NMR and elemental analysis confirm the formulas we report here for $\text{Mn}^{\text{II}}\text{-Ce}^{\text{III}}\text{-3-MeO-salpn}$, $\text{Fe}^{\text{III}}\text{-Ce}^{\text{III}}\text{-3-MeO-salpn}$ and $\text{Ce}^{\text{III}}\text{-3-MeO-salpn}$ (see Section 2.6, Experimental Methods).

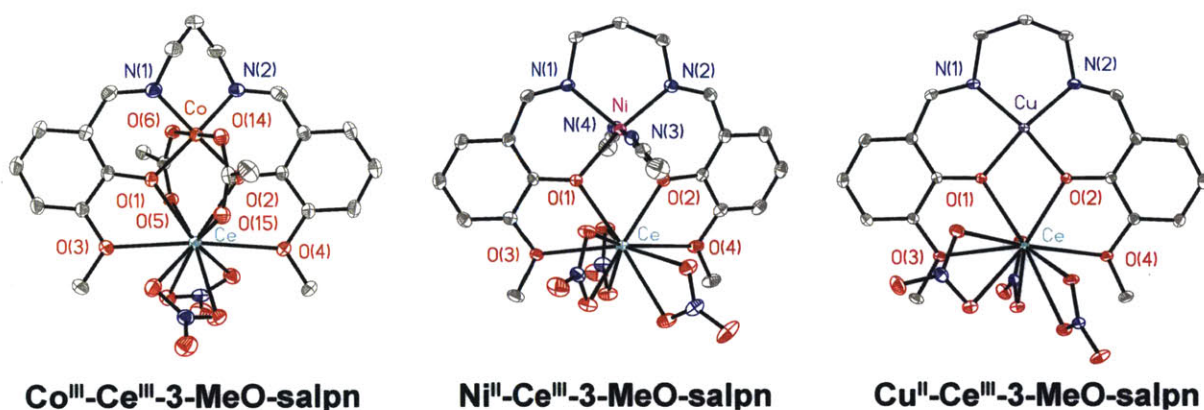


Figure 2.2 The crystal structures of $\text{Co}^{\text{III}}\text{-Ce}^{\text{III}}\text{-3-MeO-salpn}$, $\text{Ni}^{\text{II}}\text{-Ce}^{\text{III}}\text{-3-MeO-salpn}$ and $\text{Cu}^{\text{II}}\text{-Ce}^{\text{III}}\text{-3-MeO-salpn}$. Thermal ellipsoids are plotted at 50% probability and hydrogen atoms are omitted for clarity.

With a library of homologous heterobimetallic precursors in hand, monodisperse $\text{M}_{0.1}\text{Ce}_{0.9}\text{O}_{2-x}$ and CeO_2 nanoparticles were prepared through the pyrolysis of the precursors in oleylamine solutions under an argon atmosphere (Figure 2.1). Powder X-ray diffraction (PXRD) patterns for as-synthesized $\text{M}_{0.1}\text{Ce}_{0.9}\text{O}_{2-x}$ (Figure 2.3) indicate a single crystalline phase, attributed to the fluorite structure of CeO_2 (space group #225, $F_{m\bar{3}m}$). Scherrer analysis of peak broadening shows average crystallite sizes of 2 – 3 nm for $\text{M}_{0.1}\text{Ce}_{0.9}\text{O}_{2-x}$ and CeO_2 (Table 2.2). Profile fitting of PXRD data revealed that CeO_2 nanoparticles have a lattice parameter a (5.42 Å) that is slightly larger than that of bulk CeO_2 (5 mm) found in this study and in previous work (5.41 Å),¹⁵ which can be attributed to the presence of Ce^{3+} and oxygen vacancies on the particle surface.^{16,17} The lattice expansion found for 3 nm CeO_2 is not as drastic as reported earlier for similarly sized ceria nanoparticles (5.4343 Å¹⁸ and 5.5420 Å¹⁵).

The disparate synthesis and annealing conditions reported elsewhere^{15,18} may give rise to different amounts of oxygen vacancies in ceria and help explain such a discrepancy in reported lattice parameter values in nanoparticulate CeO₂.

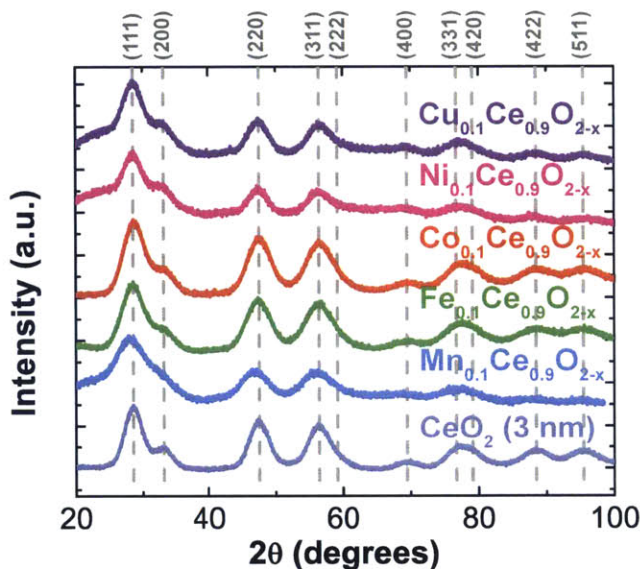


Figure 2.3 PXRD patterns for as-synthesized nanocrystalline $M_{0.1}Ce_{0.9}O_{2-x}$ and CeO_2 compounds taken at room temperature (copper $K\alpha$ source).

Similarly, the lattice parameters found for $M_{0.1}Ce_{0.9}O_{2-x}$ nanoparticles (Table 2.2) were also larger than that found for 5 μm CeO_2 . HRTEM particle-size analysis (Figure 2.4) confirms a narrow size distribution of 3.0 (\pm 0.4) nm crystallites for $M_{0.1}Ce_{0.9}O_{2-x}$. Closer inspection by HRTEM (Figure 2.4, right panels) suggests that the individual crystallites exhibit a truncated octahedral crystal habit, with crystal planes terminated in eight {111} hexagonal facets and four {100} square facets (Figure 2.5), a common crystallite shape reported for ceria nanoparticles.¹⁹

Before further characterization, the $M_{0.1}Ce_{0.9}O_{2-x}$ samples were annealed in air at 400 °C to remove the capping oleylamine layer, as revealed by thermogravimetric analysis (TGA). Ambient pressure XPS measurements of $M_{0.1}Ce_{0.9}O_{2-x}$ at 400 °C in 75 mTorr O₂ suggests that all carbon is removed from the surface of these catalysts after annealing (see Figure 4.7 in Chapter 4). PXRD (Table 2.2) and HRTEM suggest that during the annealing treatment, the mean size of the crystallites increases by as much as 1 nm, presumably through an Ostwald ripening or oriented agglomeration process.²⁰ Energy dispersive X-ray spectroscopy (EDS)

Percent substitution as determined by EDS with a typical experimental uncertainty of 10% in the measured values is in reasonable agreement with the values determined by ICP-AES. Since making Cu_yCe_{1-y}O_{2-x} with percent substitution *y* greater than 10% leads to the formation of multiple phases, we set the limit of substitution for all transition-metal samples to *y* ≈ 10%.

2.3 Identification of the local structure of transition-metal ions in M_{0.1}Ce_{0.9}O_{2-x}

In order to identify the local atomic structure of these catalysts, especially of the redox-active transition-metal centers, we turned our attention to X-ray absorption spectroscopy (XAS). The general features of the Ce L_{III}-edge spectra (Figures 2.6 – 2.9A, B and Tables 2.6 and 2.7) are similar to that of nanocrystalline CeO₂, indicating that the local coordination and oxidation-state of cerium is maintained in M_{0.1}Ce_{0.9}O_{2-x}. In the XANES region (Figures 2.6 – 2.9A) the intensity of the white line at 5729.6 eV decreases for all M_{0.1}Ce_{0.9}O_{2-x} and 3 nm CeO₂ compared to bulk (5 mm) CeO₂, which can be attributed to the decrease in covalency between Ce(4f) and O(2p) found as the particle size of CeO₂ decreases.²¹ Importantly, the intensity of the shoulder at 5724.5 eV, which is attributed to surface Ce³⁺,²¹ does not change with transition-metal substitution. Also noteworthy is that the magnitude of the scattering path (*R* = 2.3 Å) corresponding to the first coordination shell in the EXAFS (Figures 2.6 – 2.9B and Tables 2.6 – 2.7, representing eight-coordinate cerium in CeO₂) is lower for M_{0.1}Ce_{0.9}O_{2-x} and CeO₂ nanoparticles than for bulk (5 mm) CeO₂. Along with this, we found that the magnitudes of the next-nearest neighbor scattering paths (Ce-Ce and Ce-O distances, respectively, *R* = 3.9 and 4.6 Å) also decrease slightly with transition-metal substitution (Figures 2.6 – 2.9B and Table 2.6). These results, which we also found for 3 nm CeO₂ nanoparticles, support the formation of higher concentrations of undercoordinated surface CeO₂ sites with decreasing particle size, which is in good agreement with previous work on CeO₂ nanoparticles.²¹ It should be noted here, as a caveat, that the analysis of the EXAFS of Ce L_{III} spectra of materials based on CeO₂ is rather tenuous.²¹ The fact that the spectra exhibit two white lines suggests, as has previously been discussed at length,^{22,23} a many-body electronic ground state in CeO₂ (*i.e.* one which exhibits substantial configuration interaction between multiple electronic configurations). Therefore, the one-electron theory often used in EXAFS simulations²⁴ does not apply to such oxides. Furthermore, since both

the mean squared displacement (σ^2) and scattering path degeneracy (N) contribute to the magnitude of the EXAFS, a rigorous determination of coordination number could not be accomplished without temperature-dependent studies. The lower intensity magnitudes in the EXAFS are likely due to a combination of smaller values for N (as in Table 2.7) and larger values for σ^2 (as in Table 2.6), both of which are consistent with aliovalent substitution into the CeO₂ lattice.

This comparison of the Ce L_{III}-edge XAS spectra confirms that the local geometric and electronic structure of Ce in M_{0.1}Ce_{0.9}O_{2-x} remains unaltered compared to CeO₂ nanoparticles. This assertion is further supported by spectra at the oxygen K-edge (Figure 2.10A). Spectra for Cu_{0.1}Ce_{0.9}O_{2-x} are identical to unsubstituted 3 nm CeO₂, exhibiting peaks at 533.7 eV without features at lower energies, which reflects that the local density of states around the oxygen ligands is predominantly unperturbed compared to CeO₂. In contrast, the O K-edge spectra for YBa₂Cu₃O_{7- δ} (YBCO) and KCuO₂ exhibit peaks at 532 eV. The peaks at 532 eV is assigned to transitions into holes in the 2p band of oxygen, an indication of charge-transfer in formally trivalent copper compounds.^{25,26} Any contributions from oxygen ligands associated with Cu ions to the XAS spectrum either share features with the spectra of CuO or CeO₂ or are too low in intensity to be distinguished from the spectrum of CeO₂.

The transition-metal K-edge XAFS spectra for M_{0.1}Ce_{0.9}O_{2-x} are presented in Figures 2.6C – E and 2.7 – 2.9C, D. Analysis of the edge-shift in the XANES region (Table 2.5) suggests the presence of formally trivalent transition-metal substitution. In addition, EXAFS fitting (Figure 2.6D and F and Figures 2.7 – 2.9C and Table 2.8) indicates that the transition-metal ions incorporate into the lattice of CeO₂ either as isolated ions or as small oxide clusters rather than form extended MO_x phases. Using the binary transition-metal oxides (Fe₂O₃, Co₃O₄ and NiO) as starting models for EXAFS fitting (Table 2.8), we found that oxygen coordination around the transition-metal was significantly smaller (~4) than expected for the binary oxides (6). Additionally, the number of nearest neighbor transition-metal centers was found to be much smaller (<1) than expected for extended crystalline MO_x phases. It should be noted that the model did not fit the low-magnitude data well after apparent distances longer than 3 Å, which suggests a spatial averaging of several different secondary coordination sphere configurations in the CeO₂ host lattice. These data show that our synthetic approach is generalizable; a comparison of the intrinsic properties as a function

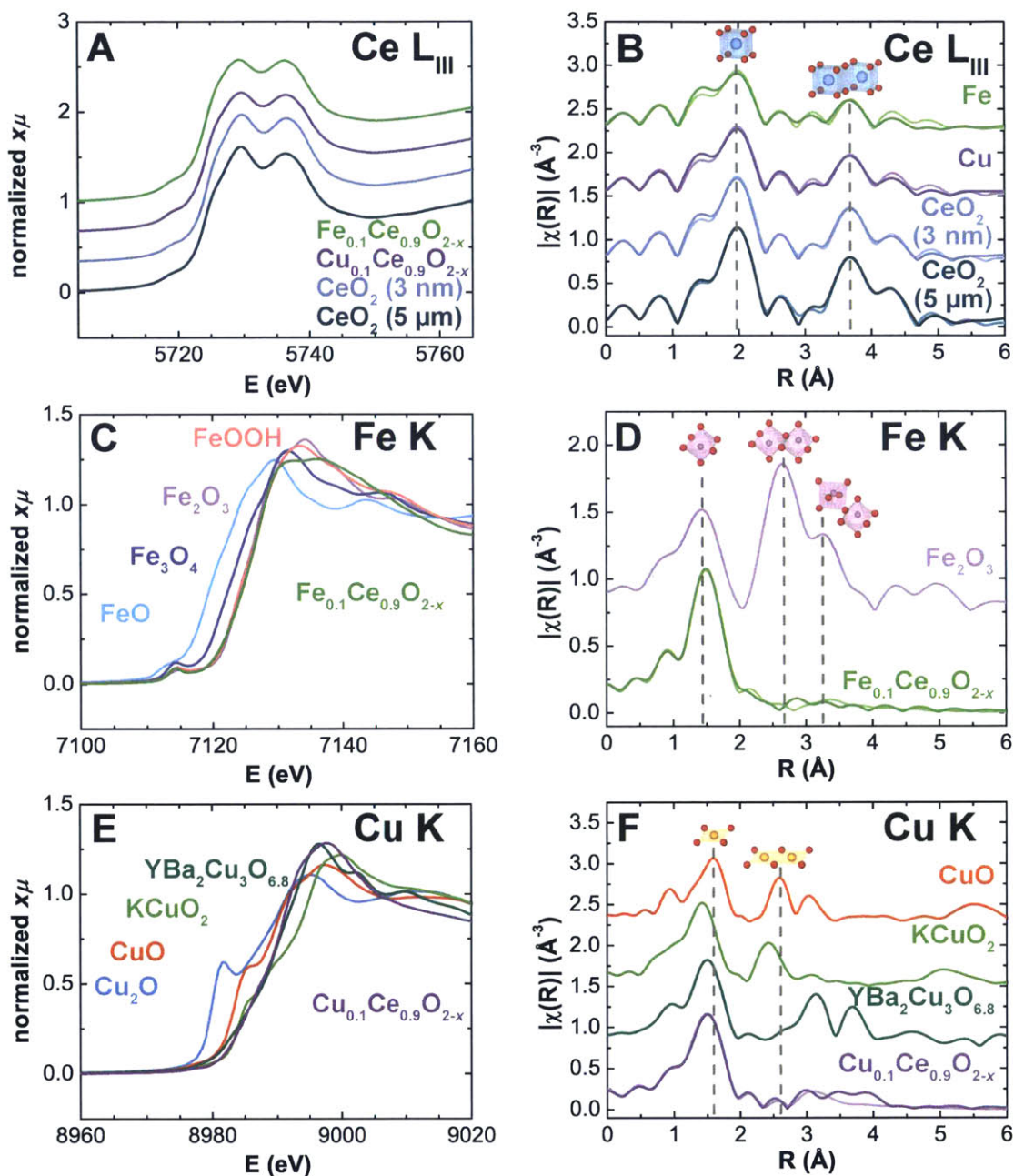


Figure 2.6 Cerium L_{III} -edge and transition-metal K-edge and XAS spectra for annealed CeO_2 , $\text{Cu}_{0.1}\text{Ce}_{0.9}\text{O}_{2-x}$ and $\text{Fe}_{0.1}\text{Ce}_{0.9}\text{O}_{2-x}$ samples; (A) Cerium L_{III} -edge XANES spectra and (B) the magnitude of the k^2 -weighted Fourier transform of the EXAFS of $\text{Cu}_{0.1}\text{Ce}_{0.9}\text{O}_{2-x}$ (purple), $\text{Fe}_{0.1}\text{Ce}_{0.9}\text{O}_{2-x}$ (green) and ceria references; (C) Iron K-edge XANES spectra and (D) the magnitude of the k^2 -weighted Fourier transform of the EXAFS of $\text{Fe}_{0.1}\text{Ce}_{0.9}\text{O}_{2-x}$ (green) and relevant iron oxides; (E) Copper K-edge XANES spectra and (F) the magnitude of the k^2 -weighted Fourier transform of the EXAFS of $\text{Cu}_{0.1}\text{Ce}_{0.9}\text{O}_{2-x}$ (purple) and relevant copper oxides. Ce L_{III} -edge spectra were collected in transmission mode, while Cu and Fe K-edge spectra were collected in total fluorescence yield mode. Lighter traces in (B), (D) and (F) are results of EXAFS fitting (see Tables 2.6 – 2.7).

of transition-metal substitution is meaningful as the $\text{Mn}_{0.1}\text{Ce}_{0.9}\text{O}_{2-x}$ powders are free from any “bulk” transition-metal-oxide impurity phases.

The Cu K-edge XAS spectra of $\text{Cu}_{0.1}\text{Ce}_{0.9}\text{O}_{2-x}$ show some surprising features in Figure 2.6E and F. The edge position for $\text{Cu}_{0.1}\text{Ce}_{0.9}\text{O}_{2-x}$ is a full 3.2 eV higher than that of CuO, which indicates a formal valence higher than 2+ (a mixture of 2+ and 3+, Figure 2.6E). Indeed, the edge energy (taken as the energy at half step-height) corresponds to a formal oxidation state of 2.9+ when fit to a calibration curve of the edge energies of copper oxide references (Table 2.5). The weak pre-edge feature at 8977 eV corroborates the presence of

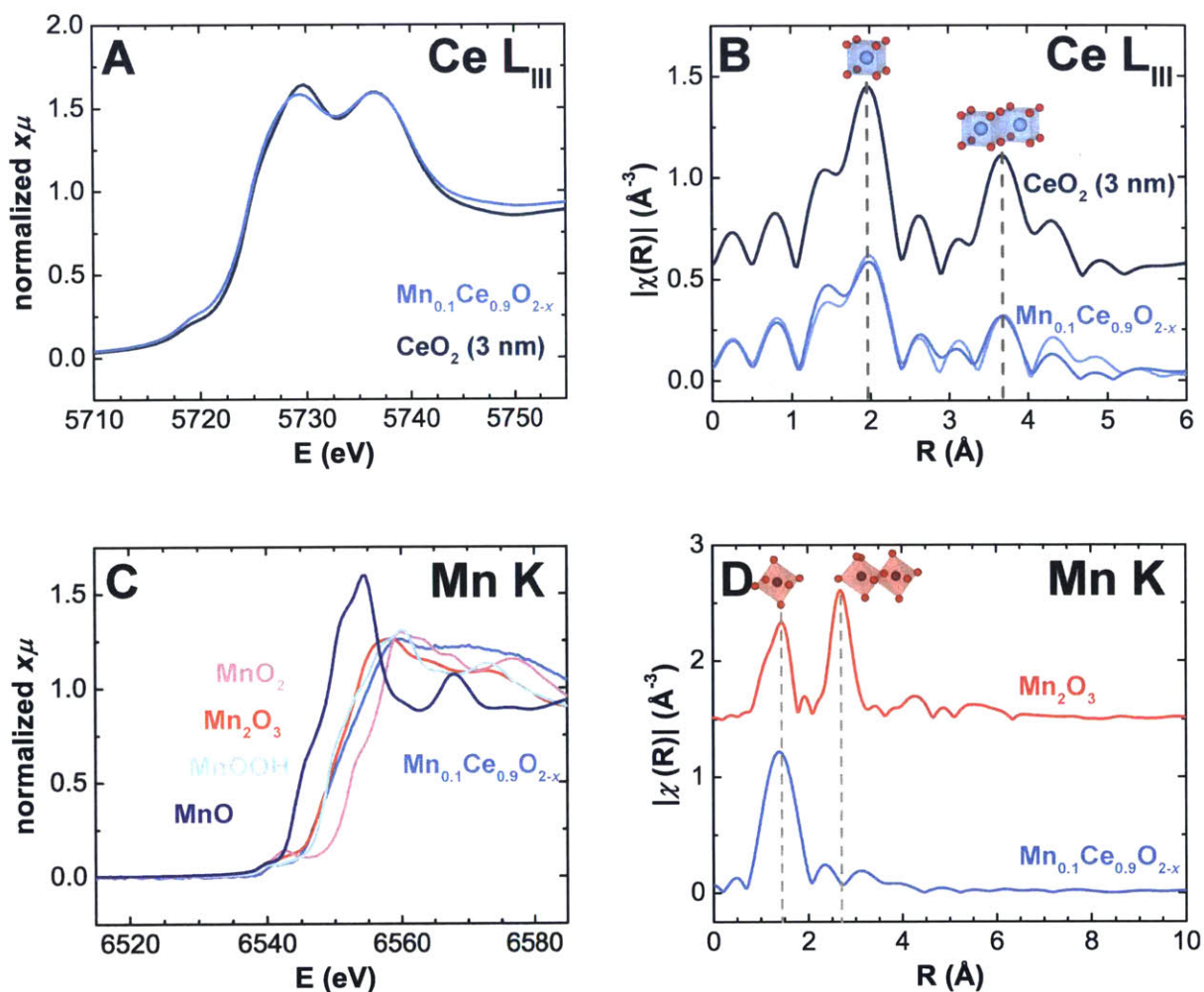


Figure 2.7 XAS spectra for $\text{Mn}_{0.1}\text{Ce}_{0.9}\text{O}_{2-x}$. (A) Ce L_{III}-edge XANES and (B) the k^2 -weighted Fourier transform of the EXAFS spectra for $\text{Mn}_{0.1}\text{Ce}_{0.9}\text{O}_{2-x}$ and nanometer-sized CeO_2 ; (C) Mn K-edge XANES and (D) the k^2 -weighted Fourier transform of the EXAFS spectra for $\text{Mn}_{0.1}\text{Ce}_{0.9}\text{O}_{2-x}$ and relevant binary oxides and oxy-hydroxides of Mn. Lighter trace in (B) is the result of EXAFS fitting.

Cu³⁺; this feature corresponds to the quadrupole-allowed 1s → 3d transition, necessitating an unfilled 3d manifold for Cu.²⁷ It should be noted here that the calculated valence of +2.9 should be taken as an upper bound, as transition-metal K-edge XAS mainly probes the dipole-allowed 1s → 4p transition and hence does not give direct information about the unfilled 3d states of copper. A more suitable method would be transition-metal L-edge XAS (*vide infra*), which probes the 2p → 3d transition.

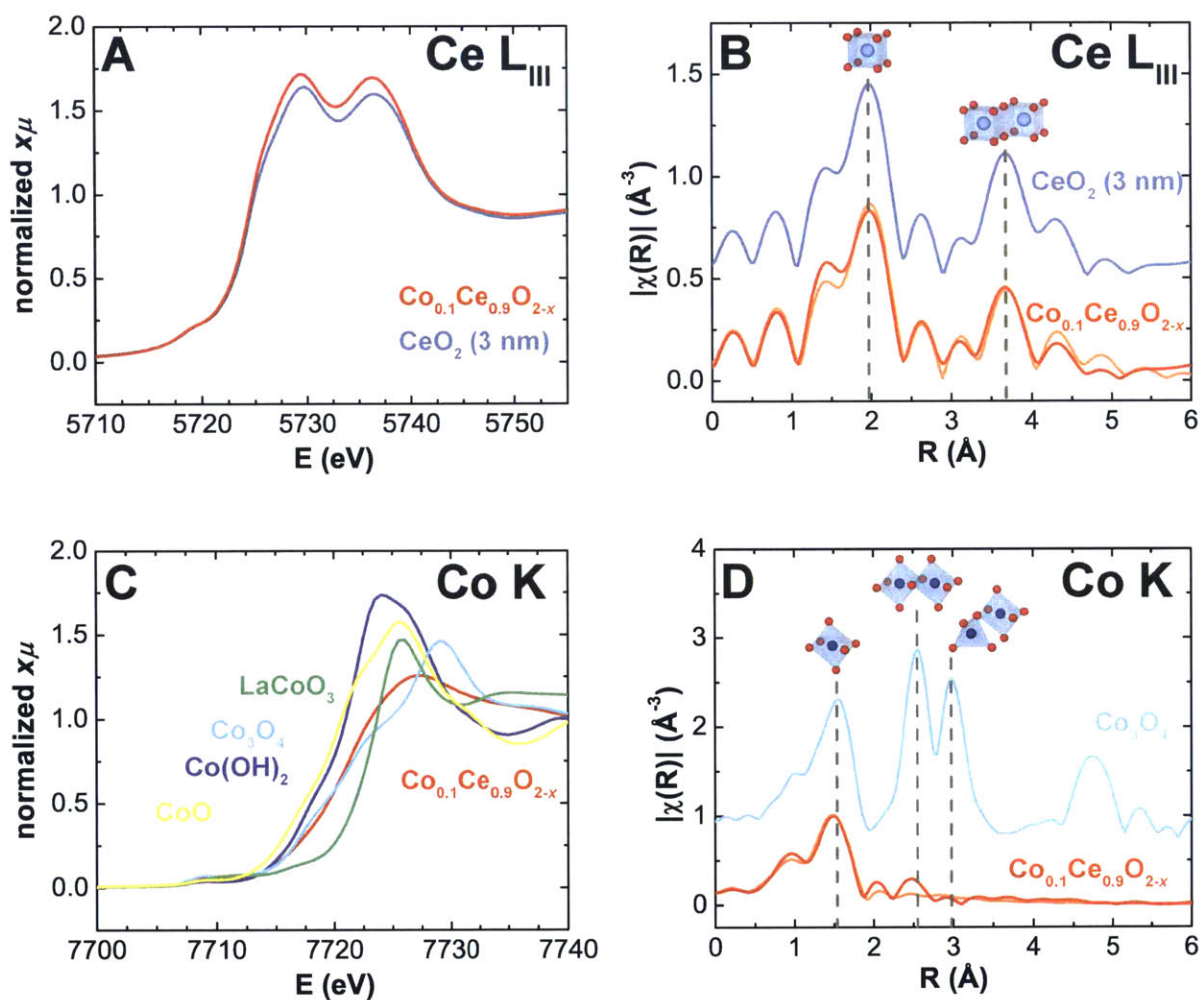


Figure 2.8 XAS spectra for Co_{0.1}Ce_{0.9}O_{2-x}. (A) Ce L_{III}-edge XANES and (B) the k^2 -weighted Fourier transform of the EXAFS spectra for Co_{0.1}Ce_{0.9}O_{2-x} and nanometer-sized CeO₂; (C) Co K-edge XANES and (D) the k^2 -weighted Fourier transform of the EXAFS spectra for Co_{0.1}Ce_{0.9}O_{2-x} and relevant binary oxides and hydroxides of Co. The lighter traces in (B) and (D) are results from EXAFS fitting.

Fitting the EXAFS to a cluster model of CuO (Figure 2.6F and Table 2.8), the dominant Cu-O bond distance was found to be 1.93 Å, which is intermediate to the values for KCuO₂ (1.85 Å fit here and 1.83 Å from neutron diffraction studies²⁸) and CuO (1.95 Å), which suggests a 20% contribution of Cu³⁺ to the EXAFS of Cu_{0.1}Ce_{0.9}O_{2-x}. Additionally, the magnitudes of the next-nearest neighbor Cu-Cu peaks (indicating edge and corner sharing square-planar CuO₄ motifs) are greatly reduced in Cu_{0.1}Ce_{0.9}O_{2-x} (0.6) compared to crystalline CuO (8) as was the case for the other transition-metals. This observation suggests the incorporation of Cu ions into the lattice of CeO₂ and not the formation of a separate, amorphous CuO phase as discussed previously.² Our DFT + *U* calculations show that phase

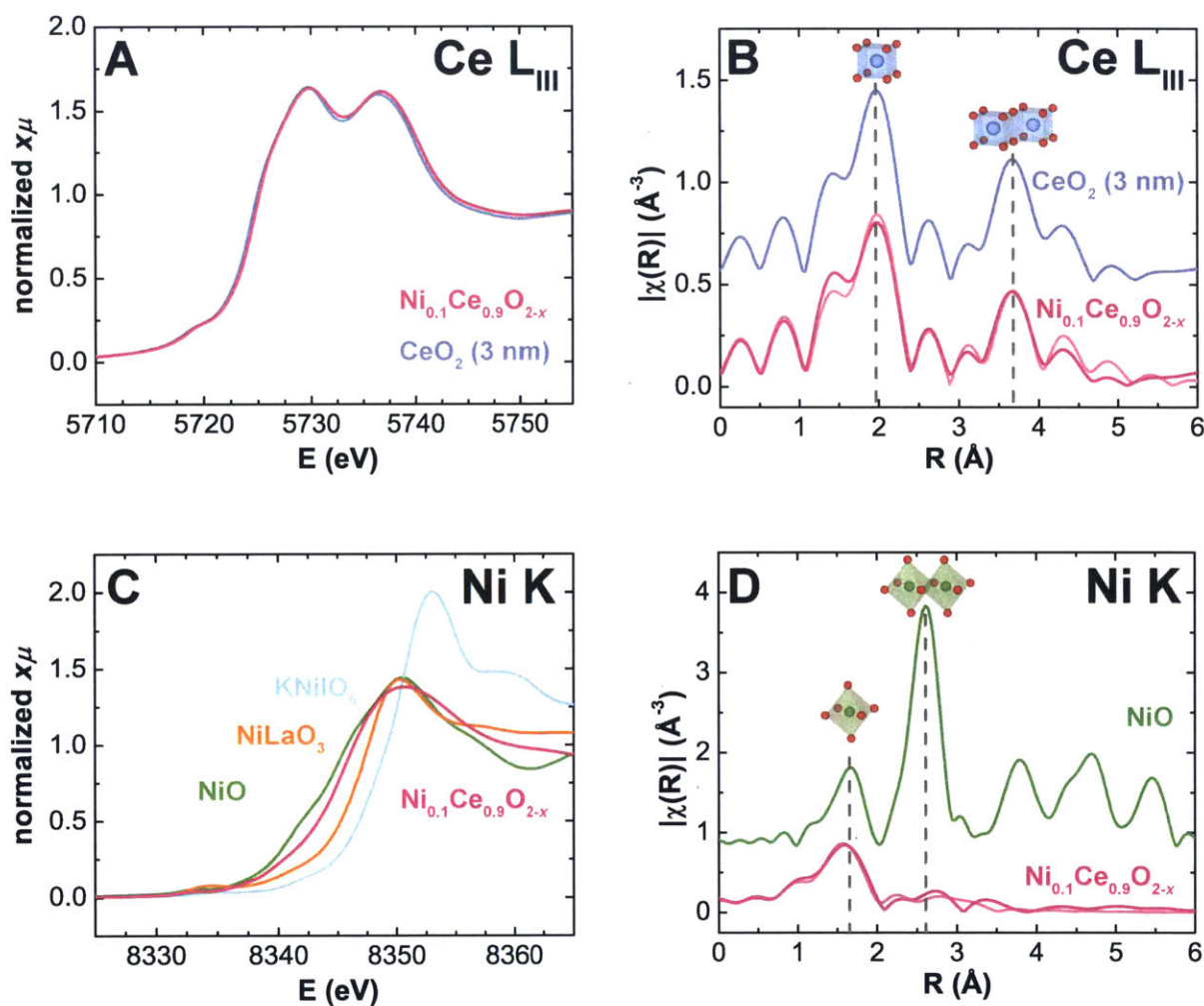


Figure 2.9 XAS spectra for $\text{Ni}_{0.1}\text{Ce}_{0.9}\text{O}_{2-x}$. (A) Ce L_{III}-edge XANES and (B) the k^2 -weighted Fourier transform of the EXAFS spectra for $\text{Ni}_{0.1}\text{Ce}_{0.9}\text{O}_{2-x}$ and nanometer-sized CeO₂; (C) Ni K-edge XANES and (D) the k^2 -weighted Fourier transform of the EXAFS spectra for $\text{Ni}_{0.1}\text{Ce}_{0.9}\text{O}_{2-x}$ and relevant binary oxides of Ni. The lighter traces in (B) and (D) are results from EXAFS fitting.

separation of bulk $\text{Cu}_{0.1}\text{Ce}_{0.9}\text{O}_{2-x}$ into stoichiometric CeO_2 and CuO is exothermic by 2.4 electron volts (Table 2.10), suggesting that our synthetic route affords the formation of a metastable solid-solution phase. These computed energies do not take configurational entropy into account, which necessitates further computational work on the exergonicity of phase separation in these materials.

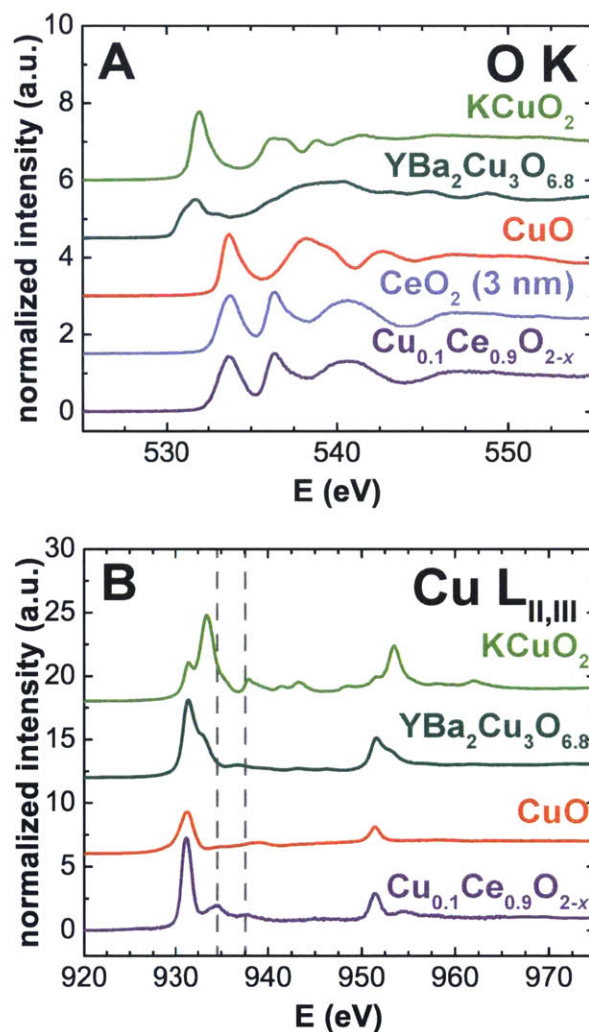


Figure 2.10 Oxygen K-edge and Copper $L_{\text{II,III}}$ -edge XAS spectra, collected in partial fluorescence yield mode, for annealed $\text{Cu}_{0.1}\text{Ce}_{0.9}\text{O}_{2-x}$; (A) Oxygen K-edge XAS spectra and (B) Copper $L_{\text{II,III}}$ -edge XAS spectra of $\text{Cu}_{0.1}\text{Ce}_{0.9}\text{O}_{2-x}$ (purple) and reference oxides. Dashed grey lines represent charge-transfer multiplet satellites for Cu^{3+} .

The presence of Cu^{3+} in $\text{Cu}_{0.1}\text{Ce}_{0.9}\text{O}_{2-x}$ is further supported by soft X-ray absorption at the Cu L-edge. Cu $L_{\text{II,III}}$ -edge XAS data (probing the $2p \rightarrow 3d$ transition) can provide information on the density of states of the copper 3d band. The Cu $L_{\text{II,III}}$ -edge XAS spectra for $\text{Cu}_{0.1}\text{Ce}_{0.9}\text{O}_{2-x}$ and reference compounds (CeO_2 , CuO , YBCO and KCuO_2), collected in

the partial fluorescence yield (PFY) mode, are given in Figure 2.10B. The prominent local maximum at 931 eV for $\text{Cu}_{0.1}\text{Ce}_{0.9}\text{O}_{2-x}$ has been assigned to the $2p^63d^9 \rightarrow 2p^53d^{10}$ transition,²⁹⁻³¹ indicative of divalent copper centers as can be found in CuO, YBCO and (as a minor impurity) in KCuO_2 . The satellite structures found at 934.5 and 937.5 eV in the XAS spectrum of $\text{Cu}_{0.1}\text{Ce}_{0.9}\text{O}_{2-x}$, indicates the presence of Cu^{3+} , as these features are similar to those of the trivalent compound $\text{KCu}(\text{biuret})_2$ ³² and other formally trivalent copper compounds.^{30,31} These features are significantly lower in energy to be attributed to transitions to the final state $2p^53d^94s^1$ of CuO (~ 938.7 eV)²⁵ and are too high in energy to be attributed to Cu^+ impurities (933.7 eV for Cu_2O).²⁹

Although further studies are required, including a rigorous treatment of charge-transfer multiplet theory, suffice to say that copper sites in $\text{Cu}_{0.1}\text{Ce}_{0.9}\text{O}_{2-x}$ exist as an admixture of Cu^{2+} and Cu^{3+} . Thus, we have demonstrated the preparation of a rare example of an air-stable Cu^{3+} -containing oxide. Typically, the ternary and quaternary Cu^{3+} oxides, such as KCuO_2 and YBCO, are unstable in air.³³ For example, NaCuO_2 and KCuO_2 readily decompose in the presence of moisture to CuO with concurrent evolution of O_2 . The CeO_2 lattice seems to play an important role in stabilizing copper in the trivalent state. Previous DFT studies have also highlighted the role of electropositive elements (in our case, Ce^{4+}) in stabilizing Cu^{3+} in oxides.³⁴ This hypothesis is further supported by density functional theory (DFT).

Our DFT + U calculations show that, under our annealing conditions, Cu exists as a mixture of Cu^{3+} and Cu^{2+} (Figure 2.11 A), consistent with our XAS results. At 700 K under 21% O_2 , the Gibbs energy of formation (ΔG_F , see Section 2.6, Experimental Methods) for the $\text{Cu}^{3+}_2\text{Ce}_{34}\text{O}_{71}$ and $\text{Cu}^{2+}_2\text{Ce}_{34}\text{O}_{70}$ slab models are nearly identical, suggesting not only that copper exists as a mixture of Cu^{3+} and Cu^{2+} , but also that the $\text{Cu}^{3+/2+}$ couple is accessible in these materials, which may have important implications for catalysis. Understanding the physical origin for the stabilization of Cu^{3+} warrants further study, but presumably it results from a thermodynamic compromise between the copper species favoring oxidation states lower than the isovalent case (Cu^{4+}) and the disruption of the CeO_2 lattice by removal of charge-compensating oxygen atoms for aliovalent (Cu^{3+}) substitution. The optimized geometry of the $\text{Cu}^{3+}_2\text{Ce}_{34}\text{O}_{71}$ model (Figure 2.11C) is also consistent with our EXAFS results. We found that copper is substituted into the CeO_2 lattice as square planar CuO_4 moieties that lie flat along the (100) lattice plane and relax along [100] toward the (100)

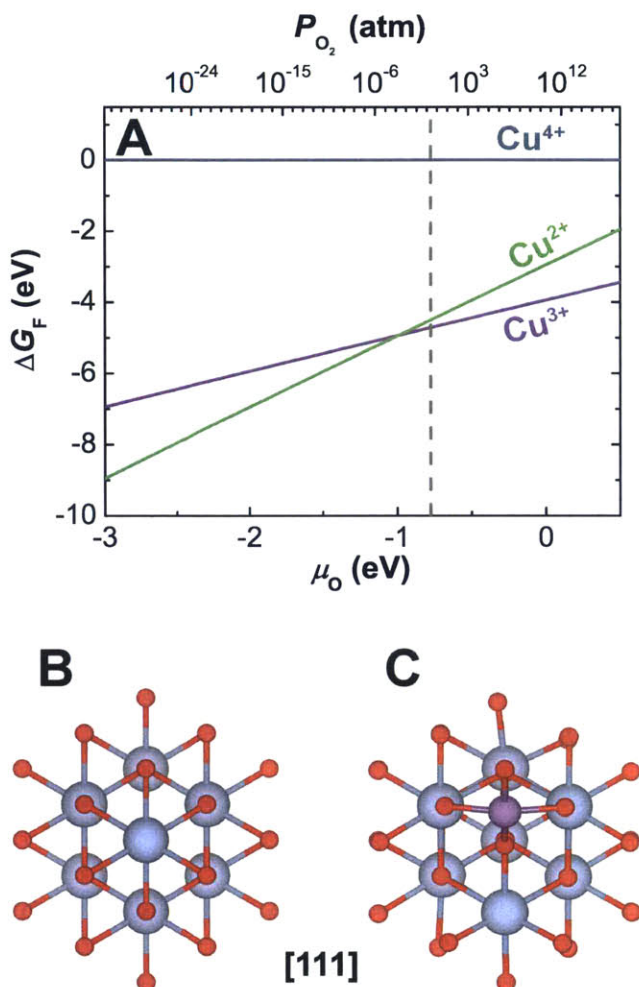


Figure 2.11 Phase diagram and local molecular structure computed for Cu^{(4-x)+}₂Ce₃₄O_{72-x} models; (A) computed ΔG_F as a function of oxygen chemical potential for three oxidation states of copper in Cu^{(4-x)+}₂Ce₃₄O_{72-x}; the local coordination of (B) Ce⁴⁺ in CeO₂ and of (C) Cu³⁺ in Cu³⁺₂Ce₃₄O₇₁ as viewed down the [111] zone axis. The pressure dependence was calculated at 700 K, with 0.21 atm O₂ indicated by the dashed grey lines and the model Cu⁴⁺₂Ce₃₄O₇₂ was taken as the reference for computing ΔG_F .

plane of oxygen atoms to compensate for a shorter Cu-O bond compared to that of CeO₂ (Figure 2.11B and C).

An important parameter to determine for oxide materials, especially in the realm of heterogeneous catalysis, is the oxygen non-stoichiometry (x in M_{0.1}Ce_{0.9}O_{2-x}), which is related to the oxygen-ion vacancy content of these materials. The oxygen-ion vacancy contents for the M_{0.1}Ce_{0.9}O_{2-x} compounds were determined by TGA analysis and X-ray photoelectron spectroscopy (XPS) at the Ce 3d region. The results of these measurements (Table 2.9) suggest that the content of oxygen-ion vacancies in nanoparticulate ceria is

relatively unchanged with transition-metal substitution, with XPS predicting an upper bound of as much as 10%. Any disparities in catalytic behavior are due to the electronic structure of the transition-metal substitute and not to differences in oxygen-ion vacancy content in these $M_{0.1}Ce_{0.9}O_{2-x}$ compounds.

2.4 CO oxidation catalysis on CeO_2 and $Cu_{0.1}Ce_{0.9}O_{2-x}$

CO oxidation catalysis was performed on annealed 3 nm $Cu_{0.1}Ce_{0.9}O_{2-x}$ and 3 nm CeO_2 nanoparticles as well as on micron-sized CeO_2 to examine if Cu in solid solution with CeO_2 can promote CO oxidation. The experimental “light-off” curves and Arrhenius plots for CO oxidation in oxygen-rich conditions (1% CO, 2.5% O_2) are presented in Figure 2.12A and B, respectively. Introduction of aliovalent Cu ions into the lattice of CeO_2 lowers the onset temperature for CO oxidation (Figure 2.12A) and increases the catalytic activity by an order of magnitude compared to CeO_2 nanoparticles and three orders of magnitude relative to micron-sized CeO_2 (Figure 2.12B). Notably, $Cu_{0.1}Ce_{0.9}O_{2-x}$ did not exhibit any irreversible sintering or phase changes during catalysis, even after exposure to 2.5% CO at 300 °C, which suggests that this catalyst could meet the rigorous demand of real-world applications of CO oxidation in catalytic converters or respirators (Table 2.3).

The promotion of CO oxidation kinetics with Cu in solid solution with CeO_2 comes as a surprise in light of recent studies which have proposed that the solid solution in CuO/CeO_2 catalysts is inactive for CO oxidation catalysis, with activities identical to bare, micron-sized CeO_2 .^{9,10} Our work calls in to question the origin of the high catalytic activity in mixed phase CuO/CeO_2 catalysts (and mixed-phase ceria-based catalysts in general), which have traditionally been attributed to the interface of crystalline CuO particles with CeO_2 ,^{1,5,9,10,35,36} and therefore offers a new paradigm for the design of CeO_2 -based catalysts.

While the mass-normalized rate of CO oxidation found here for $Cu_{0.1}Ce_{0.9}O_{2-x}$ ($0.1 \mu\text{mol CO s}^{-1} \text{g}_{cat}^{-1}$ at 35 °C) is significantly smaller than those found under similar conditions for state-of-the-art gold-based catalysts (2.5 and $2.9 \mu\text{mol CO s}^{-1} \text{g}_{cat}^{-1}$ for Au/TiO_2 ³⁷ and Au/CeO_2 ,³⁸ respectively), they are comparable to optimized CuO/CeO_2 catalysts ($0.12 \mu\text{mol CO s}^{-1} \text{g}_{cat}^{-1}$ at 45 °C).³⁶ Additionally, the as-synthesized $Cu_{0.1}Ce_{0.9}O_{2-x}$ nanoparticles are extractable in non-polar organic solvents and hence are particularly suitable for post-synthetic modifications, such as exotemplating,³⁹ that would increase the surface area of these materials (and hence their mass-normalized activities) for applications in CO oxidation.

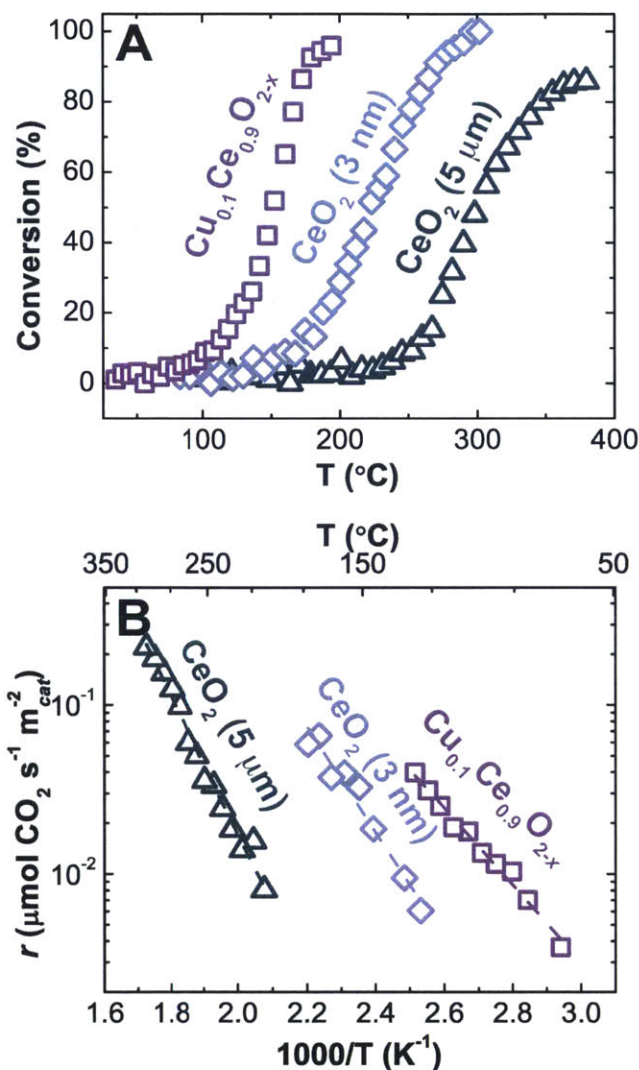


Figure 2.12 CO oxidation catalysis on annealed 3 nm Cu_{0.1}Ce_{0.9}O_{2-x}, 3 nm CeO₂ and commercial 5 μm CeO₂ (Sigma-Aldrich); (A) “Light off” curves and (B) Area-normalized Arrhenius plots, measured in 1% CO, 2.5% O₂ balanced in He at a flow rate of 1300 mL min⁻¹ g⁻¹_{cat} for 20 mg catalyst loadings.

The enhanced activity of CeO₂ nanoparticles relative to micron-sized CeO₂ is in agreement with previous work.³⁸ The origin of such structure sensitivity has been investigated previously, where it was found that CeO₂ catalysts with exposed {001} and {110} facets give significantly higher rates for CO oxidation than catalysts with predominantly {111} termination.⁴⁰ In the present case, the activity enhancement is likely due to a higher concentration of reactive {001} facets in the nanostructured CeO₂ (e.g. Figure 2.5) compared to micron-sized CeO₂, where the low-energy {111} facets are more predominant.⁴¹ This strategy has been exploited, for example, for CO oxidation on gold

catalysts where researchers found a two-order of magnitude increase in activity when employing nanostructured CeO₂ over micron-sized CeO₂.³⁸

The synthetic strategy adopted here thus decouples geometric effects (dispersion, crystallite size) from intrinsic, electronic effects in catalysis, thereby paving a way to develop design descriptors based on the electronic structure of these materials for heterogeneous catalysis. Apparent rates for CO oxidation are functions of the size and shape of the catalyst particles, the dispersion of the active sites on the surface and the intrinsic activity of each active site. The bottom-up synthetic approach outlined here enables the study of the *intrinsic* activity of these solid solutions as a function of their electronic structure and transition-metal substitution. The correlation of catalytic activity with the electronic structure of these catalysts will be explored in Chapter 5 to search for activity descriptors and potentially establish design guidelines for the development of next-generation CO oxidation catalysts.

2.5 Conclusions

In summary, we have presented a simple and generalizable route for the preparation of monodisperse nanoparticles of transition-metal substituted ceria (M_{0.1}Ce_{0.9}O_{2-x}, M = Mn, Fe, Co, Ni and Cu). Unlike preparations of similar catalysts by conventional methods, the monodispersity in size and shape, as well as the purity of the resulting single-crystalline M_{0.1}Ce_{0.9}O_{2-x}, is well controlled by the solution-based pyrolysis of heterobimetallic Schiff base complexes. To the best of our knowledge, such synthetic control has not previously been demonstrated for such a broad range of transition-metal substitutes and has implications not only for the design of novel catalysts but also for the accurate interpretation of catalytic trends and active sites in heterogeneous catalysis. As synthesized, single-crystalline M_{0.1}Ce_{0.9}O_{2-x} materials are soluble in non-polar organic solvents and, as such, can be further processed into hierarchical assemblies,⁴² thin films and devices. The bulk and local atomic structure were verified by PXRD, HRTEM and XAS, which suggest that the aliovalent transition-metal ions substitute completely into the CeO₂ lattice with truncated octahedral crystalline habits and exposed {100} and {111} facets.

Steady-state CO oxidation catalysis on Cu_{0.1}Ce_{0.9}O_{2-x} reveals that the aliovalent copper ions incorporated into the CeO₂ lattice are responsible for an increase in catalytic activity by an order of magnitude compared to nanocrystalline CeO₂. We also found that nanocrystalline CeO₂ is two orders of magnitude more active than bulk CeO₂. These results justify the

bottom-up synthetic approach we employ here, where geometrical effects in catalysis are decoupled from purely electronic effects, by comparing surface-area-normalized catalytic rates of substituted CeO₂ of nearly identical size and crystalline habit. These results suggest a new paradigm for the design of CeO₂-based catalysts while simultaneously allowing for systematic correlations between the electronic structure of M_{0.1}Ce_{0.9}O_{2-x} and catalytic activity. Notably and in opposition to previous reports suggesting Cu⁺ or Cu²⁺ to be the active sites for catalysis,^{1,2,6,7,43} XAS studies on the Cu_{0.1}Ce_{0.9}O_{2-x} catalyst reveal that copper exists as an admixture of Cu²⁺ and Cu³⁺ species. These results report, to the best of our knowledge, the first instance that Cu³⁺ has been implicated in the mechanism for CO oxidation on CuO/CeO₂ catalysts and, as such, demonstrate that considerable care must be exercised when making claims about the active site for mixed-phase heterogeneous catalysts. The origin of this stabilization of Cu³⁺ and its connection to the high catalytic activity of Cu_{0.1}Ce_{0.9}O_{2-x} will be addressed in Chapters 3 and 4, where we hypothesize that the higher activity is due to the accessible Cu³⁺/Cu²⁺ redox couple in Cu_{0.1}Ce_{0.9}O_{2-x}.

2.6 Experimental Methods

General experimental considerations. All reagents we obtained from commercial vendors and were used without further purification. All reactions were performed under ambient conditions unless otherwise noted. ¹H spectra were acquired on a Bruker 400-AVANCE spectrometer and are referenced to residual CHCl₃ (7.26 ppm) or SO(CD₃)(CD₂H) (2.50 ppm) solvent signals. ¹H NMR chemical shifts are reported as ppm with respect to trimethylsilane (TMS). IR spectra were collected on a Bruker Vertex 70 FT-IR spectrophotometer equipped with a Pike VeeMax II ATR accessory using a 45° ZnSe ATR crystal. CHN elemental microanalyses were performed at Midwest Microlab, LLC after drying at 70 °C *in vacuo* overnight. Percent substitution of transition-metal ions into CeO₂ was determined using inductively coupled plasma atomic emission spectroscopy (ICP-AES) with a Horiba ACTIVA spectrometer. Standard solutions for ICP-AES were prepared from Specpure® stock solutions available from Alfa-Aesar. Thermogravimetric analysis (TGA) was performed in air with a TA Instruments Discovery thermogravimetric analyzer using 100 μL high-temperature platinum pans from ambient temperature to 1000 °C. The copper oxide references KCuO₂ and YBa₂Cu₃O_{6.8} were prepared from solid-state reactions as described previously in the literature and were deemed pure by powder X-ray diffraction.^{28,44}

Synthesis of N,N'-bis(3-methoxysalicylidene)-propylene-1,3-diamine (H₂-3-MeO-salpn). The ligand **H₂-3-MeO-salpn** was prepared from the condensation of 1,3-diaminopropane with two equivalents of 2-hydroxy-3-methoxybenzaldehyde. To a stirred 500 mL straw-colored methanol solution of 2-hydroxy-3-methoxybenzaldehyde (30.430 g, 200.00 mmol) was added neat 1,3-diaminopropane (7.798 g, 105.2 mmol) in several portions. The bright orange solution was stirred at reflux (90 °C) for 19 hrs. The volume was reduced to ca. 50 mL by removing excess methanol *in-vacuo* before letting the orange solution crystallize, unstoppered, at rt. Large, yellow-orange block crystals of the ligand **H₂-3-MeO-salpn** were isolated after 3 days by filtration over a low-porosity fritted disk filter followed by washing in methanol (3 x 50 mL) and drying *in vacuo*; 33.227 g (97.05 mmol, 97.1 %). ¹H NMR (400 MHz, CDCl₃, δ, ppm) 13.93 (s, 2H, OH), 8.37 (s, 2H, N=CH), 6.83 (m, 6H, ArH₃), 3.91 (s, 6H, OCH₃), 3.74 (dt, J(H,H) = 6.5 Hz, 4H, N-CH₂), 2.11 (p, J(H,H) = 6.5 Hz, 4H, CH₂-CH₂-CH₂). IR (ATR, cm⁻¹) 1624, 1464, 1242.

Synthesis of Cu^{II}-Ce^{III}-3-MeO-salpn. The complex **Cu^{II}-Ce^{III}-3-MeO-salpn** was prepared in two steps from the ligand **H₂-3-MeO-salpn**. First, to a stirred yellow solution of **H₂-3-MeO-salpn** (8.56 g, 25.0 mmol) in 500 mL EtOH at 60 °C was added, dropwise, a dark cyan solution of copper(II) acetate hexahydrate (4.99 g, 25.0 mmol) in 125 mL EtOH. The dark green solution was stirred at 60 °C for 2 hrs before removing EtOH *in vacuo*. The crude product was filtered over a fine frit and washed with cold EtOH (3 x 100 mL) and dried *in vacuo* to give Cu^{II}-3-MeO-salpn as an olive-green powder; 7.37 g (18.2 mmol, 72.8 %).

A portion of Cu^{II}-3-MeO-salpn (0.8078 g, 2.000 mmol) was subsequently dissolved in 80 mL MeCN and to this was added, dropwise, a 12 mL MeCN solution of cerium(III) nitrate hexahydrate (0.8682 g, 2.000 mmol). The dark green solution was stirred at room temperature for 5 mins and was allowed to crystallize at room temperature. Dark-green needles of **Cu^{II}-Ce^{III}-3-MeO-salpn** suitable for X-ray crystallography formed after two weeks; 1.1568 g (1.5846 mmol, 79.23%). ¹H NMR (400 MHz, DMSO-d₆, δ, ppm) 8.70 (bs, N=CH), 6.59 (s, ArH₃), 4.77 (bs, N-CH₂), 4.22 (bs, OCH₃), 2.07 (s, CH₂-CH₂-CH₂). IR (ATR, cm⁻¹) 1622, 1439, 1285, 1225. Anal. calcd. for C₁₉H₂₀CeCuN₅O₁₃: C, 31.26; H, 2.76; N, 9.59. Found: C, 31.12; H, 2.82; N, 9.56.

Synthesis of Mn^{II}-Ce^{III}-3-MeO-salpn. The complex **Mn^{II}-Ce^{III}-3-MeO-salpn** was prepared from **H₂-3-MeO-salpn**, manganese(II) acetate tetrahydrate and cerium(III) nitrate

hexahydrate in a two-step procedure identical to the preparation of **Cu^{II}-Ce^{III}-3-MeO-salpn**. The product was isolated as fine dark green needles in 61.7% overall yield. ¹H NMR (400 MHz, DMSO-d₆, δ, ppm) 7.04 (bs, ArH₃), 4.70 (bs, OCH₃, N-CH₂). IR (ATR, cm⁻¹) 3389, 1609, 1452, 1294, 1254. Anal. calcd. for C₁₉H₂₀CeMnN₅O₁₃: C, 31.63; H, 2.79; N, 9.71. Found: C, 29.96; H, 3.56; N, 8.32.

Synthesis of Co^{III}-Ce^{III}-3-MeO-salpn. The complex **Co^{III}-Ce^{III}-3-MeO-salpn** was prepared from **H₂-3-MeO-salpn**, cobalt(II) acetate tetrahydrate and cerium(III) nitrate hexahydrate in a two-step procedure identical to the preparation of **Cu^{II}-Ce^{III}-3-MeO-salpn**. The product was isolated as bronze blocks in 46.3% overall yield. ¹H NMR (400 MHz, DMSO-d₆, δ, ppm) 7.77 (s, N=CH), 7.59 (s, N=CH), 7.02 (m, ArH₂), 6.65 (m, ArH), 4.68 (s, N-CH₂), 3.85 (s, OCH₃), 2.07 (CH₂-CH₂-CH₂). IR (ATR, cm⁻¹) 1641, 1460, 1288, 1439, 1321, 1246. Anal. calcd. for C₂₃H₂₆CeCoN₄O₁₄: C, 35.35; H, 3.35; N, 7.17. Found: C, 33.37; H, 3.35; N, 9.44.

Synthesis of Fe^{III}-Ce^{III}-3-MeO-salpn. The complex **Fe^{III}-Ce^{III}-3-MeO-salpn** was prepared from **H₂-3-MeO-salpn**, iron(II) acetate and cerium(III) nitrate hexahydrate in a two-step procedure identical to the preparation of **Cu^{II}-Ce^{III}-3-MeO-salpn**. The product was isolated as a dark red powder in 71.1% overall yield. ¹H NMR (400 MHz, DMSO-d₆, δ, ppm) 13.49 (bs, N=CH), 9.79 (m, ArH₃), 4.19 (bs, OCH₃, N-CH₂), 2.07 (s, CH₃CO₂), 1.33 (CH₂-CH₂-CH₂). IR (ATR, cm⁻¹) 1641, 1460, 1288, 1439, 1321, 1246. Anal. calcd. for C₂₁H₂₃CeFeN₅O₁₅: C, 32.28; H, 2.97; N, 8.96. Found: C, 34.68; H, 3.27; N, 9.37.

Synthesis of Ni^{II}-Ce^{III}-3-MeO-salpn. The complex **Ni^{II}-Ce^{III}-3-MeO-salpn** was prepared from **H₂-3-MeO-salpn**, nickel(II) acetate tetrahydrate and cerium(III) nitrate hexahydrate in a two-step procedure identical to the preparation of **Cu^{II}-Ce^{III}-3-MeO-salpn**. The product was isolated as a purple needles in 51.6% overall yield. ¹H NMR (400 MHz, DMSO-d₆, δ, ppm) 9.52 (bs, N=CH), 7.12 (bs, ArH₁), 6.24 (bs, ArH₁), 4.86 (s, OCH₃), 4.18 (N-CH₂), 2.07 (s, CH₂-CH₂-CH₂, NCCH₃). IR (ATR, cm⁻¹) 1634, 1466, 1296, 1219. Anal. calcd. for C₂₃H₂₆CeNiN₇O₁₃: C, 34.22; H, 3.25; N, 12.15. Found: C, 33.39; H, 3.26; N, 11.47.

Synthesis of Ce^{III}-3-MeO-salpn. The complex **Ce^{III}-3-MeO-salpn** was prepared from the ligand **H₂-3-MeO-salpn**. To a stirred yellow solution of **H₂-3-MeO-salpn** (4.17 g, 12.2 mmol) in 200 mL EtOH at 60 °C was added, dropwise, a colorless solution of cerium(III) nitrate hexahydrate (5.29 g, 12.2 mmol) in 20 mL EtOH, giving an immediate yellow

precipitate. The yellow suspension was stirred at reflux for 4 hours before cooling to room temperature. The crude product was filtered over a medium-porosity frit, washed with cold EtOH (3 x 100 mL) and dried *in vacuo* to give **Ce^{III}-3-MeO-salpn** as a pale yellow powder; 7.67 g (11.5 mmol, 94.3 %). ¹H NMR (400 MHz, DMSO-d₆, δ, ppm) 13.73 (s, 2H, OH), 8.58 (s, 2H, N=CH), 7.01 (m, 4H, ArH₂), 6.79 (m, 2H, ArH), 3.75 (s, 6H, OCH₃), 3.69 (t, *J*(H,H) = 6.8 Hz, 4H, N-CH₂), 2.03 (p, *J*(H,H) = 6.8 Hz, 2H, CH₂-CH₂-CH₂). IR (ATR, cm⁻¹) 2984, 1655, 1485, 1312, 1223. Anal. calcd. for C₁₉H₂₂CeN₅O₁₃: C, 34.14; H, 3.32; N, 10.48. Found: C, 34.32; H, 3.38; N, 10.34.

General Procedure for the synthesis of M_{0.1}Ce_{0.9}O_{2-x} nanoparticles. The M_{0.1}Ce_{0.9}O_{2-x} nanoparticles were prepared by heating with magnetic stirring the parent heterobimetallic **M-Ce^{III}-3-MeO-salpn** complex and an appropriate amount of **Ce^{III}-3-MeO-salpn** in 40 mL oleylamine at 180 °C under an Ar flow for 4 hours in a three-neck flask equipped with a reflux condenser and a bump trap connected to a bubbler. The resulting dark-brown solutions were divided into eight 5 mL fractions and flocculated with ethanol (40 mL each). The dark brown flocculant was isolated by centrifugation (7100 rpm for 15 mins) and redispersed in hexanes (eight 5 mL fractions). Bulk precipitates were removed by centrifugation (5000 rpm for 1 min) and subsequent decanting of these hexanes solutions. This process was repeated a total of two times to give dark-brown hexanes solutions of M_{0.1}Ce_{0.9}O_{2-x}.

As-synthesized hexanes solutions of M_{0.1}Ce_{0.9}O_{2-x} nanoparticles were drop-cast into ceramic crucibles and annealed at 400 °C in synthetic air for 4 hrs to give the bare M_{0.1}Ce_{0.9}O_{2-x} nanoparticles. This procedure generally yields 20 – 200 mg annealed nanoparticles.

Synthesis of Mn_{0.1}Ce_{0.9}O_{2-x} nanoparticles. Mn_{0.1}Ce_{0.9}O_{2-x} nanoparticles were prepared from the pyrolysis of **Mn^{II}-Ce^{III}-3-MeO-salpn** (0.361 g, 0.500 mmol) and **Ce^{III}-3-MeO-salpn** (0.501g, 0.750 mmol) in 40 mL oleylamine (*vide supra*) to give Mn_{0.1}Ce_{0.9}O_{2-x} as a dark red powder after annealing (0.077 g, 0.47 mmol, 38%).

Synthesis of Fe_{0.1}Ce_{0.9}O_{2-x} nanoparticles. Fe_{0.1}Ce_{0.9}O_{2-x} nanoparticles were prepared from the pyrolysis of **Fe^{III}-Ce^{III}-3-MeO-salpn** (0.469 g, 0.600 mmol) and **Ce^{III}-3-MeO-salpn** (0.404 g, 0.604 mmol) in 40 mL oleylamine (*vide supra*) to give Fe_{0.1}Ce_{0.9}O_{2-x} as a brick-red powder after annealing (0.125 g, 0.76 mmol, 63%).

Synthesis of Co_{0.1}Ce_{0.9}O_{2-x} nanoparticles. Co_{0.1}Ce_{0.9}O_{2-x} nanoparticles were prepared from the pyrolysis of Co^{III}-Ce^{III}-3-MeO-salpn (0.469 g, 0.600 mmol) and Ce^{III}-3-MeO-salpn (0.301 g, 0.450 mmol) in 40 mL oleylamine (*vide supra*) to give Co_{0.1}Ce_{0.9}O_{2-x} as a black powder after annealing (0.053 g, 0.32 mmol, 31%).

Synthesis of Ni_{0.1}Ce_{0.9}O_{2-x} nanoparticles. Ni_{0.1}Ce_{0.9}O_{2-x} nanoparticles were prepared from the pyrolysis of Ni^{II}-Ce^{III}-3-MeO-salpn (0.643 g, 0.797 mmol) and Ce^{III}-3-MeO-salpn (0.135 g, 0.253 mmol) in 40 mL oleylamine (*vide supra*) to give Ni_{0.1}Ce_{0.9}O_{2-x} as a red-brown powder after annealing (0.049 g, 0.30 mmol, 29%).

Synthesis of Cu_{0.1}Ce_{0.9}O_{2-x} nanoparticles. Cu_{0.1}Ce_{0.9}O_{2-x} nanoparticles were prepared from the pyrolysis of Cu^{II}-Ce^{III}-3-MeO-salpn (0.559 g, 0.766 mmol) and Ce^{III}-3-MeO-salpn (0.135 g, 0.269 mmol) in 40 mL oleylamine (*vide supra*) to give Cu_{0.1}Ce_{0.9}O_{2-x} as a khaki powder after annealing (0.144 g, 0.876 mmol, 85%).

Synthesis of 3 nm CeO₂ nanoparticles. 3 nm CeO₂ nanoparticles were prepared from the pyrolysis Ce^{III}-3-MeO-salpn (0.189 g, 0.377 mmol) in 10 mL oleylamine (*vide supra*) to give nanoparticulate CeO₂ as a pale yellow powder after annealing (0.024 g, 0.14 mmol, 37%).

X-ray diffraction (XRD, data acquisition performed by Dr. Peter Müller at MIT). X-ray diffraction data were collected on diffraction-quality single crystals with a Bruker-AXS X8 Kappa Duo diffractometer coupled to a Smart APEX II CCD area detector with Mo-K_α radiation ($\lambda = 0.71073 \text{ \AA}$) from a *I μ S* micro-source. Absorption was corrected using SADABS.⁴⁵ Structures were solved by direct methods using SHELXS and refined against F^2 by full-matrix least squares in SHELXL-97.⁴⁶ All non-hydrogen atoms were refined anisotropically. Hydrogen atoms were included in the model at geometrically calculated positions using a riding model.

Table 2.1 Crystallographic and refinement parameters for Co^{III}-Ce^{III}-3-MeO-salpn, Ni^{II}-Ce^{III}-3-MeO-salpn and Cu^{II}-Ce^{III}-3-MeO-salpn.

	Co ^{III} -Ce ^{III} -3-MeO-salpn	Ni ^{II} -Ce ^{III} -3-MeO-salpn	Cu ^{II} -Ce ^{III} -3-MeO-salpn
Empirical formula	C ₂₃ H ₂₄ Ce Co N ₄ O ₁₄	C ₂₃ H ₂₆ CeN ₇ NiO ₁₃	C ₃₈ H ₄₀ Ce ₂ Cu ₂ N ₁₀ O ₂₆
Formula weight	779.51	807.34	1460.12
Temperature (K)	100(2)	100(2)	100(2)
Wavelength (Å)	0.71073	0.71073	0.71073
Crystal system	Monoclinic	Monoclinic	Triclinic
Space group	P2 ₁ /n	P2 ₁ /n	P $\bar{1}$
Unit cell dimensions	a = 10.8661(8) Å $\alpha = 90^\circ$ b = 15.5141(11) Å $\beta = 100.5600(10)^\circ$ c = 16.9911(12) Å $\gamma = 90^\circ$	a = 9.7345(7) Å $\alpha = 90^\circ$ b = 17.2662(12) Å $\beta = 91.0030(10)^\circ$ c = 18.0756(12) Å $\gamma = 90^\circ$	a = 9.3373(9) Å $\alpha = 67.652(2)^\circ$ b = 11.5258(11) Å $\beta = 71.758(2)^\circ$ c = 13.0679(13) Å $\gamma = 70.559(2)^\circ$
Volume	2815.8(3) Å ³	3037.6(4) Å ³	1198.2(2) Å ³
Z	4	4	1
ρ_{calc} (g·cm ⁻³)	1.839	1.765	2.024
μ (mm ⁻¹)	2.262	2.174	2.843
F(000)	1548	1612	720
Crystal size (mm ³)	0.22 × 0.15 × 0.14	0.25 × 0.12 × 0.10	0.16 × 0.14 × 0.05
θ range (deg)	1.79 to 31.00	1.63 to 31.00	1.72 to 29.99
Index ranges	-15 ≤ h ≤ 15 -22 ≤ k ≤ 22 -24 ≤ l ≤ 24	-14 ≤ h ≤ 4 -25 ≤ k ≤ 25 -26 ≤ l ≤ 26	-13 ≤ h ≤ 13 -16 ≤ k ≤ 16 -18 ≤ l ≤ 18
Reflections collected	80297	108351	76098
Independent reflections	8990 [R(int) = 0.0314]	9670 [R(int) = 0.0345]	6965 [R(int) = 0.0341]
Completeness to θ_{max}	100.0 %	100.0 %	99.7 %
Absorption correction	Semi-empirical from equivalents	Semi-empirical from equivalents	Semi-empirical from equivalents
Max. and min. transmission	0.7424 and 0.6360	0.8119 and 0.6125	0.8709 and 0.6591
Refinement method	Full-matrix least-squares on F ²	Full-matrix least-squares on F ²	Full-matrix least-squares on F ²
Data / restraints / parameters	8990 / 0 / 392	9670 / 0 / 410	6965 / 0 / 354
Goodness-of-fit on F ²	1.037	1.021	1.037
Final R indices [I > 2 σ (I)]	R ₁ = 0.0284, wR ₂ = 0.0769	R ₁ = 0.0171, wR ₂ = 0.0414	R ₁ = 0.0150, wR ₂ = 0.0381
R indices (all data)	R ₁ = 0.0328, wR ₂ = 0.0806	R ₁ = 0.0199, wR ₂ = 0.0425	R ₁ = 0.0166, wR ₂ = 0.0387
Largest diff. peak/hole (e ⁻ ·Å ⁻³)	3.959 / -0.533	0.482 / -0.309	0.515 / -0.3869

Powder X-ray diffraction (PXRD). PXRD patterns were recorded on a PANalytical X'Pert PRO diffractometer with Bragg-Brentano geometry using nickel-filtered Cu-K α radiation ($\lambda = 1.54056$ Å). Samples were prepared by dropcasting onto boron-doped, *p*-type silicon zero-background plates or glass slides. PXRD profiles were fit with pseudo-Voigt functions using the FullProf software suite.⁴⁷ The crystallite sizes (*d*) of the

M_{0.1}Ce_{0.9}O_{2-x} nanoparticles were estimated by employing the Scherrer equation to the fitted (220) peak assuming a shape factor *K* of 0.94 for spherical particles of cubic symmetry, after accounting for instrumental line broadening.

Table 2.2 Crystallographic and refinement parameters for M_yCe_{1-y}O_{2-x} powders, their BET surface areas (*S*_{BET}) and elemental compositions (*y*). Standard uncertainties in the last digits are included in parentheses.

Compound	<i>a</i> (Å)	<i>H</i> _{W(220)} (°)	<i>d</i> ₍₂₂₀₎ (Å)	R factors (%)	χ ²	<i>S</i> _{BET} (m ² g ⁻¹)	<i>y</i> (EDS)	<i>y</i> (ICP-AES)
as-Mn _{0.1} Ce _{0.9} O _{2-x}	5.495(1)	4.01	22.5	1.51, 1.89	1.31			
as-Fe _{0.1} Ce _{0.9} O _{2-x}	5.425(3)	4.14	21.9	1.71, 2.17	1.11			
as-Co _{0.1} Ce _{0.9} O _{2-x}	5.415(4)	4.05	22.4	1.64, 2.07	1.11			
as-Ni _{0.1} Ce _{0.9} O _{2-x}	5.4237(8)	3.01	30.1	1.46, 1.82	1.23			
as-Cu _{0.1} Ce _{0.9} O _{2-x}	5.4215(7)	3.37	26.9	1.55, 1.96	1.35			
as-CeO ₂ (3 nm)	5.4208(3)	3.21	28.3	2.20, 2.80	1.24			
annealed-Mn _{0.1} Ce _{0.9} O _{2-x}	5.4120(4)	2.90	31.3	1.82, 2.31	1.30	77	0.083(3)	0.128(2)
annealed-Fe _{0.1} Ce _{0.9} O _{2-x}	5.412(3)	2.82	32.2	2.11, 2.66	1.29	63	0.113(3)	0.099(4)
annealed-Co _{0.1} Ce _{0.9} O _{2-x}	5.416(2)	2.33	39.0	2.19, 2.74	1.40	17	0.08(2)	0.0882(3)
annealed-Ni _{0.1} Ce _{0.9} O _{2-x}	5.4153(4)	2.52	36.1	1.65, 2.05	1.23	54	0.14(1)	0.150(3)
annealed-Cu _{0.1} Ce _{0.9} O _{2-x}	5.4203(5)	2.49	36.4	1.66, 2.10	1.17	52	0.08(1)	0.0582(7)
annealed-CeO ₂ (3 nm)	5.4143(1)	1.38	66.2	2.95, 3.80	1.41	21		

Table 2.3 Crystallographic and refinement parameters for post-mortem analysis of Cu_{0.1}Ce_{0.9}O_{2-x}. Standard uncertainties in the last digits are included in parentheses.

Compound	<i>a</i> (Å)	<i>H</i> _{W(220)} (°)	<i>d</i> ₍₂₂₀₎ (Å)	R factors (%)	χ ²
as-Cu _{0.1} Ce _{0.9} O _{2-x}	5.422(1)	2.37	38.2	2.01, 2.53	1.26
annealed-Cu _{0.1} Ce _{0.9} O _{2-x}	5.4169(6)	2.05	44.4	2.48, 3.13	1.22
post-mortem-Co _{0.1} Ce _{0.9} O _{2-x}	5.4166(5)	1.97	46.2	1.94, 2.43	1.29

Transmission electron microscopy (TEM). Samples for TEM analysis were prepared by dropcasting dilute hexanes solutions of as synthesized M_{0.1}Ce_{0.9}O_{2-x} (EtOH suspensions for annealed M_{0.1}Ce_{0.9}O_{2-x}) onto lacy carbon copper (or gold) grids. Bright field images were collected at 200 keV using a low-background beryllium sample holder on a JEOL 2010-FEG transmission electron microscope, equipped with a field-emission electron gun and an ultrahigh resolution pole piece, resulting in a point-to-point resolution of 1.9 Å. Fast Fourier transforms (FFTs) were implemented using the ImageJ software.⁴⁸ EDS elemental analysis was performed in transmission scanning mode using a 1 nm diameter electron beam. INCA software (Oxford Instruments) was used to control the beam position and analyze the data.

For point capture, the beam was placed at various positions and live acquisition time of each spectrum was 30 s. Particle size distributions using the number averaged diameters of the as-synthesized nanocrystallites were determined as described previously in our lab.⁴⁹ Adobe Photoshop CS5 was used to manually make crystallite selections using the lasso tool. In this way, the cross-sectional areas of the crystallites were determined (after calibration to the image's scale bar) and, assuming a spherical particle shape, the number averaged diameters were determined.

Hard X-ray absorption spectroscopy (XAS). Hard X-ray absorption measurements were performed at room temperature at the bending magnet station X11A of the National Synchrotron Light Source (NSLS) at Brookhaven National Laboratory.⁵⁰ The electron storage ring operated at 2.8 GeV with a stored current in the range of 200-300 mA. The excitation energies were selected with a double crystal monochromator (Si-(111)), which was detuned by 40% to suppress higher harmonics. The incident and transmitted beam intensities were monitored using ionization chambers with an appropriate combination of nitrogen and argon gas. For transition-metal K-edge spectra, the energy calibration of the monochromator was set by calibrating the inflection point of the appropriate transition-metal foil to the literature value,⁵¹ while a pressed boron nitride (BN) pellet of Ce(III) nitrate hexahydrate was used for the energy calibration of Ce L_{III} spectra, calibrating the first inflection point to 5723 eV.

Transition-metal K-edge spectra (Fe, Co, Ni, Cu) were acquired in fluorescence yield (FY) mode from pressed BN pellets of $M_{0.1}Ce_{0.9}O_{2-x}$ using a 3-grid Lytle fluorescence detector (The EXAFS Company),⁵² while cerium L_{III}-edge spectra were acquired in transmission mode from pressed BN pellets. For FY measurements, the signal passed through a $3\mu\text{x}$ iron filter and silver Soller slit assembly prior to detection by the ionization chamber, which had a continuous flow of Ar. For FY experiments, pellets were oriented 45° with respect to the incident beam direction, while transmission experiments were performed at 90° . Since the Mn K $_{\alpha}$ and Ce L $_{\beta}$ emission lines are close in energy (5899 and 5262 eV, respectively), Mn K-edge spectra were acquired in FY mode using a 13-element solid-state Ge energy-resolving detector (Canberra GL0110S) selecting the K $_{\beta}$ emission line. It should be noted that, due to the decreased signal intensity resulting from the K $_{\beta}$ emission line, the

EXAFS of the Mn K-edge data could not be analyzed as described below; in the discussion only qualitative features of the Mn EXAFS are mentioned.

Absorption spectra were normalized using the Autobk algorithm in the IFEFFIT program⁵³ of the Horae XAFS analysis suite;⁵⁴ a linear fit of the pre-edge line was subtracted from the spectrum before normalization of the edge step to unity. A fourth-order knot-spline polynomial was used to fit the post-edge line. Before the Fourier transforms, the EXAFS was multiplied by a Hanning window covering the first and last ~10% of the data range (see Table 2.4).

The EXAFS equation, which describes the EXAFS ($c_i(k)$) of a component i as a function of the photoelectron wavevector k , is given by

$$\chi_i(k) = \frac{N_i S_0^2 F_i(k)}{k R_i^2} \sin[2kR_i + \varphi_i(k)] e^{-2\sigma_i^2 k^2} e^{\frac{-2R_i}{\lambda(k)}}$$

$$R_i = R_0 + \Delta R$$

$$k^2 = \frac{2m_e(E - E_0)}{\hbar}$$

where the parameters $F_i(k)$ (effective scattering amplitude), $\varphi_i(k)$ (effective scattering phase shift), $\lambda(k)$ (mean free path length) and R_0 (initial path length) are all calculated in IFEFFIT or determined through crystallography; the parameters N_i (degeneracy of path), S_0^2 (passive electron reduction factor), E_0 (energy shift), ΔR (change in half-path length) and σ_i^2 (mean squared displacement) are all refineable in FEFF6.^{24,55,56} Note that m_e , the mass of the ejected photoelectron and \hbar , the reduced Plank's constant, are common physical constants. For fitting of the k^2 -weighted Fourier Transform of transition-metal K-edge EXAFS spectra, S_0^2 was determined for each edge by fitting the EXAFS of the appropriate foil energy reference (out to $R = 6 \text{ \AA}$).

The EXAFS data at the Ce L_{III} edge were fit in two ways using the Artemis program of the IFEFFIT suite.⁵⁴ In the first fitting model (Table 2.6), the EXAFS of micron-sized CeO₂ was fit to its crystal structure, freely refining S_0^2 , E_0 , the σ_i^2 for each single-scattering path i up to the second coordination shell (~ 4.5 Å), as well as refining an isotropic expansion variable α that takes into account the expansion or contraction of the paths with changes in

the lattice constant of CeO_2 : $\Delta R_j = R_{\text{eff},j} \cdot a$. The path degeneracies were set to the crystallographically-defined variables. Significant multiple-scattering paths up to 4.5 Å were included in the fitting and values of ΔR and σ^2 for these paths were constrained according to the scheme outlined before.^{57,58} Two values for the energy shift E_0 were employed, one for Ce-O paths and one for Ce-Ce paths, due to the fact that FEFF has difficulty calculating 4f elements. The values thus obtained for S_0^2 , E_0 and σ_i^2 were set in subsequent Ce L_{III}-edge EXAFS fits while refining for the path degeneracy (N_i) of the first three coordination shells (those corresponding to the first shell of Ce-O bonds, Ce-Ce distances of edge-sharing CeO_8^{12} cubes and “third” shell Ce-O paths at 4.5 Å). The Ce-M (M= transition-metal) single-scattering path, as determined from the DFT model (*vide infra*) was added to the fit, refining its σ_i^2 and ΔR_i simultaneously, while the path degeneracy $N_{\text{Ce-M}}$ was constrained to $N_{\text{Ce-M}}/9$ to account for 10% transition-metal substitution.

It should be noted that the above analysis is rather tentative, as the values for σ_i^2 were determined from micron-sized CeO_2 and we don't know how substitution will affect these values. In an attempt to estimate the influence of transition-metal substitution on local disorder, we performed fitting on the Ce L_{III} EXAFS of these samples, refining σ_i^2 while keeping the path degeneracies N_i fixed to the crystallographically-defined values. The results from these fits are reported in Table 2.7. As expected, the values for σ_i^2 are larger than those for nanometer-sized CeO_2 which in turn are larger than those for micron-sized CeO_2 . This highlights the influence of crystallite size and transition-metal substitution on generating local disorder in CeO_2 . It should be noted that N_i and σ_i^2 are correlated during the fitting and hence a rigorous analysis would include determining values of σ_i^2 from temperature-dependent EXAFS. Needless to say, however, that the decrease in the magnitude of the EXAFS is consistent with the incorporation of transition-metal ions into CeO_2 , perhaps through a combination of decreasing $N_{\text{Ce-Ce}}$ and increasing σ_i^2 .

The model used for the fitting of the transition-metal K-edge EXAFS (Table 2.8) takes the binary oxides Fe_2O_3 , Co_3O_4 , NiO and CuO as the starting structures. First, S_0^2 for each edge was determined by fitting the EXAFS of appropriate reference foils that were acquired simultaneously in transmission mode (*vide supra*). The EXAFS for these binary oxides were then fit, freely refining σ_i^2 and the isotropic lattice expansion coefficient α , in much the same

way as the spectrum of micron-sized CeO₂ was fit. Values thus determined for σ_i^2 were set in the subsequent fitting of the K-edge EXAFS data for M_{0.1}Ce_{0.9}O_{2-x}, while freely refining the path degeneracy N_{M-O} and N_{M-M} for the first two coordination shells (M-O bonds and M-M distances corresponding to edge and corner-sharing polyhedral in the binary oxides).

Table 2.4 Fourier transform and fitting parameters for EXAFS.

Edge	Compound	Fourier Transform ^a		Fitting ^b	
		k_i	k_f	R_i (Å)	R_f (Å)
Fe K	Fe _{0.1} Ce _{0.9} O _{2-x}	3.681	11.211	1	3.884
Co K	Co _{0.1} Ce _{0.9} O _{2-x}	3.721	11.844	1.1	2.991
Ni K	Ni _{0.1} Ce _{0.9} O _{2-x}	3.488	10.010	1	3.858
Cu K	Cu _{0.1} Ce _{0.9} O _{2-x}	3.638	10.761	1	3.189
Ce L _{III}	Mn _{0.1} Ce _{0.9} O _{2-x}	3.237	9.467	1.25	4.8
	Fe _{0.1} Ce _{0.9} O _{2-x}	3.237	9.501	1.25	4.8
	Co _{0.1} Ce _{0.9} O _{2-x}	3.220	9.484	1.25	4.8
	Ni _{0.1} Ce _{0.9} O _{2-x}	3.220	9.467	1.25	4.8
	Cu _{0.1} Ce _{0.9} O _{2-x}	3.220	9.450	1.25	4.8
	CeO ₂ (5 μm)	3.203	9.364	1.25	4.8
	CeO ₂ (3 nm)	3.220	9.415	1.25	4.8

Table 2.5 Edge energies (E_0) and nominal oxidation states from transition-metal K-edge XANES spectra of M_{0.1}Ce_{0.9}O_{2-x} and binary oxides. Values for E_0 were taken at half the edge jump and estimated oxidation states for M_{0.1}Ce_{0.9}O_{2-x} were calculated from calibration curves with the binary oxides.

Edge	Compound	E_0 (eV)	Oxidation State
Mn K	MnO	6544.84	2+
	Mn ₂ O ₃	6549.05	3+
	MnO ₂	6552.33	4+
	Mn _{0.1} Ce _{0.9} O _{2-x}	6549.64	3.2+
Fe K	FeO	7119.20	2+
	Fe ₂ O ₃	7123.87	3+
	Fe ₃ O ₄	7122.03	2.67+
	Fe _{0.1} Ce _{0.9} O _{2-x}	7124.23	3.1+
Co K	CoO	7717.19	2+
	Co ₃ O ₄	7718.92	2.67+
	LaCoO ₃	7721.68	3+
	Co _{0.1} Ce _{0.9} O _{2-x}	7719.34	2.6+
Ni K	NiO	8341.80	2+
	LaNiO ₃	8345.23	3+
	NiKIO ₆	8346.64	4+
	Ni _{0.1} Ce _{0.9} O _{2-x}	8343.35	2.5+
Cu K	Cu ₂ O	8980.47	1+
	CuO	8984.14	2+
	KCuO ₂	8987.67	3+
	Cu _{0.1} Ce _{0.9} O _{2-x}	8987.37	2.9+

^a The EXAFS was multiplied by a Hanning-type window over this range previous to its Fourier Transform

^b Fitting was carried out in R space simultaneously with k^1 , k^2 and k^3 -weighted data

Table 2.6 Parameters from the refinement of cerium L_{III}-edge EXAFS of M_{0.1}Ce_{0.9}O_{2-x} powders. Standard uncertainties in the last digits are included in parentheses.

Compound	S ²	E ₀ (O)	E ₀ (Ce)	N _{Ce-O1}	σ ² _{Ce-O1} (Å ²)	R _{Ce-O1} (EXAFS) ^a (Å)	R _{Ce-O1} (PXRD) (Å)
CeO ₂ (μm)	0.58(7)	11.1(9)	7(1)	8	0.005(2)	2.349(6)	2.342459(9)
CeO ₂ (nm)	0.58	11.1	7	8	0.008(1)	2.349(4)	2.34446(6)
Mn _{0.1} Ce _{0.9} O _{2-x}	0.58	11.1	7	8	0.016(2)	2.34(1)	2.3435(2)
Fe _{0.1} Ce _{0.9} O _{2-x}	0.58	11.1	7	8	0.014(2)	2.341(8)	2.344(1)
Co _{0.1} Ce _{0.9} O _{2-x}	0.58	11.1	7	8	0.01(1)	2.343(6)	2.3450(8)
Ni _{0.1} Ce _{0.9} O _{2-x}	0.58	11.1	7	8	0.011(1)	2.344(6)	2.3449(2)
Cu _{0.1} Ce _{0.9} O _{2-x}	0.58	11.1	7	8	0.012(1)	2.346(6)	2.3471(2)
Compound	N _{Ce-Ce} ^b	σ ² _{Ce-Ce} (Å ²)	R _{Ce-Ce} ^a (Å)	N _{Ce-O2}	σ ² _{Ce-O2} (Å ²)	R _{Ce-O2} ^a (Å)	R factor (%)
CeO ₂ (μm)	12	0.003(1)	3.84(1)	24	0.011(4)	4.50 (1)	0.79
CeO ₂ (nm)	12	0.0059(9)	3.835(6)	24	0.016(5)	4.497(7)	1.90
Mn _{0.1} Ce _{0.9} O _{2-x}	10.8	0.014(3)	3.82(2)	24	0.03(2)	4.48(2)	7.15
Fe _{0.1} Ce _{0.9} O _{2-x}	10.8	0.012(2)	3.82(1)	24	0.03(1)	4.48(2)	5.10
Co _{0.1} Ce _{0.9} O _{2-x}	10.8	0.009(2)	3.83(1)	24	0.03(1)	4.49(1)	3.26
Ni _{0.1} Ce _{0.9} O _{2-x}	10.8	0.008(2)	3.828(9)	24	0.024(8)	4.49(2)	3.10
Cu _{0.1} Ce _{0.9} O _{2-x}	10.8	0.008(1)	3.831(9)	24	0.022(7)	4.49(1)	3.34

Table 2.7 Parameters from the refinement of cerium L_{III}-edge EXAFS of M_{0.1}Ce_{0.9}O_{2-x} powders fixing the path degeneracies. Standard uncertainties in the last digits are included in parentheses.

Compound	S ²	E ₀ (O)	E ₀ (Ce)	N _{Ce-O1}	σ ² _{Ce-O1} (Å ²)	R _{Ce-O1} (EXAFS) (Å)	R _{Ce-O1} (PXRD) (Å)	N _{Ce-Ce}	σ ² _{Ce-Ce} (Å ²)	R _{Ce-Ce} ^c (Å)
CeO ₂ (5 μm)	0.58(7)	11.1(9)	7(1)	8	0.005(2)	2.349(6)	2.342459(9)	12	0.003(1)	3.84(1)
CeO ₂ (3 nm)	0.58	11.1	7	6.8(4)	0.005	2.345(3)	2.34446(6)	8.4(8)	0.003	3.829(6)
Mn _{0.1} Ce _{0.9} O _{2-x}	0.58	11.1	7	4.2(6)	0.005	2.331(8)	2.3435(2)	4(1)	0.003	3.81(1)
Fe _{0.1} Ce _{0.9} O _{2-x}	0.58	11.1	7	4.7(5)	0.005	2.332(7)	2.344(1)	4(1)	0.003	3.81(1)
Co _{0.1} Ce _{0.9} O _{2-x}	0.58	11.1	7	5.9(6)	0.005	2.338(6)	2.3450(8)	5(1)	0.003	3.82(1)
Ni _{0.1} Ce _{0.9} O _{2-x}	0.58	11.1	7	5.8(4)	0.005	2.339(5)	2.3449(2)	6.0(9)	0.003	3.819(7)
Cu _{0.1} Ce _{0.9} O _{2-x}	0.58	11.1	7	5.5(4)	0.005	2.341(4)	2.3471(2)	6.3(8)	0.003	3.823(7)
Compound	N _{Ce-O2} ^d	σ ² _{Ce-O2} (Å ²)	R _{Ce-O2} ^a (Å)	N _{Ce-M} ^e	σ ² _{Ce-M} ^f (Å ²)	R _{Ce-M} ^d (Å)	R factor (%)			
CeO ₂ (5 μm)	24	0.011(4)	4.50 (1)				0.79			
CeO ₂ (3 nm)	20(1)	0.016(6)	4.491 (6)				1.56			
Mn _{0.1} Ce _{0.9} O _{2-x}	13(2)	0.02(2)	4.46(2)				6.53			
Fe _{0.1} Ce _{0.9} O _{2-x}	14(2)	0.03(2)	4.47(1)	0.4(1)	0.03(3)	3.4(2)	5.04			
Co _{0.1} Ce _{0.9} O _{2-x}	18(2)	0.03(2)	4.48(1)	0.6(1)	0.04(5)	3.1(3)	3.59			
Ni _{0.1} Ce _{0.9} O _{2-x}	17(3)	0.02(1)	4.479(9)	0.66(9)	0.02(2)	3.3(1)	3.36			
Cu _{0.1} Ce _{0.9} O _{2-x}	16(1)	0.017(7)	4.483(8)	0.70(9)	0.02(2)	3.28(4)	2.99			

^a Scattering path lengths were refined isotropically for a single expansion constant α : $R = R_{eff}(1+\alpha)$

^b For M_{0.1}Ce_{0.9}O_{2-x}, the Ce-Ce path degeneracy was constrained to 0.9 the value of the crystallographically defined case (12*0.9 = 10.8) to account for transition-metal substitution.

^c Scattering path lengths were refined isotropically for a single expansion constant α : $R = R_{eff}(1+\alpha)$

^d N_{Ce-O2} path degeneracy was constrained with respect to the Ce-O₁ first shell path degeneracy: $N_{Ce-O2} = 3*N_{Ce-O1}$

^e N_{Ce-M} path degeneracy was constrained with respect to the Ce-Ce second shell path degeneracy in accordance with 10% M substitution: $N_{Ce-M} = N_{Ce-Ce}/9$

^f Ce-M scattering MSDs and path lengths were refined as free parameters for multiple-edge fitting

Table 2.8 Parameters from the refinement of transition-metal K-edge EXAFS of M_{0.1}Ce_{0.9}O_{2-x} powders from binary oxides. Standard uncertainties in the last digits are included in parentheses.

Compound	S ₀ ^{2a}	E ₀	N _{M-O}	σ ² _{M-O} ^b (Å ²)	R _{M-O} (Å)	Edge-sharing polyhedra		
						N _{M-M}	σ ² _{M-M} ^d (Å ²)	R _{M-M} (Å)
Fe _{0.1} Ce _{0.9} O _{2-x}	0.71	2(3)	4.1(2)	0.0041	1.95(1)	0.8(4)	0.005	3.09(3)
Co _{0.1} Ce _{0.9} O _{2-x}	0.64	3(5)	3.7(4)	0.0028	1.93(2)	0.6(4)	0.0043	2.85(5)
Ni _{0.1} Ce _{0.9} O _{2-x}	0.81	1(3)	3.5(4)	0.0057	2.02(2)	0.2(5)	0.0068	2.95(7)
Cu _{0.1} Ce _{0.9} O _{2-x}	0.83	-1(4)	4.8(6)	0.0073	1.93(2)	0.6(7)	0.0068	3.13(8)

Compound	Corner-sharing polyhedra			R factor (%)
	N _{M-M}	σ ² _{M-M} ^d (Å ²)	R _{M-M} (Å)	
Fe _{0.1} Ce _{0.9} O _{2-x}	0.8 (4)	0.03(3)	3.33 (4)	0.81
Co _{0.1} Ce _{0.9} O _{2-x}				3.01
Ni _{0.1} Ce _{0.9} O _{2-x}				4.72
Cu _{0.1} Ce _{0.9} O _{2-x}				3.79

Soft X-ray absorption spectroscopy (XAS, acquired by Dr. Marcel Risch, MIT). The ground state electronic configuration of many formally trivalent copper compounds such as the high-T_C superconductor YBa₂Cu₃O_{7-δ} (YBCO) and simple ternary copper oxides (KCuO₂ and NaCuO₂) are best described as a linear combination of (at least) 3d⁸ and 3d⁹ \underline{L} configurations, where \underline{L} represents a hole in the ligand (O) 2p band, due to the small charge-transfer gap (Δ) these compounds possess.^{30,31,59} A rigorous identification of the electronic structure of compounds such as these requires, then, probing the partially unfilled copper 3d and oxygen 2p bands. X-ray absorption spectroscopy at the copper L-edge and the oxygen K-edge, which interrogates the 2p → 3d and 1s → 2p transitions, respectively, thus provides us with a useful tool for the elucidation of the electronic structure of Cu_{0.1}Ce_{0.9}O_{2-x}.

Soft X-ray absorption spectra were obtained at the Canadian Light Source (CLS) at room temperature in vacuum at the SGM (11ID-1)⁶⁰ beamline. The electron storage ring operated at 2.9 GeV with a stored current in the range of 150-250 mA. All spectra were acquired in partial fluorescence yield (PFY) mode using four silicon drift detectors simultaneously. The energy for the Cu L_{II,III}-edge spectra were calibrated with respect to the spectrum of a copper plate that was acquired before acquisition of our samples. The inflection point for the copper plate was calibrated to 932.7 eV. After normalizing the partial fluorescence yield (PFY)

^a The passive electron amplitude reduction factors S₀² were determined from the fitting of the EXAFS of the appropriate reference foils.

^b MSDs were determined from fitting the EXAFS of binary oxide references: Fe₂O₃, Co₃O₄, NiO and CuO.

spectra with respect to the incident X-ray flux (I/I_0), the region before the L_{III} edge was fitted with a line and the entire spectrum was subtracted by this. Likewise, the region after the L_{II} edge was fitted with a line and the spectrum was normalized to unity. The energy of the O K-edge spectra was calibrated with respect to the pre-edge in the spectrum of molecular oxygen at 530.8 eV.⁶¹ O K-edge spectra were normalized by first subtracting the flux-normalized (I/I_0) spectrum by its intensity at a suitable energy before the edge (518 eV) and then by dividing the entire spectrum by its intensity at a suitable energy after the edge (574 eV).

Single-point BET surface area determination. Values for the surface areas of annealed $M_{0.1}Ce_{0.9}O_{2-x}$ were estimated from single-point BET analyses from the desorption of N_2 at room temperature (adsorption at 77 K in 30% N_2/He) using a ChemBET Pulsar apparatus (Quantachrome).

Calculation of oxygen-ion content by thermogravimetric analysis. The oxygen non-stoichiometry, x , of $M_{0.1}Ce_{0.9}O_{2-x}$ was determined by monitoring the mass change of annealed samples at 1000 °C in synthetic air by TGA. Powders were loaded onto platinum TGA pans and were pretreated at 600 °C to drive off residual moisture and adsorbed gases, were heated to 1000 °C (20 °C/min) in synthetic air and were allowed to equilibrate for 60 minutes while recording the mass change. The phases of the final products after TGA analysis were determined by PXRD and the oxygen non-stoichiometry was determined according to a procedure modified from a previous discussion.⁶² The total non-stoichiometry is given by:

$$x = \delta_0 + \frac{(W_f - W_i)/M_O}{W_f/M_f}$$

where δ_0 is the charge-compensating non-stoichiometry assuming the oxidation state of the transition-metal is identical to that found by PXRD after TGA analysis, W_f is the final weight of the sample, W_i is the initial weight of the sample, M_O is the atomic mass of oxygen and M_f is the formula weight of the ceria/transition-metal oxide mixture *after* TGA treatment. The relative amount of transition-metal with respect to cerium was determined by ICP-AES (*vide supra*) and it was assumed that all of the transition-metal in the solid solution was converted to the bulk binary oxide (determined by PXRD) and that all the cerium was converted to stoichiometric CeO_2 after TGA.

The total oxygen-ion vacancy content was determined from x assuming the oxidation states (z) for the transition-metal as determined by K-edge XANES (*vide supra*) and the percent substitution (y) as determined by ICP-AES assuming the neutral compound M^{z+}_yCe_{1-y}O_{2-x}:

$$\text{oxygen-ion vacancy content} = \frac{(yz + 2x - 4)}{2(1 - y)} + 2$$

Calculation of oxygen-ion content by X-ray Photoelectron Spectroscopy. Samples for XPS analysis were prepared by deposition of the powders onto copper foil. Since the materials here are nonconductive, the samples were placed onto the sample stage using nonconductive tape in order to minimize differential charging. High-resolution spectra at the Ce 3d region (binding energies between 930 and 875 eV) were performed at $\sim 10^{-9}$ torr on a Physical Electronics Versaprobe II X-ray photoelectron spectrometer using monochromatic Al K_α radiation ($\lambda = 8.3386 \text{ \AA}$) and a pass energy of 23.5 eV. The peaks for cerium species were fitted according to a previously described fitting model⁶³ using the CasaXPS software, which is summarized below:

Assignment	Valence	Binding Energy (eV)	FWHM (eV)	Peak shape	
Ce 3d _{5/2}	v ₀	Ce ³⁺	u''' - 36.1	4.0 - 4.5	GL(30)
	v	Ce ⁴⁺	u''' - 34.1	2.5 - 2.7	GL(30)
	v'	Ce ³⁺	u''' - 31.5	2.5 - 3.0	GL(30)
	v''	Ce ⁴⁺	u''' - 27.85	4.5 - 4.6	GL(30)
	v'''	Ce ⁴⁺	u''' - 18.3	2.2 - 2.5	GL(30)
Ce 3d _{3/2}	u ₀	Ce ³⁺	u''' - 17.8	2.0 - 2.2	GL(30)
	u	Ce ⁴⁺	u''' - 15.65	1.75 - 1.9	GL(30)
	u'	Ce ³⁺	u''' - 13.65	2.2 - 2.6	GL(30)
	u''	Ce ⁴⁺	u''' - 9.25	4.2 - 4.5	GL(30)
	u'''	Ce ⁴⁺	916.4 - 916.6	2.2 - 2.5	GL(30)

The total oxygen-ion vacancy concentration in M_{0.1}Ce_{0.9}O_{2-x} was estimated by taking the ratio of areas due to Ce³⁺, as discussed elsewhere.⁶³

$$\text{oxygen-ion vacancy content} = \frac{[\text{Ce}^{3+}]}{2} = \frac{v_0 + v' + u_0 + u'}{2(v_0 + v + v' + v'' + v''' + u_0 + u + u' + u'' + u''')}$$

Table 2.9 Oxygen non-stoichiometry and vacancy content as determined by TGA and XPS analysis of Ce 3d spectra.

Compound	Oxygen non-stoichiometry, x (TGA)	Oxygen vacancy content (% TGA)	Oxygen vacancy content (% XPS)
3 nm CeO _{2-x}	0.018	1.8	6.3
Mn _{0.128} Ce _{0.872} O _{2-x}	0.092	4.7	5.5
Fe _{0.099} Ce _{0.901} O _{2-x}			10.4
Co _{0.088} Ce _{0.912} O _{2-x}			7.7
Ni _{0.150} Ce _{0.850} O _{2-x}			10.2
Cu _{0.058} Ce _{0.942} O _{2-x}	0.053	2.3	8.2

Computational Details. Plane-wave basis set spin-polarized DFT + U calculations were performed employing the exchange and correlation energy functional expressed in the Perdew-Burke-Ernzerhof (PBE) generalized gradient approximation (GGA)⁶⁴⁻⁶⁷ using projector-augmented wave (PAW) pseudo-potentials^{68,69} within the Vienna Ab Initio Simulation Package (VASP) suite.⁶⁹⁻⁷³ All calculations were performed using either the Cray XE6 (“Hopper”) or Cray XC30 (“Edison”) supercomputers at the National Energy Research Scientific Computing Center (NERSC).

A 3x3x4 slab of the CeO₂ (111) surface separated by 15 Å of vacuum to prevent interactions between slabs was used as a starting point for models of the Cu_{0.1}Ce_{0.9}O_{2-x} catalyst, which were constructed by replacing two cerium atoms with two transition-metal atoms in the slab. To simulate aliovalent substitution, an appropriate number of oxygen atoms were also removed in the vicinity of the transition metal centers for charge-compensation; the removal of a single atom corresponds to the reduction of each transition-metal center by 1 electron. For example, the Cu₂Ce₃₄O₇₂ model restricts each of the copper centers (and all of the cerium centers) to a formal oxidation state of 4+ while the removal of one oxygen atom from the slab, now with a stoichiometry of Cu₂Ce₃₄O₇₁, suggests that the copper centers are 3+. The removal of another oxygen gives Cu₂Ce₃₄O₇₀ with copper having a formal oxidation state of 2+ and so on. These models are referred to as Cu^{(4-x)+}₂Ce₃₄O_{72-x} in the discussion, where x refers to the number of charge-compensating oxygen atoms removed (the oxygen non-stoichiometry). Reduction at the transition-metal (as opposed to cerium atoms) was confirmed by inspecting the net magnetization for each atom of the slab and careful examination of the partial density of states.

The (111) surface was chosen on the basis of our HRTEM results, indicating that the (111) surface is the most predominant termination, while a 3x3x4 slab (nominally Ce₃₆O₇₂) was chosen since substitution of two transition-metals for cerium atoms would give 5.6 % atomic substitution, which is similar to the 5.8% substitution found experimentally, while allowing enough atomic layers for the study of a bulk-like model with copper substitution homogeneously distributed within the slab. A number of different atomic configurations were tested; reported here are only the most stable structures.

Estimates for the Gibbs energy of formation (ΔG_F) of Cu^{(4-x)+}₂Ce₃₄O_{72-x} slabs as a function of oxygen partial pressure were calculated employing a strategy previously reported by Reuter, *et al.*⁷⁴ ΔG_F is determined for an arbitrary oxygen stoichiometry n , relative to a reference structure (in this case, we will use Cu⁴⁺₂Ce₃₄O₇₂), by taking into account the formation of oxygen vacancies:

$$\Delta G_{F,n} = G(\text{Cu}_2\text{Ce}_{34}\text{O}_n) - G(\text{Cu}_2\text{Ce}_{34}\text{O}_{72}) + (72 - n)\mu_O(p, T)$$

Neglecting changes in entropy,⁷⁴ we express ΔG_F in terms of the energy calculated from DFT:

$$\Delta G_{F,n} = E(\text{Cu}_2\text{Ce}_{34}\text{O}_n) - E(\text{Cu}_2\text{Ce}_{34}\text{O}_{72}) + (72 - n)\mu_O(p, T)$$

where

$$\mu_O(p, T) = \mu_O(p_0, T) + \frac{1}{2} k_B T \ln \frac{p}{p_0}$$

$\mu_O(p_0, T)$ is found from the thermodynamic tables and p_0 is 1 atm. The value $\mu_O(p, T)$ is referenced with respect to the total energy of an oxygen atom in a molecule of O₂ as determined by DFT. The temperature used in these calculations is 700K, which roughly corresponds to the temperature at which Cu_{0.1}Ce_{0.9}O_{2-x} was annealed (400 °C).

The addition of a Hubbard U_{eff} ($U_{eff} = U - J$) term of 4.0 eV acting on the 4f orbitals of cerium was employed to allow for a more accurate description of the electronic structure of both oxidized and reduced ceria, as described previously.⁷⁵ The addition of a Hubbard U_{eff} term to copper 3d orbitals may perturb the energies of oxygen vacancy formation in these

slabs (and hence the relative stability of the different formal oxidation states of copper) as has been discussed previously.⁷⁵ We found that the introduction of a Hubbard U_{eff} term to the copper 3d states did not perturb the relative values for ΔG_F for the different models. Only after applying values for U_{eff} in excess of 4.0 eV did we finally see any changes in the plots for ΔG_F , hence we set U_{eff} to 0.0 eV on Cu 3d states for all subsequent studies of $\text{Cu}^{(4-x)+}_2\text{Ce}_{34}\text{O}_{72-x}$.

To correct for systematic errors in the calculation of these asymmetric slabs arising from the periodic boundary conditions of plane-wave basis DFT, a linear electrostatic potential was applied to the local potential (the so-called dipole correction). Electronic and geometric optimization of the slabs was carried out using the conjugate gradient algorithm using a plane-wave cutoff energy of 400 eV. All slab energies are reported from the integration of the Brillouin zone at the Γ point only. We found that the slab energies calculated at the Γ point varied by less than 35 meV from those calculated using the (2x2x1) Monkhorst-Pack mesh, which justifies our use of integrating at the Γ point only.

Calculations used to compute the formation energy of the bulk model of $\text{Cu}_{0.1}\text{Ce}_{0.9}\text{O}_{2-x}$ from CuO and CeO_2 (Table 2.10) employed a (2x2x2) bulk unit cell with the stoichiometry of $\text{Cu}^{(4-2x)+}\text{Ce}_{31}\text{O}_{64-x}$ using the same parameters described above.

Table 2.10 DFT energies of formation of bulk $\text{Cu}^{(4-2x)+}\text{Ce}_{31}\text{O}_{64-x}$ from CuO and CeO_2 .

Model	Total Energy (eV)	Magnetization	E_F (eV)
O_2	-9.857	2	
Cu_4O_4	-40.993	0	
Ce_4O_8	-99.188	0	
$\text{Ce}_{32}\text{O}_{64}$	-793.226	0	
$\text{Cu}^{4+}\text{Ce}_{31}\text{O}_{64}$	-779.901	3	3.705
$\text{Cu}^{2+}\text{Ce}_{31}\text{O}_{63}$	-776.288	1	2.389

CO oxidation catalysis. CO oxidation measurements were performed in a homemade, 3.81 mm i.d. quartz plug-flow reactor. Annealed catalysts (20 mg) were mixed with 1.705 g of oven-dried sand ($V_{bed} = 1.086$ mL) and loaded into the reactor, filling the remaining volume with sand. The temperature of the catalyst bed was measured by a K-type thermocouple inserted into the catalyst bed. Temperature-programmed CO oxidation was performed in a mixture of 1.0% CO and 2.5% O_2 balanced in Ar ($1300 \text{ mL min}^{-1} \text{ g}^{-1}_{cat}$),

recording percent conversion every 5 °C. The compositions of the feed and the output gases were measured by on-line GC (Agilent 490 supplied with a molecular sieve COX column for permanent gases and a TCD detector) and percent conversions were calculated according to

$$\% \text{ Conversion} = \frac{p_{\text{CO}_2}}{p_{\text{CO}} + p_{\text{CO}_2}} \cdot 100\%$$

where p_{CO_2} and p_{CO} , the partial pressures of CO₂ and CO, respectively, were determined directly from the relative peak area of the CO₂ and CO peaks with respect to the internal He standard. Prior to and following each catalytic test, the flow rate of the gas upstream was measured directly with a bubble flowmeter and the percent conversion below 12.5% was converted to mass-normalized rates of CO oxidation (in units of $\mu\text{mol CO s}^{-1}\text{g}_{\text{cat}}^{-1}$) for the Arrhenius plots according to

$$\begin{aligned} r_{\text{mass}} &= \frac{\frac{\% \text{ Conversion}}{100} r_{\text{CO}} \cdot 1000}{V_m \cdot 60 \cdot m_{\text{cat}}} \\ &= \frac{\% \text{ Conversion} \cdot r_{\text{CO}}}{6 \cdot V_m \cdot m_{\text{cat}}} \end{aligned}$$

where r_{CO} is the volumetric flow rate of CO of the feed stream (in mL min^{-1}), V_m is the molar volume of a gas (from the ideal gas law, $V_m = RT/p$, in mol/L) and m_{cat} is the mass of the loaded catalyst in grams. The specific (area-normalized) rates for CO oxidation (in units of $\text{mol CO s}^{-1}\text{m}_{\text{cat}}^{-2}$) were thus calculated according to

$$r_{\text{area}} = \frac{r_{\text{mass}}}{A_S} \cdot 10^{-6}$$

where A_S is the surface area of the catalyst (in m^2g^{-1}) as measured by BET (*vide supra*).

2.7 References

- (1) Liu, W.; Flytzani-Stephanopoulos, M. *J. Catal.* **1995**, *153*, 317.
- (2) Wang, X.; Rodriguez, J. A.; Hanson, J. C.; Gamarra, D.; Martinez-Arias, A.; Fernandez-Garcia, M. *J. Phys. Chem. B* **2005**, *109*, 19595.
- (3) Dow, W. P.; Huang, T. J. *J. Catal.* **1994**, *147*, 322.

- (4) Wang, X.; Rodriguez, J. A.; Hanson, J. C.; Gamarra, D.; Martinez-Arias, A.; Fernandez-Garcia, M. *J. Phys. Chem. B* **2006**, *110*, 428.
- (5) Gamarra, D.; Munuera, G.; Hungria, A. B.; Fernandez-Garcia, M.; Conesa, J. C.; Midgley, P. A.; Wang, X. Q.; Hanson, J. C.; Rodriguez, J. A.; Martinez-Arias, A. *J. Phys. Chem. C* **2007**, *111*, 11026.
- (6) Soria, J.; Conesa, J. C.; Martinez-Arias, A.; Coronado, J. M. *Solid State Ionics* **1993**, *63 - 65*, 755.
- (7) Martinez-Arias, A.; Fernandez-Garcia, M.; Soria, J.; Conesa, J. C. *J. Catal.* **1999**, *182*, 367.
- (8) Gamarra, D.; Martinez-Arias, A. *J. Catal.* **2009**, *263*, 189.
- (9) Jia, A.-P.; Jiang, S.-Y.; Lu, J.-Q.; Luo, M.-F. *J. Phys. Chem. C* **2010**, *114*, 21605.
- (10) Jia, A.-P.; Hu, G.-S.; Meng, L.; Xie, Y.-L.; Lu, J.-Q.; Luo, M.-F. *J. Catal.* **2012**, *289*, 199.
- (11) Elmali, A.; Elerman, Y. Z. *Naturforsch. B* **2003**, *58*, 639.
- (12) Vigato, P. A.; Tamburini, S. *Coordin. Chem. Rev.* **2008**, *252*, 1871.
- (13) Akine, S.; Nabeshima, T. *Dalton T.* **2009**, 10395.
- (14) Andruh, M. *Chem. Commun.* **2011**, *47*, 3025.
- (15) Deshpande, S.; Patil, S.; Kuchibhatla, S. V. N. T.; Seal, S. *Appl. Phys. Lett.* **2005**, *87*, 133113.
- (16) Turner, S.; Lazar, S.; Freitag, B.; Egoavil, R.; Verbeeck, J.; Put, S.; Strauven, Y.; Van Tendeloo, G. *Nanoscale* **2011**, *3*, 3385.
- (17) Gilliss, S. R.; Bentley, J.; Carter, C. B. *Appl. Surf. Sci.* **2005**, *241*, 61.
- (18) Zhang, F.; Chan, S.-W.; Spanier, J. E.; Apak, E.; Jin, Q.; Robinson, R. D.; Herman, I. P. *Appl. Phys. Lett.* **2002**, *80*, 127.
- (19) Zhang, F.; Jin, Q.; Chan, S.-W. *J. Appl. Phys. (Melville, NY, U. S.)* **2004**, *95*, 4319.
- (20) Lin, M.; Fu, Z. Y.; Tan, H. R.; Tan, J. P. Y.; Ng, S. C.; Teo, E. *Cryst. Growth Des.* **2012**, *12*, 3296.
- (21) Nachimuthu, P.; Shih, W.-C.; Liu, R.-S.; Jang, L.-Y.; Chen, J.-M. *J. Solid State Chem.* **2000**, *149*, 408.
- (22) Bianconi, A.; Marcelli, A.; Dexpert, H.; Karnatak, R.; Kotani, A.; Jo, T.; Petiau, J. *Phys. Rev. B* **1987**, *35*, 806.

- (23) Soldatov, A. V.; Ivanchenko, T. S.; Della Longa, S.; Kotani, A.; Iwamoto, Y.; Bianconi, A. *Phys. Rev. B* **1994**, *50*, 5074.
- (24) Rehr, J. J.; Albers, R. C. *Rev. Mod. Phys.* **2000**, *72*, 621.
- (25) Flipse, C. F. J.; van der Laan, G.; Johnson, A. L.; Kadowaki, K. *Phys. Rev. B* **1990**, *42*, 1997.
- (26) Krol, A.; Lin, C. S.; Ming, Z. H.; Sher, C. J.; Kao, Y. H.; Chen, C. T.; Sette, F.; Ma, Y.; Smith, G. C.; Zhu, Y. Z.; Shaw, D. T. *Phys. Rev. B* **1990**, *42*, 2635.
- (27) Hahn, J. E.; Scott, R. A.; Hodgson, K. O.; Doniach, S.; Desjardins, S. R.; Solomon, E. I. *Chem. Phys. Lett.* **1982**, *88*, 595.
- (28) Brese, N. E.; O'Keeffe, M.; Von Dreele, R. B.; Young Jr, V. G. *J. Solid State Chem.* **1989**, *83*, 1.
- (29) Grioni, M.; Goedkoop, J. B.; Schoorl, R.; de Groot, F. M. F.; Fuggle, J. C.; Schäfers, F.; Koch, E. E.; Rossi, G.; Esteva, J. M.; Karnatak, R. C. *Phys. Rev. B* **1989**, *39*, 1541.
- (30) Kaindl, G.; Streb, O.; Kolodziejczyk, A.; Schäfer, W.; Kiemel, R.; Löscher, S.; Kemmler-Sack, S.; Hoppe, R.; Müller, H. P.; Kissel, D. *Phys. B (Amsterdam, Neth.)* **1989**, *158*, 446.
- (31) Hu, Z.; Kaindl, G.; Warda, S. A.; Reinen, D.; de Groot, F. M. F.; Müller, B. G. *Chem. Phys.* **1998**, *232*, 63.
- (32) Bianconi, A.; Castellano, A. C.; De Santis, M.; Rudolf, P.; Lagarde, P.; Flank, A. M.; Marcelli, A. *Solid State Commun.* **1987**, *63*, 1009.
- (33) Levason, W.; Spicer, M. D. *Coordin. Chem. Rev.* **1987**, *76*, 45.
- (34) Burdett, J. K.; Sevov, S. *J. Am. Chem. Soc.* **1995**, *117*, 12788.
- (35) Liu, W.; Sarofim, A. F.; Flytzani-Stephanopoulos, M. *Chem. Eng. Sci.* **1994**, *49*, 4871.
- (36) Liu, W.; Flytzani-Stephanopoulos, M. *Chem. Eng. J. (Amsterdam, Neth.)* **1996**, *64*, 283.
- (37) Walther, G.; Mowbray, D. J.; Jiang, T.; Jones, G.; Jensen, S.; Quaade, U. J.; Horch, S. *J. Catal.* **2008**, *260*, 86.
- (38) Carretin, S.; Concepción, P.; Corma, A.; López Nieto, J. M.; Puentes, V. F. *Angew. Chem. Int. Ed.* **2004**, *43*, 2538.
- (39) Schuth, F. *Angew. Chem. Int. Ed.* **2003**, *42*, 3604.
- (40) Zhou, K.; Wang, X.; Sun, X.; Peng, Q.; Li, Y. *J. Catal.* **2005**, *229*, 206.

- (41) Wang, Z. L.; Feng, X. *J. Phys. Chem. B* **2003**, *107*, 13563.
- (42) Corma, A.; Atienzar, P.; Garcia, H.; Chane-Ching, J.-Y. *Nat. Mater.* **2004**, *3*, 394.
- (43) Sedmak, G.; Hocevar, S.; Levec, J. *J. Catal.* **2004**, *222*, 87.
- (44) Baudelet, F.; Collin, G.; Dartyge, E.; Fontaine, A.; Kappler, J. P.; Krill, G.; Itie, J. P.; Jegoudez, J.; Maurer, M.; Monod, P.; Revcolevschi, A.; Tolentino, H.; Tourillon, G.; Verdaguer, M. *Z. Phys. B: Condens. Matter* **1987**, *69*, 141.
- (45) Sheldrick, G. M. *SADABS* **1996**, University of Göttingen.
- (46) Sheldrick, G. *Acta Crystallogr., Sect. A: Found. Crystallogr.* **2008**, *64*, 112.
- (47) Rodriguez-Carvajal, J. *Commission on Powder Diffraction (IUCr)* **2001**, *26*, 12.
- (48) Schneider, C. A.; Rasband, W. S.; Eliceiri, K. W. *Nat. Methods* **2012**, *9*, 671.
- (49) Lee, Y.; Suntivich, J.; May, K. J.; Perry, E. E.; Shao-Horn, Y. *J. Phys. Chem. Lett.* **2012**, *3*, 399.
- (50) Sayers, D. E.; Heald, S. M.; Pick, M. A.; Budnick, J. I.; Stern, E. A.; Wong, J. *Nucl. Instrum. Methods Phys. Res.* **1983**, *208*, 631.
- (51) Bearden, J. A.; Burr, A. F. *Rev. Mod. Phys.* **1967**, *39*, 125.
- (52) Lytle, F. W.; Gregor, R. B. a. S. D. R.; Marques, E. C.; Wong, J.; Spiro, C. L.; Huffman, G. P.; Huggins, F. E. *Nucl. Instrum. Methods A* **1984**, *226*, 542
- (53) Newville, M. *J. Synchrotron Radiat.* **2001**, *8*, 322.
- (54) Ravel, B.; Newville, M. *J. Synchrotron Radiat.* **2005**, *12*, 537.
- (55) Rehr, J. J.; Kas, J. J.; Prange, M. P.; Sorini, A. P.; Takimoto, Y.; Vila, F. *C. R. Phys.* **2009**, *10*, 548.
- (56) Zabinsky, S. I.; Rehr, J. J.; Ankudinov, A.; Albers, R. C.; Eller, M. J. *Phys. Rev. B* **1995**, *52*, 2995.
- (57) Calvin, S., City University of New York, 2001.
- (58) Calvin, S. *XAFS for Everyone*; Taylor & Francis, 2013.
- (59) Bianconi, A.; De Santis, M.; Di Cicco, A.; Flank, A. M.; Fontaine, A.; Lagarde, P.; Katayama-Yoshida, H.; Kotani, A.; Marcelli, A. *Phys. Rev. B* **1988**, *38*, 7196.
- (60) Regier, T.; Krochak, J.; Sham, T. K.; Hu, Y. F.; Thompson, J.; Blyth, R. I. R. *Nucl. Instrum. Methods Phys. Res., Sect. A* **2007**, *582*, 93.

- (61) Hitchcock, A. P.; Brion, C. E. *J. Electron Spectrosc. Relat. Phenom.* **1980**, *18*, 1.
- (62) Yang, Z.; Lin, Y. S. *Solid State Ionics* **2002**, *150*, 245.
- (63) Zhang, F.; Wang, P.; Koberstein, J.; Khalid, S.; Chan, S.-W. *Surf. Sci.* **2004**, *563*, 74.
- (64) Perdew, J. P.; Burke, K.; Ernzerhof, M. *Phys. Rev. Lett.* **1996**, *77*, 3865.
- (65) Perdew, J. P.; Burke, K.; Ernzerhof, M. *Phys. Rev. Lett.* **1997**, *78*, 1396.
- (66) Perdew, J. P.; Chevary, J. A.; Vosko, S. H.; Jackson, K. A.; Pederson, M. R.; Singh, D. J.; Fiolhais, C. *Phys. Rev. B: Condens. Matter Mater. Phys.* **1992**, *46*, 6671.
- (67) Perdew, J. P.; Chevary, J. A.; Vosko, S. H.; Jackson, K. A.; Pederson, M. R.; Singh, D. J.; Fiolhais, C. *Phys. Rev. B: Condens. Matter Mater. Phys.* **1993**, *48*, 4978.
- (68) Bochl, P. E. *Phys. Rev. B: Condens. Matter Mater. Phys.* **1994**, *50*, 17953.
- (69) Kresse, G.; Joubert, D. *Phys. Rev. B: Condens. Matter Mater. Phys.* **1999**, *59*, 1758.
- (70) Kresse, G.; Furthmüller, J. *Phys. Rev. B: Condens. Matter Mater. Phys.* **1996**, *54*, 11169.
- (71) Kresse, G.; Furthmüller, J. *Comput. Mater. Sci.* **1996**, *6*, 15.
- (72) Kresse, G.; Hafner, J. *Phys. Rev. B: Condens. Matter Mater. Phys.* **1993**, *47*, 558.
- (73) Kresse, G.; Hafner, J. *Phys. Rev. B: Condens. Matter Mater. Phys.* **1994**, *49*, 14251.
- (74) Reuter, K.; Scheffler, M. *Phys. Rev. B: Condens. Matter Mater. Phys.* **2001**, *65*, 035406.
- (75) Krcha, M. D.; Janik, M. J. *Int. J. Quantum Chem.* **2014**, *114*, 8.

Chapter 3 – Identification of the Active Phase in $\text{Cu}_y\text{Ce}_{1-y}\text{O}_{2-x}$

Portions of this chapter have appeared in print:

Elias, J. S.; Artrith, N.; Bugnet, M.; Giordano, L.; Botton, G. A.; Kolpak, A. M. & Shao-Horn, Y., “Elucidating the Nature of the Active Phase in Copper/Ceria Catalysts for CO Oxidation,” *ACS Catal.*, **2016**, 1675-1679 – Reproduced with permission. Copyright 2016 American Chemical Society.

3.1 Introduction

As we've seen previously in 1.5.3, the nature of the active site(s) for CO oxidation on the surface of CuO/CeO₂ is not fully understood despite twenty years of scientific research in the field.¹⁻⁵ According to the Flytzani-Stephanopoulos model (Figure 1.6A), CO oxidation catalysis turns over at dispersed Cu⁺ sites at the interface between CuO and CeO₂.² Subsequent studies proposed alternative models (Figure 1.6B and C) suggested that Cu²⁺ ions at the interface of bulk CuO and CeO₂ are responsible for the rate enhancement,⁶⁻⁸ and that the Cu_yCe_{1-y}O_{2-x} solid solution phase itself is inactive.⁹ As we have seen in Chapter 2, single-phase Cu_{0.1}Ce_{0.9}O_{2-x} demonstrates activities comparable to those reported for CuO/CeO₂¹⁰ in the absence of any detectable CuO or Cu⁺. XAS analysis of Cu_{0.1}Ce_{0.9}O_{2-x} has shown that the copper ions exist as an admixture of Cu²⁺ and Cu³⁺ and we hypothesized that the catalytically-active copper ions segregate to the surface of Cu_yCe_{1-y}O_{2-x}. In this chapter, we test these hypotheses by synthesizing single-phase Cu_yCe_{1-y}O_{2-x} with different copper substitution and mixed-phase samples with Cu_yCe_{1-y}O_{2-x} and CuO and compare their intrinsic activity for CO oxidation. We demonstrate that the Cu_yCe_{1-y}O_{2-x} phase is the only contributor to catalysis of CO oxidation, while computational methods paired with aberration-corrected STEM-EELS support our claim that the copper ions segregate to the surface of the nanoparticles, forming copper-segregated regions distinct in nature from bulk CuO.

3.2 CO Oxidation Catalysis on CuO/Cu_yCe_{1-y}O_{2-x} catalysts

Solid-solution Cu_yCe_{1-y}O_{2-x} and mixed-phase CuO/Cu_yCe_{1-y}O_{2-x} catalysts were prepared according to the synthetic scheme presented in Chapter 2. Powder X-ray diffraction (PXRD, Figure 3.1A) confirms that the synthesis afforded single-phase Cu_yCe_{1-y}O_{2-x} (space group #225, *F_m $\bar{3}m$*) with Cu substitution up to $y = 0.08$. Attempts to prepare samples with substitution beyond $y = 0.09$ resulted in the precipitation of bulk-phase CuO (space group #15, *C2/c*) as confirmed by PXRD (Figure 3.1A). Copper substitution in individual Cu_yCe_{1-y}O_{2-x} nanoparticles in both types of catalysts was determined by HAADF-EDS (Table 3.1).

Cu_yCe_{1-y}O_{2-x} nanoparticles of ~3 nm diameter were found in close proximity to large particles (>10-30 nm) of CuO in mixed-phase CuO/Cu_yCe_{1-y}O_{2-x} catalysts as revealed from high-resolution bright-field transmission electron microscopy (HRTEM, Figure 3.1B) and refinement of the powder patterns (Tables 3.1 and 3.2). Cu_yCe_{1-y}O_{2-x} nanoparticles of different Cu substitution and in mixed-phase CuO/Cu_yCe_{1-y}O_{2-x} were found to have truncated

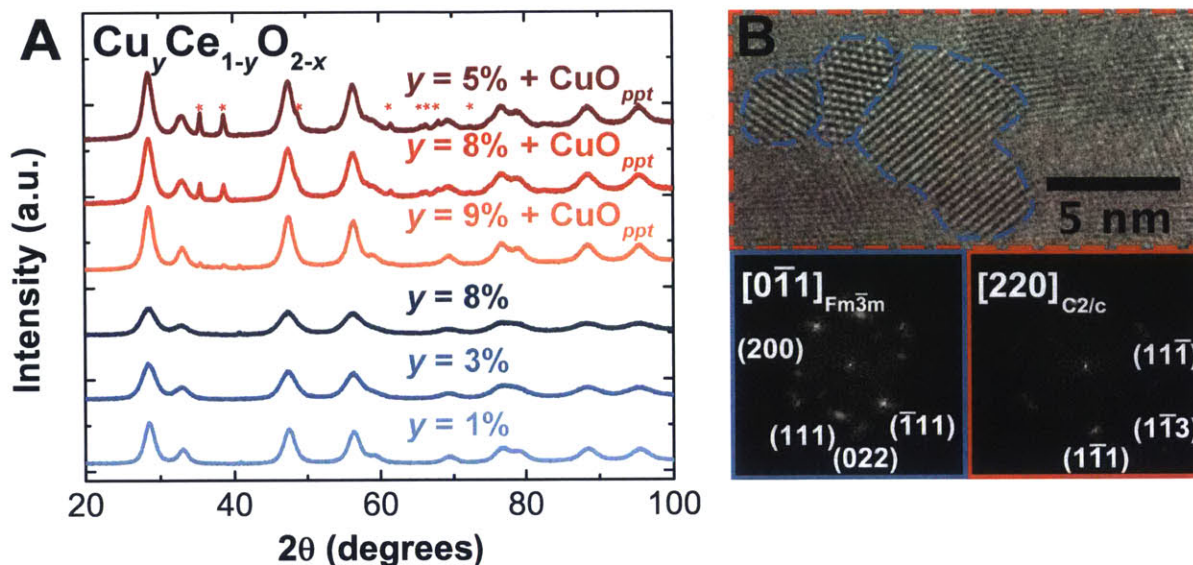


Figure 3.1 Phase identification of $\text{CuO}/\text{Cu}_y\text{Ce}_{1-y}\text{O}_{2-x}$ compounds by (A) PXRD acquired with $\text{Cu K } \alpha$ radiation and (B) HRTEM. Asterisks indicate CuO phases in A. Shown in B are representative FFT images of the two phases in $\text{CuO}/\text{Cu}_{0.05}\text{Ce}_{0.95}\text{O}_{2-x}$ outlined in the bright-field image; outlined in blue are nanoparticles of $\text{Cu}_{0.05}\text{Ce}_{0.95}\text{O}_{2-x}$ (the middle nanoparticle was chosen for the FFT) on the surface of a large crystal of CuO , outlined by the red box.

octahedral crystal habits with $\{111\}$ and $\{100\}$ terminations and crystallite sizes of ~ 3 nm, similar to those we found in Chapter 2 (Table 3.1).^{11,12} Incorporation of copper ions into the lattice of $\text{Cu}_y\text{Ce}_{1-y}\text{O}_{2-x}$ is confirmed by Raman spectroscopy (Figure 3.2), which shows a redshift in the main F_{2g} band with increased copper substitution (Figure 3.2B). The softening of the F_{2g} mode is accompanied by the appearance of a broad feature centered around 600 cm^{-1} , consistent with the formation of charge-compensating oxygen vacancies expected for aliovalent copper substitution.¹³ For mixed-phase $\text{CuO}/\text{Cu}_y\text{Ce}_{1-y}\text{O}_{2-x}$, these trends are less pronounced with increased CuO content, which is consistent with a surface-segregated CuO phase.¹³

CO oxidation catalysis was performed in excess oxygen (1% CO , 2.5% O_2). Increasing Cu substitution in $\text{Cu}_y\text{Ce}_{1-y}\text{O}_{2-x}$ led to significant catalytic rate enhancement for the mass-normalized activity for CO oxidation, with the mixed-phase $\text{CuO}/\text{Cu}_y\text{Ce}_{1-y}\text{O}_{2-x}$ catalysts having the highest activities in this study (Figure 3.3A). Notably, the most active $\text{CuO}/\text{Cu}_{0.05}\text{Ce}_{0.95}\text{O}_{2-x}$ catalyst turns over CO oxidation at a rate of $0.2 \mu\text{mol s}^{-1} \text{ g}^{-1}$ at 45°C , which is comparable to CuO/CeO_2 catalysts reported previously ($0.02 - 0.5 \mu\text{mol s}^{-1} \text{ g}^{-1}$ at 45°C).^{2,9,10} These rates were then normalized to the concentration of copper on the surface of

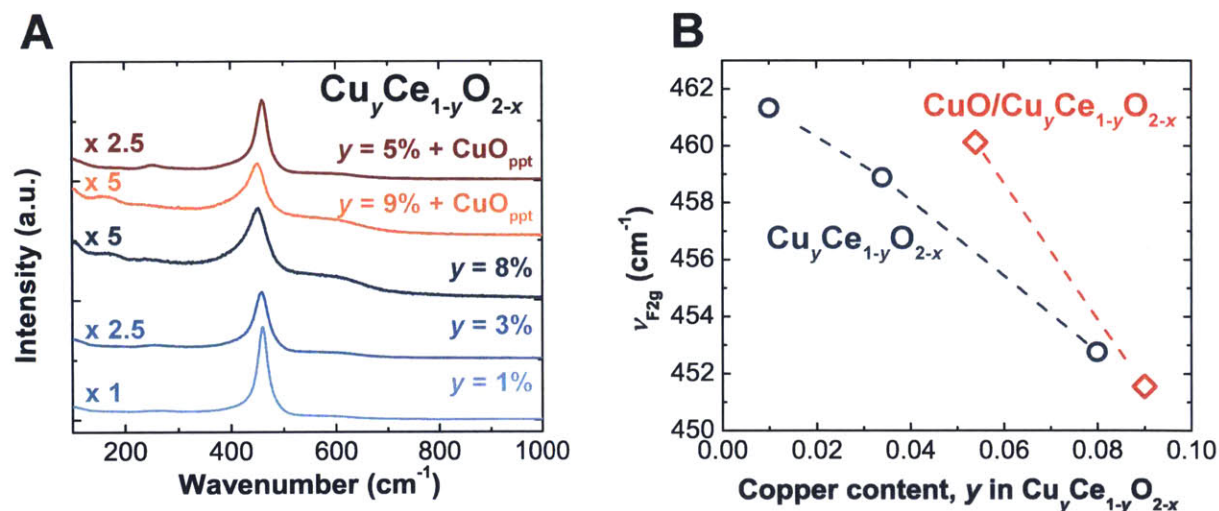


Figure 3.2 Raman spectra of $\text{Cu}_y\text{Ce}_{1-y}\text{O}_{2-x}$ and $\text{CuO}/\text{Cu}_y\text{Ce}_{1-y}\text{O}_{2-x}$ acquired at room temperature. (A) Raw spectra and (B) measured frequency of the F_{2g} mode as a function of copper substitution in $\text{Cu}_y\text{Ce}_{1-y}\text{O}_{2-x}$ (y).

solid-solution $\text{Cu}_y\text{Ce}_{1-y}\text{O}_{2-x}$ (neglecting contributions from the bulk CuO phase) assuming a homogeneous copper substitution (as determined by BET and HAADF-EDS, see Section 3.5, Experimental Methods). Remarkably, the turnover frequencies (TOFs) for all catalysts are comparable within experimental uncertainty, as shown in Figure 3.3B. This observation strongly suggests that $\text{Cu}_y\text{Ce}_{1-y}\text{O}_{2-x}$ is the active phase for CO oxidation, not the $\text{CuO}/\text{Cu}_y\text{Ce}_{1-y}\text{O}_{2-x}$ interface as proposed previously.^{2,8,9}

It should be noted that these turnover frequencies assume homogeneous substitution of copper within the entire lattice of $\text{Cu}_y\text{Ce}_{1-y}\text{O}_{2-x}$, which is, as we'll see below, unrealistic. Assuming that all copper ions segregate to the surface, these TOFs will be scaled by a factor that is proportional to $1/d$, where d is the average crystallite diameter (see Section 3.5, Experimental Methods). Since the magnitude of d changes very little between the catalysts studied here (Table 3.1), TOFs for the different catalysts calculated assuming copper surface segregation do not vary within the experimental uncertainty of the measurement (Figure 3.4), consistent with our claim. Compared to other model systems, the measured TOFs for CO oxidation are reasonable. For example, the TOF (0.07 s^{-1}) measured here at $120 \text{ }^\circ\text{C}$ for $\text{Cu}_{0.08}\text{Ce}_{0.92}\text{O}_{2-x}$ is comparable to that found for CuO/CeO_2 (0.09 s^{-1}).⁸ The CuO phase seems to improve catalysis by enhancing the surface area of the catalyst (Table 3.1) while providing a source for copper dispersion. The mixed-phase $\text{CuO}/\text{Cu}_y\text{Ce}_{1-y}\text{O}_{2-x}$ catalysts all have

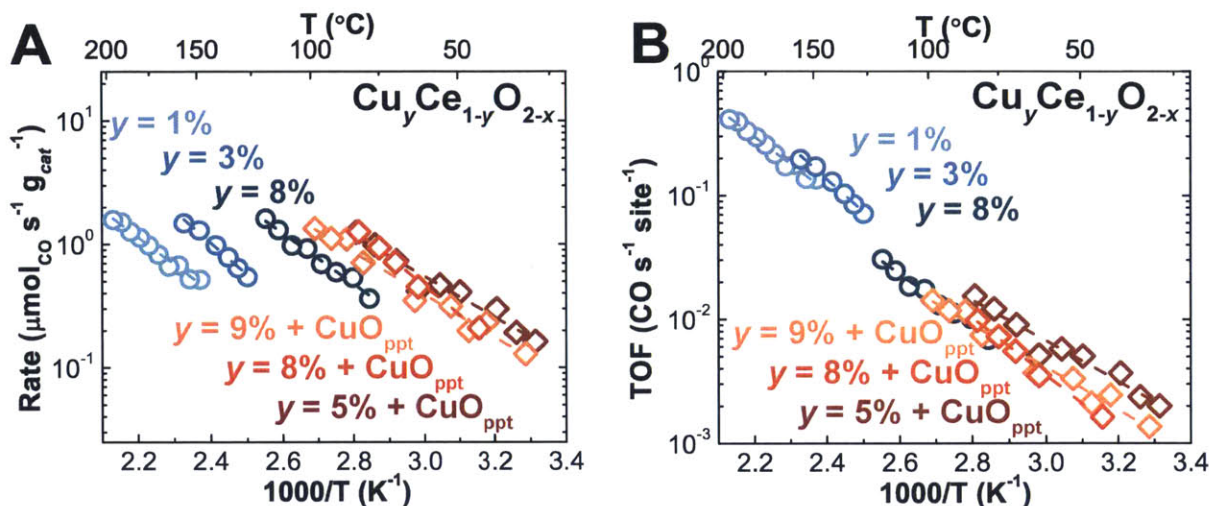


Figure 3.3 Arrhenius plots for CO oxidation over $\text{CuO}/\text{Cu}_y\text{Ce}_{1-y}\text{O}_{2-x}$ (A) normalized by mass and (B) normalized by surface copper site in $\text{Cu}_y\text{Ce}_{1-y}\text{O}_{2-x}$. Rates were measured in 1% CO, 2.5% O_2 balanced in He at a flow rate of $1300 \text{ mL min}^{-1} \text{ g}^{-1}$ and TOFs were estimated assuming homogeneous copper substitution in $\text{Cu}_y\text{Ce}_{1-y}\text{O}_{2-x}$.

significantly higher surface areas than phase-pure $\text{Cu}_y\text{Ce}_{1-y}\text{O}_{2-x}$. We believe this is due to the presence of higher concentrations of oleylamine (or polymers thereof) in the as-synthesized samples. This higher organic content would act as a soft template during the subsequent annealing step, thereby increasing the surface areas of these samples. Moreover, the apparent activation energies found for mass-normalized activities in Figure 3.3A for all the catalysts are comparable (Table 3.1), which suggests that CO oxidation follows the same reaction mechanism on $\text{Cu}_y\text{Ce}_{1-y}\text{O}_{2-x}$ independent of copper content.

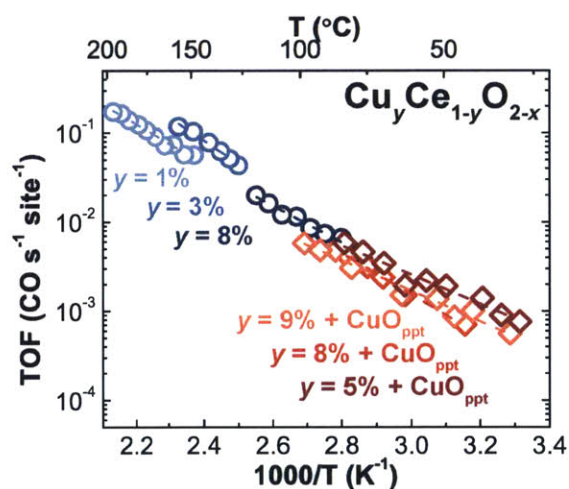


Figure 3.4 Arrhenius plots for CO oxidation over $\text{CuO}/\text{Cu}_y\text{Ce}_{1-y}\text{O}_{2-x}$ normalized by surface copper site in $\text{Cu}_y\text{Ce}_{1-y}\text{O}_{2-x}$ assuming surface segregation of copper. Rates were measured in 1% CO, 2.5% O_2 balanced in He at a flow rate of $1300 \text{ mL min}^{-1} \text{ g}^{-1}$.

3.3 Determination of the Surface Segregation and Speciation of Copper in $\text{Cu}_y\text{Ce}_{1-y}\text{O}_{2-x}$

We propose that the active sites for CO oxidation on the surfaces of $\text{Cu}_y\text{Ce}_{1-y}\text{O}_{2-x}$ nanoparticles are associated with surface oxygen vacancies induced by copper substitution at the surface. In the previous chapter, we hypothesized that Cu segregation on the nanoparticle surface promotes the formation of oxygen vacancies, which is considered central to the catalytic activity of these compounds. Using aberration-corrected STEM-EELS, we show direct evidence of the enrichment of Ce^{3+} on the surface of $\text{Cu}_{0.08}\text{Ce}_{0.92}\text{O}_{2-x}$ nanoparticles, indicative of the presence of oxygen vacancies on the surface. We carefully analyzed the Ce $M_{4,5}$ -edge across individual $\text{Cu}_{0.08}\text{Ce}_{0.92}\text{O}_{2-x}$ crystallites, where we found a high concentration of Ce^{3+} at the nanoparticle surface (Figure 3.5) as evidenced by the appearance of a sharp low-energy feature (Figure 3.5A, 882 eV at the M_5 -edge).

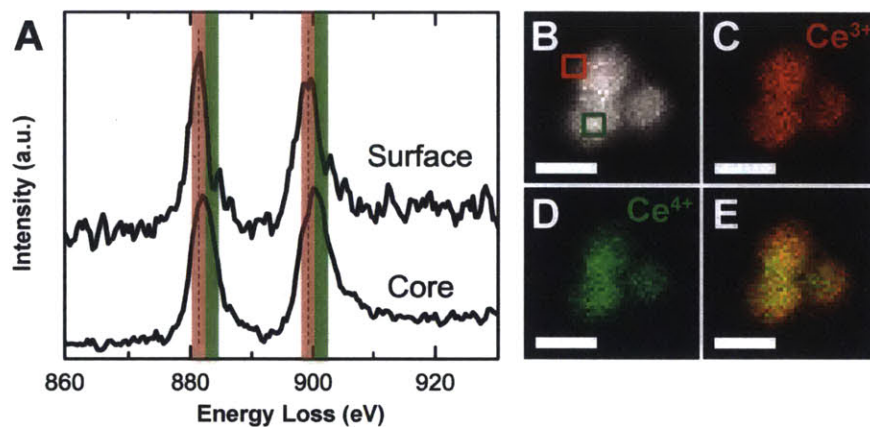


Figure 3.5 STEM-EELS analysis of a cluster of three $\text{Cu}_{0.08}\text{Ce}_{0.92}\text{O}_{2-x}$ nanoparticles. (A) Ce $M_{4,5}$ EELS spectra corresponding to surface and core areas highlighted in (B), (B) Dark field image acquired simultaneously with the spectrum image, (C) map corresponding to the signal in the ranges 880.4–882.4 eV and 898.4–900.4 eV (red windows in (A)), (D) map corresponding to the signal in the ranges 882.4–884.4 eV and 900.4–902.4 eV (green windows in (A)) and (E) sum of (C) and (D); scale bars: 5 nm.

The enrichment of Ce^{3+} on the surface of $\text{Cu}_{0.08}\text{Ce}_{0.92}\text{O}_{2-x}$ particles is correlated to the presence of surface oxygen vacancies. While reduction at surfaces of ceria can occur under the electron beam,¹⁴ and given that unsubstituted, nanoparticulate ceria can have Ce^{3+} -rich surfaces,¹⁵ our observation is in principle consistent with surface copper segregation. The copper ions exist as an admixture of Cu^{2+} and Cu^{3+} from the XAS studies in the previous chapter,¹¹ and may form oxygen vacancies more easily on the surface, which in turn can increase the concentration of Ce^{3+} measured at the surface. This argument is supported by

previous work that shows Sm-rich surfaces in Sm-doped CeO_2 nanoparticles having highly reduced Ce^{3+} ions on the surface.¹⁶ Unfortunately the Cu $L_{2,3}$ -edge, which has a weak cross-section and falls in the tail of the Ce $M_{4,5}$ -edge white lines, could not be used for the quantitative analysis of Cu compositions across individual nanoparticles from the center to surface.

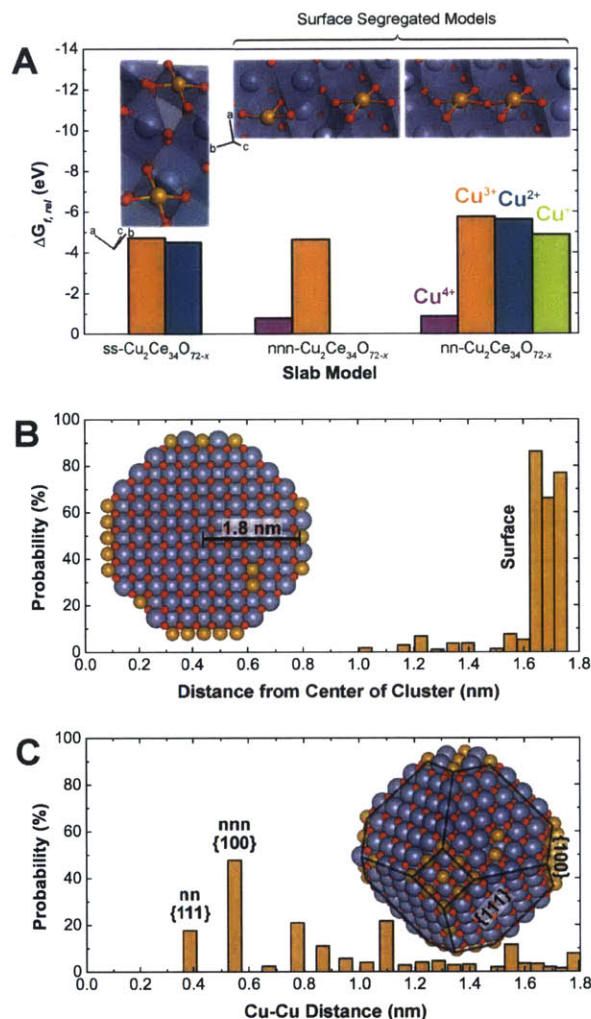


Figure 3.6 Computational modeling of $\text{Cu}_y\text{Ce}_{1-y}\text{O}_{2-x}$ catalysts by DFT + U and artificial neural network potential Monte-Carlo simulations. (A) Relative Gibbs free energy of formation for three $\{111\}$ -terminated $\text{Cu}_2\text{Ce}_{34}\text{O}_{72-x}$ models at various oxidation states, (B) radial probability of Cu substitution and (C) pair distribution function for Cu-Cu distances in 3.6 nm $\text{Cu}_{54}\text{Ce}_{405}\text{O}_{834}$ nanoparticles. Relative values for ΔG_f were calculated at 700 K using the oxygen chemical potential associated with 0.21 atm O_2 ; Monte Carlo calculations were carried out simulating annealing from 5000 to 300 K.

Surface copper segregation is further supported by DFT + U and Artificial Neural Network Potential Monte-Carlo calculations. We investigated the thermodynamic driving force for copper segregation in CeO_2 by performing DFT+ U calculations using three $\{111\}$ -

terminated, 3x3x4 slabs having the stoichiometry $\text{Cu}_2\text{Ce}_{34}\text{O}_{72-x}$, with copper substitution at cerium sites (Figure 3.6A). Three modes of copper substitution were studied to examine different degrees of dispersion of copper in ceria. The solid-solution (ss-) model simulates a homogeneous dispersion throughout the lattice of CeO_2 , while the nearest-neighbor (nn-) and next-nearest-neighbor (nnn-) models simulate surface segregation of copper (Figure 3.6A inset).

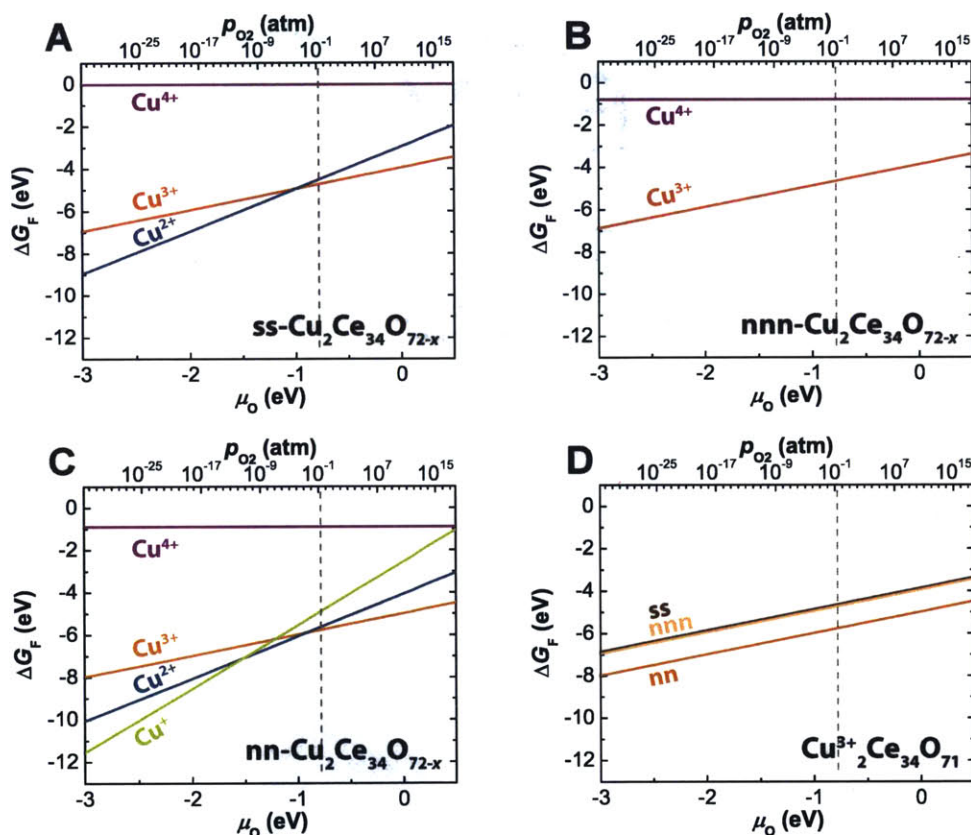


Figure 3.7 DFT + U -calculated phase diagrams for (A) ss-, (B) nnn- and (C) nn- $\text{Cu}_2\text{Ce}_{34}\text{O}_{72-x}$ slab models computed at 700 K. The dashed grey lines correspond to 0.21 atm O_2 (i.e. air). The lowest-energy slabs for each of the three models (D), corresponding to the stoichiometry $\text{Cu}^{3+}_2\text{Ce}_{34}\text{O}_{71}$, are also shown for comparison.

Consistent with our calculations on ‘bulk’ $\text{Cu}_{0.08}\text{Ce}_{0.92}\text{O}_{2-x}$ in Chapter 2, we found Cu^{3+} and Cu^{2+} to be the most thermodynamically stable forms of copper, independent of the mode of substitution (Figure 3.7) under oxygen-rich conditions. Corroborating this, we found no experimental evidence, by means of *in-situ* XAS, for the presence of Cu^+ in $\text{Cu}_{0.08}\text{Ce}_{0.92}\text{O}_{2-x}$ in air or under our experimental, oxygen-rich conditions, even at 300 °C (Figure 3.8). While we cannot rule out the presence of Cu^+ under *oxygen-lean* conditions ($< 10^{-10}$ atm O_2 according to Figure 3.7), these data suggest that copper exists as an admixture of Cu^{3+} and

Cu^{2+} under the catalytic conditions of Figure 3.3. We should also note that these studies do not necessarily negate the existence of a very small number ($< 5\%$ of all copper sites) of Cu^+ or Cu^0 species, below the detection limit of XAFS, that might be responsible for CO oxidation catalysis.

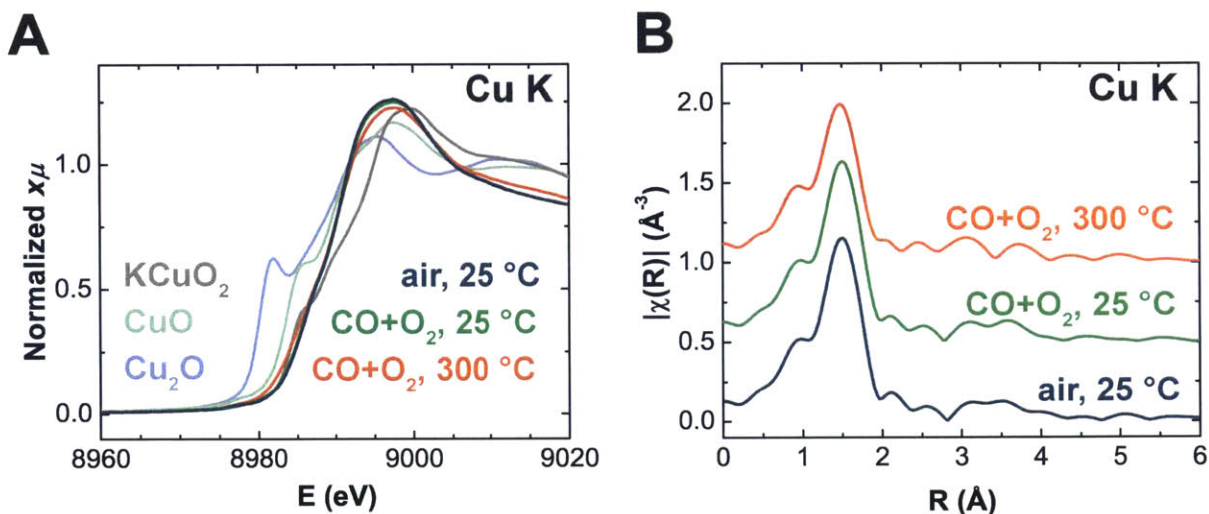


Figure 3.8 Cu K-edge XAS measurements of $\text{Cu}_{0.08}\text{Ce}_{0.92}\text{O}_{2-x}$ performed under reaction conditions; (A) near-edge spectra and (B) the Fourier transform of the EXAFS in air at 25 °C (blue traces), in 1% CO + 2.5% O_2 at 25 °C (green traces) and in 1% CO + 2.5% O_2 at 300 °C (orange traces). Measurements were performed in fluorescent yield mode. When calibrated to the copper oxide references in (A), the mean oxidation states were determined to be 2.86+ (air at 25 °C), 2.85+ (1% CO + 2.5% O_2 at 25 °C) and 2.81+ (1% CO + 2.5% O_2 at 300 °C).

Regardless of copper oxidation state, copper segregation in the nn- $\text{Cu}_2\text{Ce}_{34}\text{O}_{72-x}$ structure is consistently 1 eV more stable than ss- $\text{Cu}_2\text{Ce}_{34}\text{O}_{72-x}$, as shown in Figure 3.6A and Figure 3.7. Interestingly, the Gibbs free energy of formation for nn- $\text{Cu}^{3+}_2\text{Ce}_{34}\text{O}_{71}$, which we found to be the most stable structure of all investigated, is 1 eV more stable than the related nnn- $\text{Cu}^{3+}_2\text{Ce}_{34}\text{O}_{71}$ structure. These calculations suggest that upon segregation to the surface, it is energetically favorable for copper to aggregate to form copper-segregated regions of the $\text{Cu}_y\text{Ce}_{1-y}\text{O}_{2-x}$ surface that are distinct from CuO . In each case, copper ions relax towards the (100) plane of oxygen atoms to accommodate a square-planar coordination environment with the oxygen ligands; this manifests as a reconstruction of the $\{111\}$ surface to include (100) terraces with these square-planar copper motifs (Figure 3.6A inset).

We further examined how the copper ions are distributed within an entire nanoparticle by employing Monte-Carlo simulations of entire 3.6 nm $\text{Cu}_{54}\text{Ce}_{405}\text{O}_{834}$ nanoparticles using artificial neural network (ANN) potentials trained to DFT reference energies (Figure 3.11

and Tables 3.4 and 3.5).^{17,18} Consistent with our slab studies, copper prefers to sit at the surface of the nanoparticle (at distances 1.6 to 1.8 nm from the center) and very little is found in the subsurface or deeper layers (1.0 to 1.6 nm from center, Figure 3.6B). In addition, these simulations confirm that copper ions associate to form O^{2-} -bridged clusters (Figure 3.6C), which manifest as nearest neighbor interactions on $\{111\}$ and next nearest neighbor interactions on $\{100\}$, accounting for over 70% of the pair distribution function. It is noteworthy that the copper prefers to associate on the higher-energy $\{100\}$ and $\{100\}/\{111\}$ edge sites (Figure 3.6C inset), which requires further examination, but is generally consistent with single-crystal adsorption calorimetry studies of copper adsorption on CeO_2 (111).¹⁹ These studies found that copper preferentially adsorbs to step edges rather than (111) terraces. This preference might be attributed to a lower penalty for the formation of oxygen vacancies on the $\{100\}$ surfaces, which is supported by the fact that such preferential reduction of Ce^{4+} to Ce^{3+} on $\{100\}$ vs $\{111\}$ facets has been observed on ceria nanocrystals.¹⁴ This preferential reduction on $\{100\}$ facets was also observed experimentally in our STEM-EELS measurements of $Mn_{0.1}Ce_{0.9}O_{2-x}$ nanoparticles (Figure 3.9).

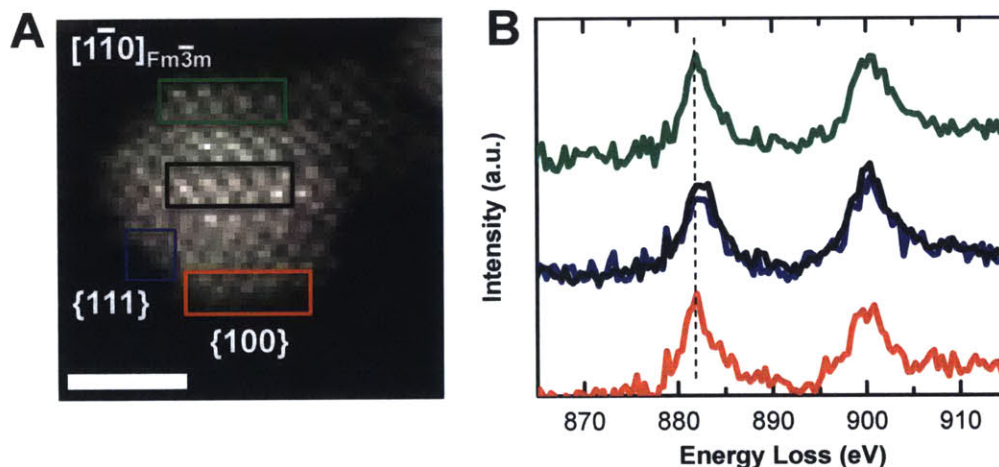


Figure 3.9 STEM-EELS analysis of an individual $Mn_{0.1}Ce_{0.9}O_{2-x}$ nanoparticle. (A) Dark field image acquired simultaneously with the spectrum images (scale bar: 2 nm), (B) Ce $M_{4,5}$ -edge spectra corresponding to the boxed regions in A. The dotted line in B refers to the peak at 882 eV ascribed to Ce^{3+} .

These calculations verify our chemical intuition that we expect copper substitution to be inhomogeneous in $Cu_yCe_{1-y}O_{2-x}$. Since Figure 3.3B assumes that copper substitution is homogeneous throughout the ceria lattice, this plot likely overestimates the TOF since copper

segregates to the surface. If, on the other hand, we assume surface copper segregation, we expect there to be more catalytically-active sites on the surface, hence an overall smaller TOF (see Section 3.5, Experimental Methods). According to this inhomogeneous substitution model, the TOFs reported in Figure 3.3B should be scaled by a factor of

$$\frac{n_{\text{Cu, homogeneous}}}{n_{\text{Cu, surface segregation}}} = \frac{(6 + 12\sqrt{3}) \cdot PD_{111}}{8\sqrt{2}a \left(\frac{Z}{V_{\text{cell}}} \right)}$$

where PD_{111} is the planar density of cerium atoms on the $\{111\}$ surface, a is the edge length of the truncated octahedron ($d \approx 3a$), Z is the number of cerium atoms per unit cell of CeO_2 and V_{cell} is the volume of the unit cell. Since the crystallite size of $\text{Cu}_y\text{Ce}_{1-y}\text{O}_{2-x}$ doesn't change drastically between the samples, the correction varies only moderately (0.4 – 0.6) among the samples measured for CO oxidation catalysis (Table 3.1). Applying these corrections to the TOFs in Figure 3.3B gives an Arrhenius plot assuming inhomogeneous substitution (Figure 3.4), which is consistent with our hypothesis that dispersed surface copper sites in $\text{Cu}_y\text{Ce}_{1-y}\text{O}_{2-x}$ are the active sites for catalysis.

These calculations shed light on what structural features might be present for the catalytically-active copper sites. They suggest that site-isolated, square-planar copper centers, stabilized in the Cu^{3+} oxidation state on (100) terraces, are responsible for the catalytic rate enhancement for CO oxidation we see in Figure 3.3, which can be used for the design of highly active catalysts for CO oxidation.

3.4 Conclusions

In this chapter, we show that the mass activity of CO oxidation increases with copper content in both single-phase $\text{Cu}_y\text{Ce}_{1-y}\text{O}_{2-x}$ and two-phase-mixtures $\text{CuO}/\text{Cu}_y\text{Ce}_{1-y}\text{O}_{2-x}$, while the TOFs are comparable, independent of copper content. This observation indicates that CO oxidation is catalyzed directly by dispersed copper ions in the $\text{Cu}_y\text{Ce}_{1-y}\text{O}_{2-x}$ phase, not by bulk CuO or its interface with $\text{Cu}_y\text{Ce}_{1-y}\text{O}_{2-x}$, as reported previously.^{2,8,9} Supported by DFT + U calculations, *in-situ* XAS reveals that the surface-substituted copper ions remain as Cu^{3+} and Cu^{2+} under oxygen-rich conditions, even at elevated temperatures. While these observations suggest that Cu^{3+} and Cu^{2+} in $\text{Cu}_y\text{Ce}_{1-y}\text{O}_{2-x}$ are the active sites, we cannot rule out the possibility of the existence of a very small number (<5%) of undetectable Cu^+ species that could be responsible for CO oxidation catalysis.^{20,21} We propose that the active sites for

CO oxidation are associated with surface oxygen vacancies induced by copper segregation. Aberration-corrected STEM-EELS shows direct evidence of an enrichment of Ce^{3+} sites on the surface of $\text{Cu}_{0.08}\text{Ce}_{0.92}\text{O}_{2-x}$ nanoparticles, which is consistent with surface segregation. A thorough computational treatment of the local structure and distribution of copper in $\text{Cu}_{0.1}\text{Ce}_{0.9}\text{O}_{2-x}$ nanoparticles supports copper segregation on the $\{100\}$ and, to a lesser extent, on the $\{111\}$ surfaces. These results have important consequences for practical and fundamental aspects of CO oxidation catalysis. In the following two chapters, we will interrogate the mechanism of CO oxidation on these compounds to provide an atomic-level description of the active site during catalysis and to establish reliable descriptors for the rational design of the next generation of catalysts.

3.5 Experimental Methods

General experimental considerations. All reagents were obtained from commercial vendors and were used without further purification. All reactions were performed under ambient conditions unless otherwise noted. The precursor compounds **$\text{Cu}^{\text{II}}\text{-3-MeO-salpn}$** , **$\text{Ce}^{\text{III}}\text{-3-MeO-salpn}$** and **$\text{Cu}^{\text{II}}\text{-Ce}^{\text{III}}\text{-3-MeO-salpn}$** were prepared according to the procedure outlined in Chapter 2.

General procedure for the preparation of single-phase $\text{Cu}_y\text{Ce}_{1-y}\text{O}_{2-x}$ nanoparticles. Single-phase nanoparticles with the stoichiometry $\text{Cu}_y\text{Ce}_{1-y}\text{O}_{2-x}$ for $y = 1, 3, 8\%$ were prepared according to the procedure outlined in Chapter 2. Appropriate amounts, not exceeding 1.0 mmol total, of the parent **$\text{Ce}^{\text{III}}\text{-3-MeO-salpn}$** and **$\text{Cu}^{\text{II}}\text{-Ce}^{\text{III}}\text{-3-MeO-salpn}$** complexes were heated with magnetic stirring in 40 mL oleylamine at 180 °C under an Ar flow for 4 hours in a three-neck flask equipped with a reflux condenser and bump trap. The resulting dark brown solutions were divided into eight 5 mL fractions, flocculated with ethanol (40 mL each) and the flocculant was isolated by centrifugation (7100 rpm for 15 min). The flocculant was then redissolved in hexanes (5 mL each) and bulk precipitates were removed by centrifugation (5000 rpm for 1 min) and decanting of the dark brown hexanes solutions. This process was repeated once to give dark-brown hexanes solutions of phase-pure $\text{Cu}_y\text{Ce}_{1-y}\text{O}_{2-x}$.

To remove the organic capping layer for catalysis and further characterization, as-prepared solutions of $\text{Cu}_y\text{Ce}_{1-y}\text{O}_{2-x}$ were dropcast into alumina crucibles and annealed at 400 °C in synthetic air for 4 hrs to give phase-pure, free-flowing powders of $\text{Cu}_y\text{Ce}_{1-y}\text{O}_{2-x}$.

Synthesis of $Cu_{0.01}Ce_{0.99}O_{2-x}$ nanoparticles. $Cu_{0.01}Ce_{0.99}O_{2-x}$ was prepared from the pyrolysis of **Ce^{III} -3-MeO-salpn** (0.633 g, 0.947 mmol) and **Cu^{II} - Ce^{III} -3-MeO-salpn** (0.038 g, 0.052 mmol) in 40 mL oleylamine (*vide supra*) to give $Cu_{0.01}Ce_{0.99}O_{2-x}$ as a pale khaki powder after annealing (0.091 g, 0.53 mmol, 53%).

Synthesis of $Cu_{0.03}Ce_{0.97}O_{2-x}$ nanoparticles. $Cu_{0.03}Ce_{0.97}O_{2-x}$ was prepared from the pyrolysis of **Ce^{III} -3-MeO-salpn** (0.501 g, 0.749 mmol) and **Cu^{II} - Ce^{III} -3-MeO-salpn** (0.183 g, 0.250 mmol) in 40 mL oleylamine (*vide supra*) to give $Cu_{0.03}Ce_{0.97}O_{2-x}$ as a khaki powder after annealing (0.040 g, 0.24 mmol, 24%).

Synthesis of $Cu_{0.08}Ce_{0.92}O_{2-x}$ nanoparticles. $Cu_{0.08}Ce_{0.92}O_{2-x}$ was prepared from the pyrolysis of **Ce^{III} -3-MeO-salpn** (0.223 g, 0.333 mmol) and **Cu^{II} - Ce^{III} -3-MeO-salpn** (0.487 g, 0.667 mmol) in 40 mL oleylamine (*vide supra*) to give $Cu_{0.08}Ce_{0.92}O_{2-x}$ as a dark khaki powder after annealing (0.127 g, 0.675 mmol, 76.5%).

General procedure for the preparation of $CuO/Cu_yCe_{1-y}O_{2-x}$. Mixed-phase $CuO/Cu_yCe_{1-y}O_{2-x}$ materials were prepared under conditions similar to the preparation of single-phase $Cu_yCe_{1-y}O_{2-x}$ described above but with notable differences; the reaction was carried out in air and with excess **Cu^{II} -3-MeO-salpn** precursor. Appropriate amounts of **Cu^{II} - Ce^{III} -3-MeO-salpn** and **Cu^{II} -3-MeO-salpn** were heated with magnetic stirring in 40 mL oleylamine at 180 °C in air for 4 hours in a three-neck flask equipped with a reflux condenser and bump trap. The resulting dark-brown solutions were worked up with ethanol and hexanes as described above for $Cu_yCe_{1-y}O_{2-x}$, dropcast into alumina crucibles and annealed in air at 400 °C for 4 hours to give free-flowing powders of $CuO/Cu_yCe_{1-y}O_{2-x}$.

Synthesis of $CuO/Cu_{0.05}Ce_{0.95}O_{2-x}$ nanoparticles. $CuO/Cu_{0.05}Ce_{0.95}O_{2-x}$ was prepared from the pyrolysis of **Cu^{II} -3-MeO-salpn** (0.807 g, 2.00 mmol) and **Cu^{II} - Ce^{III} -3-MeO-salpn** (0.730 g, 1.00 mmol) in 40 mL oleylamine (*vide supra*) to give $CuO/Cu_{0.05}Ce_{0.95}O_{2-x}$ as an olive powder after annealing (0.119 g).

Synthesis of $CuO/Cu_{0.08}Ce_{0.92}O_{2-x}$ nanoparticles. $CuO/Cu_{0.08}Ce_{0.92}O_{2-x}$ was prepared from the pyrolysis of **Cu^{II} -3-MeO-salpn** (0.332 g, 0.822 mmol) and **Cu^{II} - Ce^{III} -3-MeO-salpn** (0.730 g, 1.00 mmol) in 40 mL oleylamine (*vide supra*) to give $CuO/Cu_{0.08}Ce_{0.92}O_{2-x}$ as an olive powder after annealing (0.050 g).

Synthesis of $CuO/Cu_{0.09}Ce_{0.91}O_{2-x}$ nanoparticles. $CuO/Cu_{0.09}Ce_{0.91}O_{2-x}$ was prepared from the pyrolysis of **Cu^{II} -3-MeO-salpn** (0.167 g, 0.413 mmol) and **Cu^{II} - Ce^{III} -3-MeO-**

salpn (0.730 g, 1.00 mmol) in 40 mL oleylamine (*vide supra*) to give CuO/Cu_{0.09}Ce_{0.91}O_{2-x} as an olive powder after annealing (0.078 g).

Powder X-ray diffraction (PXRD). Powder X-ray diffraction patterns were collected on a PANalytical X'Pert PRO diffractometer using Bragg-Brentano geometry and nickel-filtered Cu-K_α radiation ($\lambda = 1.54056 \text{ \AA}$). Samples were prepared using 0.2 mm deep zero-background sample wells composed of boron-doped, *p*-type silicon from MTI Corporation. Powder profiles were fit with pseudo-Voigt functions using the FullProf suite.²² In each case, the crystallite sizes (*d*) of the Cu_yCe_{1-y}O_{2-x} phase were estimated using the Scherrer equation to the fitted (220) peak assuming a shape factor *K* of 0.94 for spherical crystallites of cubic symmetry, after accounting for instrumental line broadening. The crystallite sizes thus obtained were used to estimate the turnover frequencies assuming surface segregation of copper sites (*vide infra*).

Table 3.1 Apparent activation energies (E_A) for CO oxidation on CuO/Cu_yCe_{1-y}O_{2-x} powders, their BET surface areas, (A_S) and crystallographic parameters for the Cu_yCe_{1-y}O_{2-x} phase. Standard uncertainties in the last digits are included in parentheses.

Compound	E_A (kJ mol ⁻¹)	A_S (m ² g ⁻¹)	a (Å)	$d_{(220)}$ (Å)	R factors (%)	χ^2	$n_{homog}/$ $n_{surf. seg.}$	y (EDS)
CuO/Cu _{0.05} Ce _{0.95} O _{2-x}	31	114	5.4143(2)	59.0	1.55, 1.97	1.16	0.38	0.054(6)
CuO/Cu _{0.08} Ce _{0.92} O _{2-x}	44	119	5.4159(6)	52.0	1.94, 2.66	2.01	0.43	0.08(3)
CuO/Cu _{0.09} Ce _{0.91} O _{2-x}	33	78	5.4145(1)	54.7	2.45, 3.19	2.24	0.41	0.09(1)
Cu _{0.08} Ce _{0.92} O _{2-x}	40	52	5.420(3)	33.8	2.15, 2.80	1.23	0.66	0.08(1)
Cu _{0.03} Ce _{0.97} O _{2-x}	50	17	5.426(4)	36.6	2.25, 2.84	1.28	0.61	0.034(7)
Cu _{0.01} Ce _{0.99} O _{2-x}	42	29	5.4156(6)	52.8	2.16, 2.79	1.17	0.42	0.010(2)

Table 3.2 Crystallographic parameters for the CuO phase in CuO/Cu_yCe_{1-y}O_{2-x} powders. Standard uncertainties in the last digits are included in parentheses.

Compound	a (Å)	b (Å)	c (Å)	β (°)	$d_{Scherrer (111)}$ (Å)
CuO/Cu _{0.05} Ce _{0.95} O _{2-x}	4.6836(3)	3.4341(3)	5.1338(4)	99.360(4)	274.5
CuO/Cu _{0.08} Ce _{0.92} O _{2-x}	4.693(1)	3.435(1)	5.129(2)	99.34(2)	152.1
CuO/Cu _{0.09} Ce _{0.91} O _{2-x}	4.646(4)	3.439(2)	5.146(4)	99.31(3)	115.5

Transmission electron microscopy (TEM). Samples studied by transmission electron microscopy were prepared by dropcasting dilute ethanol suspensions of annealed (CuO)/Cu_yCe_{1-y}O_{2-x} onto lacey carbon gold TEM grids. Bright field images were acquired at 200 keV using a low-background beryllium sample holder on a JEOL 2010-FEG

transmission electron microscope at MIT, which is equipped with a field-emission electron gun and an ultra-high resolution pole piece, resulting in a point-to-point resolution of 1.9 Å. Fast Fourier transforms (FFTs) were implemented using the ImageJ software.²³ For the acquisition of bright-field images, care was taken to prevent beam-induced reconstruction of individual nanocrystals by minimizing the duration of beam exposure. Energy dispersive X-ray spectroscopy (EDS) was performed in scanning transmission mode using a 1 nm diameter electron beam. Quantification was carried out by using a simple ratio technique in INCA (Oxford Instruments), which accounts for X-ray absorption and thickness effects. Nevertheless, the thickness parameter used in quantification was varied to determine if the inconsistent apparent thicknesses of the samples contribute to the inconsistencies in the copper quantification. For all samples measured, we saw no significant change in copper content, suggesting that X-ray absorption is minimal in these samples. Copper substitution was quantified for the $\text{Cu}_y\text{Ce}_{1-y}\text{O}_{2-x}$ phase only by judicious choice of probe position; CuO phases were avoided by differentiating them by image contrast.

Electron Energy Loss Spectroscopy (performed by Dr. Matthieu Bugnet, McMaster University). $\text{Cu}_{0.1}\text{Ce}_{0.9}\text{O}_{2-x}$ and $\text{Mn}_{0.1}\text{Ce}_{0.9}\text{O}_{2-x}$ samples were prepared by diluting annealed nanoparticle powders in HPLC grade methanol, ultrasonicated and dropcasting onto Si_3N_4 window grids (Norcada Inc.). Experiments were carried out on a FEI Titan cubed (80-300) (S)TEM at McMaster University, equipped with aberration correctors of the probe and image forming lenses and a high resolution GIF Quantum spectrometer. The microscope was operated at 80 kV in STEM mode and the spectrum images were recorded with a collection angle of ~55 mrad and a current below 40 pA to minimize beam damage.

Raman Spectroscopy. Raman spectra were acquired at room temperature on a LabRAM HR800 microscope (Horiba Jobin Yvon) using an external 17 mW HeNe 632.8 nm laser (Melles Griot) focused with a 50× objective lens and a 25% filter. A silicon substrate was used to calibrate the Raman shift. The sampling time and range were identical for all spectra ($100\text{-}1000\text{ cm}^{-1}$, $5 \times 10\text{ s}$) using a 600 mm^{-1} grating.

X-ray absorption spectroscopy (XAS). X-ray absorption measurements at the copper K-edge were performed at the bending magnet station X11A of the National Synchrotron Light Source (NSLS) at Brookhaven National Laboratory.²⁴ The electron storage ring operated at 2.8 GeV with a stored current in the range of 200 – 300 mA. The excitation

energies were selected with a double crystal monochromator (Si-(111)), which was detuned by 40% to suppress higher harmonics. The incident and transmitted beams were monitored using ionization chambers equilibrated with appropriate mixtures of nitrogen and argon gas. The energy calibration of the monochromator was set by calibrating the inflection point of the absorption spectrum of transition-metal foils to their literature values.²⁵

Copper K-edge spectra were acquired in fluorescence yield (FY) mode using a resistively-heated *in-situ* catalyst furnace equipped with a 5-grid Lytle fluorescence detector²⁶ (both from the EXAFS Company). For FY measurements, the signal passed through a silver Soller slit assembly prior to detection by the ionization chamber, which had a continuous flow of Ar. The pellet for *in-situ* studies was prepared by first sieving Cu_{0.08}Ce_{0.92}O_{2-x} (10.5 wt%), boron nitride (75.5 wt%) and high-surface area Vulcan XC-72 carbon (14 wt%, Cabot) to 400 mesh followed by thorough mixing and grinding with an agate mortar and pestle. A 50 mg pellet (5 mm x 12 mm) was pressed and introduced into the catalyst furnace, the window of which was sealed with Kapton tape. Gas mixtures (CO and O₂ balanced in He) were flowed through the catalyst pellet by means of mass-flow controllers at a total flow-rate of 50 mL min⁻¹. The pellet was slowly heated to 300 °C under lean conditions (0.01 atm CO and 0.025 atm O₂ at a flow rate of 50 mL min⁻¹) and gases were allowed to equilibrate for 15 minutes before the acquisition of XAFS spectra.

Absorption spectra were normalized using the Autobk algorithm found in the IFEFFIT program²⁷ of the Horae XAFS analysis suite.²⁸ First, a linear fit of the pre-edge line was subtracted from the spectrum. A fourth-order knot-spline polynomial was used to fit the post-edge line and the edge step was normalized to unity. Prior to Fourier transforms, the EXAFS was multiplied by a Hanning window covering the first and last ~10% of the data range, from $k = 3.7$ to 11.1 \AA^{-1} .

EXAFS for CuO was fit, freely refining σ_i^2 and an isotropic lattice expansion coefficient α (taking into account the expansion/contraction of the lattice by $\Delta R_j = R_{eff, j} \cdot \alpha$) while constraining N_i to the crystallographic values. Values obtained for $\sigma_{\text{Cu-O}}^2$ were set in the subsequent fitting of the room temperature K-edge spectra for Cu_{0.1}Ce_{0.9}O_{2-x}, while refining the path degeneracy $N_{\text{Cu-O}}$ and $N_{\text{Cu-Cu}}$ for the first two coordination shells (Cu-O bonds in the oxide phase and Cu-Cu distances corresponding to metallic copper). The refinement was performed in R space from $R = 1$ to 3 \AA simultaneously with k -weights of 1, 2 and 3.

The model for fitting the copper K-edge EXAFS spectra of $\text{Cu}_{0.1}\text{Ce}_{0.9}\text{O}_{2-x}$ at room temperature was modified from the one described in Chapter 2 to take into account the presence of two separate phases contributing to the EXAFS, metallic copper and copper oxide clusters. First, EXAFS for copper foil was fit, freely refining $\sigma_{\text{Cu-Cu}}^2$ and an isotropic lattice expansion coefficient α while constraining N_i to the crystallographic values. Values obtained for $\sigma_{\text{Cu-Cu}}^2$ for copper foil were set as a constraint in the subsequent fitting of the room temperature K-edge spectra for $\text{Cu}_{0.1}\text{Ce}_{0.9}\text{O}_{2-x}$, while refining the path degeneracies ($N_{\text{Cu-O}}$ and $N_{\text{Cu-Cu}}$) and shared values for bond lengths ($R_{\text{Cu-O}}$ and $R_{\text{Cu-Cu}}$) for the first coordination shell (Cu-O bonds in the oxide phase and Cu-Cu distances corresponding to metallic copper) and a common value of $\sigma_{\text{Cu-O}}^2$ simultaneously for both room temperature spectra. The refinement was performed in R space from $R = 1$ to 3 \AA simultaneously with k -weights of 1, 2 and 3. The spectrum at $300 \text{ }^\circ\text{C}$ was fit in a similar way, simultaneously with six other spectra at $300 \text{ }^\circ\text{C}$, this time freely refining the σ_i^2 value for the metallic copper component (see Section 4.7 for further details).

Table 3.3 Parameters from the refinement of Cu K-edge EXAFS of $\text{Cu}_{0.1}\text{Ce}_{0.9}\text{O}_{2-x}$ powders under catalytically-relevant conditions at room temperature and $300 \text{ }^\circ\text{C}$. Standard uncertainties in the last digits are included in parentheses.

Condition	S_0^{2a}	E_0	$N_{\text{Cu-O}}$	$\sigma_{\text{Cu-O}}^b$ (\AA^2)	$R_{\text{Cu-O}}$ (\AA)	$N_{\text{Cu-Cu}}$	$\sigma_{\text{Cu-Cu}}^b$ (\AA^2)	$R_{\text{Cu-Cu}}$ (\AA)	R factor (%)
rt, air	0.90	-2(1)	3.7(3)	0.005(1)	1.933(7)	0.1(1)	0.0085	2.41(6)	0.55
rt, 1% CO + 2.5% O ₂	0.90	-2(1)	3.6(4)	0.005(1)	1.933(7)	0.2(2)	0.0085	2.41(6)	0.55
300 °C, 1% CO + 2.5% O ₂	0.90	-5(1)	3.5(3)	0.0065(9)	1.902(8)	0.3(3)	0.014(2)	2.467(8)	0.88

Single-point BET surface area determination. Values for the surface areas of annealed (CuO)/ $\text{Cu}_y\text{Ce}_{1-y}\text{O}_{2-x}$ powders were estimated from single-point BET measurements from desorption of N_2 at room temperature (after adsorption at 77 K in 30% N_2/He) using a ChemBET Pulsar apparatus (Quantachrome). For the calculation of the turnover frequency (TOF) in mixed phase $\text{CuO}/\text{Cu}_y\text{Ce}_{1-y}\text{O}_{2-x}$ powders, it was assumed in that the measured BET surface area was attributed to the $\text{Cu}_y\text{Ce}_{1-y}\text{O}_{2-x}$ phase since the crystallite size is significantly smaller than CuO by TEM and PXRD.

^a The passive electron amplitude reduction factors S_0^2 were determined from the fitting of the EXAFS of the appropriate reference foils.

^b MSDs were determined from fitting the EXAFS of binary oxide references: Fe_2O_3 , Co_3O_4 , NiO and CuO.

CO oxidation catalysis. CO oxidation kinetic measurements were acquired in a home-made 3.81 mm i.d. quartz plug-flow reactor. For each measurement, the annealed catalyst powder (20 mg) was mixed with 1.705 g oven-dried sand ($V_{\text{bed}} = 1.086 \text{ cm}^3$) and was then loaded into center of the reactor, filling the remaining volume with sand. The temperature of the catalyst was recorded using a K-type thermocouple inserted into the catalyst bed. The compositions of the feed and down-stream gases were recorded by on-line gas chromatography (Agilent 490 supplied with a molecular sieve COX column and a thermal conductivity reactor), recording every 5 °C. The percent conversion was calculated according to

$$\% \text{ Conversion} = \frac{p_{\text{CO}_2}}{p_{\text{CO}} + p_{\text{CO}_2}} \cdot 100\%$$

where p_{CO_2} and p_{CO} , the partial pressures of CO_2 and CO , respectively, are determined directly from the relative peak area of the CO_2 and CO peaks normalized to the internal He standard. Prior to and following each catalytic test, the flow rate of the gas upstream was measured directly with a bubble flowmeter and the percent conversion below 12.5% was converted to mass-normalized rates of CO oxidation (in units of $\mu\text{mol CO s}^{-1}\text{g}_{\text{cat}}^{-1}$) for the Arrhenius plots according to

$$\begin{aligned} r_{\text{mass}} &= \frac{\frac{\% \text{ Conversion}}{100} r_{\text{CO}} \cdot 1000}{V_m \cdot 60 \cdot m_{\text{cat}}} \\ &= \frac{\% \text{ Conversion} \cdot r_{\text{CO}}}{6 \cdot V_m \cdot m_{\text{cat}}} \end{aligned}$$

where r_{CO} is the volumetric flow rate of CO of the feed stream (in mL min^{-1}), V_m is the molar volume of a gas (from the ideal gas law, $V_m = RT/p$, in mol/L) and m_{cat} is the mass of the loaded catalyst in grams. The specific (area-normalized) rates for CO oxidation (in units of $\text{mol CO s}^{-1}\text{m}_{\text{cat}}^{-2}$) were thus calculated according to

$$r_{\text{area}} = \frac{r_{\text{mass}}}{A_S} \cdot 10^{-6}$$

where A_S is the surface area of the catalyst (in m^2g^{-1}) as measured by BET (*vide supra*). Finally, the turnover frequency (TOF) as reported in Figure 3.3B was estimated according to the formula

$$TOF = \frac{r_{area} \cdot N_A}{PD_{111} \cdot y}$$

where N_A is Avogadro's number, PD_{111} is the planar density of cerium atoms in the {111} plane of CeO_2 (in units of atoms m^{-2}) and y is the amount of copper ions substituted into the $Cu_yCe_{1-y}O_{2-x}$ phase as determined by STEM-EDS. The planar density of the {111} facet was used in the calculation of the TOF because (a) it was found by HRTEM to be the most predominant crystallographic termination in individual $Cu_yCe_{1-y}O_{2-x}$ nanoparticles (the other being {100}),¹¹ and (b) PD_{111} is only 15.5% larger than PD_{100} ($7.89 \cdot 10^{18}$ Ce m^{-2} and $6.83 \cdot 10^{18}$ Ce m^{-2} , respectively) and hence likely *underestimates* the actual TOF.

This calculation assumes homogeneous copper substitution into the CeO_2 lattice and, according to the discussion in the main text, is thus likely *overestimating* the actual TOF because copper segregates to the surface. To take surface segregation into account, we can estimate a correction factor to the TOF reported above based on the geometry and crystal structure of a representative nanoparticle

$$\frac{n_{Cu, homogeneous}}{n_{Cu, surface segregation}} = \frac{A_{S, np} \cdot PD_{111} \cdot y}{V_{np} \cdot \left(\frac{Z}{V_{cell}}\right) \cdot y}$$

where $n_{Cu, surface segregation}$ is the number of copper sites that segregate to the surface, which, for our purposes, we assume to be all of the copper sites in the nanoparticle. $n_{Cu, homogeneous}$ is the total number of copper sites at the surface of an individual nanoparticle assuming that copper is distributed evenly within the ceria lattice. Here, V_{np} and $A_{S, np}$ are the volume and surface area of the nanoparticle, respectively and Z is the number of cerium atoms in the unit cell of CeO_2 (which has a volume of V_{cell}). In the case of $Cu_yCe_{1-y}O_{2-x}$, we have established that the crystal habit is a truncated octahedron, which has a known volume and surface area:

$$\frac{n_{Cu, homogeneous}}{n_{Cu, surface segregation}} = \frac{(6 + 12\sqrt{3})a^2 \cdot PD_{111}}{8\sqrt{2}a^3 \cdot \left(\frac{Z}{V_{cell}}\right)}$$

$$= \frac{(6 + 12\sqrt{3}) \cdot PD_{111}}{8\sqrt{2}a \cdot \left(\frac{Z}{V_{cell}}\right)}$$

where a is the edge length of the truncated octahedron. In the previous chapter, we found the diameter of annealed $\text{Cu}_{0.08}\text{Ce}_{0.92}\text{O}_{2-x}$ to be 36 Å from Scherrer analysis of the X-ray powder diffraction patterns, which is consistent with our HRTEM results here. If we define the diameter of a truncated octahedron as $3a$ and use crystallographic parameters for CeO_2 ($Z = 4$, $V_{cell} = 158.46 \text{ Å}^3$), this correction is ~ 0.62 , which is within the scatter of the kinetic measurements summarized in Figure 3.3B. Nevertheless, these corrections are tabulated in Table 3.1 and are used as the basis for the estimation of the turnover frequencies (assuming *surface segregation* of copper sites) summarized in Figure 3.4. Although the turnover frequencies for the catalysts studied here do decrease assuming surface segregation of copper sites, this decrease is systematic. The turnover frequencies for the different catalysts are identical within the scatter of the measurement.

DFT + U slab studies of {111}-terminated $\text{Cu}_2\text{Ce}_{34}\text{O}_{72-x}$. Plane-wave basis set spin-polarized DFT + U calculations were executed employing the exchange and correlation energy functional expressed in the Perdew-Burk-Ernzerhof (PBE) generalized gradient approximation (GGA)²⁹⁻³² using projector-augmented wave (PAW) pseudopotentials.^{33,34} All calculations were performed within the Vienna Ab Initio Simulation Package (VASP) suite³⁴⁻³⁸ using either the Cray XE6 (“Hopper”) or Cray XC30 (“Edison”) supercomputers at the National Energy Research Scientific Computing Center (NERSC).

A 3x3x4 hexagonal slab model of the CeO_2 (111) surface ($\text{Ce}_{36}\text{O}_{72}$) was used as the starting point for models of the $\text{Cu}_y\text{Ce}_{1-y}\text{O}_{2-x}$ catalyst, separated by 15 Å of vacuum to prevent interactions between slabs. To simulate copper substitution, two copper atoms were placed in cerium vacancies ($\text{Cu}_{\text{Ce}}^{\times}$ in Kröger-Vink notation) in the parent $\text{Ce}_{36}\text{O}_{72}$ slab to give the aliovalent, copper-substituted models of stoichiometry $\text{Cu}_2\text{Ce}_{34}\text{O}_{72}$. As described in Section 3.3, three configurations were considered to study the relative thermodynamic stability of copper segregation and agglomeration (Figure 3.6A inset). In the solid solution (ss-) models, copper atoms replace cerium atoms in the first and third CeO_2 layers (Ce-Ce interatomic distance = 12.859 Å). In the nearest-neighbor (nn-) models, copper atoms replace nearest-neighbor cerium atoms on the first CeO_2 layer of the slab (Ce-Ce interatomic distance = 3.877 Å) and in the next-nearest-neighbor (nnn-) model, copper atoms replace next-nearest-

neighbor cerium atoms on the first CeO_2 layer (Ce-Ce interatomic distance = 6.715 Å). To simulate aliovalent substitution of the copper ions (Cu^{3+} , Cu^{2+} and Cu^+ , or Cu'_{Ce} , Cu''_{Ce} and Cu'''_{Ce} in Kröger-Vink notation), an appropriate number of oxygen atoms were removed in the vicinity of the transition-metal centers for charge compensation; the removal of a single oxygen atom corresponds to the reduction of each copper atom by 1 electron. For example, removal of a single oxygen atom from $\text{Cu}_2\text{Ce}_{34}\text{O}_{72}$ to give $\text{Cu}_2\text{Ce}_{34}\text{O}_{71}$ suggests that each of the copper atoms in the slab has been reduced by one electron from Cu^{4+} to Cu^{3+} . Hence, these models are denoted as $\text{Cu}^{(4-x)+}_2\text{Ce}_{34}\text{O}_{72-x}$, where x refers to the number of charge-compensating oxygen atoms removed (the oxygen non-stoichiometry). For all nn- $\text{Cu}_2\text{Ce}_{34}\text{O}_{72-x}$ structures, as well as ss- $\text{Cu}^{4+}_2\text{Ce}_{34}\text{O}_{72}$, ss- $\text{Cu}^{3+}_2\text{Ce}_{34}\text{O}_{71}$, nnn- $\text{Cu}^{4+}_2\text{Ce}_{34}\text{O}_{72}$ and nnn- $\text{Cu}^{3+}_2\text{Ce}_{34}\text{O}_{71}$ surfaces, reduction at the copper (as opposed to surrounding cerium atoms) was confirmed by inspecting the net magnetization for each atom of the slab and examination of the partial density of states. Interestingly, for the ss- $\text{Cu}^{2+}_2\text{Ce}_{34}\text{O}_{70}$ slab, copper reduction was accompanied by reduction of the cerium atoms surrounding the oxygen vacancy.

The (111) surface of CeO_2 was chosen on the basis of HRTEM analysis both here and in the previous chapter, which indicate that the (111) is the predominant surface exposed in truncated octahedral $\text{Cu}_y\text{Ce}_{1-y}\text{O}_{2-x}$ crystallites. The choice of a 3x3x4 slab with substitution of two copper atoms was also rationalized in terms of experimental data; these models give 5.6% Cu substitution in CeO_2 while we have found here that y in $\text{Cu}_y\text{Ce}_{1-y}\text{O}_{2-x}$ can vary between 1 and 9% Cu (*vide supra*). A 3x3x4 slab was also chosen in order to simulate varying degrees of substitutional homogeneity (*i.e.* the ss-, nn- and nnn- models mentioned above).

A Hubbard U_{eff} ($U_{\text{eff}} = U - J$) correction term of 4.0 eV acting on the 4f orbitals of cerium was included in all calculations to allow for a more accurate description of the electronic structure of both oxidized and reduced ceria, which has been discussed previously.³⁹ The inclusion of a Hubbard U_{eff} term acting on the copper 3d orbitals may perturb the energies of oxygen formation in the model slabs and hence the thermodynamic preference of one oxidation state over the other.³⁹ We found that the introduction of a Hubbard U_{eff} term on the copper 3d states did not perturb the relative values of ΔG_{F} for the slabs studied here. Only after applying values for U_{eff} in excess of 4.0 eV did we see any changes in the ordering of

ΔG_F vs. μ_O plots, hence we set U_{eff} to 0.0 eV for copper 3d states for all studies on $\text{Cu}^{(4-x)+}_2\text{Ce}_{34}\text{O}_{72-x}$.

To correct for any systematic errors arising from the periodic boundary conditions with the asymmetric slabs studied here, a linear electrostatic potential (*i.e.* a dipole correction) was applied to the local potential. Electronic and ionic optimization of the slabs was carried out using the conjugate gradient algorithm employing a plane-wave cutoff of 400 eV. All atomic layers were allowed to relax until all the forces acting on the atoms reached a value below 0.01 eV \AA^{-1} . Owing to the large size of the slabs studied here, all data were reported from the integration of the Brillouin zone at the Γ point only. We found that the slab energies calculated at the Γ point varied by less than 35 meV from those calculated using a 2x2x1 Monkhorst-Pack mesh, which justifies our choice of integration at the Γ point only.

Estimates for the Gibbs energy of formation (ΔG_F) of the different slabs of $\text{Cu}^{(4-x)+}_2\text{Ce}_{34}\text{O}_{72-x}$ as a function of oxygen partial pressure were determined according to a strategy previously reported by Reuter, *et al.*⁴⁰ ΔG_F was determined relative to a reference structure (ss- $\text{Cu}_2\text{Ce}_{34}\text{O}_{72}$) by taking into account the formation of oxygen vacancies:

$$\Delta G_{F,x} = G(\text{Cu}_2\text{Ce}_{34}\text{O}_{72-x}) - G(\text{ss-Cu}_2\text{Ce}_{34}\text{O}_{72}) + x\mu_O(p,T)$$

If changes in entropy of the solid phases are neglected,⁴⁰ we can express ΔG_F in terms of energy (E) calculated by DFT:

$$\Delta G_{F,x} = E(\text{Cu}_2\text{Ce}_{34}\text{O}_{72-x}) - E(\text{ss-Cu}_2\text{Ce}_{34}\text{O}_{72}) + x\mu_O(p,T)$$

where the chemical potential for oxygen (μ_O) is

$$\mu_O(p,T) = \mu_O(p_0,T) + \frac{1}{2}k_B T \ln \frac{p}{p_0}$$

The standard chemical potential for oxygen at $p_0 = 1$ atm ($\mu_O(p_0,T)$) is found from thermodynamic tables. The value for $\mu_O(p,T)$ is referenced with respect to the total energy of an oxygen atom in a molecule of O_2 as calculated by DFT. The temperature used in these calculations (700 K where $\mu_O(p_0,T) = -0.73$ eV)⁴⁰ was chosen to roughly correspond to the temperature at which $\text{Cu}_y\text{Ce}_{1-y}\text{O}_{2-x}$ samples were annealed (400 °C).

Nanoparticle model for Monte-Carlo simulations (performed by Dr. Nongnuch Artrith, MIT). To allow a direct comparison with experiment, we devised an atomistic nanoparticle model based on the experimentally observed Wulff shape with a $\{111\}$ to $\{100\}$ surface ratio of 3:1. The relative areas of the two crystal faces as function of their relative distance from the particle center, $h_{\{111\}}/h_{\{100\}}$, are

$$A_{\{100\}} = 12 \left(\sqrt{3} \frac{h_{\{111\}}}{h_{\{100\}}} - 1 \right)^2 \quad \text{and} \quad A_{\{111\}} = 6\sqrt{3} - 8\sqrt{3} \left(\sqrt{3} \frac{h_{\{111\}}}{h_{\{100\}}} - \frac{3}{2} \right)^2 \quad \text{for} \quad \frac{1}{\sqrt{3}} \leq \frac{h_{\{111\}}}{h_{\{100\}}} \leq \frac{2}{\sqrt{3}}$$

so that $A_{\{111\}}/A_{\{100\}} = 3$ corresponds to $h_{\{111\}}/h_{\{100\}} \approx 0.887$ (see graphical solution in Figure 3.10). We used this relationship to build the nanoparticle structure with approximately 3.5 nm diameter and the desired relative surface areas shown in Figure 3.6B and C.

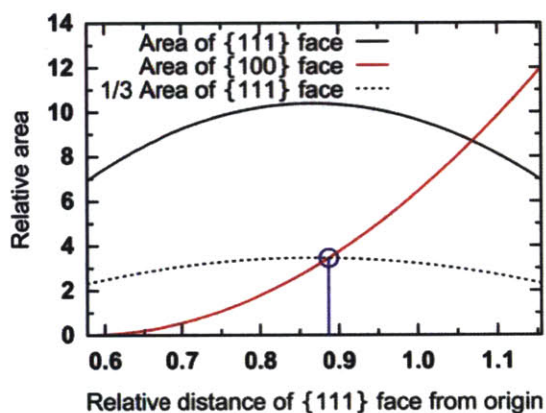


Figure 3.10 Graphical solution of the surface area ratio as function of the surface distance from the particle center. The solid black and red lines indicate the $\{111\}$ and $\{100\}$ surface areas, respectively. The dotted black line corresponds to $1/3$ of the $\{111\}$ surface area and the blue circle points out the $\{111\}:\{100\}$ ratio of 3:1.

Artificial neural network potential for $\text{Cu}_y\text{Ce}_{1-y}\text{O}_{2-x}$ nanoparticles (performed by Dr. Nongnuch Artrith, MIT). The size of the nanoparticle model and the extensive sampling required to determine the copper distribution throughout the particle prevent the direct application of density functional theory (DFT). We therefore follow the approach by Behler and Parrinello and employ artificial neural networks (ANNs) for the accurate interpolation of DFT reference calculations.^{17,41} An invariant representation of the local atomic environment is achieved by using a basis set of radial and angular functions (Behler *symmetry functions*). The basis parameters employed in this work are given in Table 3.4 and Table 3.5; see

previous work for the analytical function definitions.⁴² The atomic energy network ($\text{\ae}net$) package was used for all simulations with ANN potentials.¹⁸

Table 3.4 Parameters of the radial basis function (Behler *symmetry function*) G^2 of reference⁴² used for the description of the local atomic structure within a cutoff radius of $R_c = 6.5 \text{ \AA}$.

No.	Species	$\eta (\text{\AA}^{-2})$	No.	Species	$\eta (\text{\AA}^{-2})$
1	Ce	0.003214	12	Cu	0.124987
2	O	0.003214	13	Ce	0.214264
3	Cu	0.003214	14	O	0.214264
4	Ce	0.035711	15	Cu	0.214264
5	O	0.035711	16	Ce	0.357106
6	Cu	0.035711	17	O	0.357106
7	Ce	0.071421	18	Cu	0.357106
8	O	0.071421	19	Ce	0.714213
9	Cu	0.071421	20	O	0.714213
10	Ce	0.124987	21	Cu	0.714213
11	O	0.124987			

In total, around 1100 $\text{Cu}_y\text{Ce}_{1-y}\text{O}_{2-x}$ periodic bulk, surface ($\{111\}$ and $\{100\}$) and isolated cluster structures were used for the construction of the ANN potential. The DFT calculations of these reference structures were carried out using the FHI-aims package⁴³ using *tight* settings (6th order expansion of the Hartree potential, radial integration grids with 434 points in the outer shell and a tier 2 basis set). Relativistic effects were included with atomic ZORA.⁴⁴ Structural energies were generally converged to 1 meV/atom and atomic forces to 10 meV/Å. For all calculations the exchange-correlation functional by Perdew, Burke and Ernzerhof was used.³⁰

Around 1000 reference structures were used for the training of the ANN potential and the accuracy of the interpolation was verified against an independent testing set of around 100 structures that were not used for training. The root-mean squared error (RMSE) of the final ANN potential is 6.8 meV/atom for the training set and 8.7 meV/atom for the testing set. The mean absolute errors are 5.4 and 7.1 meV/atom for the training and the testing set, respectively. The ANN potential energies of all structures in the reference set are compared to their DFT references in Figure 3.11. We stress that the excellent accuracy of the ANN potential could only be achieved because all reference structures are closely related to the nanoparticle model of the previous section. The ANN potential of this work would not be suitable for the investigation of structurally very different Cu/Ce/O systems.

Table 3.5 Parameters of the angular basis function (Behler *symmetry function*) G^4 of reference ⁴² used for the description of the local atomic structure within a cutoff radius of $R_c = 6.5 \text{ \AA}$. Each set of parameters listed in the table corresponds to 6 equivalent functions for the 6 possible combinations of atomic species (Ce-Ce, Ce-O, Ce-Cu, O-O, O-Cu, Cu-Cu) among neighboring atom pairs in the local structural environment of an atom (Ce, O, Cu).

No.	$\eta (\text{\AA}^{-2})$	λ	ζ
22-27	0.000357	1.0	1.0
28-33	0.000357	-1.0	1.0
34-39	0.000357	1.0	4.0
40-45	0.000357	-1.0	4.0
46-51	0.010713	1.0	1.0
52-57	0.010713	-1.0	1.0
58-63	0.010713	1.0	4.0
64-69	0.010713	-1.0	4.0
70-75	0.028569	1.0	1.0
76-81	0.028569	-1.0	1.0
82-87	0.028569	1.0	4.0
88-93	0.028569	-1.0	4.0

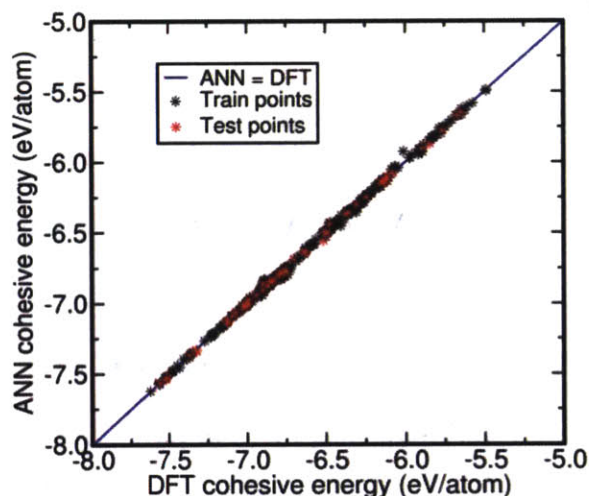


Figure 3.11 Comparison of the cohesive energies predicted by the ANN potential and their DFT reference values. The diagonal (blue line) corresponds to perfect correlation. The energies of structures from the training and test sets are shown as black and red points, respectively.

Monte-Carlo simulations (performed by Dr. Nongnuch Artrith, MIT). The Monte-Carlo (MC) simulations were carried out in the grand canonical ensemble, *i.e.*, the copper grand potential

$$\Phi_{\text{Cu}} = E^{\text{ANN}} - TS - \mu_{\text{Cu}} N_{\text{Cu}}$$

was minimized in the simulated annealing runs for a given oxygen vacancy concentration and copper chemical potential, μ_{Cu} . In the above equation, E^{ANN} is the configurational energy predicted by the ANN potential, T is the temperature, S is the configurational entropy and N_{Cu} is the number of copper atoms in the nanoparticle.

All MC simulations were repeated at least three times to guarantee reproducibility. The nanoparticle that was analyzed for the article is representative and has a copper concentration closest to the experimentally observed 8%.

3.6 References

- (1) Soria, J.; Conesa, J. C.; Martinez-Arias, A.; Coronado, J. M. *Solid State Ionics* **1993**, *63 - 65*, 755.
- (2) Liu, W.; Flytzani-Stephanopoulos, M. *J. Catal.* **1995**, *153*, 317.
- (3) Martinez-Arias, A.; Fernandez-Garcia, M.; Soria, J.; Conesa, J. C. *J. Catal.* **1999**, *182*, 367.
- (4) Sedmak, G.; Hocevar, S.; Levec, J. *J. Catal.* **2004**, *222*, 87.
- (5) Wang, X.; Rodriguez, J. A.; Hanson, J. C.; Gamarra, D.; Martinez-Arias, A.; Fernandez-Garcia, M. *J. Phys. Chem. B* **2005**, *109*, 19595.
- (6) Harrison, P. G.; Ball, I. K.; Azelee, W.; Daniell, W.; Goldfarb, D. *Chem. Mater.* **2000**, *12*, 3715.
- (7) Martinez-Arias, A.; Fernandez-Garcia, M.; Galvez, O.; Coronado, J. M.; Anderson, J. A.; Conesa, J. C.; Soria, J.; Munuera, G. *J. Catal.* **2000**, *195*, 207.
- (8) Jia, A.-P.; Jiang, S.-Y.; Lu, J.-Q.; Luo, M.-F. *J. Phys. Chem. C* **2010**, *114*, 21605.
- (9) Jia, A.-P.; Hu, G.-S.; Meng, L.; Xie, Y.-L.; Lu, J.-Q.; Luo, M.-F. *J. Catal.* **2012**, *289*, 199.
- (10) Liu, W.; Flytzani-Stephanopoulos, M. *Chem. Eng. J. (Amsterdam, Neth.)* **1996**, *64*, 283.
- (11) Elias, J. S.; Risch, M.; Giordano, L.; Mansour, A. N.; Shao-Horn, Y. *J. Am. Chem. Soc.* **2014**, *136*, 17193.
- (12) Zhang, F.; Jin, Q.; Chan, S.-W. *J. Appl. Phys. (Melville, NY, U. S.)* **2004**, *95*, 4319.
- (13) Gamarra, D.; Munuera, G.; Hungria, A. B.; Fernandez-Garcia, M.; Conesa, J. C.; Midgley, P. A.; Wang, X. Q.; Hanson, J. C.; Rodriguez, J. A.; Martinez-Arias, A. *J. Phys. Chem. C* **2007**, *111*, 11026.

- (14) Turner, S.; Lazar, S.; Freitag, B.; Egoavil, R.; Verbeeck, J.; Put, S.; Strauven, Y.; Van Tendeloo, G. *Nanoscale* **2011**, *3*, 3385.
- (15) Paun, C.; Safonova, O. V.; Szlachetko, J.; Abdala, P. M.; Nachtegaal, M.; Sa, J.; Kleymenov, E.; Cervellino, A.; Krumeich, F.; van Bokhoven, J. A. *J. Phys. Chem. C* **2012**, *116*, 7312.
- (16) Chen, S.-Y.; Chen, R.-J.; Lee, W.; Dong, C.-L.; Gloter, A. *Phys. Chem. Chem. Phys.* **2014**, *16*, 3274.
- (17) Behler, J.; Parrinello, M. *Phys. Rev. Lett.* **2007**, *98*, 146401.
- (18) Artrith, N.; Urban, A. *Comput. Mater. Sci.* **2016**, *114*, 135.
- (19) James, T. E.; Hemmingson, S. L.; Ito, T.; Campbell, C. T. *J. Phys. Chem. C* **2015**, *119*, 17209.
- (20) Liu, W.; Sarofim, A. F.; Flytzani-Stephanopoulos, M. *Chem. Eng. Sci.* **1994**, *49*, 4871.
- (21) Liu, W.; Flytzani-Stephanopoulos, M. *J. Catal.* **1995**, *153*, 304.
- (22) Rodriguez-Carvajal, J. *Commission on Powder Diffraction (IUCr)* **2001**, *26*, 12.
- (23) Schneider, C. A.; Rasband, W. S.; Eliceiri, K. W. *Nat. Methods* **2012**, *9*, 671.
- (24) Sayers, D. E.; Heald, S. M.; Pick, M. A.; Budnick, J. I.; Stern, E. A.; Wong, J. *Nucl. Instrum. Methods Phys. Res.* **1983**, *208*, 631.
- (25) Bearden, J. A.; Burr, A. F. *Rev. Mod. Phys.* **1967**, *39*, 125.
- (26) Lytle, F. W.; Greegor, R. B. a. S. D. R.; Marques, E. C.; Wong, J.; Spiro, C. L.; Huffman, G. P.; Huggins, F. E. *Nucl. Instrum. Methods A* **1984**, *226*, 542
- (27) Newville, M. *J. Synchrotron Radiat.* **2001**, *8*, 322.
- (28) Ravel, B.; Newville, M. *J. Synchrotron Radiat.* **2005**, *12*, 537.
- (29) Perdew, J. P.; Burke, K.; Ernzerhof, M. *Phys. Rev. Lett.* **1996**, *77*, 3865.
- (30) Perdew, J. P.; Burke, K.; Ernzerhof, M. *Phys. Rev. Lett.* **1997**, *78*, 1396.
- (31) Perdew, J. P.; Chevary, J. A.; Vosko, S. H.; Jackson, K. A.; Pederson, M. R.; Singh, D. J.; Fiolhais, C. *Phys. Rev. B: Condens. Matter Mater. Phys.* **1992**, *46*, 6671.
- (32) Perdew, J. P.; Chevary, J. A.; Vosko, S. H.; Jackson, K. A.; Pederson, M. R.; Singh, D. J.; Fiolhais, C. *Phys. Rev. B: Condens. Matter Mater. Phys.* **1993**, *48*, 4978.
- (33) Bochl, P. E. *Phys. Rev. B: Condens. Matter Mater. Phys.* **1994**, *50*, 17953.

Chapter 3

- (34) Kresse, G.; Joubert, D. *Phys. Rev. B: Condens. Matter Mater. Phys.* **1999**, *59*, 1758.
- (35) Kresse, G.; Furthmüller, J. *Phys. Rev. B: Condens. Matter Mater. Phys.* **1996**, *54*, 11169.
- (36) Kresse, G.; Furthmüller, J. *Comput. Mater. Sci.* **1996**, *6*, 15.
- (37) Kresse, G.; Hafner, J. *Phys. Rev. B: Condens. Matter Mater. Phys.* **1993**, *47*, 558.
- (38) Kresse, G.; Hafner, J. *Phys. Rev. B: Condens. Matter Mater. Phys.* **1994**, *49*, 14251.
- (39) Krcha, M. D.; Janik, M. J. *Int. J. Quantum Chem.* **2014**, *114*, 8.
- (40) Reuter, K.; Scheffler, M. *Phys. Rev. B: Condens. Matter Mater. Phys.* **2001**, *65*, 035406.
- (41) Behler, J. *J. Phys.: Condens. Matter* **2014**, *26*, 183001.
- (42) Behler, J. *J. Chem. Phys.* **2011**, *134*, 074106.
- (43) Blum, V.; Gehrke, R.; Hanke, F.; Havu, P.; Havu, V.; Ren, X.; Reuter, K.; Scheffler, M. *Comput. Phys. Commun.* **2009**, *180*, 2175.
- (44) van Lenthe, E.; Baerends, E. J.; Snijders, J. G. *J. Chem. Phys.* **1994**, *101*, 9783.

**Chapter 4 – The Mechanism for CO Oxidation on
 $\text{Cu}_y\text{Ce}_{1-y}\text{O}_{2-x}$**

4.1 Introduction:

In Chapters 2 and 3, we provided evidence that the active sites in CuO/CeO₂ catalysts are associated with atomically-dispersed Cu³⁺ and Cu²⁺ ions at the surface of Cu_yCe_{1-y}O_{2-x}. On the basis of density functional calculations and STEM-EELS mapping of individual nanoparticles, we proposed that the majority of the copper ions in Cu_yCe_{1-y}O_{2-x} segregate to the {100} and {111} surfaces and that Cu_yCe_{1-y}O_{2-x} should not be thought of as a classical solid solution. We also found that the bulk CuO phase in mixed-phase CuO/Cu_yCe_{1-y}O_{2-x} catalysts are not responsible for the special catalytic enhancement found in these materials, as was previously proposed by Jia *et al.*^{1,2}

In this chapter, we investigate the mechanism for CO oxidation on phase pure Cu_yCe_{1-y}O_{2-x} catalysts. In Chapter 1, we introduced three popular reaction mechanisms used to describe CO oxidation on mixed-phase CuO/CeO₂ (Figure 1.6), each of which relied on the interaction between bulk CuO and CeO₂ phases. We now revisit these mechanisms in light of our understanding of the active copper species on the surfaces of Cu_yCe_{1-y}O_{2-x}, not in the context of CuO/CeO₂ interfaces, but rather, in the context of the interaction of site-isolated Cu³⁺ and Cu²⁺ ions with Ce⁴⁺ ions from the CeO₂ host. A broader understanding of the mechanism for CO oxidation catalysis on these surfaces will, in turn, reveal potential candidates for design descriptors to rationally designing next-generation catalysts.

Combining a suite of *in-situ* spectroscopic techniques including XAS, XPS and DRIFTS, our kinetic analysis on Cu_{0.1}Ce_{0.9}O_{2-x} model catalysts has lead us to propose a Mars-van Krevelen mechanism for CO oxidation catalysis. *In-situ* XPS and DRIFTS reveal that CO₂ can be generated from CO in the absence of O₂, suggesting that lattice oxygen can be directly involved in oxidation catalysis. Indeed, we proposed that the rate-determining step most likely includes the formation of oxygen vacancies at surface copper centers. Thus a key barrier to CO oxidation catalysis is associated with the reducibility of the transition-metal. *In-situ* XAS measurements of Cu_{0.1}Ce_{0.9}O_{2-x} under oxygen-rich and -lean conditions illustrate that the dispersed copper ions exhibit surprising fluxionality, which may help explain the particular durability of this family of catalysts.

4.2 Partial Pressure Dependence of CO Oxidation Catalysis

In order to interrogate the mechanism for CO oxidation on Cu_yCe_{1-y}O_{2-x}, the partial-pressure dependence on Cu_{0.1}Ce_{0.9}O_{2-x} nanoparticles was investigated under a number of

reaction conditions. At 75 °C and under oxygen-rich conditions, $\text{Cu}_{0.1}\text{Ce}_{0.9}\text{O}_{2-x}$, had a strong partial pressure dependence on CO (Figure 4.1A). These data suggest that the presence of pre-adsorbed CO on the surface contributes to the rate-determining step of the reaction mechanism, while the adsorption of oxygen doesn't, which is consistent with a Mars-van Krevelen type mechanism for CO oxidation (Figure 4.2).

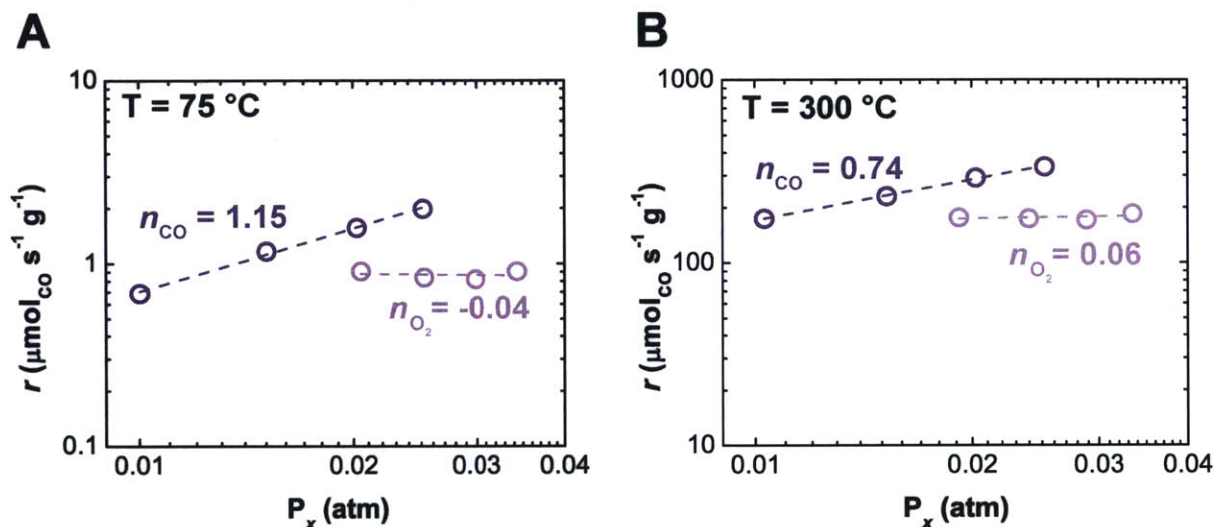


Figure 4.1 The partial pressure dependence of CO oxidation on $\text{Cu}_{0.1}\text{Ce}_{0.9}\text{O}_{2-x}$; (A) recorded at 75 °C and (B) 300 °C under differential flow conditions. Reaction rates were measured with flow rates of $1300 \text{ mL min}^{-1} \text{ g}^{-1}_{\text{cat}}$ for 20 mg catalyst loadings, holding either the partial pressure of CO (0.01 atm) or O_2 (0.025 atm) constant while varying the partial pressure of the other gas.

As we've seen in Section 1.4.2, the rate law would be given by (see Appendix A.1 for full derivation)

$$r = \frac{k_2 K_{\text{CO ads}} P_{\text{CO}}}{1 + K_{\text{CO ads}} P_{\text{CO}}} \quad (4.1)$$

where $K_{\text{CO ads}}$ is the equilibrium constant for the adsorption of CO by copper centers. At sufficiently low pressures, the derived rate law is first order with respect to carbon monoxide and zeroth order with respect to O_2 , consistent with Figure 4.1A. Dispersed Cu^{3+} centers, represented in Figure 4.2 as the $\mu\text{-O}^{2-}$ -bridged dimers found from our DFT studies in 3.3, first adsorb CO end-on in step 1. We shall see that CO adsorption to Cu^{3+} isn't very strong, which shouldn't be surprising considering the electronic structure of square planar $3d^8 \text{Cu}^{3+}$. In a low-spin D_{4h} ligand field, all of the 3d antibonding orbitals are filled with the exception of the b_{1g} orbital, which has $3d_{x^2-y^2}$ parentage. Since the filled a_{1g} orbital ($3d_{z^2}$ parentage) is

the only orbital that can accept σ -bonding, CO can only interact with Cu^{3+} through π -backbonding with filled orbitals of appropriate symmetry, the e_g set of ($3d_{xz}$, $3d_{yz}$) parentage. As a result, CO bonding with Cu^{3+} is not very enthalpically favorable. Nevertheless, an oxygen atom is transferred to the adsorbed CO in step 2, forming an oxygen vacancy on the catalyst surface. In Figure 4.2 this is accompanied by the localized reduction of the two Cu^{3+} centers by two electrons, although as we have seen in our discussion in 1.5.3, there can be many ways in which we can envision the surface being reduced. In step 3, the resulting CO_2 adduct desorbs to leave the bare, $2e^-$ -reduced surface. The dissociative adsorption of O_2 in step 4, by no means meant to represent an elementary reaction step, refills the oxygen vacancy and oxidizes the surface to complete the catalytic cycle.

The partial pressure dependence for the $\text{Cu}_{0.1}\text{Ce}_{0.9}\text{O}_{2-x}$ catalyst was also measured at 300 °C (Figure 4.1B) under oxygen-rich conditions. While the kinetic order for CO drops slightly to 0.74, the kinetics remain zeroth order with respect to O_2 , indicating that the reaction mechanism is relatively unperturbed at elevated temperatures.

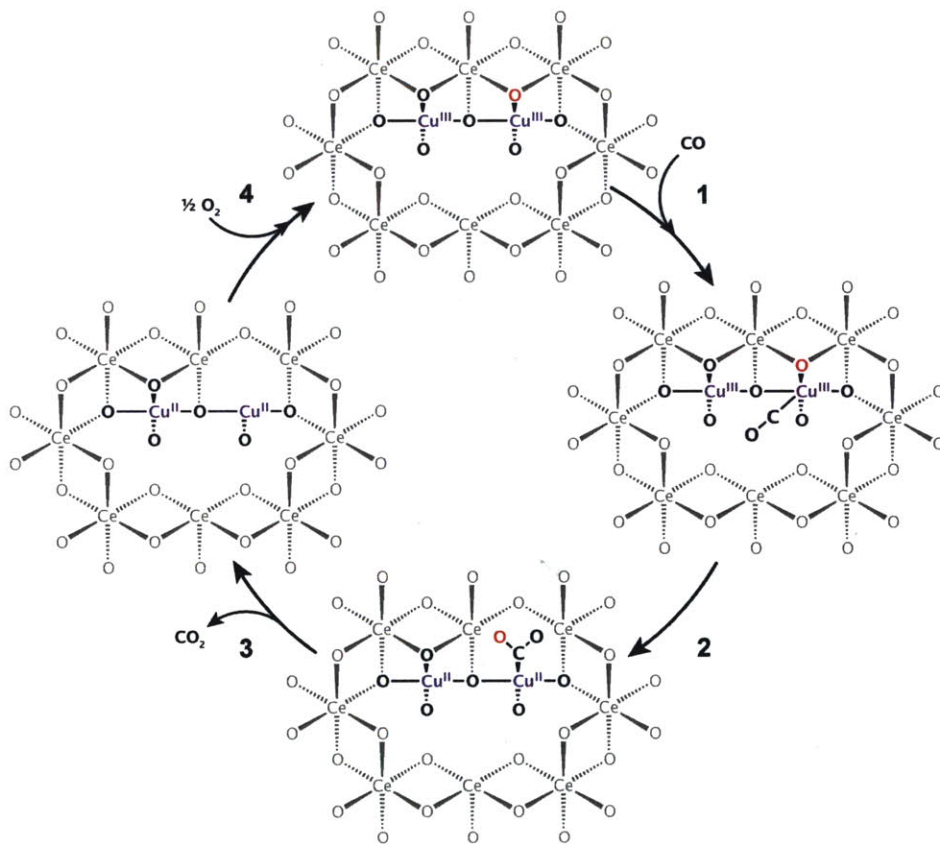


Figure 4.2 Schematic reaction mechanism for CO oxidation on $\text{Cu}_y\text{Ce}_{1-y}\text{O}_{2-x}$ catalysts. Light grey wedges correspond to Ce – O bonds in the subsurface layer.

4.3 Evolution of Surface Adsorbates

Over the past several years, the development of *in-situ* spectroscopic techniques has enabled researchers in the heterogeneous catalysis community to probe the mechanistic origins of chemical reactions on surfaces at an unprecedented, atomic-level scale.^{3,4} Specifically, probing reaction mechanisms using surface-sensitive *in-situ* vibrational spectroscopies furnishes information regarding adsorbate binding and surface interactions.⁵ Particularly relevant for CO oxidation catalysis, Fourier Transform Infrared Spectroscopy (FT-IR), especially in the Diffuse Reflectance Infrared Fourier Transform Spectroscopy (DRIFTS) mode, has been employed to gain mechanistic insights into CO oxidation catalysis on Au/TiO_2 ,^{6,7} Co_3O_4 ,⁸ and other material systems from the detection of vibrational modes of surface-adsorbed intermediates such as CO, CO_2 , carbonates (CO_3^{2-}) and formates (HCO_2^-) as well as their gas-phase counterparts. In a recent study on mixed-phase CuO/CeO_2 catalysts,⁹ researchers demonstrated that carbon monoxide binds to the surface as either carbonyl or is transformed into bidentate CO_3^{2-} . These data are consistent with the rate-determining step for CO oxidation being one that involves the abstraction of an oxygen atom by copper-bound CO from a neighboring CeO_2 site, analogous to our proposed mechanism (Figure 4.2). In order to interrogate our mechanism further we acquired DRIFTS spectra of $\text{Cu}_{0.1}\text{Ce}_{0.9}\text{O}_{2-x}$ *in-situ* under catalytically-relevant conditions.

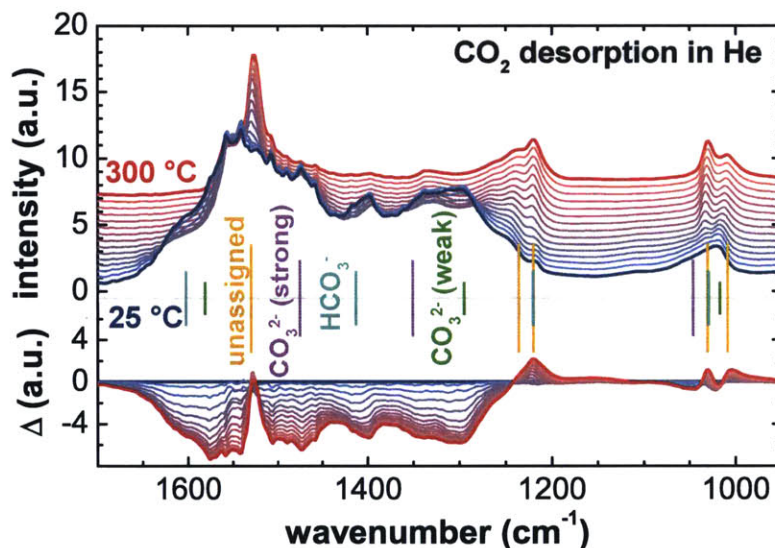


Figure 4.3 DRIFTS spectra (top) and difference spectra (Δ , bottom) for $\text{Cu}_{0.1}\text{Ce}_{0.9}\text{O}_{2-x}$ upon thermal desorption of CO_2 . CO_2 was first adsorbed at rt and then desorbed in He. Spectra were recorded every 20 °C.

The *in-situ* DRIFTS spectra for $\text{Cu}_{0.1}\text{Ce}_{0.9}\text{O}_{2-x}$ as a function of the catalyst bed temperature indicate salient features consistent with oxygen-ion-vacancy-mediated CO oxidation being the rate-determining step (Figures 4.3 – 4.6). The heating of surface-adsorbed CO_2 in He (Figure 4.3) leads to the formation and subsequent desorption of various carbonates (CO_3^{2-}) and hydrogen carbonates (HCO_3^-) that spontaneously form on the surface of $\text{Cu}_{0.1}\text{Ce}_{0.9}\text{O}_{2-x}$ when CO_2 adsorbs. Vibrational bands at 1581 (C-O stretching), 1296 (asymmetric O-C-O stretching) and 1018 cm^{-1} (symmetric O-C-O stretching) can be ascribed to weakly bound CO_3^{2-} , while the peaks at 1474 (C-O stretching), 1350 (asymmetric O-C-O stretching) and 1047 cm^{-1} (symmetric O-C-O stretching), which disappear at higher temperatures, are assigned to CO_3^{2-} species strongly bound to edge and kink sites of $\text{Cu}_{0.1}\text{Ce}_{0.9}\text{O}_{2-x}$.¹⁰ Additionally, the disappearance of features ascribed to HCO_3^- at 3606 (O-H stretch), 1602 (C-O stretching), 1414 (asymmetric O-C-O stretching), 1220 (C-O-H bending) and 1030 cm^{-1} (symmetric O-C-O stretching) suggest that the surface of $\text{Cu}_{0.1}\text{Ce}_{0.9}\text{O}_{2-x}$ is partially hydroxylated. It should be noted that some features in Figure 4.3 have not been identified, namely sharp bands at 1530, 1236 and 1005 cm^{-1} that increase in intensity with temperature. While we cannot confidently assign these bands, they fall just outside the range expected for the C-O stretching, asymmetric and symmetric O-C-O stretching frequencies for a (hydrogen) carbonate. Assigning these bands to a carbonate group, we see that this species is particularly stable on the surface of $\text{Cu}_{0.1}\text{Ce}_{0.9}\text{O}_{2-x}$.

The general features of the DRIFTS spectra for $\text{Cu}_{0.1}\text{Ce}_{0.9}\text{O}_{2-x}$ heated under different CO_2 conditions (Figure 4.4A and B) are similar to those described above for CO_2 desorption in Figure 4.3. The heating of $\text{Cu}_{0.1}\text{Ce}_{0.9}\text{O}_{2-x}$ in a CO_2 flow (Figure 4.4A) and the desorption of CO_2 in an O_2 stream (Figure 4.4B) both lead to the desorption of the strong and weakly-bound CO_3^{2-} and HCO_3^- species, with the appearance of the stable carbonate species at higher temperatures. Participation of the lattice O^{2-} in CO oxidation is supported by CO desorption DRIFTS experiments with $\text{Cu}_{0.1}\text{Ce}_{0.9}\text{O}_{2-x}$ (Figure 4.5). These spectra show the formation, at temperatures below $\sim 60\text{ }^\circ\text{C}$, of the above-mentioned peaks for both types of CO_3^{2-} and HCO_3^- followed by their gradual disappearance at higher temperatures (Figure 4.5A). Concurrent with the appearance and desorption of these species is the gradual desorption of CO bound to the Cu sites of $\text{Cu}_{0.1}\text{Ce}_{0.9}\text{O}_{2-x}$ as evidenced by the disappearance of the C-O stretching peak at 2110 cm^{-1} (Figure 4.5B). These trends suggest that, even in the absence of

O_2 , adsorbed CO abstracts an oxygen atom from the surface of $Cu_{0.1}Ce_{0.9}O_{2-x}$ forming CO_2 , which goes on to react further with the surface, producing (hydrogen) carbonates. It should be noted that the features ascribed to the stable carbonate species also appear in these spectra at higher temperatures, suggesting a partial poisoning of the surface.

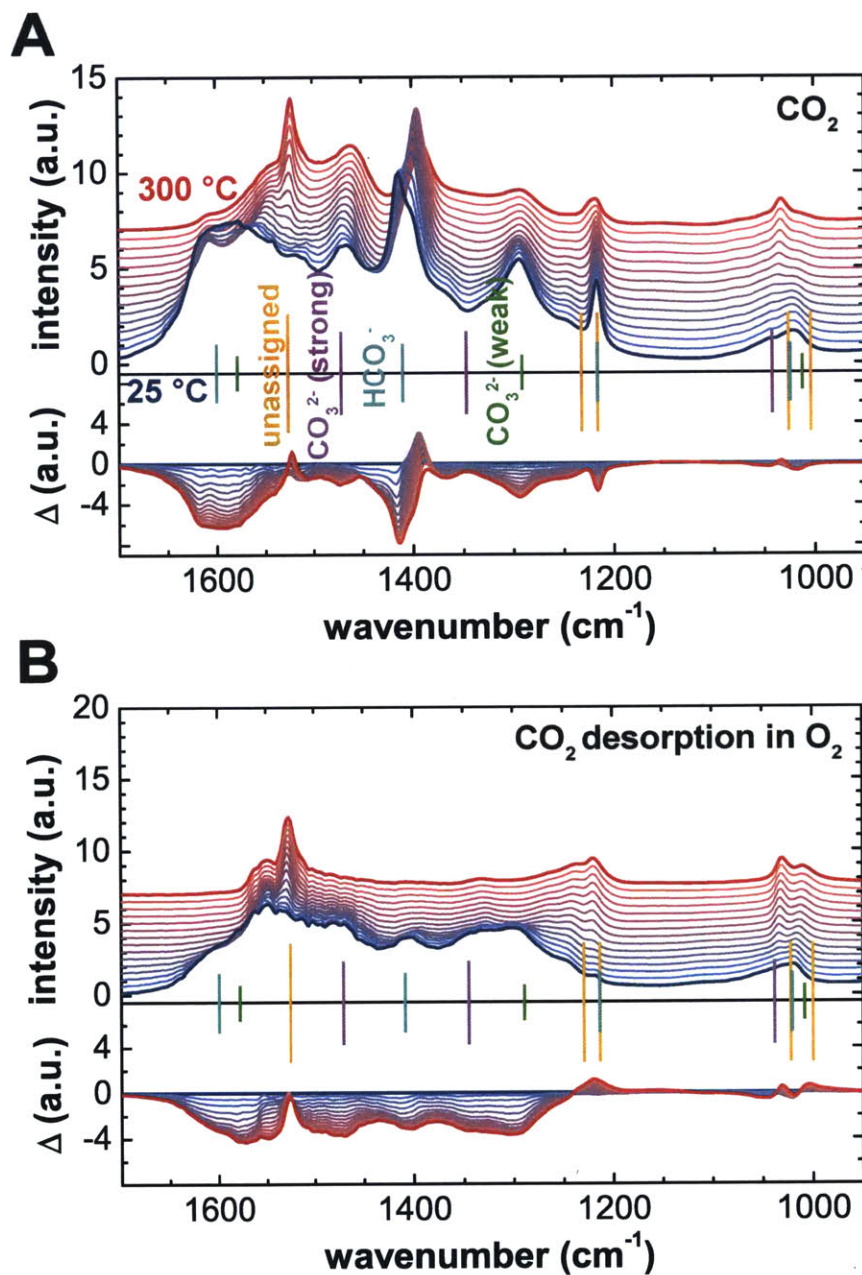


Figure 4.4 DRIFTS spectra (top) and difference spectra (Δ , bottom) for $Cu_{0.1}Ce_{0.9}O_{2-x}$ upon heating under CO_2 desorption conditions. (A) $Cu_{0.1}Ce_{0.9}O_{2-x}$ heated under a flow of 1% CO_2 and (B) CO_2 was adsorbed and then the catalyst was heated in 2.5% O_2 . Spectra were recorded every 20 °C.

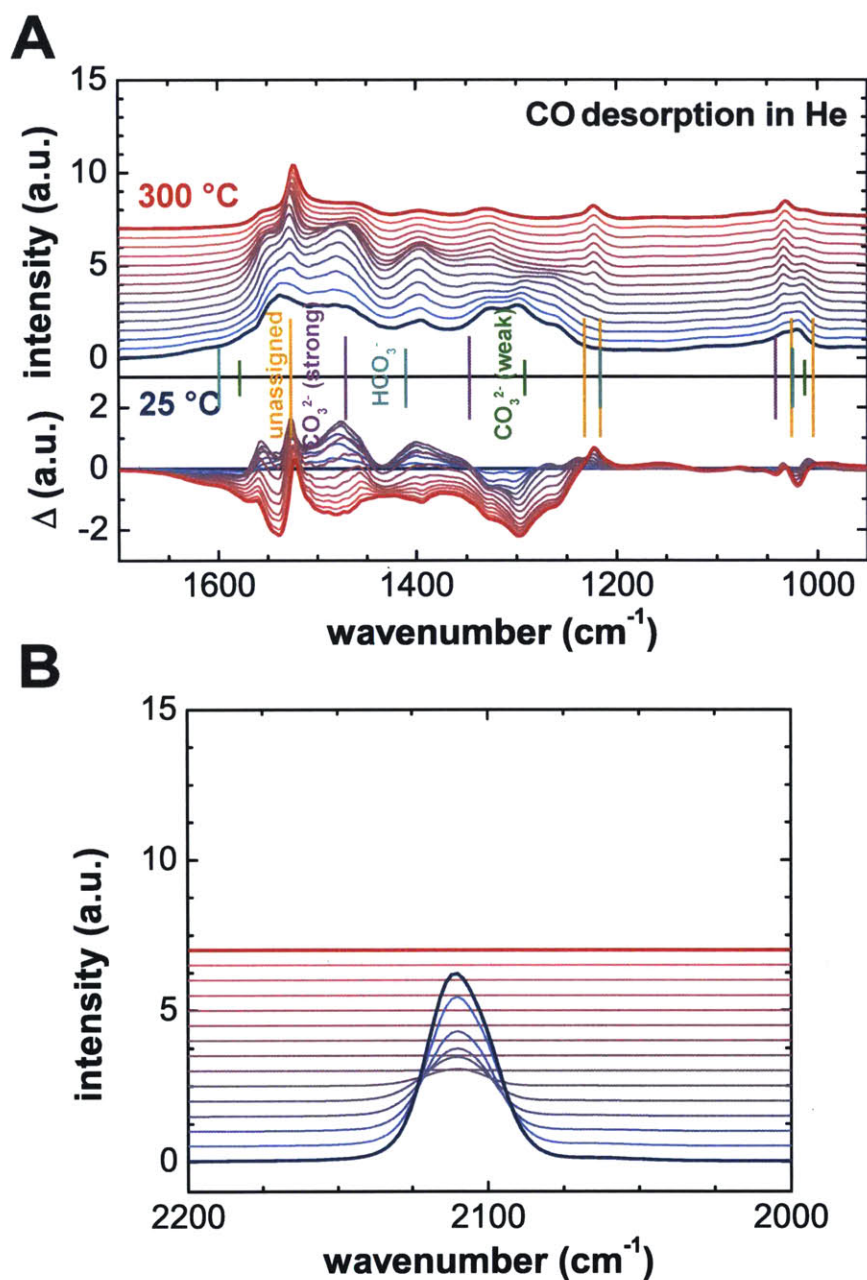


Figure 4.5 DRIFTS spectra (top) and difference spectra (Δ , bottom) for $\text{Cu}_{0.1}\text{Ce}_{0.9}\text{O}_{2-x}$ upon CO desorption experiments in He. CO was adsorbed and then the catalyst was heated in He; shown in (A) is the carbonate region and in (B) the CO region. Spectra were recorded every 20 °C.

DRIFTS spectra were also acquired as a function of temperature on $\text{Cu}_{0.1}\text{Ce}_{0.9}\text{O}_{2-x}$ under catalytically-relevant conditions (Figure 4.6). These spectra share many common features with the spectra for CO desorption; at lower temperatures, features assigned to both types of CO_3^{2-} and HCO^- initially increase, while at higher temperatures, these features begin to

decrease in intensity. A notable difference is that the bands at 1530, 1236 and 1005 cm^{-1} , which we are assigning to stable, poisoning CO_3^{2-} species, begin to decrease in intensity at higher temperatures. These data suggests that the catalytic turnover in $\text{Cu}_{0.1}\text{Ce}_{0.9}\text{O}_{2-x}$ at the surface can aid in the desorption of these strongly bound species and may reveal insights into the role of the copper ions in CO oxidation catalysis. Adsorbed CO can oxidize to CO_2 in the absence of gaseous O_2 (Figure 4.5) with the aid of lattice oxygen ions, forming an oxygen vacancy as in step 3 of our reaction mechanism (Figure 4.2), but the strongly-bound carbonates that form during this process can only desorb with the refilling of the oxygen vacancy from the reduction of O_2 and subsequent adsorption of a second equivalent of CO. This suggests that CO_2 desorption (step 3) may be concerted with the filling of the oxygen vacancy (step 4) or that CO_2 can only desorb following the filling of the oxygen vacancy. According to either hypotheses, however, we can see clearly from Figure 4.6 that the filling of the oxygen vacancy is paramount to CO oxidation catalysis on $\text{Cu}_{0.1}\text{Ce}_{0.9}\text{O}_{2-x}$.

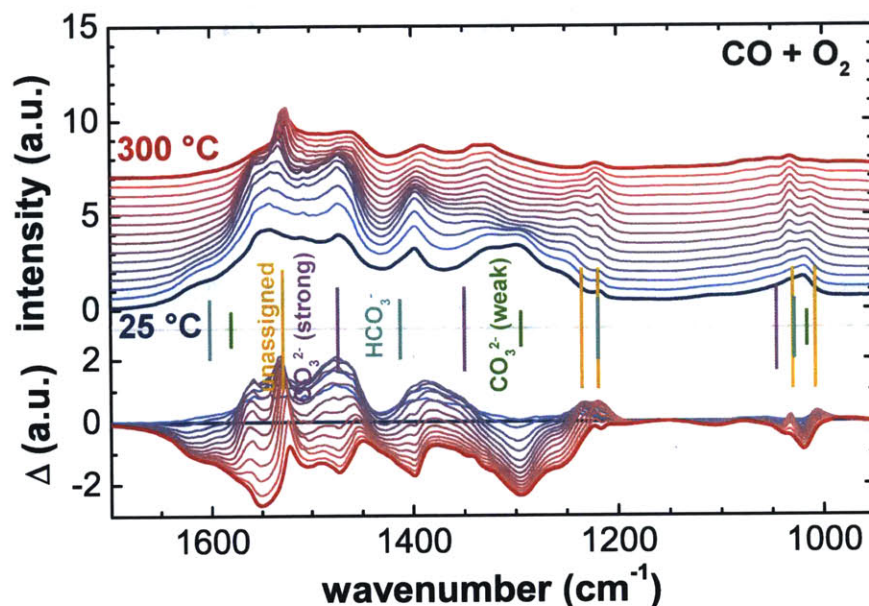


Figure 4.6 DRIFTS spectra (top) and difference spectra (Δ , bottom) for $\text{Cu}_{0.1}\text{Ce}_{0.9}\text{O}_{2-x}$ upon heating in an oxygen-rich CO oxidation stream. The catalyst was heated under a flow of 1% CO + 2.5% O_2 , recording spectra every 20 °C.

To further investigate the surface dynamics of CO oxidation on $\text{Cu}_{0.1}\text{Ce}_{0.9}\text{O}_{2-x}$ we carried out Near-Ambient Pressure X-ray Photoelectron Spectroscopy (NAP-XPS) studies on $\text{Cu}_{0.1}\text{Ce}_{0.9}\text{O}_{2-x}$ nanoparticles under catalytic conditions (30 – 75 mTorr CO, 0 – 75 mTorr O_2). In recent years NAP-XPS has proven to be an invaluable tool for the characterization of

heterogeneous catalyst surfaces under reaction conditions and for the elucidation of reaction mechanisms on surfaces.¹¹⁻¹³ Although this powerful technique has been employed extensively to probe surface dynamics under CO oxidation conditions for noble-metal-based catalysts,¹⁴⁻²⁰ to the best of our knowledge similar studies on transition-metal-substituted ceria (or even CuO/CeO₂) are absent from the literature. After introducing the Cu_{0.1}Ce_{0.9}O_{2-x} sample into the analysis chamber and cleaning the surface of any carbonaceous species at 400 °C in 75 mTorr O₂, the temperature was lowered to 300 °C and an atmosphere of 30 mTorr CO and 75 mTorr O₂ was introduced into the chamber. Isotherms were recorded for each reaction condition at 300 °C, which are summarized in Figure 4.7 for the oxygen and carbon 1s regions.

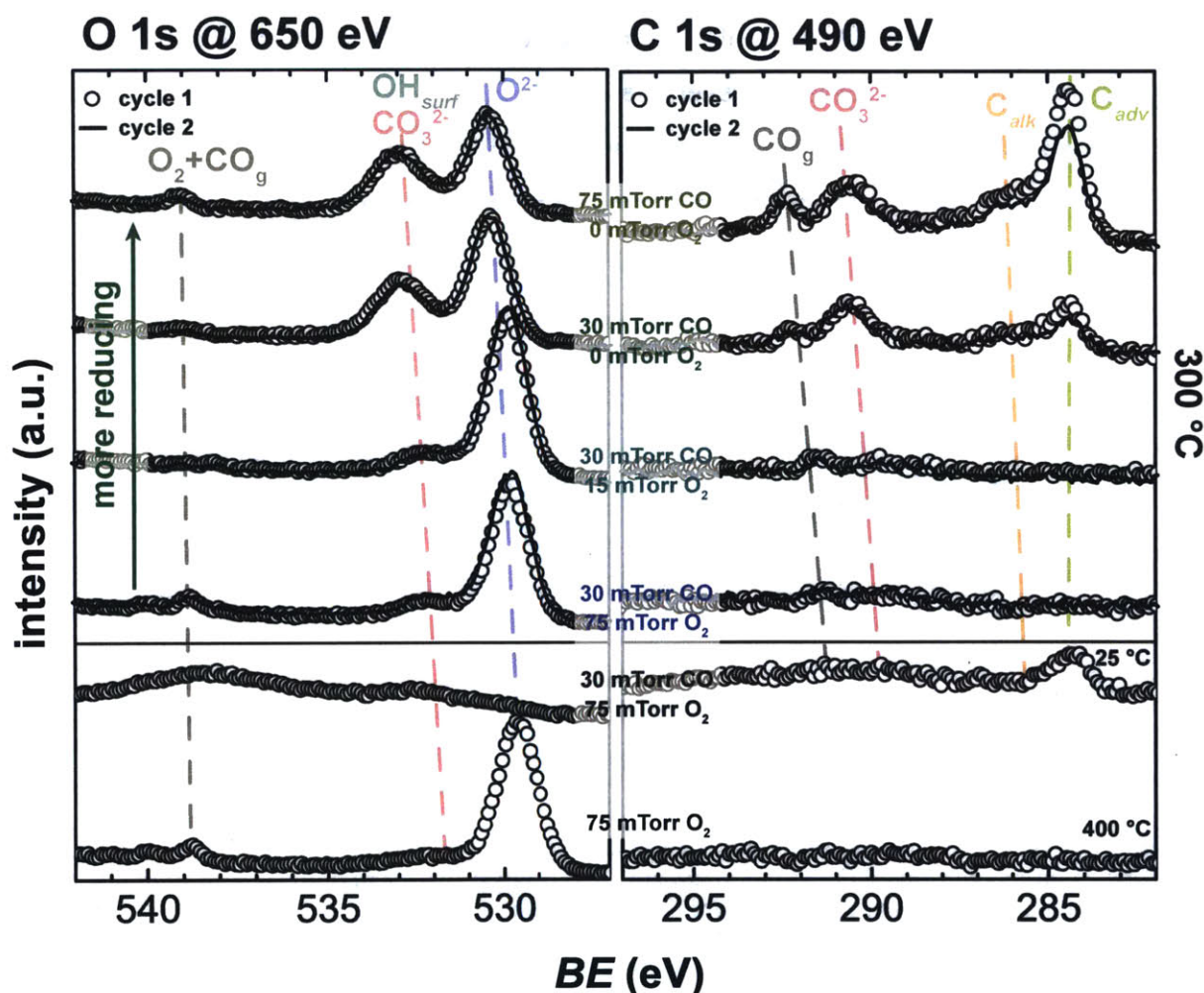


Figure 4.7 Raw NAP-XPS spectra for Cu_{0.1}Ce_{0.9}O_{2-x} during and after annealing at 400 °C in 75 mTorr O₂ and under different CO oxidation conditions. Shown are the O and C 1s spectra acquired at 650 and 490 eV, respectively. Circles indicate data from cycle 1 while solid lines indicate data from cycle 2.

Under oxygen rich conditions (30 mTorr CO, 75 mTorr O_2) two peaks are present in the O 1s region that are attributed to features of the oxide surface, a strong feature at ~ 530 eV and a shoulder at ~ 532 eV which are attributed to bulk O^{2-} and surface OH^- groups of $\text{Cu}_{0.1}\text{Ce}_{0.9}\text{O}_{2-x}$. Additionally, as confirmed in the C 1s spectra where a weak feature at ~ 290 eV appears, there appears to be a minor peak, also at ~ 532 eV, which we can attribute to surface-bound CO_3^{2-} . In order to quantify trends in the evolution of the surface-bound intermediates, we fit the data in Figure 4.7, taking care to restrain the area of the peak associated with CO_3^{2-} in the O 1s region using the integrated intensity of the corresponding peak in the C 1s region and the relative sensitivity factors for C and O at these two photon energies. The results of these fits are shown in Figure 4.8.

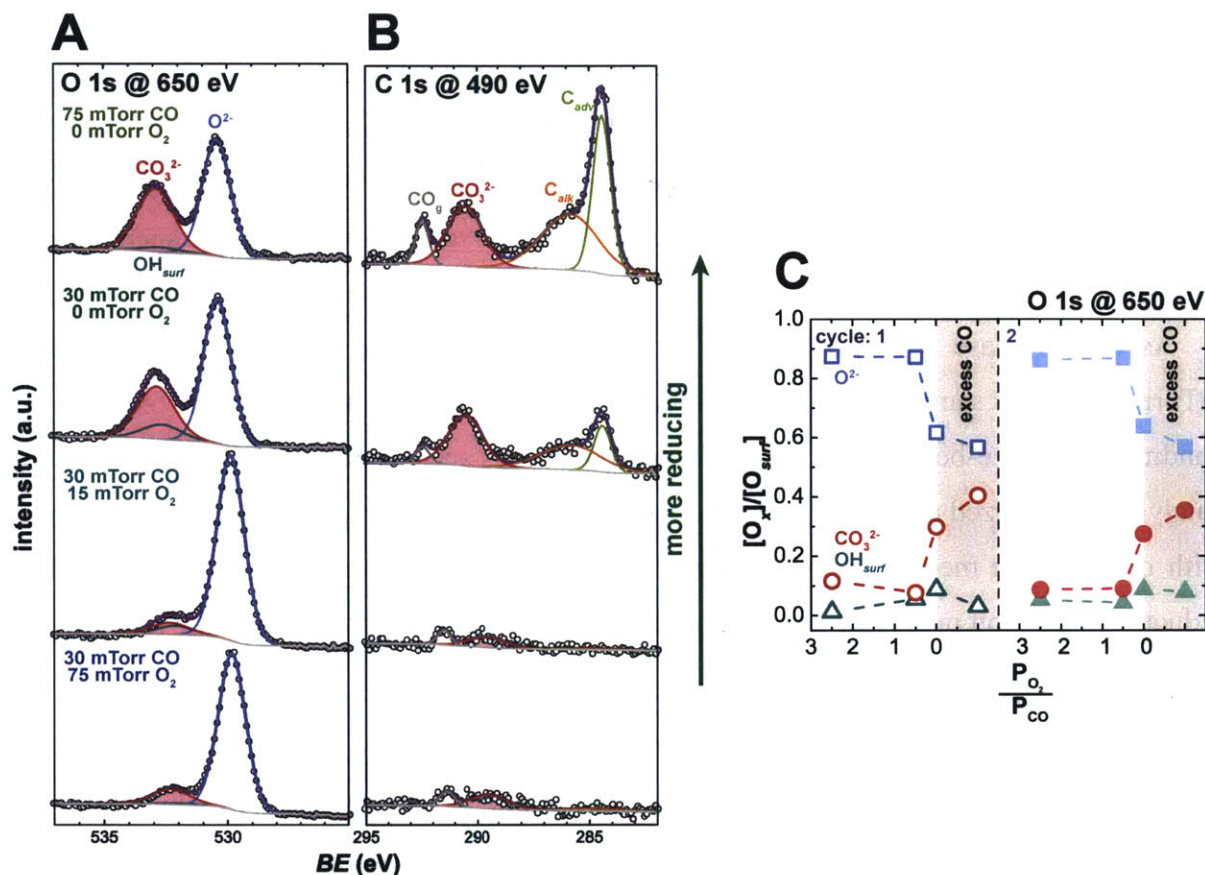


Figure 4.8 Fitted NAP-XPS spectra at four partial-pressure conditions at the (A) O 1s and (B) C 1s regions and (C) the surface-normalized intensities at the O 1s region as a function of oxygen partial pressure at 300 °C. The incident energies used for NAP-XPS were 490 eV (C 1s) and 650 eV (O 1s), and only data from the first cycle are displayed in A and B.

When the partial pressure of oxygen decreases to below stoichiometric (< 15 mTorr) values, the features associated with CO_3^{2-} in the C and O 1s regions increase in intensity at

the expense of the main O^{2-} feature at ~ 530 eV (Figure 4.8). Additionally, new peaks appear in the C 1s region at ~ 285 and ~ 286 eV, which are attributed to adventitious and alkyl-based carbonaceous species. Together, these trends are consistent with DRIFTS data and our proposed mechanism; under oxygen-rich conditions, the formation of CO_2 from the abstraction of a surface O atom is rate-determining. However, under oxygen-lean conditions, reforming the oxygen vacancy at the surface becomes rate-determining and the surface of the catalyst is poisoned by oxidized CO_3^{2-} intermediates which cannot desorb. The decrease in the intensity of the O^{2-} feature at ~ 530 eV could be attributed to either the loss of O^{2-} species at the surface as they are transferred to CO or to signal attenuation from the formation of a layer of CO_3^{2-} and coke under oxygen-lean conditions. A rigorous analysis of the data to rule out one of these hypotheses by a multilayer electron attenuation model is impossible, however, as the sample studied is a polycrystalline powder. Nevertheless, it is tempting to ascribe the decrease of the intensity of the O^{2-} feature to the formation of oxygen vacancies at the surface as steps 3 or 4 become the rate-determining step under oxygen-lean conditions. This question will be further addressed below using *in-situ* X-ray absorption spectroscopy (XAS).

As was the case with the DRIFTS data, upon reintroduction of 30 mTorr CO and 75 mTorr O_2 into the sample chamber, the spectra show very little hysteresis. Under oxygen-rich conditions, surface-bound CO_3^{2-} and other carbonaceous species desorb as the surface of the catalyst is reoxidized and surface oxygen vacancies are filled. These data are again consistent with our reaction mechanism and suggest that the catalyst surface can undergo reversible reduction/oxidation processes depending on the partial-pressure conditions of the system.

4.4 Structural Evolution of Cu in $Cu_yCe_{1-y}O_{2-x}$

In order to probe whether this special reversible reducibility may be attributed to the catalytically-active copper sites, we next turned our attention to *in-situ* XAS which gives us information on changes in the oxidation state and local structure of the copper site under catalytic conditions. XAS has emerged as an invaluable tool for the characterization of extended inorganic solids, where it gives information about the oxidation state, site symmetry and local coordination environment of the absorbing element in materials that may have limited long-range order, as is the case for $Cu_{0.1}Ce_{0.9}O_{2-x}$. As such, XAS is an invaluable tool when used *in-situ* or *operando* for the elucidation of reaction mechanisms in heterogeneous

catalysis due to its superior element specificity and the breadth of information about the absorbing atom.²¹ Shown in Figure 4.9A are spectral changes in the Cu K-edge XANES spectra of $Cu_{0.1}Ce_{0.9}O_{2-x}$ under different partial pressure conditions (0 – 0.01 atm CO and 0 – 0.025 atm O_2) at 300 °C. As we saw previously in Chapter 3, the XANES appears relatively unperturbed upon introduction of an oxygen-rich atmosphere (0.01 atm CO and 0.025 atm O_2) into the sample cell and subsequent heating compared to room-temperature air conditions (Figure 3.8 and Table 3.3), which suggests that the oxidation state of copper is unperturbed (2.8+) under catalytic conditions. As the partial pressure of oxygen is decreased below the stoichiometric amount (0.005 atm), however, the XANES shifts to lower energies with the appearance of a feature at ~8980 eV and the disappearance of the white line at ~9000 eV. These data are consistent with reduction at the copper center by as much as 1 electron (Figure 4.9B). The reduction at the copper appears to be completely reversible since the reintroduction of an oxygen-rich stream reverses the changes observed in the near edge. Cycling the conditions and superimposing the spectra in Figure 4.9A, it is clear that this reduction at the copper center is completely reproducible and the existence of two isosbestic points at ~8990 and ~9010 eV suggests that two copper species are in equilibrium under these conditions, presumably Cu^{3+} and Cu^{2+} sites.

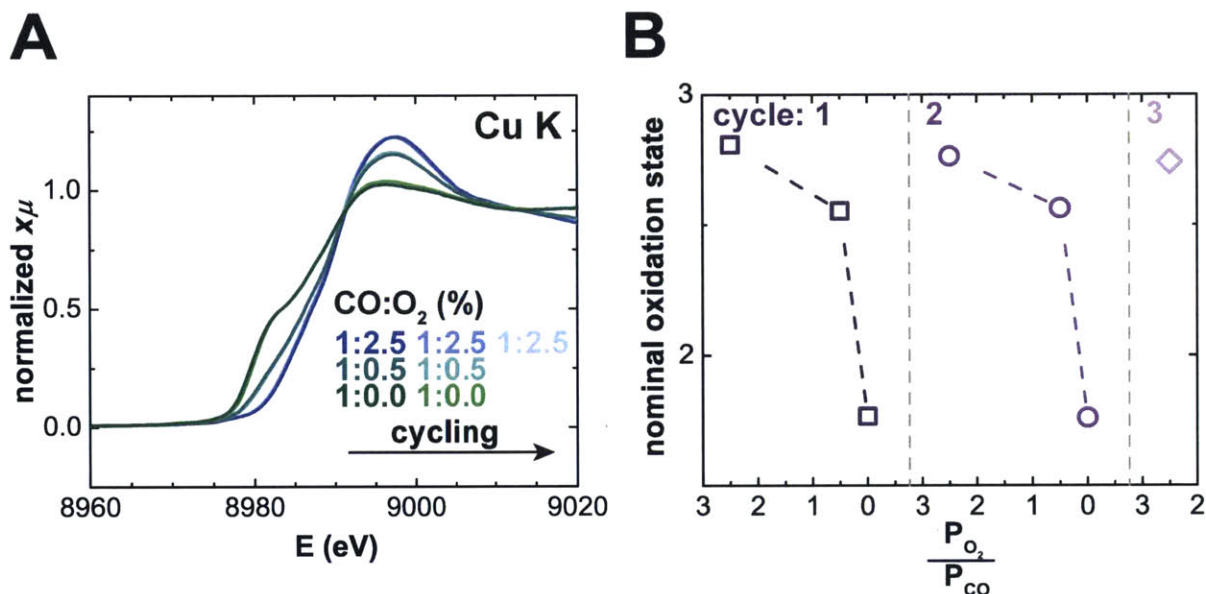


Figure 4.9 Cu K-edge XANES spectra of $Cu_{0.1}Ce_{0.9}O_{2-x}$ in 1% CO and 300 °C as a function of O_2 partial pressure cycling. The raw Cu K-edge spectra are given in (A), while (B) tracks the nominal oxidation state of the Cu absorber as a function of oxygen partial pressure.

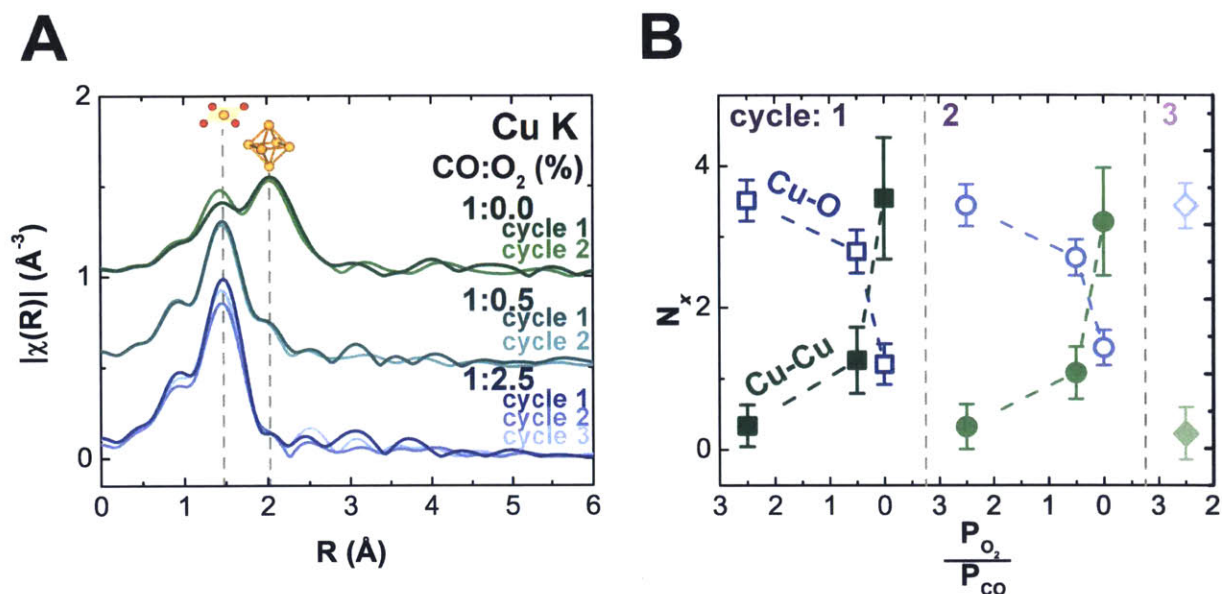


Figure 4.10 Structural changes in $\text{Cu}_{0.1}\text{Ce}_{0.9}\text{O}_{2-x}$ under CO oxidation conditions at 300 °C as measured by Cu K-edge EXAFS. (A) The k^2 -weighted magnitude of the Fourier transform of the EXAFS and (B) the extracted changes in the first coordination sphere of Cu in $\text{Cu}_{0.1}\text{Ce}_{0.9}\text{O}_{2-x}$ in 1% CO as a function of oxygen partial pressure.

Concurrent with changes observed in the Cu K-edge XANES are changes in the EXAFS of $\text{Cu}_{0.1}\text{Ce}_{0.9}\text{O}_{2-x}$ powders (Figure 4.10). As the partial pressure of oxygen is reduced, the magnitude of the main feature of the Fourier transform of the EXAFS at ~ 1.5 \AA decreases, which is ascribed to Cu-O scattering paths in the first coordination shell of square-planar CuO_4 motifs. Concomitant with this decrease in the magnitude of the Cu-O peak is the appearance of a new feature at 2.47 \AA (~ 2 \AA reduced distance in Figure 4.10A). While significantly shorter than the Cu-Cu bond length found in bulk metallic copper (2.56 \AA), it should be noted that the EXAFS Cu-Cu scattering path shortens with decreasing copper particle size, with scattering lengths found to be as low as 2.23 \AA in Cu_2 clusters and 2.33 \AA in 5 \AA copper clusters supported on carbon.^{22,23} Therefore, we are ascribing the feature at 2.47 \AA to Cu-Cu scattering in very small metallic copper clusters that form under reducing conditions. Again, cycling between conditions at 300 °C shows very little hysteresis in the EXAFS as demonstrated by the reappearance of the Cu-O scattering path and the disappearance of the Cu-Cu scattering path upon reintroduction of oxygen-rich atmospheres. Careful fitting of the EXAFS bears out these reversible structural changes as shown in Figure 4.10B. Under oxygen-rich conditions, copper is fully coordinated to four O^{2-} ligands. As the partial pressure of oxygen decreases, the copper ions lose up to three O^{2-} ligands in favor of

forming Cu-Cu bonds. Once an oxygen-rich stream is reintroduced, however, there is ample oxygen for the copper sites to bind once again to four O^{2-} ligands.

Taken together, these *in-situ* data support our hypothesis that under oxygen-rich conditions, elementary step 2 of our proposed mechanism (Figure 4.2) is rate-determining. Under these conditions, the copper ions appear to be fully oxidized (Cu^{3+}) and have full O^{2-} coordination since oxygen-ion-vacancy formation is rate-determining. However, under oxygen-lean conditions, desorption of the surface-bound CO_2 (step 3) or the refilling of the oxygen vacancy (step 4) is rate determining and so copper is predominantly reduced (to Cu^{2+} or below) and becomes coordinatively unsaturated. Therefore, it appears that the oxygen-vacancy formation energy, that is, the energy penalty for the removal of an oxygen atom and the reduction of the transition-metal(s) by two electrons, may serve as an important parameter to rationally design next-generation catalysts for CO oxidation. In order to further investigate this hypothesis and to flesh out some of the mechanistic details, we performed density-functional theory studies on model slabs of $\text{Cu}_{0.1}\text{Ce}_{0.9}\text{O}_{2-x}$.

4.5 Revisiting the Mechanism for CO Oxidation on $\text{Cu}_y\text{Ce}_{1-y}\text{O}_{2-x}$

In order to investigate the feasibility of our proposed Mars-van Krevelen mechanism (Figure 4.2) we turned to density functional theory (DFT) studies at the GGA + U level on reaction intermediates of model slabs of $\text{Cu}_{0.1}\text{Ce}_{0.9}\text{O}_{2-x}$. In the previous chapter, we employed GGA + U on {111}-terminated copper-substituted CeO_2 slabs to successfully rationalize the thermodynamic preference for copper ions to segregate to the surface as small Cu^{3+} clusters. Again, we turned to {111}-terminated slabs since this surface is the thermodynamically most stable and prevalent for nanoparticulate CeO_2 . The Cu^{3+} -substituted nn- $\text{Cu}_2\text{Ce}_{34}\text{O}_{71}$ slab was chosen as the starting configuration for the DFT studies since we have shown previously that it is the most stable configuration, which is verified by our *in-situ* EXAFS measurements above.

The reaction coordinate diagram as computed by DFT is summarized in Figure 4.11, which is analogous to our simplified mechanism (Figure 4.2) and to computed mechanisms for CO oxidation on Au/ CeO_2 catalysts.^{24,25} After binding of CO to a surface Cu^{3+} site in step 1, an adjacent oxygen atom is transferred exergonically to the adsorbed CO to form a bent CO_2 adduct to Cu (step 2). Desorption of the CO_2 gives the two-electron reduced surface with an oxygen vacancy adjacent to the copper site (step 3). A close inspection of the partial

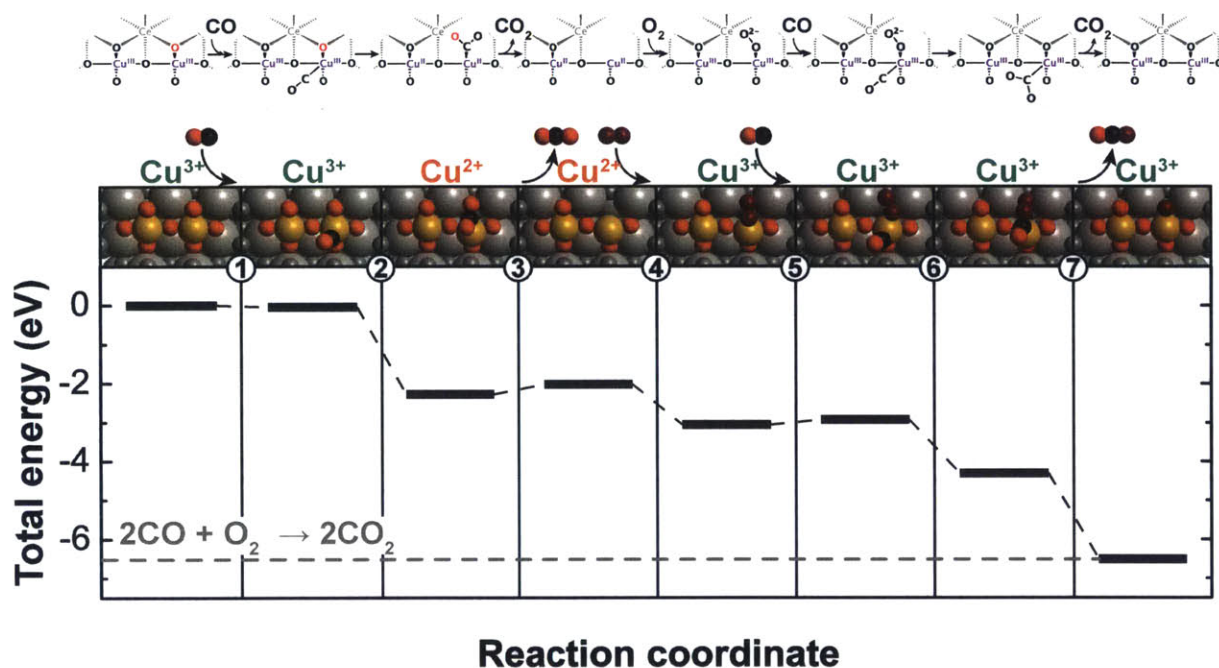


Figure 4.11 The DFT-computed reaction mechanism of CO oxidation on {111}-terminated $\text{Cu}_y\text{Ce}_{1-y}\text{O}_{2-x}$. For each step, the total energy is the sum of the slab (including bound adsorbates) and any non-participating adsorbates. The calculated total reaction energy for the overall reaction $2\text{CO} + \text{O}_2 \rightarrow 2\text{CO}_2$ is given by the dashed grey line. CO adsorbs to Cu^{3+} in step 1 followed by the oxygen-atom transfer in step 2 to form a bent CO_2 adduct. CO_2 desorbs in step 3 to leave an oxygen vacancy on the surface. O_2 adsorbs to this vacancy forming an O_2^{2-} intermediate (step 4), which then adsorbs the second equivalent of CO (step 5). A second oxygen-atom transfer to CO (step 6) gives another bent CO_2 intermediate, which desorbs in step 7 and closes the catalytic loop.

density of states of this two-electron reduced surface (Figure 4.12) suggests that the μ -oxo-linked copper sites accommodate the two electrons evenly such that the formal oxidation state for each site is $2+$. In step 4 an equivalent of O_2 adsorbs to the coordinatively-unsaturated copper site at the oxygen vacancy to form a bent peroxo (O_2^{2-}) adduct, thus reoxidizing the copper sites to Cu^{3+} . A second equivalent of CO adsorbs to the copper site (step 5) and, to relieve the instability of this copper intermediate, an oxygen atom is transferred from O_2^{2-} to CO to form a second bent CO_2 intermediate (step 6). In step 7 CO_2 desorbs exergonically (to relieve the unusual 5-fold coordinate copper geometry), thus refilling the oxygen vacancy and closing the catalytic loop. Compounds that are structurally analogous to the η^1 bent CO_2 adduct formed in step 2 of Figure 4.11 have been observed and isolated previously in both organometallic and bioinorganic systems. For example, the reaction of square planar PNP and PCP pincer complexes of Pt(II), Ir(II) and Ni(II)

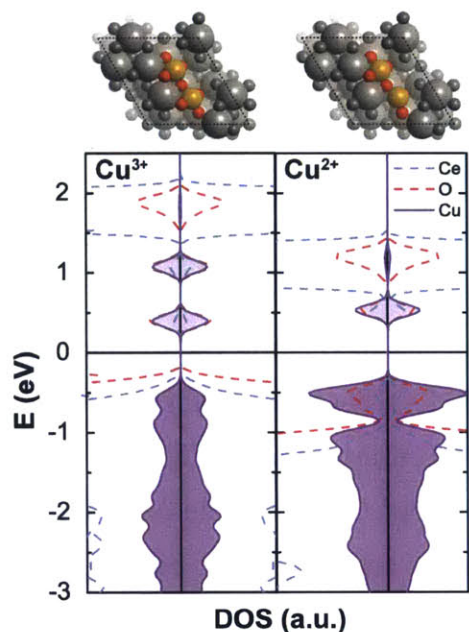


Figure 4.12 The density of states for oxidized ($\text{Cu}^{3+}_2\text{Ce}_{34}\text{O}_{71}$) and reduced ($\text{Cu}^{2+}_2\text{Ce}_{34}\text{O}_{71}$) as calculated for $\{111\}$ -terminated slab models for $\text{Cu}_{0.1}\text{Ce}_{0.9}\text{O}_{2-x}$. Highlighted in purple are the occupied and unoccupied partial density of states of copper parentage.

hydroxides with carbon monoxide yields isolable metal hydroxycarbonyl compounds that bear similarities to the bent CO_2 intermediate of Figure 4.11.²⁶⁻²⁸ Indeed, the insertion of CO into the metal-oxygen bond for these complexes mirrors the second elementary step of our mechanism (Figure 4.13). Certain organometallic complexes of Ir, Re and Fe have also been shown to coordinate CO_2 in a bent fashion,^{27,29,30} although to the best of our knowledge no such CO_2 or hydroxycarbonyl adducts of copper complexes exist in literature. Additionally, the CO_2 -bound intermediate of the enzyme carbon monoxide dehydrogenase (CODH II) has been isolated which clearly shows CO_2 coordinating to the nickel center of the $[\text{NiFe}_4\text{S}_5]$ cluster in a bent fashion η^1 through the carbon atom (see also Figure 5.7B).³¹

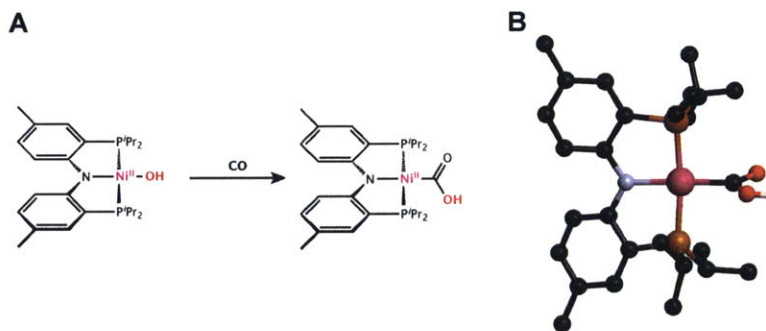


Figure 4.13 The hydroxide insertion reaction of carbon monoxide by a Ni(II) PNP pincer complex (A) and the crystal structure of the resulting η^1 hydroxycarbonyl adduct (B). Hydrogen atoms (besides the hydroxycarbonyl) are omitted for clarity. Crystallographic data are from reference 28.

The mechanism proposed in Figure 4.11 allows us to further refine what we could consider as an activity descriptor for CO oxidation on transition-metal-substituted ceria nanoparticles. We've investigated the energetics for the adsorption of CO onto Cu^{3+} sites (Figure 4.14) by DFT + U and found it to be barrierless and only mildly exergonic (50 meV). Since the subsequent intermediates are at least 2 eV more exergonic, it is likely that the second step, where CO abstracts an oxygen atom to form a bent CO_2 adduct, is the rate-determining step. Overall this step is downhill in energy since the oxidation of CO to CO_2 is exergonic by 2.67 eV (Equation 1.4), but there is still an energy penalty associated with the formation of an oxygen vacancy on the surface (Figure 4.11). According to the theory of linear-free-energy relationships, then, E_A for the rate determining step for CO oxidation and by extension the overall catalytic activity of the catalyst, is linearly dependent on this thermodynamic oxygen vacancy formation (E_{vac}). According to this hypothesis, in order to design better catalysts for CO oxidation one must tune the surface for an optimal E_{vac} .

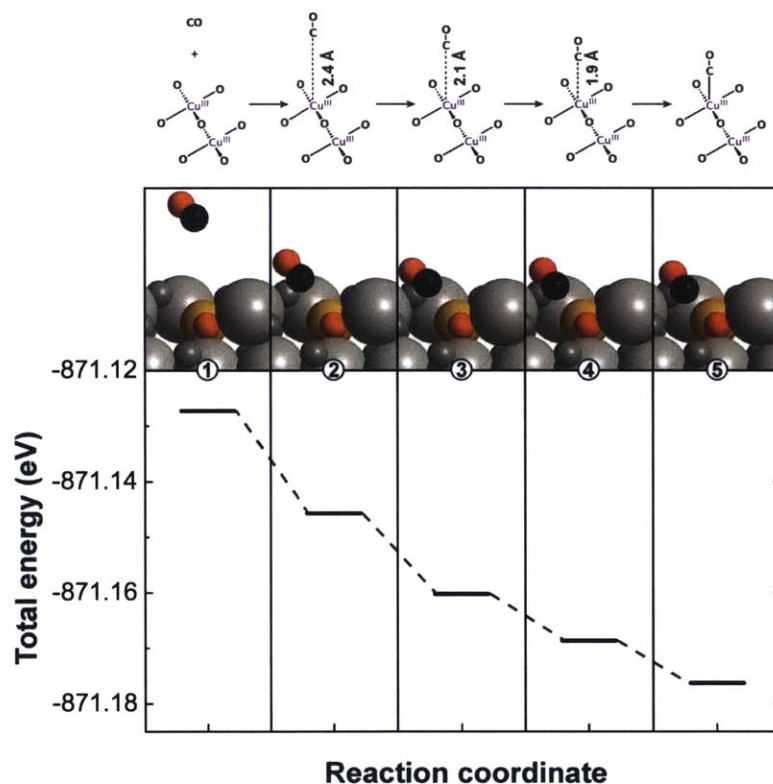


Figure 4.14 Reaction coordinate diagram for CO adsorption to nn- $\text{Cu}_2\text{Ce}_{34}\text{O}_{71}$. Intermediate 1 simulates non-interacting gaseous CO. Intermediates 2 – 4 were calculated by constraining the CO adsorbate 2.4, 2.1 and 1.9 Å from the copper center, while intermediate 5 represents fully adsorbed CO. Total energies ($\text{Cu}_2\text{Ce}_{34}\text{O}_{71} + \text{CO}$) along the adsorption pathway were calculated by constraining the z-height of the carbon of CO.

4.6 Conclusions

A suite of *in-situ* spectroscopic techniques support a mechanism for CO oxidation catalysis by $\text{Cu}_y\text{Ce}_{1-y}\text{O}_{2-x}$ in which lattice oxygen is directly transferred to copper-bound CO during the catalytic cycle. The proposed Mars-van Krevelen mechanism is analogous to the mechanisms introduced by Harrison and Martínez-Arias (Figure 1.6B and C),^{32,33} with a few notable exceptions. Firstly, we found that CO oxidation turns over at site-isolated, atomically-dispersed copper ions located at the surface of the $\text{Cu}_y\text{Ce}_{1-y}\text{O}_{2-x}$ phase, independent of bulk CuO as proposed by earlier research. More importantly, we show that Cu^{3+} plays a major role in catalysis. We propose that the stabilization of this high oxidation state of copper by the ceria lattice serves to reduce the energy penalty associated with forming an oxygen vacancy during the rate-determining step of the reaction mechanism. During this step, Cu^{3+} is reduced to Cu^{2+} and/or Cu^+ , which is reoxidized by subsequent dissociative oxygen reduction. Hence, the accessibility of the $\text{Cu}^{3+}/\text{Cu}^{2+}$ couple facilitates the electron transfer involved in CO oxidation catalysis.

Another related contributing factor to the resilience of $\text{Cu}_y\text{Ce}_{1-y}\text{O}_{2-x}$ catalysts is the structural fluxionality of the copper sites as seen by *in-situ* XAFS under different CO oxidation conditions. The Cu^{3+} species ordinarily present under oxygen-rich conditions can be reduced down to small clusters of metallic copper when exposed to oxygen-lean conditions, with very little hysteresis. In terms of linear free energy scaling relationships, we can leverage these observations to design catalysts for CO oxidation that meet technological requirements by recognizing that the reducibility of the transition-metal substituent may modulate the energetic penalties involved with the rate-determining step and hence the overall rate of the reaction.

4.7 Experimental Methods

General experimental considerations. All reagents were purchased from commercial vendors and were used without further purification. All synthetic manipulations were performed under ambient conditions unless otherwise noted. $\text{Cu}_{0.1}\text{Ce}_{0.9}\text{O}_{2-x}$ was obtained from the pyrolysis of heterobimetallic Schiff-base precursors as detailed in Chapter 2.

Kinetic orders for CO oxidation. Kinetic measurements of CO oxidation on $\text{Cu}_{0.1}\text{Ce}_{0.9}\text{O}_{2-x}$ nanoparticles were performed in a home-made 3.81 mm i.d. quartz plug-flow reactor. For each measurement, the catalyst powder (20 mg) was mixed with 1.705 g oven-

dried sand ($V_{bed} = 1.09 \text{ cm}^3$) and loaded into the center of the quartz tube along with a K-type thermocouple. The remaining volume of the quartz tube was filled with oven-dried sand. The compositions of the feed and down-stream gases were obtained by on-line gas chromatography (Agilent 490 with COX column and thermal conductivity detector). The catalyst was heated to the desired temperature under oxygen-rich conditions (0.01 atm CO and 0.025 atm O₂) and then the partial pressure dependence of CO and O₂ was recorded by measuring the catalytic conversion under different partial pressures of CO and O₂ according to

$$\% \text{ Conversion} = \frac{p_{\text{CO}_2}}{p_{\text{CO}} + p_{\text{CO}_2}} \cdot 100\%$$

where p_{CO} and p_{CO_2} , the partial pressures of CO and CO₂, were determined from the integrated peak areas of the respective gas peaks normalized to the internal He standard. Following each measurement, the volumetric flow rate of the gas upstream of the reactor was measured with a manual volumetric flowmeter. Mass-normalized rates of CO oxidation (in units of $\mu\text{mol CO s}^{-1} \text{g}_{cat}^{-1}$) were obtained from the data below 12.5% conversion according to

$$\begin{aligned} r_{mass} &= \frac{\frac{\% \text{ Conversion}}{100} r_{\text{CO}} \cdot 1000}{V_m \cdot 60 \cdot m_{cat}} \\ &= \frac{\% \text{ Conversion} \cdot r_{\text{CO}}}{6 \cdot V_m \cdot m_{cat}} \end{aligned}$$

where r_{CO} is the flow rate of CO of the feed stream (in mL min⁻¹), V_m is the molar volume of CO (from the ideal gas law, $V_m = RT/p$, in mol/L) and m_{cat} is the mass of the catalyst in grams.

Diffuse reflectance infrared Fourier transform spectroscopy (DRIFTS). DRIFTS measurements were performed in the mid-infrared with a Bruker Vertex 70 FT-IR spectrophotometer equipped with a Praying Mantis DRIFTS accessory (Harrick) using a high-temperature environmental chamber with KBr windows (Harrick model HVC-DRP-4). Approximately 110 mg of Cu_{0.1}Ce_{0.9}O_{2-x} (400 mesh) was loaded into the environmental chamber for the *in-situ* studies and was slowly heated to the desired temperature under a flow of 100 mL min⁻¹ He. Background spectra were collected on KBr powder at room temperature by averaging 32 scans. For each temperature condition, the gas was switched to the desired

partial-pressure condition at a constant flow rate of 100 mL min^{-1} and 32 sample scans were acquired after 15 minute equilibration.

Near ambient pressure X-ray photoelectron spectroscopy (NAP-XPS). NAP-XPS studies were carried out at beamline 9.3.2 at the Advanced Light Source (ALS) at Lawrence Berkeley National Laboratory (LBNL).³⁴ The $Cu_{0.1}Ce_{0.9}O_{2-x}$ powder (400 mesh) were sonicated in acetone, dropcast onto gold foil and were gently heated to remove excess solvent. After introduction into the sample chamber, each sample was exposed to an atmosphere of 75 mTorr O_2 and was slowly heated to 400 °C. Monitoring the C 1s region, samples were heated until no more surface carbon contamination was detected and was cooled to the desired temperature. C 1s, O 1s and Au 4f spectra were acquired after letting the desired partial pressures of CO and O_2 equilibrate in the chamber for 15 minutes. Shirley background correction was applied to the photoemission lines, which were fitted using a combined Gaussian/Lorentzian line shape according to the fitting model outlined in Tables 4.1 and 4.2. Binding energy calibration was performed by fitting the main feature of Au foil (Au 4f 7/2) to a binding energy of 84.0 eV.

Table 4.1 NAP-XPS fitting parameters for studies on $Cu_{0.08}Ce_{0.092}O_{2-x}$ and CeO_{2-x} in the C 1s region.

		C_{adv}	C_{alk}	$CO_{2\ ads}$	CO_g
$Cu_{0.08}Ce_{0.92}O_{2-x}$	% Lorentzian	30	30	30	30
	FWHH (eV)	0.8 - 1	2.8 - 3.1	1.75 - 2	0.8 - 1
	BE (eV)	284.5 - 284.4	$C_{adv} + 1.3925$	$C_{adv} + 6.0774$	$C_{adv} + 8.0133$
CeO_2 (5 nm)	% Lorentzian	30	30	30	30
	FWHH (eV)	0.8 - 1	2.5 - 2.75	1.75 - 2	0.8 - 1
	BE (eV)	285 - 283	$C_{adv} + 1.2782$	$C_{adv} + 5.9253$	$C_{adv} + 7.7511$

Table 4.2 NAP-XPS fitting parameters for studies on $Cu_{0.08}Ce_{0.092}O_{2-x}$ and CeO_{2-x} in the O 1s region.

		O^{2-}	OH^-	$CO_{2\ ads}$	O_2 (3/2)	O_2 (1/2)	CO_x
$Cu_{0.08}Ce_{0.92}O_{2-x}$	% Lorentzian	30	30	30	30	30	30
	FWHH (eV)	1.35 - 1.45	1.7 - 1.8	1.75 - 1.85	0.8 - 1.1	0.8 - 1.2	0.7 - 1
	BE (eV)	530.7-529.45	$O^{2-} + 2.2491$	$O^{2-} + 2.479$	$O^{2-} + 8.8882$	$O^{2-} + 9.9882$	$O^{2-} + 8.5497$
CeO_2 (5 nm)	% Lorentzian	30	30	30	30	30	30
	FWHH (eV)	1.35 - 1.45	2 - 2.3	1.3 - 1.5	0.8 - 1.1	0.8 - 1.2	0.7 - 1
	BE (eV)	530.7-529.45	$O^{2-} + 1.2815$	$O^{2-} + 2.479$	$O^{2-} + 8.8882$	$O^{2-} + 9.9882$	$O^{2-} + 8.5497$

X-ray absorption spectroscopy (XAS). X-ray absorption measurements at the transition-metal K-edges were performed at the bending magnet station X11A of the National

Synchrotron Light Source (NSLS) at Brookhaven National Laboratory.³⁵ The electron storage ring operated at 2.8 GeV with a stored current in the range of 200 – 300 mA. The excitation energies were selected with a double crystal monochromator (Si-(111)), which was detuned by 40% to suppress higher harmonics. The incident and transmitted beams were monitored using ionization chambers equilibrated with appropriate mixtures of nitrogen and argon gas. The energy calibration of the monochromator was set by calibrating the inflection point of the absorption spectrum of transition-metal foils to their literature values.³⁶

Copper K-edge spectra were acquired in fluorescence yield (FY) mode using a resistively-heated *in-situ* catalyst furnace equipped with a 5-grid Lytle fluorescence detector³⁷ (both from the EXAFS Company). For FY measurements, the signal passed through a silver Soller slit assembly prior to detection by the ionization chamber, which had a continuous flow of Ar. Pellets for *in-situ* studies were prepared by first sieving Cu_{0.1}Ce_{0.9}O_{2-x} (10.5 wt%), boron nitride (75.5 wt%) and high-surface area Vulcan XC-72 carbon (14 wt%, Cabot) to 400 mesh followed by thorough mixing and grinding with an agate mortar and pestle. 50 mg pellets (5 mm x 12 mm) were pressed and introduced into the catalyst furnace, the window of which was sealed with Kapton tape. Gas mixtures (CO and O₂ balanced in He) were flowed through the catalyst pellet by means of mass-flow controllers at flow-rates of 50 mL min⁻¹. For each catalyst, pellets were slowly heated to the desired temperature (200 or 300 °C) under lean conditions (0.01 atm CO and 0.025 atm O₂ at a flow rate of 50 mL min⁻¹) and gases were allowed to equilibrate for 15 minutes before the acquisition of XAFS spectra for each partial-pressure condition.

Absorption spectra were normalized using the Autobk algorithm found in the IFEFFIT program³⁸ of the Horae XAFS analysis suite.³⁹ First, a linear fit of the pre-edge line was subtracted from the spectrum. A fourth-order knot-spline polynomial was used to fit the post-edge line and the edge step was normalized to unity. Prior to Fourier transforms, the EXAFS was multiplied by a Hanning window covering the first and last ~10% of the data range, from $k = 3.7$ to 11.1 \AA^{-1} .

The model for fitting the copper K-edge EXAFS spectra of Cu_{0.1}Ce_{0.9}O_{2-x} at room temperature was described in Chapter 3, which takes into account the presence of two separate phases contributing to the EXAFS, namely metallic copper and copper oxide clusters. The EXAFS for all seven spectra acquired at 300 °C were fit by refining shared

values for $\sigma_{\text{Cu-Cu}}^2$, $\sigma_{\text{Cu-O}}^2$, $R_{\text{Cu-Cu}}$ and $R_{\text{Cu-O}}$ and the path degeneracies ($N_{\text{Cu-O}}$ and $N_{\text{Cu-Cu}}$) for each spectrum. The refinement was performed in R space from $R = 1$ to 3 \AA simultaneously with k -weights of 1, 2 and 3. The spectrum at $300 \text{ }^\circ\text{C}$ was fit in a similar way, simultaneously with six other spectra at $300 \text{ }^\circ\text{C}$, this time freely refining the σ_i^2 value for the metallic copper component.

Table 4.3 Parameters from the refinement of Cu K-edge EXAFS of $\text{Cu}_{0.1}\text{Ce}_{0.9}\text{O}_{2-x}$ powders under catalytically-relevant conditions at $300 \text{ }^\circ\text{C}$. Standard uncertainties in the last digits are included in parentheses.

Cycle	Gas Composition	$S_0^{2^a}$	E_0	$N_{\text{Cu-O}}$	$\sigma_{\text{Cu-O}}^b$ (\AA^2)	$R_{\text{Cu-O}}$ (\AA)	$N_{\text{Cu-Cu}}$	$\sigma_{\text{Cu-Cu}}^b$ (\AA^2)	$R_{\text{Cu-Cu}}$ (\AA)	R factor (%)
1	1% CO + 2.5% O ₂	0.90	-5(1)	3.5(3)	0.0065(9)	1.902(8)	0.3(3)	0.014(2)	2.467(8)	0.88
	1% CO + 0.5% O ₂	0.90	-5(1)	2.8(3)	0.0065(9)	1.89(1)	1.3(5)	0.014(2)	2.467(8)	0.88
	1% CO + 0% O ₂	0.90	-5(1)	1.2(3)	0.0065(9)	1.86(2)	3.6(9)	0.014(2)	2.467(8)	0.88
2	1% CO + 2.5% O ₂	0.90	-5(1)	3.5(3)	0.0065(9)	1.897(8)	0.3(3)	0.014(2)	2.467(8)	0.88
	1% CO + 0.5% O ₂	0.90	-5(1)	2.7(3)	0.0065(9)	1.891(8)	1.1(4)	0.014(2)	2.467(8)	0.88
	1% CO + 0% O ₂	0.90	-5(1)	1.4(3)	0.0065(9)	1.85(1)	3.2(8)	0.014(2)	2.467(8)	0.88
3	1% CO + 2.5% O ₂	0.90	-5(1)	3.4(3)	0.0065(9)	1.898(9)	0.2(4)	0.014(2)	2.467(8)	0.88

DFT + U calculations of {111}-terminated $\text{Cu}_2\text{Ce}_{34}\text{O}_{72-x}$ intermediates. The energies of {111}-terminated $\text{nn-Cu}^{(4-x)+}_2\text{Ce}_{34}\text{O}_{72-x}$ slabs were calculated using DFT employing GGA + U along with PAW pseudopotentials as described in Chapter 3. All calculations were performed using either the Cray XE6 (“Hopper”) or Cray XC30 (“Edison”) supercomputers at the National Energy Research Scientific Computing Center (NERSC). Models for the intermediates were based off of the most stable $\text{nn-Cu}^{3+}_2\text{Ce}_{34}\text{O}_{71}$ model found in Chapter 3. Atoms of carbon and oxygen were added and removed according to the mechanism. As before, a Hubbard U_{eff} on-site correction term of 4.0 eV was applied to the 4f orbitals of cerium to allow for an accurate description of the electronic structure of oxidized and reduced ceria. Also, a dipole correction was applied to the local potential to correct for systematic errors arising from periodic boundary conditions. Electronic and ionic optimization of the slabs was carried out using the conjugate gradient algorithm with a plane-wave cutoff of 400 eV within the VASP suite. All atomic layers were allowed to relax until all the forces acting on the atoms reached a value below 0.01 eV \AA^{-1} . Owing to the large size

^a The passive electron amplitude reduction factors S_0^2 were determined from the fitting of the EXAFS of the appropriate reference foils.

^b MSDs were determined from fitting the EXAFS of binary oxide references: Fe_2O_3 , Co_3O_4 , NiO and CuO.

of the slabs studied here, all data were reported from the integration of the Brillouin zone at the Γ point only.

4.8 References

- (1) Jia, A.-P.; Hu, G.-S.; Meng, L.; Xie, Y.-L.; Lu, J.-Q.; Luo, M.-F. *J. Catal.* **2012**, *289*, 199.
- (2) Jia, A.-P.; Jiang, S.-Y.; Lu, J.-Q.; Luo, M.-F. *J. Phys. Chem. C* **2010**, *114*, 21605.
- (3) Weckhuysen, B. M. *Chem. Soc. Rev.* **2010**, *39*, 4557.
- (4) Foster, A. J.; Lobo, R. F. *Chem. Soc. Rev.* **2010**, *39*, 4783.
- (5) Lamberti, C.; Zecchina, A.; Groppo, E.; Bordiga, S. *Chem. Soc. Rev.* **2010**, *39*, 4951.
- (6) Bollinger, M. A.; Vannice, M. A. *Appl. Catal., B* **1996**, *8*, 417.
- (7) Green, I. X.; Tang, W.; Neurock, M.; Yates, J. T. *Science* **2011**, *333*, 736.
- (8) Jia, C.-J.; Schwickardi, M.; Weidenthaler, C.; Schmidt, W.; Korhonen, S.; Weckhuysen, B. M.; Schüth, F. *J. Am. Chem. Soc.* **2011**, *133*, 11279.
- (9) Luo, J.-Y.; Meng, M.; Zha, Y.-Q.; Guo, L.-H. *J. Phys. Chem. C* **2008**, *112*, 8694.
- (10) Vayssilov, G. N.; Mihaylov, M.; Petkov, P. S.; Hadjiivanov, K. I.; Neyman, K. M. *J. Phys. Chem. C* **2011**, *115*, 23435.
- (11) Ogletree, D. F.; Bluhm, H.; Lebedev, G.; Fadley, C. S.; Hussain, Z.; Salmeron, M. *Rev. Sci. Instrum.* **2002**, *73*, 3872.
- (12) Salmeron, M.; Schlögl, R. *Surf. Sci. Rep.* **2008**, *63*, 169.
- (13) Frank Ogletree, D.; Bluhm, H.; Hebenstreit, E. D.; Salmeron, M. *Nucl. Instrum. Methods A* **2009**, *601*, 151.
- (14) Grass, M. E.; Zhang, Y.; Butcher, D. R.; Park, J. Y.; Li, Y.; Bluhm, H.; Bratlie, K. M.; Zhang, T.; Somorjai, G. A. *Angew. Chem. Int. Ed.* **2008**, *47*, 8893.
- (15) Tao, F.; Grass, M. E.; Zhang, Y.; Butcher, D. R.; Renzas, J. R.; Liu, Z.; Chung, J. Y.; Mun, B. S.; Salmeron, M.; Somorjai, G. A. *Science* **2008**, *322*, 932.
- (16) Jugnet, Y.; Loffreda, D.; Dupont, C. à. l.; Delbecq, F. à. ü.; Ehret, E.; Cadete Santos Aires, F. J.; Mun, B. S.; Aksoy Akgul, F.; Liu, Z. *J. Phys. Chem. Lett.* **2012**, *3*, 3707.
- (17) Toyoshima, R.; Yoshida, M.; Monya, Y.; Suzuki, K.; Mun, B. S.; Amemiya, K.; Mase, K.; Kondoh, H. *J. Phys. Chem. Lett.* **2012**, *3*, 3182.

- (18) Toyoshima, R.; Yoshida, M.; Monya, Y.; Kousa, Y.; Suzuki, K.; Abe, H.; Mun, B. S.; Mase, K.; Amemiya, K.; Kondoh, H. *J. Phys. Chem. C* **2012**, *116*, 18691.
- (19) Qadir, K.; Joo, S. H.; Mun, B. S.; Butcher, D. R.; Renzas, J. R.; Aksoy, F.; Liu, Z.; Somorjai, G. A.; Park, J. Y. *Nano Lett.* **2012**, *12*, 5761.
- (20) Toyoshima, R.; Yoshida, M.; Monya, Y.; Suzuki, K.; Amemiya, K.; Mase, K.; Mun, B. S.; Kondoh, H. *J. Phys. Chem. C* **2013**, *117*, 20617.
- (21) Singh, J.; Lamberti, C.; van Bokhoven, J. A. *Chem. Soc. Rev.* **2010**, *39*, 4754.
- (22) Montano, P. A.; Shenoy, G. K.; Alp, E. E.; Schulze, W.; Urban, J. *Phys. Rev. Lett.* **1986**, *56*, 2076.
- (23) Apai, G.; Hamilton, J. F.; Stohr, J.; Thompson, A. *Phys. Rev. Lett.* **1979**, *43*, 165.
- (24) Camellone, M. F.; Fabris, S. *J. Am. Chem. Soc.* **2009**, *131*, 10473.
- (25) Kim, H. Y.; Lee, H. M.; Henkelman, G. *J. Am. Chem. Soc.* **2011**, *134*, 1560.
- (26) Bennett, M. A.; Jin, H.; Willis, A. C. *J. Organomet. Chem.* **1993**, *451*, 249.
- (27) Lee, D. W.; Jensen, C. M.; Morales-Morales, D. *Organometallics* **2003**, *22*, 4744.
- (28) Yoo, C.; Kim, J.; Lee, Y. *Organometallics* **2013**, *32*, 7195.
- (29) Yang, Y.-L.; Chen, J.-D.; Lin, Y.-C.; Cheng, M.-C.; Wang, Y. *J. Organomet. Chem.* **1994**, *467*, C6.
- (30) Gibson, D. H.; Ye, M.; Sleadd, B. A.; Mehta, J. M.; Mbadike, O. P.; Richardson, J. F.; Mashuta, M. S. *Organometallics* **1995**, *14*, 1242.
- (31) Fessler, J.; Jeoung, J.-H.; Dobbek, H. *Angew. Chem. Int. Ed.* **2015**, *54*, 8560.
- (32) Harrison, P. G.; Ball, I. K.; Azelee, W.; Daniell, W.; Goldfarb, D. *Chem. Mater.* **2000**, *12*, 3715.
- (33) Martinez-Arias, A.; Fernandez-Garcia, M.; Galvez, O.; Coronado, J. M.; Anderson, J. A.; Conesa, J. C.; Soria, J.; Munuera, G. *J. Catal.* **2000**, *195*, 207.
- (34) Grass, M. E.; Karlsson, P. G.; Aksoy, F.; Lundqvist, M. n.; Wannberg, B. r.; Mun, B. S.; Hussain, Z.; Liu, Z. *Rev. Sci. Instrum.* **2010**, *81*, 053106.
- (35) Sayers, D. E.; Heald, S. M.; Pick, M. A.; Budnick, J. I.; Stern, E. A.; Wong, J. *Nucl. Instrum. Methods Phys. Res.* **1983**, *208*, 631.
- (36) Bearden, J. A.; Burr, A. F. *Rev. Mod. Phys.* **1967**, *39*, 125.

Chapter 4

- (37) Lytle, F. W.; Gregor, R. B. a. S. D. R.; Marques, E. C.; Wong, J.; Spiro, C. L.; Huffman, G. P.; Huggins, F. E. *Nucl. Instrum. Methods A* **1984**, 226, 542
- (38) Newville, M. J. *Synchrotron Radiat.* **2001**, 8, 322.
- (39) Ravel, B.; Newville, M. J. *Synchrotron Radiat.* **2005**, 12, 537.

Chapter 5 – A Design Descriptor for CO Oxidation on Substituted Ceria

5.1 Introduction

Through our investigations in Chapters 2 – 4, we have come to a more realistic understanding of the nature of the active site and catalytic mechanism at play for $\text{Cu}_y\text{Ce}_{1-y}\text{O}_{2-x}$ for CO oxidation catalysis. Motivated particularly by the reaction mechanism we proposed in Chapter 4 (Figure 4.11), in this chapter we seek to identify an activity descriptor for CO oxidation on this family of ceria-based catalysts. Such a descriptor-based approach to catalyst design, hinging on the linear free energy scaling relationships we introduced in Section 1.3, has been successfully used for perovskite oxide type catalysts for such diverse transformations as CO oxidation^{1,2} as well as oxygen electrocatalysis,^{3,4} but to the best of our knowledge, such an analysis hasn't been carried out for mixed-phase ceria-based catalysts. Indeed, up until recently the atomic structure of the active site has eluded identification and therefore has deemed such an analysis problematic. Our synthesis and characterization of phase-pure, monodisperse transition-metal-substituted CeO_2 ($\text{M}_{0.1}\text{Ce}_{0.9}\text{O}_{2-x}$, M = Mn, Fe, Co, Ni and Cu) nanoparticles in Chapter 2 has enabled a rigorous analysis of design descriptors for CO oxidation catalysis.

In this chapter, we propose that the oxygen-ion vacancy formation energy (E_{vac}) behaves as a suitable descriptor for CO oxidation on CeO_2 -based catalysts. We compare the intrinsic CO oxidation activity for our library of $\text{M}_{0.1}\text{Ce}_{0.9}\text{O}_{2-x}$ nanoparticles (M = Mn, Fe, Co, Ni and Cu) and find that turnover frequencies vary by over three orders of magnitude. In a qualitative sense, we can rationalize the trends in CO oxidation activity in terms of the expected reducibility of the transition-metal ion; the more reducible the transition-metal site, the more active it is to oxidize CO. Density functional theory implemented at the GGA + U level on (111)-oriented slab models rationalizes activity trends for $\text{M}_{0.1}\text{Ce}_{0.9}\text{O}_{2-x}$ and we introduce the E_{vac} as a suitable descriptor for CO oxidation catalysis, adding predictive power to the search for next-generation CO oxidation catalysts.

5.2 General Trends in CO Oxidation Activity for $\text{M}_{0.1}\text{Ce}_{0.9}\text{O}_{2-x}$

In order to quantify trends in the catalytic activity of $\text{M}_{0.1}\text{Ce}_{0.9}\text{O}_{2-x}$ nanoparticles, CO oxidation catalysis was performed under oxygen-rich conditions in a fixed-bed tube reactor. The light-off curves (Figure 5.1A) suggest that ceria nanoparticles substituted with late transition-metals (nickel and copper) oxidize carbon monoxide at temperatures nearly 100 degrees lower than with earlier transition-metals (cobalt, iron and manganese). $\text{Cu}_{0.1}\text{Ce}_{0.9}\text{O}_{2-x}$

and $\text{Ni}_{0.1}\text{Ce}_{0.9}\text{O}_{2-x}$ exhibit 100% conversion at 200 °C under a $1300 \text{ mL min}^{-1} \text{ g}^{-1}$ stream of 0.01 atm CO and 0.025 atm O_2 . The trends become clearer once the intrinsic catalytic activity per transition-metal site (the turnover frequency, TOF) is estimated by taking into account the surface-area and percent substitution of the transition-metal at the surface of ceria (Figure 5.1B). For a given TOF the activity follows the trend $\text{Cu} > \text{Ni} > \text{Co} \approx \text{Mn} > \text{Fe}$ with a remarkable difference of at least three orders of magnitude between $\text{Cu}_{0.1}\text{Ce}_{0.9}\text{O}_{2-x}$ and $\text{Fe}_{0.1}\text{Ce}_{0.9}\text{O}_{2-x}$. Consistent with these trends in overall rates for CO oxidation, the apparent activation energies (E_A) measured from the slope of these Arrhenius plots decreases nearly monotonically from the most active catalyst ($E_A = 40 \text{ kJ mol}^{-1}$ for $\text{Cu}_{0.1}\text{Ce}_{0.9}\text{O}_{2-x}$) to the least active catalyst ($E_A = 100 \text{ kJ mol}^{-1}$ for $\text{Fe}_{0.1}\text{Ce}_{0.9}\text{O}_{2-x}$, Table 5.2).

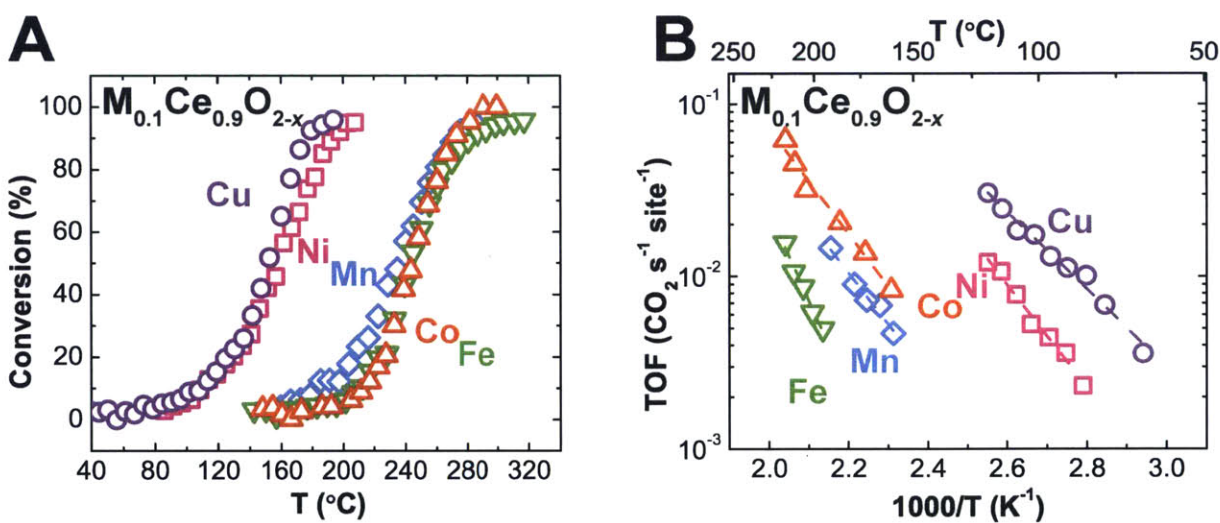


Figure 5.1 CO oxidation catalysis on $\text{M}_{0.1}\text{Ce}_{0.9}\text{O}_{2-x}$ nanoparticles; (A) light-off curves and (B) site-normalized Arrhenius plots for CO oxidation under CO lean conditions. Rates were measured at a flow rate of $1300 \text{ mL min}^{-1} \text{ g}^{-1}$ and with 0.01 atm CO and 0.025 atm O_2 balanced in He. TOFs were estimated assuming homogeneous transition-metal substitution in $\text{M}_{0.1}\text{Ce}_{0.9}\text{O}_{2-x}$.

These data indicate that the catalytic trends are due to intrinsic differences in the energetics of the reaction intermediates along the mechanism for CO oxidation on these catalysts and not simply due to differences in active site dispersion between the catalysts, which would be associated with the pre-exponential factor A for the rate constant. The partial-pressure dependence of CO oxidation catalysis on the $\text{M}_{0.1}\text{Ce}_{0.9}\text{O}_{2-x}$ materials was also investigated (Figure 5.2). With the exception of $\text{Co}_{0.1}\text{Ce}_{0.9}\text{O}_{2-x}$, all catalysts exhibited zeroth-order kinetics with respect to oxygen and fractional-order kinetics with respect to carbon monoxide. These data suggest that the presence of pre-adsorbed CO on the surface

contributes to the rate-determining step of the reaction mechanism, while the adsorption of oxygen doesn't, which is consistent with the Mars-van Krevelen type mechanism for CO oxidation that we proposed in the previous chapter (Figure 4.2).

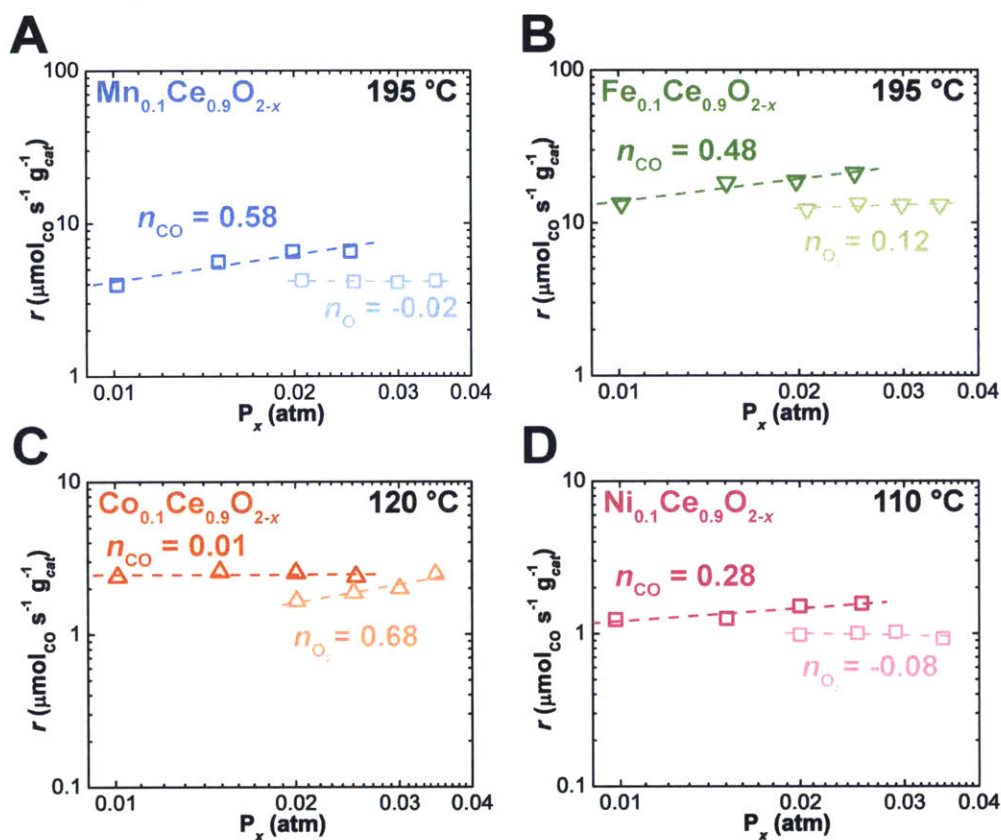


Figure 5.2 The partial pressure dependence of CO oxidation on $M_{0.1}Ce_{0.9}O_{2-x}$ catalysts; (B) $Mn_{0.1}Ce_{0.9}O_{2-x}$ at 195 °C, (B) $Fe_{0.1}Ce_{0.9}O_{2-x}$ at 195 °C, (C) $Co_{0.1}Ce_{0.9}O_{2-x}$ at 120 °C and (D) $Ni_{0.1}Ce_{0.9}O_{2-x}$ at 120 °C. Reaction rates were measured with flow rates of $1300 \text{ mL min}^{-1} \text{ g}^{-1}_{cat}$ for 20 mg catalyst loadings, holding either the partial pressure of CO (0.01 atm) or O_2 (0.025 atm) constant while varying the partial pressure of the other gas.

The local atomic and electronic structure of the transition metal in this series of materials was characterized by X-ray absorption spectroscopy in Chapter 2. We found that the transition metal substitutes into the cubic ceria host lattice as four-coordinate square-planar MO_4 motifs with oxidation states close to 3+. Given the trends in catalytic activity and the partial-pressure dependence in $M_{0.1}Ce_{0.9}O_{2-x}$ nanoparticles, it is tempting to describe CO oxidation catalysis on these materials using pre-existing periodic trends. For example, if we assume all transition-metal active sites are in their trivalent form, the catalytic activity follows the expected reduction behavior of the transition-metal; Cu^{3+} is the easiest species to reduce, followed by Ni^{3+} , Co^{3+} , Mn^{3+} and finally Fe^{3+} (which has a half-filled 3d shell). This

qualitative description of the catalytic activity of these compounds would be consistent with elementary step 2 of our proposed reaction mechanism being rate-determining, where an oxygen atom from the surface of the oxide is transferred to the adsorbed carbon monoxide thereby reducing the surface of the catalyst by two electrons and forming an oxygen-ion vacancy. Indeed, the simple microkinetic solution to the Mars-van Krevelen mechanism proposed in Figure 4.2 using reaction step 2 as the rate-determining step gives the following rate law:

$$r = \frac{k_2 K_{\text{CO ads}} P_{\text{CO}}}{1 + K_{\text{CO ads}} P_{\text{CO}}} \quad (5.1)$$

At sufficiently low pressures, the rate law follows zeroth-order kinetics for O₂ and first-order kinetics for CO (see Appendix A.1 for full derivation of Equation 5.1), which is consistent with our experimentally-determined kinetic orders (Figure 5.2). Furthermore, carrying out the micokinetic analysis assuming that any of the other steps are rate-determining gives theoretical kinetic orders inconsistent with our measured partial pressure dependences. Recently, similar Mars-van Krevelen mechanisms have been proposed for CO oxidation on CuO/CeO₂ catalysts where CO adsorbs onto dispersed CuO crystallites, migrates to the CuO/CeO₂ interface where CO gets oxidized from a lattice oxygen of CeO₂ origin.⁵⁻⁸ Along with our previous study on the active site for CO oxidation in CuO/CeO₂-based catalysts in Chapter 3, we propose here that no crystallographic interface between CuO and CeO₂ is required for the high catalytic activity of these catalysts. Rather, dispersed Cu³⁺ sites on the surface of the single-phase Cu_{0.1}Ce_{0.9}O_{2-x} catalyst are responsible for the adsorption and subsequent oxidation of CO by adjacent surface oxygen ions without CO migration along a separate CuO phase. These studies also highlight the importance of having copper stabilized in the trivalent oxidation state to afford highly-active catalysts. In order to further rationalize the trends we see in CO oxidation catalysis (Figure 5.1), we turned our attention to the calculation of oxygen-vacancy formation energies (E_{vac}) from DFT. As we have discussed previously in Section 4.5, E_{vac} describes the energy penalty associated with the structural rearrangement and reduction of the transition-metal active site during the rate-determining step of our proposed reaction mechanism (step 2 in Figure 4.2). Since E_{vac} is associated with the energetics of intermediates involved with the rate-determining step, we

propose that a change in E_{vac} will dramatically affect the kinetics of CO oxidation through the linear free-energy scaling relationships we introduced in Section 1.3 (Figure 1.2A).

5.3 E_{vac} as a Descriptor for CO Oxidation on $M_{0.1}Ce_{0.9}O_{2-x}$

To extend this hypothesis to ceria catalysts with other transition-metal substitution, $\{111\}$ -terminated slab models with 6% M (M = Mn, Fe, Co and Ni) substitution at the surface were investigated with DFT + U . Consistent with our previous XAFS previous characterization of the $M_{0.1}Ce_{0.9}O_{2-x}$ catalysts in Chapter 2, all of the transition-metals investigated here have a thermodynamic preference to exist in the 3+ oxidation state in ceria under annealing conditions (Figure 5.3), where they exhibit the familiar μ -oxo-bridged, square-planar coordination to oxygen atoms that we found for nn- $Cu_2Ce_{34}O_{71}$ (Figure 5.4).

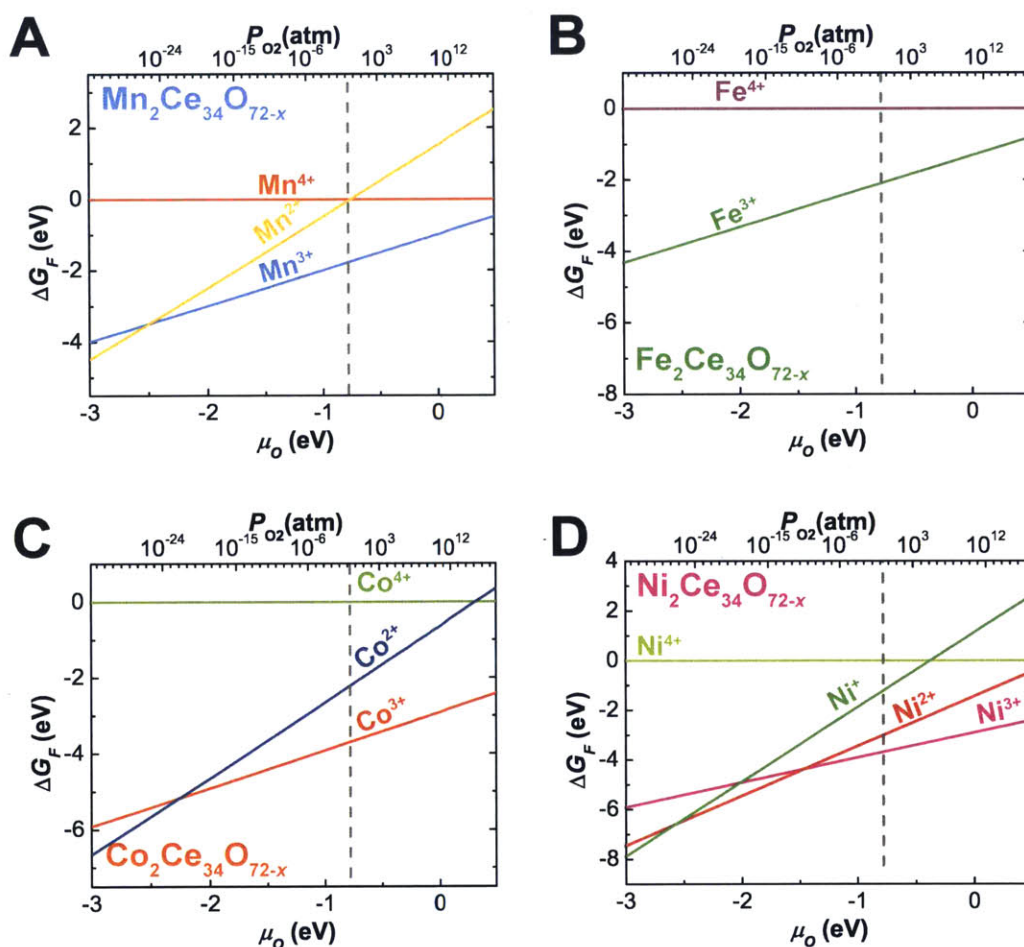


Figure 5.3 Calculated phase diagrams for $\{111\}$ -terminated nn- $M_2Ce_{34}O_{72-x}$ model slabs for M = (A) Mn, (B) Fe, (C) Co and (D) Ni. Gibbs free energies of formation, relative to nn- $M_2Ce_{34}O_{72}$ for each metal, were computed at 700 K with energies calculated at the DFT + U level of theory. The dashed grey lines correspond to 0.21 atm O_2 .

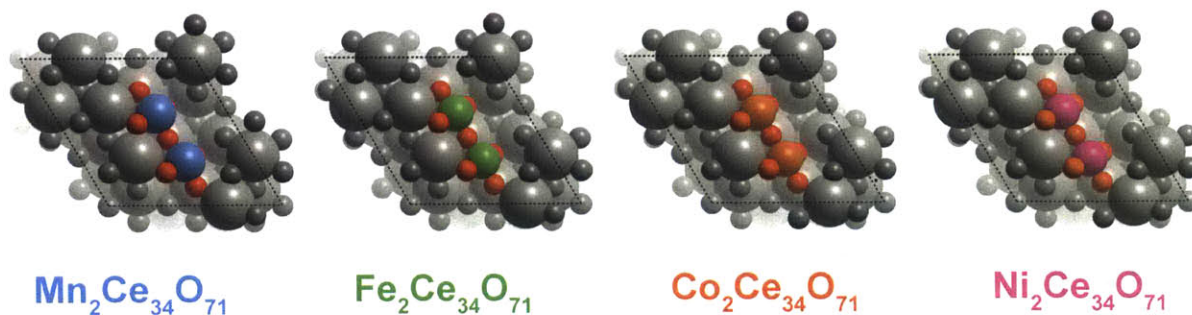


Figure 5.4 The lowest energy structures calculated for $\{111\}$ -terminated $\text{nn-M}_2\text{Ce}_{34}\text{O}_{72-x}$ slabs at 700 K and 0.21 atm O_2 , as determined by **Figure 5.3**.

Next, E_{vac} was calculated for each model slab according to Figure 5.5 with the exception of the model for $\text{Fe}_{0.1}\text{Ce}_{0.9}\text{O}_{2-x}$ since the structure of the Fe^{2+} surface would not converge to a global minimum. Nevertheless, plotting the measured turnover frequency for each catalyst at 100 °C from Figure 5.1B as a function of its calculated E_{vac} shows the expected trend (Figure 5.6). For this library of ceria-based catalysts, the measured catalytic activity increases with decreasing E_{vac} , which is consistent with our initial chemical intuition; the more reducible the transition-metal, the faster the rate-determining step is and hence the better the catalyst it is (Figure 5.6). It should be noted (somewhat optimistically) that the TOF increases monotonically with decreasing E_{vac} without reversing direction. That is to say, Figure 5.6 represents the “strong binding” side of the Sabatier plot; at some optimal value for E_{vac} we expect the catalytic activity for CO oxidation to start decreasing with decreasing E_{vac} in accordance with the Sabatier principle we’ve discussed in Section 1.3. Thus, to design potentially better catalysts for CO oxidation, we must tune E_{vac} to be smaller than that found for $\text{Cu}_{0.1}\text{Ce}_{0.9}\text{O}_{2-x}$ (~ 0.85 eV) but we don’t know when E_{vac} will be small enough so that another elementary step becomes rate-determining and the activity decreases.

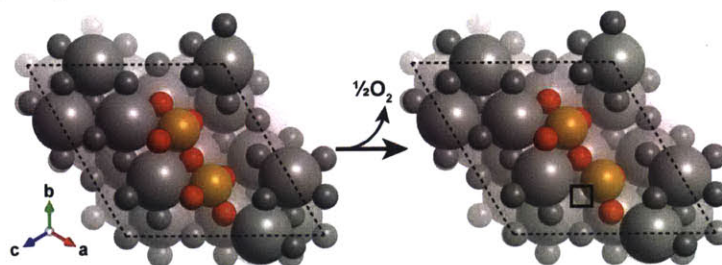


Figure 5.5 Oxygen vacancy formation in $\{111\}$ -terminated slabs of $\text{M}_2\text{Ce}_{34}\text{O}_{71}$.

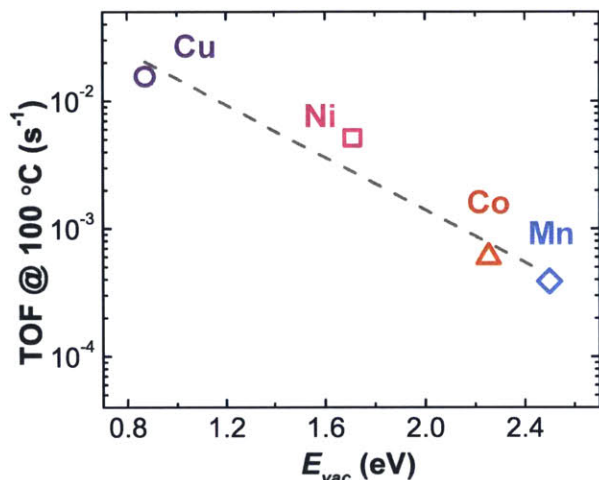


Figure 5.6 Turnover frequencies for $M_{0.1}Ce_{0.9}O_{2-x}$ measured at 100 °C as a function of the calculated oxygen ion vacancy formation energies of $M_2Ce_{34}O_{71}$.

5.4 Going Beyond $Cu_{0.1}Ce_{0.9}O_{2-x}$ and E_{vac}

In the previous section, we determined that the energy penalty involved with the formation of an oxygen vacancy (E_{vac}), as determined by DFT + U calculations, serves as a suitable descriptor for CO oxidation on ceria-based materials. In theory, Figure 5.6 serves as a training set and the search for more active catalysts can now be performed through computational, rather than experimental, screening. Since the substituted ceria we measured fall in the “strong binding” regime of the Sabatier curve, the search for better catalysts amounts to decreasing E_{vac} to values below those for $Cu_{0.1}Ce_{0.9}O_{2-x}$ (0.85 eV). Table 5.1 shows the calculated values for E_{vac} for a small selection of candidate $M_2Ce_{34}O_{72-x}$ slabs. While none of the structures would give activities greater than that for $Cu_{0.1}Ce_{0.9}O_{2-x}$ based on E_{vac} , DFT + U predicts that rhodium, gold and mercury-substituted CeO_2 would have vacancy formation energies between those for $Cu_{0.1}Ce_{0.9}O_{2-x}$ and $Ni_{0.1}Ce_{0.9}O_{2-x}$. While rhodium-substituted CeO_2 has been studied as an effective catalyst for CO oxidation,⁹ the prohibitive high cost of rhodium precludes it from wide-spread application in low-temperature CO oxidation. As far as we can tell from literature searches, mercury(II)-substituted CeO_2 hasn’t been studied for CO oxidation so far, and hence may be a viable candidate for low temperature catalysis.

Table 5.1 Calculated oxygen vacancy formation energies for substituted slabs of {111}-terminated CeO₂.

Candidate	Stable Oxidation State	E_{vac} (eV)
Rh ₂ Ce ₃₄ O _{72-x}	3+	1.00
Au ₂ Ce ₃₄ O _{72-x}	3+	1.09
Hg ₂ Ce ₃₄ O _{72-x}	2+	1.16
Pd ₂ Ce ₃₄ O ₇₂₋	2+	3.06

According to Table 5.1, we would expect gold-substituted ceria to have a catalytic activity lower than that of Cu_{0.1}Ce_{0.9}O_{2-x}. As we've discussed in Section 1.5.1, however, optimized gold-based catalysts, including Au/CeO₂,¹⁰ most likely go through a reaction mechanism that involves the interface between CeO₂ and bulk metallic Au. A recent DFT + *U* study modeling CO oxidation catalysis on Au clusters on CeO₂ surfaces found that the Mars-van Krevelen mechanism analogous to the mechanism we proposed in Chapter 4 would have activation energies prohibitively high (≥ 2.17 eV) compared to mechanisms that involve the direct reaction of coadsorbed CO and O₂ (0.08 – 0.33 eV).¹¹ In other words, the slab model of Au₂Ce₃₄O_{72-x} doesn't reflect the actual structure of multi-phase Au/CeO₂ catalysts, which leverage structurally complex interfaces to optimize CO oxidation catalysis.

While our investigation into the reactivity of substituted ceria nanoparticles has lead us to consider E_{vac} as a viable activity descriptor for CO oxidation, we must once again mention the potential shortcomings of linear free energy scaling relationships. As we've already seen in the case of Au/CeO₂, the construction of Sabatier plots such as Figure 5.6 implies that the design descriptor is only valid if the catalyst follows identical reaction mechanisms and that the structural model of the catalyst surface is accurate. Implicit in Figure 5.6 is an optimized catalyst at the apex of a Sabatier plot in which lattice oxygen binds neither too strongly (as in the case of the late first-row transition-metal ions studied in this chapter) nor too weakly. Such an optimized catalyst most certainly would have activities less than that given by the *y*-intercept of Figure 5.6, where there is no energy penalty associated with the formation of an oxygen vacancy. For this hypothetical catalyst, the activity towards CO oxidation would only be an order of magnitude greater than that for Cu_{0.1}Ce_{0.9}O_{2-x} (0.12 s⁻¹ at 100 °C compared to 0.016 s⁻¹ for Cu_{0.1}Ce_{0.9}O_{2-x}), which is not sufficient to replace gold-based materials in terms of catalytic activity (Figure 1.5). To design compounds with drastically higher catalytic

activities requires breaking the linear free-energy scaling relationships associated with substituted ceria nanoparticles. In terms of our proposed reaction mechanism (Figure 4.11), the activation energy associated with the rate-determining step is linearly dependent on the change in the free energy of the elementary step through Equation 1.3. In a simplified picture, ΔG for the rate-determining step is associated with the sum of the enthalpic contributions associated with making the chemical bonds in the bound CO_2 ($\Delta H < 0$ kJ/mol) and breaking transition-metal-oxygen bonds ($\Delta H > 0$ kJ/mol). In our model, the bound CO_2 intermediate is common for all transition metals, and ΔG is only a function of the enthalpic penalty (E_{vac}), which we can only modulate by changing the transition-metal. However, any additional interaction that stabilizes the CO_2 -bound intermediate in Figure 4.11 serves to make ΔG of the elementary step more favorable and, according to Equation 1.3, speeds up the overall rate of catalysis. In this sense, the scaling relationships that dictate optimal catalytic activity can be broken if the active site for catalysis is modified so as to introduce orthogonal functional groups that stabilize the intermediate without altering the energetics of adsorption.

It is perhaps no surprise then that, after millions of years of evolutionary optimization, nature has designed efficient CO oxidation catalysts that break scaling relationships through second coordination interactions. At the heart of the metabolic machinery for anaerobic microorganisms such as *Moorella thermoacetica* and *Carboxydotherrmus hydrogenoformans* is carbon monoxide dehydrogenase II (CODH II), an enzyme that contains a distinct $[\text{NiFe}_4\text{S}_5]$ cluster at the active site for the reversible interconversion of CO (as a source of energy) with CO_2 (as a source of carbon). Remarkably, CODH II has been shown to oxidize CO at turnover frequencies in excess of 40000 s^{-1} .¹² Crystallographic studies have supported a reaction mechanism and key reaction intermediate not dissimilar to the mechanism we proposed in Chapter 4 for CO oxidation (Figure 5.7).¹³ Additionally, second coordination sphere interactions in CODH II, specifically hydrogen-bonding networks, seem to play a crucial role in stabilizing the key CO_2^- intermediate (Figure 5.7B). Proton-donating histidine and lysine residues, in concert with a Lewis acidic iron center, are optimally poised in the second coordination sphere of the $[\text{NiFe}_4\text{S}_5]$ cluster to aid in the stabilization of bent CO_2^- , thereby speeding up the oxidation reaction to CO_2 .¹⁴ Computational studies have argued that the stabilizing interactions between bound CO_2 and the proton-donating second coordination

sphere of CODH II break linear free energy scaling relationships that ordinarily restrict the binding strengths of key reaction intermediates (COOH and CO) to solid catalysts.¹⁵

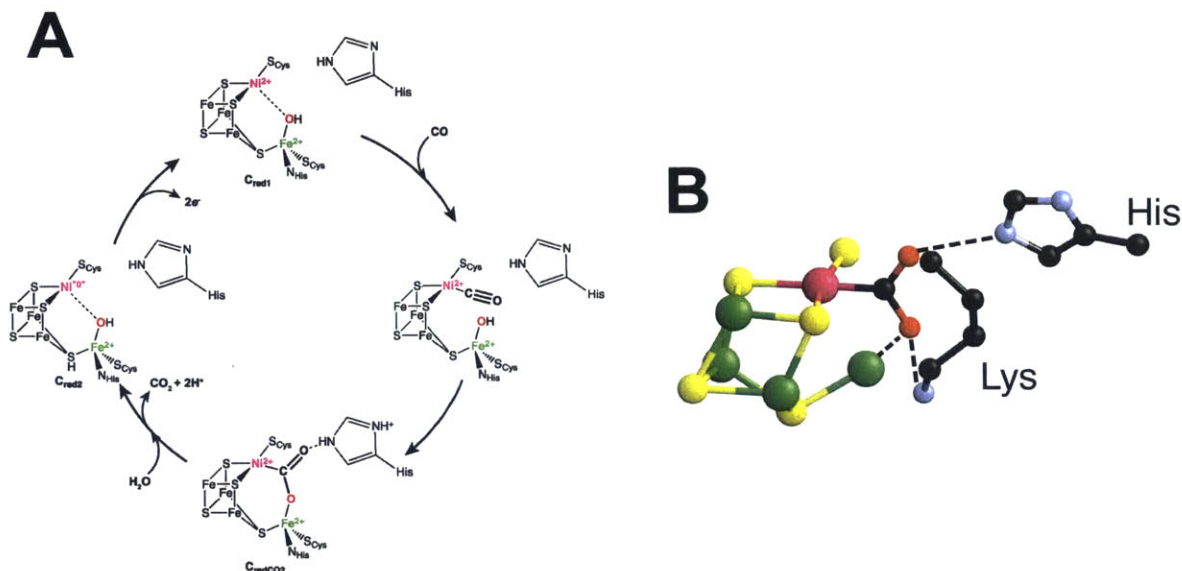


Figure 5.7 Reversible CO oxidation at the C cluster of CODH II; (A) the proposed mechanism and (B) the structure of the key reactive intermediate (C_{redCO_2}) from crystallography. Hydrogen atoms are omitted for clarity. Crystallographic data are from reference 13.

Thus, a potential strategy for breaking the scaling relationships inherent in CO oxidation catalysis on substituted ceria catalysts would be the introduction of a hydrogen-bonding secondary coordination sphere that stabilizes the bent CO_2 adduct we've also proposed to be the key intermediate for CO oxidation (Figure 4.11). In this way, the surface functionalization of solid catalysts will be an attractive strategy for the modulation of reaction kinetics through the stabilization of previously inaccessible reactive intermediates.

5.5 Conclusions

In this chapter, we show that the oxygen-vacancy formation energy (E_{vac}) is a suitable descriptor for CO oxidation catalysis on ceria-based materials, with $Cu_{0.1}Ce_{0.9}O_{2-x}$ exhibiting the highest activity of the catalysts measured with $E_{vac} = 0.85$ eV. Taken with the discussion of the mechanism for CO oxidation $Cu_{0.1}Ce_{0.9}O_{2-x}$ in Chapter 4, the high catalytic activity of mixed-phase CuO/CeO_2 catalysts originates not from interfacial interactions, but rather from the stabilization of Cu^{3+} sites in these materials.

These results suggest a strategy for the rational design of next-generation catalysts for CO oxidation by decreasing E_{vac} for example by further substitution of Zr^{4+} into $Cu_{0.1}Ce_{0.9}O_{2-x}$, which has been demonstrated to lower the vacancy formation energy in pure ceria.¹⁶ An

equally promising strategy to increase the catalytic turnover in these materials involves stabilizing the high-energy intermediate associated with the rate-determining step (the third panel of Figure 4.11). Taking a cue from catalytic centers prevalent in bioinorganic chemistry such as the C cluster of CODH-II, the development of second-coordination sphere interactions through surface functionalization of catalysts such as $\text{Cu}_{0.1}\text{Ce}_{0.9}\text{O}_{2-x}$ is critical to enable the breaking of restricting linear free-energy scaling relationships that exist for CO oxidation.

5.6 Experimental Methods

General experimental considerations. All reagents were purchased from commercial vendors and were used without further purification. All synthetic manipulations were performed under ambient conditions unless otherwise noted. Powders of $\text{M}_{0.1}\text{Ce}_{0.9}\text{O}_{2-x}$ (M = Mn, Fe, Co, Ni, Cu) were obtained from the pyrolysis of heterobimetallic Schiff-base precursors as detailed in Chapter 2.

CO oxidation catalysis. Kinetic measurements of CO oxidation on $\text{M}_{0.1}\text{Ce}_{0.9}\text{O}_{2-x}$ nanoparticles were performed in a home-made 3.81 mm i.d. quartz plug-flow reactor. For each measurement, the catalyst powder (20 mg) was mixed with 1.705 g oven-dried sand ($V_{bed} = 1.09 \text{ cm}^3$) and loaded into the center of the quartz tube along with a K-type thermocouple. The remaining volume of the quartz tube was filled with oven-dried sand. The compositions of the feed and down-stream gases were obtained by on-line gas chromatography (Agilent 490 with COX column and thermal conductivity detector). After cooling the catalyst bed to room temperature, a stream of 0.01 atm CO and 0.025 atm O_2 balanced in He was passed through the catalyst with the use of mass-flow controllers and the catalyst was gradually heated, recording gas chromatographs and catalyst bed temperatures every 5 °C. The percent conversion of CO to CO_2 was determined according to

$$\% \text{ Conversion} = \frac{p_{\text{CO}_2}}{p_{\text{CO}} + p_{\text{CO}_2}} \cdot 100\%$$

where p_{CO} and p_{CO_2} , the partial pressures of CO and CO_2 , were determined from the integrated peak areas of the respective gas peaks normalized to the internal He standard. Following each catalytic measurement, the volumetric flow rate of the gas upstream of the reactor was measured with a manual volumetric flowmeter. Mass-normalized rates of CO

oxidation (in units of $\mu\text{mol CO s}^{-1}\text{g}_{\text{cat}}^{-1}$) were obtained from the data below 12.5% conversion according to

$$r_{\text{mass}} = \frac{\frac{\% \text{ Conversion}}{100} r_{\text{CO}} \cdot 1000}{V_m \cdot 60 \cdot m_{\text{cat}}}$$

$$= \frac{\% \text{ Conversion} \cdot r_{\text{CO}}}{6 \cdot V_m \cdot m_{\text{cat}}}$$

where r_{CO} is the flow rate of CO of the feed stream (in mL min^{-1}), V_m is the molar volume of CO (from the ideal gas law, $V_m = RT/p$, in mol/L) and m_{cat} is the mass of the catalyst in grams. The specific rate for CO oxidation (in $\text{mol CO s}^{-1}\text{m}_{\text{cat}}^{-2}$) can be obtained by taking into account the measured BET surface area of the catalyst (A_S)

$$r_{\text{area}} = \frac{r_{\text{mass}}}{A_S} \cdot 10^{-6}$$

An estimate of the turnover frequency (TOF) was calculated assuming our familiar equation

$$\text{TOF} = \frac{r_{\text{area}} \cdot N_A}{PD_{111} \cdot y}$$

where N_A is Avogadro's number, PD_{111} is the planar density of cerium atoms in the {111} plane of CeO_2 (in units of atoms m^{-2}) and y is the amount of transition-metal substitution in ceria determined by STEM-EDS.

Table 5.2 BET surface areas (A_S), apparent activation energies (E_A) and kinetic orders for CO oxidation catalysis on $\text{M}_{0.1}\text{Ce}_{0.9}\text{O}_{2-x}$.

Compound	A_S ($\text{m}^2 \text{g}^{-1}$)	E_A (kJ mol^{-1})	n_{CO}	n_{O_2}
$\text{Mn}_{0.1}\text{Ce}_{0.9}\text{O}_{2-x}$	77.22	56.9	0.58	-0.02
$\text{Fe}_{0.1}\text{Ce}_{0.9}\text{O}_{2-x}$	62.71	98.6	0.48	0.12
$\text{Co}_{0.1}\text{Ce}_{0.9}\text{O}_{2-x}$	17.37	58.5	0.01	0.68
$\text{Ni}_{0.1}\text{Ce}_{0.9}\text{O}_{2-x}$	54.11	57.1	0.28	-0.08
$\text{Cu}_{0.1}\text{Ce}_{0.9}\text{O}_{2-x}$	51.78	43.0	1.15	-0.04

DFT + U slab studies of {111}-terminated $\text{M}_2\text{Ce}_{34}\text{O}_{72-x}$. The energies of {111}-terminated $\text{M}_2\text{Ce}_{34}\text{O}_{72-x}$ slabs ($M = \text{Mn, Fe, Co and Ni}$) were calculated using DFT employing GGA+ U along with PAW pseudopotentials as described in Chapter 3. All calculations were performed using either the Cray XE6 (“Hopper”) or Cray XC30 (“Edison”)

supercomputers at the National Energy Research Scientific Computing Center (NERSC). Only the most stable $\text{nn-M}^{(4-x)+}_2\text{Ce}_{34}\text{O}_{72-x}$ models were employed for energy calculations, removing oxygen atoms at the surface region to simulate the reduction of the transition-metal. As with the previous three chapters, a Hubbard U_{eff} on-site correction term of 4.0 eV was applied to the 4f orbitals of cerium to allow for an accurate description of the electronic structure of oxidized and reduced ceria. Again, a dipole correction was applied to the local potential to correct for systematic errors arising from periodic boundary conditions. Electronic and ionic optimization of the slabs was carried out using the conjugate gradient algorithm with a plane-wave cutoff of 400 eV within the VASP suite. All atomic layers were allowed to relax until all the forces acting on the atoms reached a value below 0.01 eV Å⁻¹. Owing to the large size of the slabs studied here, all data were reported from the integration of the Brillouin zone at the Γ point only.

Estimates for the Gibbs energy of formation (ΔG_{F}) of the different slabs of $\text{nn-M}^{(4-x)+}_2\text{Ce}_{34}\text{O}_{72-x}$ as a function of oxygen partial pressure were determined, as described in detail in Chapter 3, according to the strategy employed by Reuter, *et al.*,¹⁷ referenced to the highest energy $\text{nn-M}^{4+}_2\text{Ce}_{34}\text{O}_{72}$ slab. The oxygen-ion vacancy formation energy for each set of metal-substituted ceria models were calculated directly from the DFT energies of the slabs and molecular oxygen

$$E_{\text{vac}} = E(\text{M}_2\text{Ce}_{34}\text{O}_{70}) + \frac{1}{2}E(\text{O}_2) - E(\text{M}_2\text{Ce}_{34}\text{O}_{71})$$

5.7 References

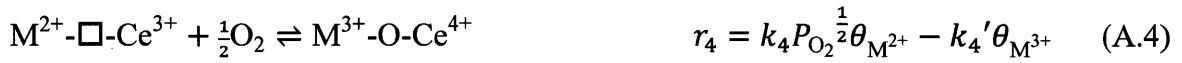
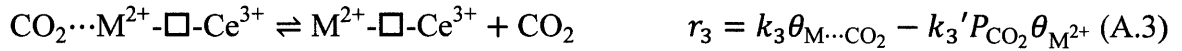
- (1) Tascon, J. M. D.; Gonzalez Tejuca, L. *Reaction Kinetics and Catalysis Letters* **1980**, *15*, 185.
- (2) Tejuca, L. G.; Fierro, J. L. G.; Tascon, J. M. D. *Adv. Catal.* **1989**, *36*, 237.
- (3) Suntivich, J.; Gasteiger, H. A.; Yabuuchi, N.; Nakanishi, H.; Goodenough, J. B.; Shao-Horn, Y. *Nat. Chem.* **2011**, *3*, 546.
- (4) Suntivich, J.; May, K. J.; Gasteiger, H. A.; Goodenough, J. B.; Shao-Horn, Y. *Science* **2011**, *334*, 1383.
- (5) Sedmak, G.; Hocevar, S.; Levec, J. *J. Catal.* **2004**, *222*, 87.
- (6) Jia, A.-P.; Hu, G.-S.; Meng, L.; Xie, Y.-L.; Lu, J.-Q.; Luo, M.-F. *J. Catal.* **2012**, *289*, 199.

- (7) Sedmak, G.; Hocevar, S.; Levec, J. *J. Catal.* **2003**, *213*, 135.
- (8) Luo, J.-Y.; Meng, M.; Zha, Y.-Q.; Guo, L.-H. *J. Phys. Chem. C* **2008**, *112*, 8694.
- (9) Sevcikova, K.; Nehasil, V.; Vorokhta, M.; Haviar, S.; Matolin, V.; Matolinova, I.; Masek, K.; Pis, I.; Kobayashi, K.; Kobata, M.; Nagata, T.; Matsushita, Y.; Yoshikawa, H. *Mater. Res. Bull.* **2015**, *67*, 5.
- (10) Carrettin, S.; Concepción, P.; Corma, A.; López Nieto, J. M.; Puentes, V. F. *Angew. Chem. Int. Ed.* **2004**, *43*, 2538.
- (11) Kim, H. Y.; Lee, H. M.; Henkelman, G. *J. Am. Chem. Soc.* **2011**, *134*, 1560.
- (12) Svetlitchnyi, V.; Peschel, C.; Acker, G.; Meyer, O. *J. Bacteriol.* **2001**, *183*, 5134.
- (13) Jeoung, J.-H.; Dobbek, H. *Science* **2007**, *318*, 1461.
- (14) Fessler, J.; Jeoung, J.-H.; Dobbek, H. *Angew. Chem. Int. Ed.* **2015**, *54*, 8560.
- (15) Hansen, H. A.; Varley, J. B.; Peterson, A. A.; Nørskov, J. K. *J. Phys. Chem. Lett.* **2013**, *4*, 388.
- (16) Kuhn, M.; Bishop, S. R.; Rupp, J. L. M.; Tuller, H. L. *Acta Mater.* **2013**, *61*, 4277.
- (17) Reuter, K.; Scheffler, M. *Phys. Rev. B: Condens. Matter Mater. Phys.* **2001**, *65*, 035406.

Appendix A – Derivation of Rate Expressions

A.1 Mars-van Krevelen

According to the Mars-van Krevelen mechanism proposed in Figure 4.2, there are four elementary steps involved in CO oxidation on ceria-based materials. The rates (r_i) for these steps are determined by their respective rate laws:



where P are partial pressures of gases, θ are coverages for different copper sites and k are kinetic rate constants for each elementary step. Note that the reaction mechanism is identical to that described in Chapter 1 (Figure 1.4B) if Ce^{4+} and M^{3+} are replaced with M^{n+} . The site balance is given by:

$$\theta_{\text{M}^{3+}} + \theta_{\text{M}\cdots\text{CO}} + \theta_{\text{M}\cdots\text{CO}_2} + \theta_{\text{M}^{2+}} = 1 \quad (\text{A.5})$$

Now, assuming that elementary step 2 is rate-determining, the overall reaction rate is given by equation 2 and the other steps can be considered to follow the steady-state approximation ($r_1 = r_3 = r_4 = 0$). For elementary step 1 (Equation A.1), we can write

$$0 = k_1 P_{\text{CO}} \theta_{\text{M}^{3+}} - k_1' \theta_{\text{M}\cdots\text{CO}}$$

$$\theta_{\text{M}\cdots\text{CO}} = \frac{k_1 P_{\text{CO}}}{k_1'} \theta_{\text{M}^{3+}} \quad (\text{A.6})$$

Similarly, for elementary step 3 (Equation A.3)

$$0 = k_3 \theta_{\text{M}\cdots\text{CO}_2} - k_3' P_{\text{CO}_2} \theta_{\text{M}^{2+}}$$

$$\theta_{\text{M}\cdots\text{CO}_2} = \frac{k_3' P_{\text{CO}_2}}{k_3} \theta_{\text{M}^{2+}} \quad (\text{A.7})$$

Combining Equations A.2, A.6 and A.7, we can write an expression for the overall rate of CO oxidation:

$$r_{M-vK} = \frac{k_1 k_2 P_{CO}}{k_1'} \theta_{M^{3+}} - \frac{k_2' k_3' P_{CO_2}}{k_3} \theta_{M^{2+}} \quad (A.8)$$

Under our steady-state approximation, elementary step 4 (Equation A.4) can also be written as

$$0 = k_4 P_{O_2}^{\frac{1}{2}} \theta_{M^{2+}} - k_4' \theta_{M^{3+}}$$

$$\theta_{M^{2+}} = \frac{k_4'}{k_4 P_{O_2}^{\frac{1}{2}}} \theta_{M^{3+}} \quad (A.9)$$

Combining Equations A.8 and A.9 gives

$$r_{M-vk} = \left(\frac{k_1 k_2 P_{CO}}{k_1'} - \frac{k_2' k_3' k_4' P_{CO_2}}{k_3 k_4 P_{O_2}^{\frac{1}{2}}} \right) \theta_{M^{3+}} \quad (A.10)$$

Finally, from the site-balance (Equation A.5) and Equations A.6, A.7 and A.9, we have

$$\theta_{M^{3+}} = 1 - \theta_{M \cdots CO} - \theta_{M \cdots CO_2} - \theta_{M^{2+}}$$

$$\theta_{M^{3+}} = 1 - \frac{k_1 P_{CO}}{k_1'} \theta_{M^{3+}} - \frac{k_3' k_4' P_{CO_2}}{k_3 k_4 P_{O_2}^{\frac{1}{2}}} \theta_{M^{3+}} - \frac{k_4'}{k_4 P_{O_2}^{\frac{1}{2}}} \theta_{M^{3+}}$$

$$\theta_{M^{3+}} = \frac{1}{1 + \frac{k_1 P_{CO}}{k_1'} + \frac{k_4'}{k_4 P_{O_2}^{\frac{1}{2}}} \left(1 + \frac{k_3' P_{CO_2}}{k_3} \right)} \quad (A.11)$$

Under steady-state conditions, we can define equilibrium constants for CO adsorption ($K_{CO \text{ ads}}$), CO_2 desorption ($K_{CO_2 \text{ des}}$) and oxygen vacancy formation (K_{vac}) as

$$K_{CO \text{ ads}} = \frac{k_1}{k_1'}$$

$$K_{CO_2 \text{ des}} = \frac{k_3}{k_3'}$$

$$K_{vac} = \frac{k_4'}{k_4}$$

Hence Equations A.10 and A.11 can be combined using these definitions to give our overall rate law

Appendix A

$$r_{M-vK} = \left(k_2 K_{CO\ ads} P_{CO} - \frac{k_2' K_{vac} P_{CO_2}^{\frac{1}{2}}}{K_{CO_2\ des} P_{O_2}^{\frac{1}{2}}} \right) \theta_{M^{3+}}$$

$$r_{M-vK} = \frac{k_2 K_{CO\ ads} P_{CO} - \frac{k_2' K_{vac} P_{CO_2}^{\frac{1}{2}}}{K_{CO_2\ des} P_{O_2}^{\frac{1}{2}}}}{1 + K_{CO\ ads} P_{CO} + \frac{K_{vac}}{P_{O_2}^{\frac{1}{2}}} \left(1 + \frac{P_{CO_2}}{K_{CO_2\ des}} \right)} \quad (A.12)$$

The desorption of CO₂ from transition-metal ions is considered quite facile ($1/K_{CO_2\ des} = 0$), hence our rate expression simplifies to

$$r_{M-vK} = \frac{k_2 K_{CO\ ads} P_{CO}}{1 + K_{CO\ ads} P_{CO} + \frac{K_{vac}}{P_{O_2}^{\frac{1}{2}}}}$$

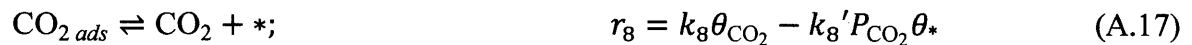
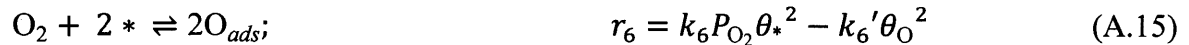
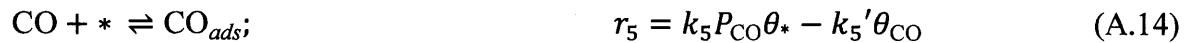
The formation of oxygen vacancies is generally considered thermodynamically unfavorable ($K_{vac} \approx 0$), so we can further simplify our rate expression to

$$r_{M-vK} = \frac{k_2 K_{CO\ ads} P_{CO}}{1 + K_{CO\ ads} P_{CO}} \quad (A.13)$$

Hence, at sufficiently low pressures, our simplified rate expression predicts that CO oxidation is first-order with CO and zeroth order with O₂.

A.2 Langmuir-Hinshelwood

According to the Langmuir-Hinshelwood mechanism, which is often cited for catalysis on metallic surfaces, CO oxidation undergoes proceeds through four elementary steps. The rates (r_i) for these elementary steps are given by the following equations:



where, as before, the partial pressures of the gases are given by P , the surface coverages are given by θ and the kinetic rate constants are given by k . In contrast to the Mars-van Krevelen

mechanism, CO adsorption (Equation A.14) and dissociative O₂ adsorption (Equation A.15) compete for the same surface adsorption sites on the metal (represented by *). The subsequent reaction of adsorbed CO and O to form adsorbed CO₂ (Equation A.16) is generally considered the rate determining step, while the desorption of CO₂ (Equation A.17) is considered to be very fast as it does not interact strongly with metallic surfaces. The site balance is

$$\theta_* + \theta_{\text{CO}} + \theta_{\text{O}} + \theta_{\text{CO}_2} = 1 \quad (\text{A.18})$$

Assuming that the third elementary step is rate-determining, the overall rate of the reaction is given by its rate expression (Equation A.16). Under steady-state conditions all other rate expressions are zero. The rate expression for the first elementary step (Equation A.14) thus becomes

$$0 = k_5 P_{\text{CO}} \theta_* - k_5' \theta_{\text{CO}}$$

$$\theta_{\text{CO}} = \frac{k_5 P_{\text{CO}}}{k_5'} \theta_* \quad (\text{A.19})$$

Similarly, for the second elementary step (Equation A.15) and fourth elementary step (Equation A.17) we can write

$$\theta_{\text{O}} = \left(\frac{k_6 P_{\text{O}_2}}{k_6'} \right)^{1/2} \theta_* \quad (\text{A.20})$$

$$\theta_{\text{CO}_2} = \frac{k_8' P_{\text{CO}_2}}{k_8} \theta_* \quad (\text{A.21})$$

Combining Equations A.16 with A.19-A.21, we have our overall rate law expressed in terms of θ_* :

$$r_{L-H} = \left(\frac{k_5 k_7}{k_5'} \left(\frac{k_6}{k_6'} \right)^{1/2} P_{\text{CO}} P_{\text{O}_2}^{1/2} - \frac{k_5' k_8'}{k_8} P_{\text{CO}_2} \right) \theta_*^2 \quad (\text{A.22})$$

The value of θ_* can be solved by applying Equations A.19-A.21 with our equation for site balance (Equation A.18)

Appendix A

$$\left(1 + \frac{k_5 P_{CO}}{k_{5'}} + \left(\frac{k_6 P_{O_2}}{k_{6'}}\right)^{1/2} + \frac{k_{8'} P_{CO_2}}{k_8}\right) \theta_* = 1$$

$$\theta_* = \frac{1}{\left(1 + \frac{k_5 P_{CO}}{k_{5'}} + \left(\frac{k_6 P_{O_2}}{k_{6'}}\right)^{1/2} + \frac{k_{8'} P_{CO_2}}{k_8}\right)} \quad (A.23)$$

Since we are assuming steady-state conditions, we can define some equilibrium constants as before

$$K_{CO\ ads} = \frac{k_5}{k_{5'}}$$

$$K_{O_2\ ads} = \frac{k_6}{k_{6'}}$$

$$K_{CO_2\ des} = \frac{k_8}{k_{8'}}$$

Substituting these equilibrium constants and combining Equations A.22 and A.23 gives our overall rate expression for the Langmuir-Hinshellwood mechanism for CO oxidation,

$$r_{L-H} = \frac{k_7 K_{CO\ ads} K_{O_2\ ads}^{1/2} P_{CO} P_{O_2}^{1/2} - \frac{k_{7'}}{K_{CO_2\ des}} P_{CO_2}}{\left(1 + K_{CO\ ads} P_{CO} + K_{O_2\ ads}^{1/2} P_{O_2}^{1/2} + \frac{1}{K_{CO_2\ des}} P_{CO_2}\right)^2} \quad (A.24)$$

As stated earlier, CO₂ desorption is facile on most metallic surfaces ($1/K_{CO_2\ des} \approx 0$), so Equation A.24 can be simplified to

$$r_{L-H} = \frac{k_7 K_{CO\ ads} K_{O_2\ ads}^{1/2} P_{CO} P_{O_2}^{1/2}}{\left(1 + K_{CO\ ads} P_{CO} + K_{O_2\ ads}^{1/2} P_{O_2}^{1/2}\right)^2} \quad (A.25)$$

In most cases, CO adsorption is much more enthalpically favored than dissociative O₂ adsorption on metallic surfaces ($K_{CO\ ads} P_{CO} \gg (1 + (K_{O_2\ ads} P_{O_2})^{1/2})$), hence Equation A.25 can be further simplified:

$$r_{L-H} = \frac{k_7 K_{CO\ ads} K_{O_2\ ads}^{1/2} P_{CO} P_{O_2}^{1/2}}{(K_{CO\ ads} P_{CO})^2}$$

$$r_{L-H} = \frac{k_7 K_{O_2\ ads}^{1/2} P_{O_2}^{1/2}}{K_{CO\ ads} P_{CO}} \quad (A.26)$$

Thus the Langmuir-Hinshelwood mechanism for CO oxidation on metallic surfaces predicts a negative first order partial pressure dependence on CO and a half-order dependence on O₂.

Biographical Note

The author was born on September 28th, 1986, in Philadelphia, PA. At an early age, he expressed interest in the natural world and human anatomy and he memorized all of the bones in the human skeleton. As a child, he wanted to grow up to perform autopsies for a living. Inspired by works of science fiction such as *Dune* and *the X-Files*, his childhood was characterized by a fascination in space exploration and extraterrestrial life in particular. Under the guidance of many great science educators (Ms. Nutt, Mr. Clark and Ms. Hillink) throughout his time at Chestnut Hill Academy in Philadelphia, he explored many facets of science and technology through his own experiments and inventions, such as a study on static and kinetic friction of common household oils and the development of more efficient systems for the delivery of breakfast cereals. He enrolled in Reed College in 2005 as a biology major, but quickly changed his focus to biochemistry and then chemistry. In 2007, he began work in the laboratory of Professor Ronald McClard at Reed, synthesizing and characterizing new pyrrolidine-based transition-state inhibitors for orotate phosphoribosyltransferase. In the summer of 2008, he participated in the first NSF-sponsored research experience for undergraduates (REU) program to take place in Brasil, where, under the guidance of Professor Marcelo Ganzarolli de Oliveira at UNICAMP, he developed novel polynitrosylated polyester blends for controlled nitric oxide release for application in biomedical coatings. His senior thesis project was supervised by Professor Margret J. Gesselbracht, where he employed advanced NMR techniques to investigate the mechanism of formation of vanadium pentoxide gels for application in lithium-ion battery cathodes. After receiving a B.A. in Inorganic Chemistry at Reed, he began his PhD in Inorganic Chemistry at the Massachusetts Institute of Technology in 2010, and joined the Electrochemical Energy Lab under the guidance of Professor Yang Shao-Horn in 2011. His thesis sought to understand the molecular structure, mechanism and design descriptors for CO oxidation catalysis on substituted ceria nanoparticles. Following his PhD, Joe plans to join the laboratory of Professor Daniel G. Nocera at Harvard University as a postdoctoral researcher in the field of carbon dioxide reduction electrocatalysis.

JOSEPH S. ELIAS

Department of Chemistry
Massachusetts Institute of Technology
77 Massachusetts Ave.
Cambridge, MA 02139

Building 31, Room 064
phone: (610)-304-2647
email: jselias@mit.edu

EDUCATION

B.A. in Chemistry, Reed College, Portland, OR. 2009

CURRENT POSITION

Ph.D. (expected June 2016), Department of Chemistry, MIT. 2010 – present
Thesis Advisor: Professor Yang Shao-Horn

RESEARCH EXPERIENCE

Research Assistant, Department of Chemistry, MIT. 2011 – present
Advisor: Professor Yang Shao-Horn

- Developed synthetic strategies for the preparation of monodisperse, phase-pure transition-metal-substituted ceria nanoparticles.
- Identified the active site for copper/cerium oxide catalysts for CO oxidation.
- Proposed and tested a new mechanism of CO oxidation catalysis on ceria-based catalysts that centers on the formation of oxygen vacancies at high-valent transition-metal ions using *in-situ* synchrotron-based spectroscopies.
- Determined design descriptors for CO oxidation catalysis on oxides by synergizing density-functional theory calculations with experiment.

Research Assistant, Department of Chemistry, Reed College. 2008 – 2009
Advisor: Professor Margret J. Geselbracht

- Investigated the mechanism of formation of vanadium pentoxide ambigels for application in lithium-ion battery cathodes.
- Employed NMR spectroscopy to determine the coordination chemistry of vanadium complexes in solution.

NSF-REU Research Assistant, Department of Chemistry, UNICAMP. 2008
Advisor: Professor Marcelo Ganzarolli de Oliveira

- Developed novel polynitrosated polyester blends for controlled nitric oxide release for biomedical coatings.
- Quantified platelet aggregation on polynitrosated polyester-coated surfaces.

RESEARCH INTERESTS

Descriptor-driven design, synthesis and characterization of solid state inorganic materials and their coupling to theory through computational modeling for applications in energy and environmental challenges, particularly in:

Heterogeneous Catalysis

- Design of nanoparticulate, ceria-based materials for CO oxidation catalysis.
- Multi-site, bifunctional oxide catalysts to break linear free energy scaling relationships.

Electrochemical Conversion and Storage

- Nanostructured materials for supercapacitors.
- Inorganic materials for water electrolysis and CO₂ reduction.

HONORS

- National Science Foundation Graduate Research Fellow 2011 – 2016
- Best Poster Prize, Gordon Research Conference: Chemical Reactions at Surfaces 2015
- Phi Beta Kappa 2009

PUBLICATIONS

Refereed Journals:

- Elias, J. S.; Artrith, N.; Bugnet, M.; Giordano, L.; Botton, G. A.; Kolpak, A. M. & Shao-Horn, Y. "Elucidating the Nature of the Active Phase in Copper/Ceria Catalysts for CO Oxidation," *ACS Catalysis*, **2016** 1675-1679.
- Stephens, I. E. L.; Elias, J. S. & Shao-Horn, Y. "The importance of being together: Controlling the coordination of platinum boosts catalytic reaction rates," *Science*, **2015**, *350*, 164-165.
- Elias, J. S.; Risch, M.; Giordano, L.; Mansour, A. N. & Shao-Horn, Y. "Structure, Bonding, and Catalytic Activity of Monodisperse, Transition-Metal-Substituted CeO₂ Nanoparticles," *J. Am. Chem. Soc.*, **2014**, *136*, 17193-17200.

INVITED PRESENTATIONS

- 250th American Chemical Society National Meeting, Boston, MA *August 2015*
- ICMAT & IUMRS-ICA Conference, Singapore *July 2015*
- Chinese University of Hong Kong, Hong Kong *June 2015*

CONTRIBUTING PRESENTATIONS

- Oral Presentation, NanoKorea Expo, Seoul, Korea *July 2015*
- Poster and Oral Presentations, Chemical Reactions at Surfaces Gordon Research Conference, Ventura, CA *March 2015*
- Poster Presentation, ISE Annual Meeting, Lausanne, Switzerland *September 2014*
- Poster Presentation, Inorganic Chemistry Gordon Conference, Biddeford, ME *June 2014*
- Poster Presentation, MRS Fall Meeting and Exhibit, Boston, MA *December 2013*
- Poster Presentation, SUNCAT Summer Institute, Stanford, CA *August 2013*

Acknowledgements

This thesis is not a collection of hypotheses, experiments, data, analyses and conclusions. I believe those are just the byproducts of the relationships (old and new) I've had with some incredible people over the past several years. The science contained in these words and figures would not come into existence were it not for the amazing people who inspired me to pick up a round bottom flask or to put another catalyst in the reactor. I realize that I owe a tremendous debt of gratitude to these people. Not simply because they helped me with an experiment or made me look at something with a new perspective, but because they have guided me, through the example of their own lives, on how to become a better chemist. I think that is the true purpose of a PhD.

I would like to thank Yang first. When I first met you, I thought my life in the Electrochemical Energy Lab would be a walk in the park. Thank you for not living up to my expectations. I cannot imagine a tougher boss! I'm so fortunate to have had an advisor whose skepticism and curiosity, especially concerning topics in chemistry, made me reevaluate my personal standards of scientific proof. Thank you for making me realize that I need to hold myself to higher standards and for encouraging me to grow with added responsibilities (or 'burdens' to the uninitiated).

Believe it or not, Mircea, but you have inspired me in more ways than you can ever imagine! I've really enjoyed our semi-annual chats in your office, which have often left me with a tremendous feeling of hope and an elevated self-esteem. To me you're like a fine wine. With age you become even more complex and palatable! I'd like to thank Tim as well, for being a great collaborator with the PMI project and for being an all-around nice professor to work with. Most of my work would simply not have existed without your help!

I've had the tremendous good fortune of being taught by several great educators at MIT and elsewhere. There would not have been any catalysis without Yuriy Román, who, with his students and postdocs, taught me everything there is to know about plug-flow reactors. A physically intimidating and yet an extraordinarily friendly and approachable Grizzly bear of a man, you are a model educator! I'd also like to thank Alexie Kolpak and Nongnuch Artrith for sharing their expertise in DFT and applying concepts in machine learning to understand how copper ions in nanoparticles arrange. It was a rare treat working alongside you. Similarly, I owe a huge debt of gratitude to Gianluigi Botton and his students and postdocs,

Acknowledgements

especially Matthieu Bugnet, for actually visualizing such atomic-level arrangements. Thanks to Peter Müller, who acquired the single crystal data and who gave me advice on crystal structure refinement. More importantly, thanks for enabling me to join the ranks of “real chemists” by letting me solve my own crystal structures. I would also like to thank all of the folks at PMI for their generous support and continued collaboration. In particular, I’d like to thank Gianluca, Ping, Silvia, Aurelian and Firooz with whom I’ve had great conversations over the years about low-temperature CO oxidation in more catalytically demanding applications.

Marcel Risch and Azzam Mansour, you are my heroes. Who would have thought that physicists would be so cool! Thank you so much for teaching me all I know about XAFS, and for sharing the pain that was collecting those spectra at NSLS. Both of you have taught me tough lessons on how to value data quality above everything else (even my personal happiness and health!). I constantly daydream of a situation where we could all have beamtime together again with ample portions of all-you-can-eat shrimp at Popei’s.

While we didn’t have as extensive adventures in Berkeley, I owe a huge debt to Kelsey Stoerzinger and Wesley Hong for their expertise at 9.3.2 and for helping me acquire, analyze and appreciate near-ambient pressure XPS. I’m so glad we splurged on that convertible! I also had the great opportunity to work with some fantastic scientists at NSLS, ALS, and CLS. My thanks go out to Kumi Pandya, Ethan Crumlin and Tom Regier at those respective establishments.

Some of the people I met along the way have encouraged me in unconventional ways. Thank you Nir Pour, Alexis Jules Louis Grimaud and Jin Suntivich for reminding me to be politically incorrect. I had the privilege of working alongside so many wonderful students and postdocs at EEL, and I would like to especially acknowledge my co-inhabitants of 31-064, past and present, for bringing a smile to my face every single day: Betar Gallant, David Fenning, Dongkyu Lee, Dongwook Lee, Youngmin Lee, Reshma Rao, Jonathan Hwang and Karthik Akkiraju. I would like to especially thank Youngmin, Chris Carlton and Livia Giordano who taught me everything I needed to know about colloidal syntheses, TEM and DFT, respectively. Over the last nine months, I’ve had the pleasure of working alongside Karthik, who’s taught me to think of things in the context of non-dualism (nothing is good or bad, but rather, everything is “not-bad”). I am looking forward to see what directions you

will take the gas-phase catalysis research to. I'd also like to give a shout out to Kevin May, Chris Kuryak, Koffi Pierre Claver Yao, Alex Binghong Han and David Kwabi, who, along with Kelsey and Wesley, joined EEL about the same time I did and who have commiserated with me over the years. In the last couple of years, I've had the rare treat of also working alongside Jennifer and Raivo, a pair of very talented undergrads who both have bright futures ahead of them. Good luck finishing up at MIT!

Finally, I would like to thank my cheering squad. I'm fortunate to have three older sisters, Abi, Margaret and Clara, that collectively act as the voice of reason, and I'd like to thank the kiddos, Zeke, Susie, Pierce and Baby Jenny, for reminding me to always enjoy the simple things in life. Tim and Amias continue to be extremely encouraging brothers-in-law. Many thanks go to Nickel for being the greatest friend anyone could have. I'm so sorry nickel turned out to be such a disappointment! Thanks for your continued support, Clémence; I will certainly file this into the 'nice folder!' I'd also like to thank the members of the Harvard/MIT District, especially Tanya, Daniel, Cherese, Carlos and Dee, for never giving up on me (even when I did), and for helping me understand how I can transform my personal struggles into valuable, character-building experiences. Finally, I'd like to share my appreciation of my fairy god-parents Charlotte, Peggy and Beau, who have helped me along in so many ways over the years. Thank you!